JYU DISSERTATIONS 839

Aku Lempelto

Computational Modelling of Carbon Dioxide Reduction to Methanol on Heterogeneous Zirconia-Supported Copper Catalysts

UNIVERSITY OF JYVÄSKYLÄ
FACULTY OF MATHEMATICS
AND SCIENCE

JYU DISSERTATIONS 839

Aku Lempelto

Computational Modelling of Carbon Dioxide Reduction to Methanol on Heterogeneous Zirconia-Supported Copper Catalysts

Esitetään Jyväskylän yliopiston matemaattis-luonnontieteellisen tiedekunnan suostumuksella
julkisesti tarkastettavaksi Ylistönrinteen auditoriossa FYS1
marraskuun 8. päivänä 2024 kello 12.

Academic dissertation to be publicly discussed, by permission of
the Faculty of Mathematics and Science of the University of Jyväskylä,
in Ylistönrinne, auditorium FYS1, on November 8, 2024, at 12 o'clock.

JYVÄSKYLÄN YLIOPISTO
UNIVERSITY OF JYVÄSKYLÄ

JYVÄSKYLÄ 2024

Editors
Karoliina Honkala
Department of Chemistry, University of Jyväskylä
Päivi Vuorio
Open Science Centre, University of Jyväskylä

ISBN 978-952-86-0360-3
ISSN 2489-9003

Permanent link to this publication: http://urn.fi/URN:ISBN:978-952-86-0360-3

ABSTRACT

Lempelto, Aku
Computational modelling of carbon dioxide reduction to methanol on heterogeneous zirconia-supported copper catalysts
Jyväskylä: University of Jyväskylä, 2024, 78 p. (+included articles)

In this dissertation, computational modelling methods based in density functional theory (DFT) were used to investigate the structure and adsorption characteristics of a heterogeneous catalytic system, consisting of zirconia-supported copper nanoparticles with a zinc oxide promoter (CZZ), that is used for carbon dioxide conversion to methanol (CTM). Supplementary analysis methods, such as the energetic span model and atomistic thermodynamics, were used to examine the stability and catalytic performance of the ternary Cu–Zn(O)–ZrO_2 interface.

An extended screening was conducted to establish a suitable computational model for representing the metal–zirconia interface. Our results demonstrate how the specific internal geometry of a nanorod model and strains caused by lattice mismatch between Cu and ZrO_2 affect CO_2 adsorption at the interface, even leading to an overestimation of binding strength. The effect of Zn centres at the active interface sites was examined by using mixed CuZn interfaces and modelling the full catalytic network of CO_2 CTM using DFT and energetic span analysis. The calculated binding of reaction intermediates demonstrated how Zn incorporated into the catalyst metal selectively stabilizes certain species, such as CO_2, COOH and H_2CO. The energetic span analysis suggests that a reverse water–gas shift reaction followed by CO hydrogenation is the mechanistic pathway with the highest turnover frequency. An examination of ZnO monomers and sub-nano clusters on the zirconia surface suggests that the ZrO_2 support offers some resistance to the initial stages of agglomeration. An atomistic thermodynamics analysis suggests that the complete reduction of zirconia-bound ZnO into metallic Zn is unfavourable. Our results offer an atomic-level view of the behaviour of the ZnO promoter and its effect on CO_2 adsorption and conversion.

Keywords: heterogeneous catalysis, density functional theory, metal–oxide interface, methanol

TIIVISTELMÄ

Lempelto, Aku
Hiilidioksidin katalyyttiseen vedyttämiseen metanoliksi käytettävien heterogeenisten kuparikatalyyttien laskennallinen mallinnus
Jyväskylä: University of Jyväskylä, 2024, 78 s. (+artikkelit)

Tässä väitöskirjassa tarkasteltiin hiilidioksidin vedyttämiseen metanoliksi käytettävien, heterogeenisten Cu/ZnO/zirkoniakatalyyttien (CZZ) rakennetta ja adsorptio-ominaisuuksia, käyttäen työvälineenä tiheysfunktionaaliteoriaan (density functional theory, DFT) perustuvia mallinnusmenetelmiä. Muita matemattisia malleja, kuten energiavälimallia (energetic span model) ja atomistista termodynamiikkaa, käytettiin CZZ systeemin kolmen komponentin välisen rajapinnan katalyyttisen aktiivisuuden ja stabiilisuuden arviointiin.

Sopiva laskennallinen malli kuvaamaan metalli–zirkonia rajapintaa valittiin laajan seulonnan pohjalta. Sen tulokset osoittavat, kuinka käytetyn nanosauvamallin rakenne ja yksikkökopin valinnasta aiheutuva jännite johtavat sekä hiilidioksidin liian voimakkaaseen kiinnittymiseen. Sinkkipromoottorin vaikutusta tarkasteltiin käyttäen mallia, jossa Cu–zirkonia-rajapintaan seostettiin sinkkiatomeja. Hiilidioksidin vedytyksen alkeisreaktiot CuZn–ZrO_2 mallinnettiin Cu ja CuZn rajapinnoilla DFT:tä ja energiavälimallia käyttäen. Laskut havainnollistavat, kuinka Zn keskukset rajapinnalla stabiloivat valikoivasti tiettyjä adsorbaatteja ja reaktiovälituotteita, kuten CO_2, COOH, ja H_2CO. Energiavälianalyysin ennakoi vedytyksen kulkevan nopeiten käänteisen vesikaasun siirtoreaktion ja hiilimonoksidin vedytyksen kautta. Työssä tutkittiin myös suuresti hajaantuneen sinkkipromoottorin rakennetta ja hapetus–pelkistysominaisuuksia zirkonian pinnalla. Laskujen osoittama sinkkioksidimonomeerien ja pienten agglomeraattien stabiilisuus zirkoniapinnalla viittaa niiden taipumukseen vastustaa suurempien partikkeleiden kasvua. Atomistinen termodynaaminen tarkastelu vahvistaa, että zirkonia estää myös sinkkioksidia pelkistymistä täysin, myös reaktio-olosuhteissa. Tulokset tarjoavat atomitason tietoa sinkkioksidipromoottorin toiminnasta ja vaikutuksesta hiilidioksidin kiinnittymiseen ja vedytykseen.

Avainsanat: heterogeeninen katalyysi, tiheysfunktionaaliteoria, metalli–oksidi rajapinta, metanoli

Author

Aku Lempelto

https://orcid.org/0000-0002-7731-0395
Faculty of Mathematics and Science,
University of Jyväskylä,
Finland

Supervisor

Prof. Karoliina Honkala
Faculty of Mathematics and Science,
University of Jyväskylä,
Finland

Reviewers

Dr. Ping Liu
Chemistry Division,
Brookhaven National Laboratory,
The United States of America

Asst. Prof. Ivo Filot
Department of Chemical Engineering and Chemistry,
Eindhoven University of Technology,
The Netherlands

Opponent

Dr. Carine Michel
Chemistry Laboratory,
CNRS / École Normale Supérieure of Lyon,
France

PREFACE

The original publications that are the basis for this dissertation were created over the course of four-odd years at the Nanoscience Centre of the University of Jyväskylä, starting in April 2020. This work would not have been possible without the financial support of the Research Council of Finland through the C1 Value Academy Programme, as well as a kind personal grant given to me by the Vilho, Yrjö, and Kalle Väisälä Foundation of the Finnish Academy of Science and Letters. I also wish to acknowledge CSC – IT Centre for Science for generously providing the computing resources used herein.

I want to deeply thank my opponent, research director Dr. Carine Michel, as well as the reviewers Dr. Ping Liu and Asst. Prof. Ivo Filot, who have all dedicated much of their time for the benefit of both this dissertation and its public defence. Thank you to my supervisor Prof. Karoliina Honkala for providing her guidance and expertise to our research throughout this project. I have appreciated your investment in the day-to-day research that we carried out, as well as the push that made sure it all got finished in the end. Thank you, Dr. Lars Gell who acted as my computational partner in crime, troubleshooting and scratching our collective heads for three years. Similarly, I want to thank Dr. Toni Kiljunen and Dr. Minttu Kauppinen who both participated greatly in the calculations and authoring of the papers that make up this dissertation. Thank you for offering your invaluable guidance along the way. Additionally, I want to acknowledge the past and present members of the catalysis research group of Assoc. Prof. Riikka Puurunen, located at the Aalto university School for Chemical Engineering, for our collaboration and for the many discussions over the years that have, in part, shaped the direction of the computational studies presented.

Thank you to my family, and all the friends at the Nanoscience Centre whose paths have crossed with mine, for cheering me on along the way.

Aku Lempelto
Jyväskylä,
Friday 8th November, 2024

LIST OF ACRONYMS

ALD	Atomic Layer Deposition
CTM	Conversion to Methanol or CO_2 Transformation to Methanol
CZA	$Cu/ZnO/Al_2O_3$
CZZ	$Cu/ZnO/ZrO_2$
DFT	Density Functional Theory
DME	Dimethyl Ether
DOS	Density of States
ESM	Energetic Span Model
GGA	Generalized Gradient Approximation
LCAO	Linear Combination of Atomic Orbitals
LDA	Local Density Approximation
MD	Molecular Dynamics
MEP	Minimum-Energy Pathway
MH	Minima Hopping
NEB	Nudged Elastic Band
PES	Potential Energy Surface
SIE	Self-interaction error
TDI	TOF-Determining Intermediate
TDTS	TOF-Determining Transition State
TOF	Turnover Frequency
TS	Transition State
vdW	Van der Waals
WF	Wavefunction
XC	Exchange–Correlation
ZP	Zero-point

LIST OF FIGURES

LIST OF TABLES

CONTENTS

LIST OF INCLUDED ARTICLES

I Gell, L.; Lempelto, A.; Kiljunen, T.; Honkala, K. Influence of a Cu–zirconia interface structure on CO_2 adsorption and activation. *J. Chem. Phys.* **2021**, *154*, 214707.
https://doi.org/10.1063/5.0049293

II Arandia, A.; Yim, J.; Warraich, H.; Leppäkangas, E.; Bes, R.; Lempelto, A.; Gell, L.; Jiang, H.; Meinander, K.; Viinikainen, T.; Huotari, S.; Honkala, K.; Puurunen, R. Effect of atomic layer deposited zinc promoter on the activity of copper-on-zirconia catalysts in the hydrogenation of carbon dioxide to methanol. *Appl. Catal. B Environ.* **2023**, *321*, 122046.
https://doi.org/10.1016/j.apcatb.2022.122046

III Lempelto, A.; Gell, L.; Kiljunen, T.; Honkala, K. Exploring CO_2 hydrogenation to methanol at a CuZn–ZrO_2 interface via DFT calculations. *Catal. Sci. Technol.* **2023**, *13*, 4387.
https://doi.org/10.1039/d3cy00549f

IV Lempelto, A.; Kauppinen, M.; Honkala, K. Computational exploration of subnano Zn and Cu species on Cu/ZrO_2: implications for methanol synthesis. *J. Phys. Chem. C* **2024**, *128*, 9492.
https://doi.org/10.1021/acs.jpcc.4c01300

The author carried out half of the DFT calculations in paper I and participated in its writing, contributing equally with L. G. The author completed IR calculations for and co-wrote the computational sections in paper II, again contributing equally with L. G. The author carried out the DFT calculations with the Cu interface and Zn-dilute interface, optimized and completed the energetic span analysis for all interfaces, and acted as the primary author of paper III. He was also the primary author of paper IV, carrying out all DFT and thermodynamic calculations and writing the majority of the manuscript.

1 CARBON DIOXIDE REDUCTION TO METHANOL

1.1 Visions of a methanol economy

Methanol is the simplest of the alcohols. To a chemist, it is a volatile organic solvent with a relatively low boiling point and high vapour pressure. In the common consciousness, it is arguably infamous due to its toxicity to humans, and is often thought of more as an unwanted side product of wood distillation or natural fermentation. Despite this, it is a versatile and ubiquitous industrial platform chemical. Most methanol produced in the world today is converted into acetic acid, acetates, methyl methacrylate, formaldehyde, and many other chemicals that are used in large quantities in the production of polymers such as plastics, synthetic fibres, paints, and adhesives as well as acting as a precursor for several active ingredients in biomedicine and agriculture.[1,2] Since the commercialization of methanol production nearly 200 years ago, its demand has increased continuously, with the current global industry consuming roughly 100 million tonnes of methanol yearly.[2,3] In recent decades, new uses still have been suggested in response to anthropogenic climate change.

As the pressure builds to move away from fossil fuels, groups responsible for the global shipping industry are making plans to cut their CO_2 emissions in half by the year 2050.[4,5] While private and public transit on land have recently shifted towards electrification, it is unlikely that global supply chains will be able to do the same. According to a study by A.P. Møller–Maersk,[6] battery-electric or fuel cell powered ships are not seen as commercially viable in the near future. Instead, the maritime industry has shown significant interest in a variety of so-called e-fuels such as methanol, liquefied natural gas, and ammonia.[4,6,7] Ammonia contains no carbon and thus produces no CO_2 emissions when burnt. However, it is highly toxic and corrosive which can cause concerns of large-scale accidents leading to considerable damage to the environment. Furthermore, while burning ammonia does not produce CO_2, it can lead to the release of some of the harmful oxides of nitrogen, such as N_2O and NO_x, requiring efficient catalytic treatment before release.

The use of methanol in consumer applications, such as personal vehicles is also possible. For example, green methanol may be used as a fuel additive. Very low blends of no more than a few percent require no modifications to modern petrol engines.[3,7] However, more concentrated blends or pure methanol would necessitate the use of corrosion inhibitors and alcohol-resistant engine materials.[7] Methanol could also be used as a precursor to other alternative fuels. For example, catalysts exist that can dimerize methanol into dimethyl ether (DME), a product that could replace diesel or LNG.[8,9] Additionally, methanol can be used in direct methanol fuel cells or internal combustion engines specifically designed for the purpose. In this regard, it competes with generators that run on natural gas or other biofuels. However, the advantage of methanol is that it burns very cleanly due to having many easy-to-break H–C bonds but no C–C bonds that could lead to the release of soot. Furthermore, it is significantly less likely to contain nitrogen and sulfur contaminants than traditional fuels, and consequently it releases only a fraction of the NO_x and SO_x emissions.[7,10] There are other practical considerations, however. Electric vehicle technology has already become fairly ubiquitous in personal transport and large investments have been made to expand charger infrastructure in many places around the world, although it is possible that the challenges and environmental strain of EV battery production as well as uncertainty around electric supply could hold back the adoption of electric vehicles for now. Regardless, it is possible that by now methanol technology is too far behind to compete with electrification in this sector. Instead, methanol may find a more fitting role as a part of the supply, storage, and balancing of electricity in the grid, rather than as a fuel for personal vehicles.

There is a commonly noted problem with our power grids: the supply and demand must match at all times. This has been quoted as a limitation for the adoption of renewable energy, as it is often dependent on unpredictable natural phenomena, such as sunshine and wind. Potential solutions for generating and storing energy when it is available and retrieving it later when it is needed have been suggested. However, they tend to have problems of their own relating to cost and availability, as in the case of large batteries, or geographical dependence, as with pumped hydro-storage. Methanol, on the other hand, may be a practical option here. Excess energy produced when conditions are favourable can be used to power CO_2 conversion to methanol, which can then be stored easily and indefinitely, and used when more electricity is needed. The largest obstacle to this way of storing energy is the relatively low energy efficiency of current conversion-storage methods.[11] However, other recent studies[12,13] considered the practical aspects of this type of closed-loop energy storage system and deemed the idea a feasible solution to long-term energy storage.

Today, the majority of methanol produced at an industrial scale is made using synthesis gas (or syngas)—a mixture of carbon monoxide and hydrogen that is often generated from natural gas and coal through steam reforming. In the midst of global efforts to reduce the use of high-emissions and non-renewable feedstocks, research has been conducted into ways to produce methanol in more renewable ways such as by using biomass as the feedstock. As was already

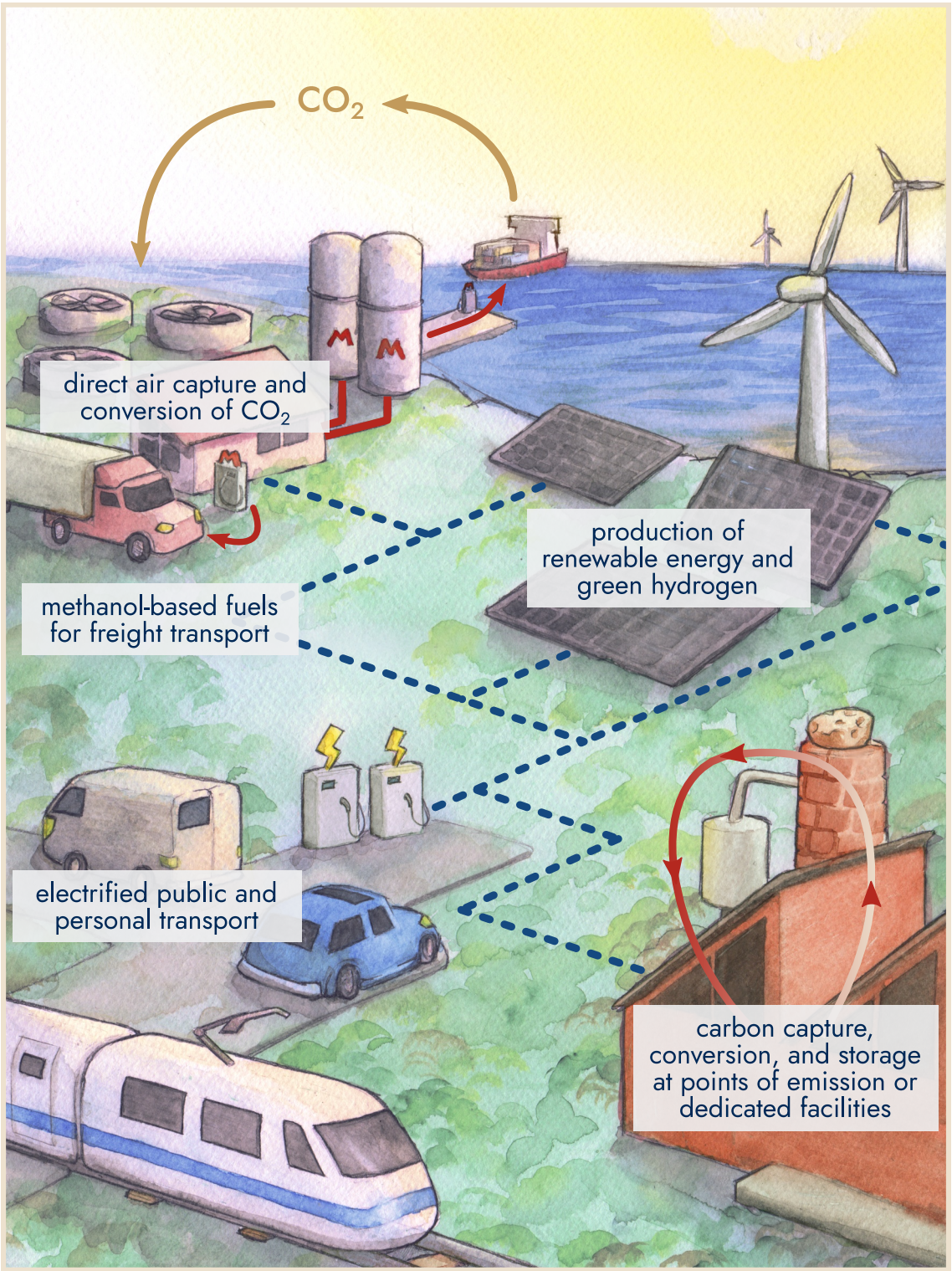

FIGURE 1 Potential uses of methanol in a sustainable economy. CO_2 captured at points of emission or from the atmosphere can be transformed into methanol, providing a means storing energy from renewable or intermittent sources in the molecule's chemical bonds.

hinted, however, another option exists: carbon dioxide conversion to methanol (CTM). The product may also be called e-methanol, as it effectively stores the electric energy used for the conversion in the bonds of the methanol molecule. Operating since 2012, the CRI George Olah Renewable Methanol plant in Iceland was the first of its kind in the world,[8] converting CO_2 from nearby sources into methanol at an industrial scale. At the time of writing, there are also plans in motion for two e-methanol facilities located in Finland—one in Haapavesi and one in Lappeenranta—to begin operation within the next five years.[2,14,15] The current global production of renewable methanol is less than one million tonnes per year,[2,7] less than one hundredth of the global demand. However, estimates by the Methanol Institute[2] suggest that the capacity for e-methanol will reach 16.8 million tonnes per year by 2030, with biomethanol and low carbon methanol bringing the total to 36.1 million. Still, in order to create a fully carbon-neutral supply of methanol for global needs, and perhaps even realize the vision of a future based on carbon recycling as that presented in Figure 1, the catalysts for carbon dioxide conversion into methanol need to be efficient and practical.

1.2 Methanol made from carbon dioxide

In a CTM reaction, a 1:3 mixture of carbon dioxide and hydrogen gas reacts to form methanol according to:

$$CO_2 + 3\,H_2 \longrightarrow CH_3OH + H_2O\,\cdot \tag{R1}$$

This reaction is thermodynamically favourable, as it is exothermic by 0.52 eV (or $50\,\mathrm{kJ\,mol^{-1}}$). This, assisted by high reaction pressures, shifts the equilibrium firmly on the side of the products. However, carbon dioxide is a highly stable molecule with higher-order covalent C–O bonds that are difficult to disrupt.[16] Therefore, its chemically activation and conversion into other products requires harsh reaction conditions. Current research in the field aims mainly at designing and discovering catalytic materials with maximal selectivity and activity for methanol production that are still active at less demanding conditions.

CARBON CAPTURE AND STORAGE. Points of emission, such as power plants and industrial locations, are well suited for carbon capture. Amine gas treating (or "scrubbing") efficiently removes CO_2 and H_2S from gas mixtures, and has been used to clean industrial waste gases for decades.[17,18] The process typically produces "sour gas", or a mixture of the H_2S and CO_2 components, from which the latter can be separated, although this can be a relatively expensive. Several technologies also exist that can be used to capture CO_2 released when natural gases or similar fuels are burned for power generation, *e.g.* SCOC-CC,[19] the CES cycle (or water cycle),[20] and the Allam–Fetvedt cycle.[21–23] With these systems, it is actually feasible to capture up to 100 % of the CO_2 produced.[19,21,24] In theory, these generators could also easily be adapted to run on methanol, enclosing the carbon cycle in one location. The idea of directly capturing carbon

dioxide from the atmosphere using various synthetic and bio-derived adsorbents has also gained significant attention.[18,25,26] Air capture is somewhat limited by the relatively low concentration of CO_2 in the atmosphere,[25,26] but could provide a type of "carbon negative" solution to reducing the greenhouse gases that have already been released. It is also a more feasible option for capturing emissions produced by vehicles than fitting them with individual exhaust scrubbers.

After the successful capture of CO_2, it will typically need to be stored—either permanently or for later use. As a gas, it can be stored in pressurized containers. This is already common practice but can become challenging if there is a need to store very large quantities of CO_2. Numerous studies and reviews are dedicated to the storage of carbon dioxide in geological or deep-sea repositories and saline aquifers.[27–30] These efforts are typically aimed at CO_2 capture and permanent sequestration. The main problems are in the availability of suitable sites as well as risks of seismic activity.[27,28] Metal–organic-frameworks (MOF) are another emerging category of systems that are capable of adsorbing a variety of molecules, including hydrogen and CO_2.[31,32]

SUPPLY OF SUSTAINABLY SOURCED HYDROGEN. The idea of a future built on a hydrogen economy has gained much attention for several decades now.[33] On the surface, the push for hydrogen fuel cells to become universal power sources seems to be in direct competition with equivalent methanol technologies. However, while there are benefits to methanol that are related to storage and handling, this is ultimately a matter of societal enactment. Widespread adoption of hydrogen and methanol technologies are not mutually exclusive or necessarily in conflict with one another. In fact, because carbon dioxide conversion to methanol requires a sustainable supply of hydrogen gas, the two are inherently linked.

On a large scale, H_2 can be made using one of several methods. Hydrogen gas is a component of syngas, and thus a product of steam methane reforming. For applications where only the hydrogen is needed, it can be separated from the gas mixture. This is commonly called either "grey" or "blue" hydrogen, depending on if the carbon byproducts are captured. However, the alternative, so-called "green" hydrogen that is produced through water electrolysis is more relevant to the purposes of renewable processes. Indeed, relying on hydrogen produced using methods with high carbon emissions would arguably defeat the purpose of CO_2 recycling. Therefore, the current focus is mainly on making green hydrogen more sustainable and accessible. Similarly to CO_2, storing and transporting large quantities of hydrogen may be a great challenge. Due to being a gas, hydrogen has a very low energy density under atmospheric pressure and needs to be compressed for storage and transport. Luckily some progress has already been made into building the necessary infrastructure. A further increase in energy density can be achieved by liquefying the hydrogen. However, this requires that its temperature is brought all the way down to below 20 K.[34] At worst, the process of cooling can take ca. 30 % of the amount of energy that would be stored in the hydrogen itself.[33] The flammability and reactivity of hydrogen pose further risks that need to be considered in large-scale hydrogen storage. Fortunately, however, hydrogen is not considered a significant environmental pollutant.

1.3 Heterogeneous Cu catalysts for CO_2 conversion to methanol

Current catalysts used for CO_2 hydrogenation into methanol are based on the heterogeneous $Cu/ZnO/Al_2O_3$ (CZA) catalysts that have historically been used to produce methanol from syngas.[35] While the same catalyst is able to react carbon dioxide into methanol, the conversion of CO_2 is typically low and the catalyst shows poor selectivity for the desired reaction.[35–39] Because of this, several combinations of metals and oxide supports have been studied with the aim of enhancing the selectivity, tailored to CO_2 used as the main feedstock.[35–38,40–50] Some of these combinations include copper, gold, and silver metals supported on zinc oxide (ZnO), titania (TiO_2), zirconia (ZrO_2), or alumina (Al_2O_3). Of the metals, Cu has been proven capable of methanol selectivities in excess of 60 %,[35,51] making it a typical choice. On the other hand, gold has a higher selectivity, even reaching 100 %, but suffers from very low activity.[49]

In terms of the oxide supports, zirconia (ZrO_2) was discovered to have a significant enhancing effect on the activity and selectivity towards methanol of the Cu catalyst compared to the more traditional CZA system.[35,52–54] Thanks to the high thermal and mechanical resistance of zirconia, it also prevents catalyst deactivation during operation.[35,52,55,56] The high activity has also been attributed to an increase in favourable adsorption sites as ZrO_2 is able to adsorb more CO_2, for example, than ZnO.[54,57] For these reasons, Cu on ZrO_2 was chosen as the starting point for the studies presented.

An additional increase in the rate of methanol production can be achieved by the addition of a ZnO promoter to Cu/ZrO_2,[58,59] creating the ternary $Cu/Zn/ZrO_2$ (CZZ) system. The exact mechanisms for the promotion effect of Zn is not settled, but several have been suggested. The ZnO component may increase the dispersion and surface area of the Cu particles.[60] However, the associated increase in activity also came with a decreased selectivity towards methanol,[60] suggesting that specifically the zirconia surface or Cu–ZrO_2 interfaces are responsible for selectivity.[53] Secondly, a type of "reverse spillover" where zinc oxide acts as a hydrogen reservoir was first suggested on $Cu/ZnO/SiO_2$,[61] and subsequently observed on CZZ.[57] There is some evidence that the promotion is specific to the catalyst metal, as ZnO added to a Ag/ZrO_2 system was shown to have no such effect.[50] Cu particles were also found to gather close to the ZnO component, whereas other noble metals spread more evenly on ZnO/ZrO_2.[49]

THE METAL–OXIDE INTERFACE. The interfaces where the catalyst metal and the support oxide meet have been suggested by past research to be the active domain for many industrially important catalytic reactions such as the water–gas shift reaction,[62,63] and CO oxidation.[64,65] Similarly, both experimental[35,52,58,66–68] and computational[35,52,58,68–70] studies have identified the interface between Cu and ZrO_2 as a favourable location for CO_2 adsorption. This has implications for possible reaction mechanisms, as strong CO_2 adsorption enables a Langmuir–Hinshelwood type reaction, where hydrogen dissociated on the Cu readily combines with CO_2 adsorbed at the Cu–support interface. Instead, in studies using

Cu(111) model catalysts, activation of CO_2 is not possible which effectively implies an Eley–Rideal type mechanism where gas-phase or loosely bound CO_2 reacts with surface hydrogens.

PHYSICO-CHEMICAL CHANGES OVER THE CATALYST LIFETIME. Several methods of preparing the catalyst can be found in literature, *e.g.* variants of precipitation,[58,59,71,72] flame-spray pyrolysis,[73] sol–gel methods,[74] and lately atomic layer deposition (ALD),[75] as also featured in paper II. The preparation methods can have a profound effect on the dispersion of the components and the size distribution of the catalyst nanoparticles,[35,76] likely contributing to some confusion and conflicting results. However, it is also known that catalytic systems experiences changes during operation, such as particle sintering[43,77] or reduction of active components due to the reaction gas mixture.[67,68,73,78,79]

Much research has been aimed at understanding the physical and chemical state and role of Zn in Cu/ZnO and CZA systems, yet some conflicting opinions persist.[35,37,40,43,68,80–82] Under reductive conditions, the ZnO component can interact strongly with the metallic Cu catalyst,[37,43,79,83] leading to ZnO migration onto the catalyst metal and/or the Cu particle wetting the oxide surface. This has been observed in CZA systems as the formation of graphitic* ZnO overlayer on the surface of Cu particles.[41,66,84]

Previous *in situ* studies have confirmed the existence of both oxidized (ZnO) and reduced Zn phases in Cu/ZnO systems, with reversible conversion between the two when gas-phase conditions are changed.[43,68,85] Opinions have differed, however, on which is the active phase. Ultimately much of the conflicting information may stem from the multitude of different conditions used when characterizing the catalysts,[43,67,79] as many analyses can only be done in low-pressure environments. Still, some suggest that the reduced Zn may include (surface) alloys with Cu that have been suggested as enhancing activity.[37,40,43,86,87] There are also suggestions that activity in Cu/ZnO systems is dependent specifically reactive Zn–formate species created by reduced sites,[81,88,89] though it is not clear if this latter effect is relevant CZZ system, as formates are known to adsorb very strongly on zirconia.[69,90,91] However, there are other results suggesting that the alloy is likely to re-oxidize and separate in the reaction gas flow or otherwise lose its activity.[67,85] Instead, the oxidic ZnO may promote the reaction *via* enhanced adsorbate binding, structural modification, and hydrogen distribution.[67,85,92] Recent studies[85,92] have directly linked alloy formation with decreased activity. Finally, it may also be that the true active Zn sites are partially oxidized ones—either oxygen vacancies in ZnO_x overlayers[93] or partially reduced alloys.[37] However, while the strong metal–support interaction is often discussed in the context of Cu/ZnO and CZA catalysts, there is little information available of the role it plays in $Cu/ZnO/ZrO_2$ systems. Kordus et al.[92] recently examined CZZ systems by *operando* methods and showed that, while most ZnO does indeed stay on the surface of Cu particles, some of it migrated onto the ZrO_2 under reaction conditions.

---

* "graphitic" referring to the honeycomb-like structure, rather than electronic properties.

SUPPLY OF ATOMIC HYDROGEN. It is generally believed that the metallic copper is responsible for the task of supplying the hydrogen needed for CTM reactions.[37,53,58,94–96] Lattice edge and defect sites in particular have been credited with high efficiency for hydrogen dissociation due to increased reactivity brought about by the lower coordination.[95,97] Indeed, it has been shown that the same materials without the Cu component see little catalytic activity.[35] Furthermore, experimental studies have suggested the existence of a hydrogen spillover effect where the activated hydrogen is able to move from the Cu onto the support or promoter oxides after dissociation.[98,99] Therefore, the ZrO_2 surface could be covered by reactive H, allowing also the hydrogenation of adsorbates that are not bound to the Cu–ZrO_2 interface. In fact, H/D exchange experiments suggested that the process is very fast and thus does not act to limit turnover frequencies.[98] While the same effect is known to exist in other metal–oxide systems,[100] especially ones involving reducible oxides, there is also some debate over whether spillover is possible on irreducible oxides, such as ZrO_2 and TiO_2.[101] Irreducibility of the surface could be considered an obstacle, as it is effectively hydrogenated during spillover from the metal. However, subsequent studies have suggested that spillover is still possible but may involve a different mechanism or the involvement of defect sites.[102–104]

2 COMPUTATIONAL MATERIALS MODELLING USING DENSITY FUNCTIONAL THEORY

2.1 Electronic structure calculations

By our current understanding of quantum mechanics, any time-independent and non-relativistic chemical problem is, in theory, described fully by the famous Schrödinger equation:

$$\hat{H}|\Psi\rangle = E|\Psi\rangle \tag{1}$$

where $\hat{H}$ is the Hamiltonian operator, and E is the (total) energy. The time-independent wavefunction $|\Psi\rangle = \Psi(\mathbf{x}_1, \mathbf{x}_2, \ldots, \mathbf{x}_n)$ is a function of the coordinates of all dynamic particles. In the Born–Oppenheimer approximation, we will assume that only electrons are considered dynamic, and that interactions with and between nuclei are included in the Hamiltonian as an external potential. Generally, the exact form of the Hamiltonian is system-dependent.

The basis of many methods in use today, Hartree–Fock theory, was formulated in over the course of the 1920s and '30s, providing a theoretical framework for determining the wavefunctions of a many-particle system *ab initio*—from first principles. While HF contains some approximations that could be considered crude, post-HF methods such as configuration interaction, coupled cluster, or methods involving perturbation theory are able to offer impressive accuracy. However, while the leaps in computational power in recent decades have enabled these methods to be used for small and medium-sized systems, an inherent problem with scaling persists. As the wavefunction is a function of the coordinates of each electron in the system—three coordinates per electron—the number of pairs that one would need to calculate in order to eventually find the optimal wavefunction grows exponentially with each atom added. For this reason, density functional theory (DFT) has become one of the most utilized methods for examining larger systems.

2.1.1 Density functional theory

The Hohenberg–Kohn theorems, formulated in the 1960s, state that the total energy of a system where electrons move in an external potential is a functional of the total ground-state electron density.[105] Importantly, minimizing the energy associated with a three-dimensional electron density is significantly simpler, computationally, than doing the same for a wavefunction of $3N$ spatial coordinates. In practice, this makes DFT significantly less demanding in terms of processing power and thus allows a computational chemist to study much larger model systems than WF methods. This is particularly helpful for heterogeneous systems where a model of a specific structure may include hundreds of atoms.

A general expression for the DFT energy functional of a system with an electron density ρ is:

$$E[\rho] = F[\rho] + \int \rho(\mathbf{r}) v^{\text{ext}}(\mathbf{r})\, d\mathbf{r}, \tag{2}$$

where the last term describes electron-nucleus interactions with the nuclei included as an external potential $v^{\text{ext}}(\mathbf{r})$. The so-called Hohenberg–Kohn functional $F[\rho]$ in eqn 2 is:

$$F[\rho] = T[\rho] + J[\rho] + E_{\text{XC}}[\rho]. \tag{3}$$

Here $T[\rho]$ is the functional describing kinetic energy, $J[\rho]$ is the electron–electron repulsion energy, and $E_{\text{XC}}[\rho]$ is the exchange–correlation functional. Density functional theory without further approximations is exact and, unlike Hartree–Fock theory, it includes the effects of electron correlation, *i.e.* all non-classical electron–electron interactions, within the E_{XC} term. Unfortunately, there is no analytical form for the total energy functional that is solvable computationally and applicable to an arbitrary system. Therefore, practically all applications of DFT are based on some methods of numerical approximation.

In the (most common type of) local density approximation (LDA), the exchange term is calculated using the known expression for the exchange energy of a uniform electron gas as well as parametrized data of its calculated correlation energy.[105] Calculating the XC term with these simplifications is computationally undemanding but may end up giving a somewhat crude description of the electronic structure. While the LDA may provide a good estimate when the electron density is devoid of severe gradients,[106] it can cause inaccuracies when modelling reactions, as it has a tendency to overestimate bond/atomization energies,[107–109] as well as underestimating the band gaps for oxides.[106,110] Several methods exist which introduce the gradients of the electron density into the equation in order to improve the XC estimate, the most established of which is the generalized gradient approximation (GGA). All calculations presented in this work used the Bayesian error estimation functional with a van der Waals correlation component (BEEF-vdW) which is in the category of GGA functionals.[111] Both LDAs and GGAs feature residual errors regarding exchange self-interaction of the electrons, seen especially clearly with strongly correlated states such as transition metal orbitals of higher angular momenta. This self-interaction error (SIE) may manifest as overly delocalized states and significantly narrowed (or vanishing, in extreme

cases) band gaps in insulating or semiconducting materials.[105,110,112] A simple and computationally inexpensive way to mitigate the SIE is the addition of a Hubbard correction,[113] also known as the DFT+U method. In the work presented, the Hubbard correction was applied to zirconium *d* orbitals and the appropriate parameters were determined using the self-consistent method described in ref. 114. There are more elaborate variations of DFT, which can be used for increased accuracy, such as meta-GGAs and hybrid functionals.[109,115] Hybrid functionals include some amount of exact exchange calculated using methods such as Hartree–Fock theory which also has the effect of correcting for the self-interaction error. However, these methods are computationally expensive and the benefits in accuracy over GGA may not outweigh the computational burden when modelling heterogeneous systems. Therefore, they are typically reserved for use with small systems or when their use is particularly relevant.[109,115]

An important aspect that motivated our choice of BEEF-vdW as the XC functional is its inclusion of van der Waals correlation. Dispersion forces should be included in computational studies of heterogeneous systems, as they may play a large part in how species without permanent dipole moments adsorb on the surfaces of the catalyst. Most density functionals, especially at the LDA and GGA levels, fail to properly describe these effects.[109] To address this, different (semi)empirical dispersion corrections or vdW terms exist that can be added to the approximate functionals in use.[116–118] BEEF-vdW, on the other hand, was deliberately built using semi-empirical machine learning methods which included van der Waals interactions in the training set. As a result, functional is able to match or surpass the accuracy of other vdW-DF methods.[111] However, as it is based in machine learning, large errors may emerge when operating outside the training domain such as in gas-phase reactions.[115]

The projector augmented-wave (PAW) formalism[119] was used in all calculations to describe electrons near the nucleus. To comply with orthogonality around the relatively "crowded" atomic nuclei, the wavefunctions of the electrons oscillate wildly near the centre. Because of this, many high-energy basis functions are required for accurate description when using LCAO or plane-wave methods and the issues of the spacing of a real-space grid basis are exacerbated. Instead, following the PAW method,[119] a smooth wavefunction $|\tilde{\Psi}\rangle$ is related to the original wavefunction through a linear relation:

$$|\Psi\rangle = \hat{T}|\tilde{\Psi}\rangle. \tag{4}$$

The operator $\hat{T}$ contains (pseudo)partial waves $\phi/\tilde{\phi}$ as well as projector functions $\langle\tilde{p}_i|$ localized only to inner part (augmentation region) around a nucleus:

$$\hat{T} = 1 - \sum_i \left(|\tilde{\phi}_i\rangle - |\phi_i\rangle\right) \langle\tilde{p}_i|. \tag{5}$$

The equations for observables such as energy can now be written in PAW formalism, allowing the calculations to be completed while separating the inner oscillating region. Furthermore, the transformation is easily reversed to obtain the true Kohn–Sham wavefunctions. In this work, all electronic structure calculations

were carried out using the GPAW package,[120,121] which implements the necessary mathematics, supplemented by tools included in the Atomic Simulation Environment (ASE).[122]

2.2 Geometry optimization

Density functional theory is a method for finding the ground-state energy for the specified atomic configuration. However, in most situations the computational chemist will also want to find the most optimal atomic structure. To this end, programs for computational chemistry include geometry optimization algorithms designed to make small, iterative adjustments to the position of the nuclei in the simulation, leading it gradually towards the direction of lower ground-state energy. At different stages of this work, two different methods were used: The Broyden–Fletcher–Goldfarb–Shanno (BFGS) algorithm[122] and the Fast Inertial Relaxation Engine (FIRE),[123] both implemented in ASE. The former was used in paper I. However, through further testing, FIRE was found to converge slightly faster with the specific systems studied and was therefore used in papers II–IV. In the ideal case, the choice of optimization algorithm does not affect the final result. In reality, some care should be taken to obtain correct results from structure optimization.

2.2.1 Global optimization using minima hopping

Starting from a mostly arbitrary initial geometry will not guarantee that the minimum that is found is the lowest point in the massive set of all possible geometries; it is simply the one directly downhill from the starting point. While the computational chemist's professional intuition is often adequate to find minima that are meaningful, efforts have been made to develop algorithms and methods for so–called global optimization. Global optimization schemes use a variety of tactics to find the global minimum of the potential energy surface. There are two more general categories for these algorithms: thermodynamics-based methods, such as basin hopping[124] and simulated annealing,[122] and non-thermodynamics-based, such as genetic algorithms[125,126] and the minima hopping method.[127] The mathematical field of global optimization is vast and many more algorithms and ways to classify them exist, but are less commonly used in chemistry. Basin hopping essentially aims to discretize the PES, eliminating the barriers between basins.[124] A transformed energy landscape is created, consisting of local minima only, after which the minimum of the new surface is found using Monte Carlo sampling methods. Simulated annealing, at its simplest, is based on simulating the structural changes in the system using molecular dynamics (MD), while slowly cooling the simulation temperature in the process. The weakness of thermodynamics-based methods is that they are potentially very slow to equilibrate. Evolutionary or genetic algorithms have also been utilized in finding

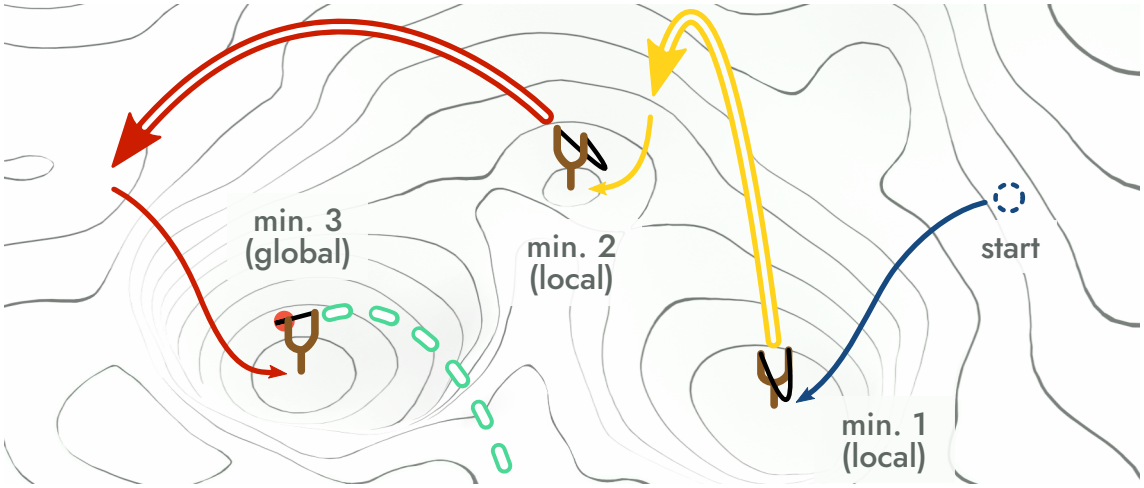

FIGURE 2 Simple illustration of minima hopping. Algorithmically determined candidate structures are optimized, after which a molecular dynamics step escapes the structure out of its current basin and optimizes the next one.

the global minima of both supported and unsupported metal and metal–oxide clusters.[125,128–131] Genetic algorithms are somewhat complicated multistep processes that are designed to create, combine, and mutate the system or its components in chemically significant ways that are analogous, in a sense, to natural selection. Finally, the minima hopping method[127] includes a component of MD but is not dependent on thermodynamic principles for locating the global minimum. It was chosen as the method to assist in finding stable adsorption geometries for Cu/Zn sub-nano clusters in paper IV.

Conceptually, the minima hopping (MH) procedure consists of an "inner part" which jumps between basins and optimizes the new local minima, and an "outer part" which compares the energies of new minima to those that have already been found, rejecting those that are less favourable by some set parameter. In practice, minima hopping optimization alternates between two phases illustrated in Figure 2: a molecular dynamics (MD) phase that is used to escape the current basin and find new candidates for minima and a (local) geometry optimization phase using a conventional gradient-descending algorithm. The optimized structures are accepted or rejected based on their relative stability to previously found minima and the sequence repeats.

The temperature used during the MD portion of the process is quite significant. On one hand—and applying the Bell–Evans–Polanyi principle—traversing from one basin towards another of a lower energy is equivalent to an exothermic reaction, in which case the barriers we encounter should not be massive. By this logic, a lower kinetic energy should be sufficient during the MD phase. On the other hand, if the temperature is too low, the system may get stuck in a stable basin for a prolonged time instead of sampling new ones. A proper implementation of minima hopping is therefore self-correcting, and the kinetic energy is automatically adjusted so that roughly half of all escape attempts are successful.[127] This aspect of making adjustments based on history can, in some cases, make minima hopping significantly faster than Monte Carlo methods. Also, while there

is some evidence suggesting that evolutionary/genetic algorithms are faster than MH with large cluster models,[132,133] minima hopping is likely superior for optimizing systems with complex energy landscapes.[133]

Depending on implementation, constraints can be placed on the system to preserve identifying aspects of the system.[134] For example, molecules adsorbed on a surface can be given internal forces that push or pull the atoms together if the kinetic energy in the simulation is strong enough to break bonds. In paper IV, where sub-nano clusters were optimized on Cu(111) and ZrO_2, constraints were placed on the atoms in each cluster to both keep them attached to the surface and to discourage cluster dissociation. However, the constraints were implemented with thresholds to ensure that no force at all is applied when the atoms are within 4 Å of the surface and each other. Therefore, clusters that cohered and adsorbed strongly on the surface likely experienced no forces.

2.2.2 The nudged elastic band method

For kinetic analysis, it is necessary to find the minimum-energy pathway (MEP) between two basins on the potential energy surface (PES) that correspond to the reactants and products of an elementary reaction. The atomic configuration at the highest-energy point along the MEP is the transition state (TS) of the reaction and represents the barrier that needs to be crossed for the reaction to take place. The energy difference between the reactant and transition state structures is the activation energy ΔE_a of the reaction. Mathematically, the transition state is a saddle point in the PES and thus its gradient is zero. The PES at this point is positively curved in all but one direction—the reaction coordinate. If we want to find this saddle point computationally, the optimization algorithms used to find energy minima are not enough, as we now need to optimize to a minimum along most coordinates but simultaneously find the local maximum in one. Therefore, some restrictions will need to be placed on the optimization process. The (climbing-image) nudged elastic band method was used in the articles presented in this work wherever reaction barriers are reported, but most notably in paper III to find the activation energies for each elementary reaction step.

The nudged elastic band (NEB) method[135] involves creating multiple intermediate structures (images) that are interpolated between the reactant and product structures. The images are treated as a sequence with spring forces connecting them. These spring forces set the necessary constraints to the geometric degrees of freedom and ensure that the structures evolve sequentially. Moreover, they offer resistance against structural changes in the direction of the reaction coordinate when the geometries are relaxed. If the spring forces are set appropriately, the chain of images moves down the gradient of the PES, eventually approximating the minimum-energy pathway. Spring constants should be chosen so that they keep the spacing of the images relatively consistent but are not too stiff to prevent relaxation to the MEP.

However, one practical complication remains in the original NEB method. While the intermediate states are approximately on the minimum-energy path-

way, there is no guarantee that any of them lay exactly at the transition state. A modification to the NEB method, the climbing-image nudged elastic band (CI-NEB) method[136] addresses this by removing the spring forces from the image with the highest energy after a period of time, while the image is simultaneously "pushed" towards the TS by inverting the force in the direction of the reaction coordinate. The calculations should run until the energy gradient reaches zero, at which point the highest-energy image represents the transition state geometry. The transition state energy $E^{\ddagger}$ is used to calculate the activation energy by:

$$\Delta E_a = E^{\ddagger} - E(\text{reactant}), \tag{6}$$

where $E(\text{reactant})$ is the energy of the stable state preceding the transition state in the direction of the reaction coordinate. Depending on this direction, each elementary step has separate forward and backward activation energies.

2.3 Analysis of DFT data

In its simplest form, analysis of the DFT data may be about calculating the relative change in energy during a process. A specific case that is fundamental in this work is the adsorption energy E_{ads}. Let us define the adsorption energy of an adsorbate species M as:

$$E_{ads}(\text{M}) = E(\text{M*}) - [E(\text{M}) + E(*)], \tag{7}$$

where $E(\text{M*})$ is the energy of the configuration where M is adsorbed at the active site on the adsorbent. $E(\text{M})$ and $E(*)$ are the energies of the separated components, optimized in isolation. Note that all adsorption energies in this work have been calculated using total energies without zero-point- of gas-phase corrections, unless otherwise specified. Adsorption energies are central in all papers included, where a variety of systems were used as active sites, including Cu(111), and zirconia surfaces as well as metal–zirconia interfaces. Several similar interaction energies with slight differences were used in the examination in paper paper I.

2.3.1 Analysis of molecular vibrations

By using the energetic information contained by in the potential energy surface, it is also possible to calculate the forces acting on each atom in a system. This allows us to use *ab initio* methods to model molecular vibrations and, by extension, determine theoretical infrared and Raman spectra which are important analysis methods used by chemists. Generally speaking, IR frequencies determined using DFT should not be expected to match experimental values in their absolute values, and often some kind of experimental fitting is used to scale the frequencies. However, even without corrections, the relative positions of predicted peaks can be valuable for use in characterization.

To determine vibrational modes, the PES is sampled by systematically introducing small, finite displacements to the coordinates of the atoms (nuclei) that have been chosen for examination.[137,138] Note also that this is done using the Born–Oppenheimer approximation. Following Pederson et al.,[137] we can present the collective displacements of N atoms by using a set of orthogonal $3N$-dimensional vectors $\mathbf{X_n}$. The forces calculated at each of these configurations are used in eqn 8 to build the so-called Hessian matrix (or dynamical matrix) $\mathbf{H}$, which describes the shape of the PES.

$$\mathbf{H}_{ij} = -\frac{\sum_n \mathbf{X_{nj}} \mathbf{F_{ni}}}{\delta^2}, \tag{8}$$

where $\mathbf{F_n}$ is the force at displacement $\mathbf{X_n}$ and δ is the magnitude of the displacement. In our calculations, a displacement of 0.01 Å was used. Combined with the known masses of the atomic nuclei, a diagonalized Hessian matrix can be used to retrieve the vibrational frequencies, typically by employing the (double) harmonic approximation.[137,138] When using a real-space grid basis, an additional momentum-conserving correction can be included to reduce the so-called egg box effect.[139] This correction was used in all of our calculations.

The fact that the examination is based on sampling the potential energy surface around the nuclear coordinates means that the structure first needs to be fully optimized to a stationary point, *i.e.* stable minimum or saddle point. In fact, the vibrational modes can be used to check whether such a point has been found. All frequencies for minimum-energy geometries are real and positive, while an n^{th} order saddle point is expected to have n frequencies whose values are imaginary. Vibrational frequencies computed for arbitrary and unoptimized structures are largely meaningless.

2.3.2 Population analysis

The rules of quantum mechanics and the molecular orbital theory tell us that electrons are distributed over the entirety of a molecule or other similarly interacting system (metal lattice, crystal structure, etc.) to a point where assigning them unambiguously to specific atomic nuclei becomes impossible. As a consequence, we lose the simple and useful concepts of atoms and the bonds between them that chemists rely on to make predictions of reactivity. Therefore, some method of charge and population analysis is desirable, as knowledge of oxidation states is useful when studying metal-containing or ionic systems. In other words, we need a way to determine the effective number of electrons that surround a given nucleus using only the calculated electron density.

When basis set-based DFT is used, Mulliken analysis is a simple method of assigning charges. If the wave function is expanded in terms of single-atom wave functions centred on the nuclei, the charge of an atom A in a molecule can be expressed as:

$$q_A = Z_A - \sum_{n \in A} (\mathbf{PS})_{nn},$$

where Z_A is the charge of atomic nucleus A. The sum is over all diagonal elements of the product of density and overlap matrices **PS** that correspond to basis functions centred on A. Mulliken charges can thus be problematic, as they are often highly basis-set dependent.[140,141] On the other hand, this problem is likely more pronounced for LCAO-type basis sets, and it has been suggested that the inaccuracies are minimal when using *e.g.* a plane-wave basis.[142] Löwdin analysis is largely similar but with the **PS** matrix replaced by the orthogonalized density matrix $\mathbf{P}'$. Regardless, other less basis-dependent methods are often preferred.

As an alternative, so-called Bader partitioning is an application of the more comprehensive Quantum Theory of Atoms In Molecules (QTAIM), credited to Richard Bader.[143] The method is built on the observation that the electron density ρ forms peaks where atomic nuclei are located, while minima in the density may be thought to correspond to their confines. Therefore, the topology of the electron density can be used to unambiguously define the positions and boundaries of atoms in molecules, as well as their identities and the bonds between them, if desired.[143] The electron population around a nucleus can then be determined by integration within these bounds, also known as Bader volumes. By basing the analysis on the three-dimensional electron density instead of basis functions, we avoid the problems discussed regarding Mulliken partitioning. It has, however, been noted that Bader partitioning has the tendency to make compounds more ionic than in reality, effectively overestimating the polarity of bonds.[141] Furthermore, the robustness over Mulliken analysis comes at a cost of a larger computational burden, as the algorithms to find and traverse stationary points in the charge density are often computationally demanding.[144,145] In the work presented, Bader partitioning was used in papers I, III, and IV as a tool to estimate charge distributions in a heterogeneous system, for which the method is sufficient. A mature grid-based implementation created by Tang et al.[146] was used, as it scales linearly with the size of the fine grid used and thus is suitable for the larger systems.

2.3.3 Analysis of metal *d*-bands

As heterogeneous systems can be complex and modelling them computationally is time-consuming and costly, easy-to-use descriptors of (catalytic) reactivity are valuable for the screening of materials. An examination of the electronic structure of transition metals lead Hammer and Nørskov[147] to develop a simple but powerful predictor of the reactivity of metal surfaces that we now simply call the *d*-band model. The shapes of the *d*-orbitals on the surface of transition metals are relatively localized and likely to protrude perpendicularly from the surface, compared to their *s* or *p*-orbitals which are confined to the lattice. Thus, they can be thought to be more involved in the formation of bonds between the metal and adsorbate.[148,149] The *d*-states of transition metals also tend to form narrow bands near the Fermi level, making it reasonable to think that they interact with adsorbates similarly to atomic- or molecular orbitals, forming new bonding and anti-bonding states.[148] Therefore, while estimating the absolute values for ad-

sorption energies on different metals is not possible from just the metal's electronic structure, it turns out that the differences in binding can be explained by differences in *d*-band energy.

This analysis is useful for comparing the different reactivities between several transition metals that are used as catalysts as well as their alloys. It has been observed, that straining metal surfaces causes a shift in their reactivity that is consistent with the shift in *d*-band energy.[96,150] There are also results showing that adsorbate-induced effects (or ligand effects), such as the weakening of oxygen adsorption as a result of increasing oxygen coverage on Au and Pt (111) surfaces,[151] can be explained using the model. The *d*-band model is obviously not sufficient in cases where the *d* states do not take part in bond formation or if the metal particles get too small to have continuous *sp* states.[149] However, in many cases involving catalytic reactions on metal surfaces, the *d*-band centres and their shifts are a good indicator of reactivity.[96,147,149,150] In paper I, we investigated whether the model could similarly explain differences in CO_2 adsorption at strained Cu–ZrO_2 interfaces.

For the purposes of the analysis, we begin by determining the density of states (DOS) of the system: a description of the number of states that exist at a given energy level. Mathematically, this is expressed as:

$$\rho(\varepsilon) = \sum_n \langle \psi_n \mid \psi_n \rangle \delta(\varepsilon - \varepsilon_n). \tag{9}$$

Here ε_n are the energies corresponding to eigenstates $|\psi_n\rangle$. The delta function $\delta(\varepsilon - \varepsilon_n)$ ensures that the function at any given ε is the sum over states with $\varepsilon_i = \varepsilon$ only. As we are interested in states with a specific angular momentum, we use projection operators to get the *d*-projected density of states:

$$\rho_p(\varepsilon) = \sum_n \langle \psi_n \mid p \rangle \langle p \mid \psi_n \rangle \delta(\varepsilon - \varepsilon_n), \tag{10}$$

where $|p\rangle\langle p|$ is the *p*-projection operator. In practice, a program such as GPAW which uses the projector augmented-wave formalism will use corresponding equations that involve projectors and partial waves. Regardless, once we have obtained the DOS and projected it onto the *d*-band, the centre can be determined by means of integration:

$$\varepsilon_d = \frac{\int \varepsilon \rho_d \, d\varepsilon}{\int \rho_d \, d\varepsilon}. \tag{11}$$

For the *d*-band centres to be useful in comparisons, the energy ε should be given relative to the Fermi level.

2.3.4 Atomistic thermodynamics

The Gibbs free energy *G* is a ubiquitous physical quantity used in many thermodynamic analyses in chemistry, as a negative change in Gibbs energy during a reaction ($\Delta G_r < 0$) is indicative of the reaction being spontaneous. Formally, this

is only true for a closed system under conditions of constant temperature and pressure. Thus, the change becomes

$$\Delta G = \Delta H - T\Delta S = \Delta U + p\Delta V - T\Delta S. \tag{12}$$

If the system is not closed and can exchange particles with the surroundings, we can define the chemical potential for a species i as the change in Gibbs energy relative to the change in the number of i entering or leaving the system, *i.e.* the molar Gibbs energy of i,

$$\mu_i = \left(\frac{\partial G}{\partial n_i}\right)_{n_{j\neq i}, p, T}. \tag{13}$$

Furthermore, it follows that

$$G = \sum_i n_i \mu_i. \tag{14}$$

Similarly to G, a decreasing μ tends to indicate a spontaneous process. It is convenient that we can also define the change in the Gibbs energy of a system by the chemical potentials of its components:

$$\Delta G = \sum_i \Delta n_i \mu_i. \tag{15}$$

It is noteworthy to us that the free energy and, by extension, the chemical potential are functions of temperature and pressure. However, by its nature, DFT is a method for examining electronic structures and does not directly describe the more macroscopic phenomena of temperature*, pressure, and ultimately entropy. We need a way to match information we get from the model system with the finite and measurable conditions that real-life catalysts are subject to. To do this, we can take advantage of pre-existing thermodynamic data that has been determined experimentally. For example, the NIST JANAF tables,[152] where values for standard thermodynamic quantities are provided. Alternatively, the data we obtain through DFT, such as vibrational frequencies (subsection 2.3.1), together with well-known atomic properties are enough for us to calculate these effects. This can be accomplished through the use of partition functions, for example. If all contributions to the chemical potential are calculated using first-principles computational methods, we could speak of true *ab initio* thermodynamics.

For the purposes of this work, we determine the change in chemical potential relative to absolute zero following eqn 16. Because the molecules studied here are common, and the models quite simplified, it is easiest to do the thermodynamic examination using values for standard entropies S° at certain temperatures along with standard enthalpies H° relative to a reference temperature T_r, which are available in the JANAF tables.[152]

$$\begin{aligned}\Delta\mu^\circ(T) &= \Delta H^\circ + T\Delta S^\circ \\ &= \left[H^\circ(T) - H^\circ(T_r)\right] - \left[H^\circ(0\,\mathrm{K}) - H^\circ(T_r)\right] - T \times \left[S^\circ(T) - S^\circ(0\,\mathrm{K})\right].\end{aligned} \tag{16}$$

* Ignoring methods that introduce artificial temperatures, *e.g.* occupation smearing.

Thus we can calculate the contribution of temperature and pressure to the chemical potential as

$$\Delta\mu(T,p) = \Delta\mu^{\circ}(T) + k_{\mathrm{B}}T\log\frac{p}{p^{\circ}}. \tag{17}$$

We can determine the partial pressures using Dalton's law:

$$p_i = x_i p, \tag{18}$$

where x_i is the molar fraction of component i. Finally, by adding the contribution $\Delta\mu_i$ together with the ZP-corrected DFT energy for species i, we get the chemical potential

$$\mu_i(T,p) = E_i^{\mathrm{total}} + E_i^{\mathrm{ZP}} + \Delta\mu_i(T,p). \tag{19}$$

Atomistic thermodynamics was used in paper IV to determine reaction energies for the oxidation of metallic sub-nano clusters. This was to assist in studying the stability of the Zn(O) component under synthesis and reaction conditions that could be simulated by varying the chemical potential of gas-phase oxygen. We will now get be able to calculate this using eqns 16 to 19.

$$\mu_{\mathrm{O_2}}(T,p) = E_{\mathrm{O_2}}^{\mathrm{total}} + E_{\mathrm{O_2}}^{\mathrm{ZP}} + \Delta\mu_{\mathrm{O_2}}(T,p^{\circ}) + k_B T\ln\frac{p_{\mathrm{O_2}}}{p^{\circ}}. \tag{20}$$

However, it is well known that the energy of a gas-phase oxygen molecule calculated using DFT includes a considerable error.[153–155] Instead, we use the reaction enthalpy of $\mathrm{O_2} + 2\,\mathrm{H_2} \longrightarrow 2\,\mathrm{H_2O}$ to calculate a more accurate value, as the formation enthalpy for water is well known (and available from the JANAF tables,[152] for example)

$$\begin{aligned} E(\mathrm{O_2}) &= 2E(\mathrm{H_2O}) - 2E(\mathrm{H_2}) - 2\Delta_f H^{\circ}(\mathrm{H_2O},T) \\ &= -32.977\,\mathrm{eV}. \end{aligned} \tag{21}$$

This corresponds to a gas-phase error of $\varepsilon_{\mathrm{O_2}} = -0.83$ eV, which is consistent with previously calculated values.[153,154] The chemical potential of a gas-phase oxygen atom now becomes

$$\mu_{\mathrm{O}}(T,p) = \frac{1}{2}\left[E(\mathrm{O_2}) + \Delta\mu_{\mathrm{O_2}} + k_B T\ln\frac{p_{\mathrm{O_2}}}{p^{\circ}}\right]. \tag{22}$$

To further simplify the computational examination, we will use the total energies for surface-bound species in place of free energies, effectively excluding entropic contributions.

2.4 Methods of kinetic analysis

The fundamental result obtained from DFT calculations is the potential energy surface, or some specific points of it. However, in most cases simply knowing

energetic values is of limited usefulness when interpreting the results of experiments, where obtaining reaction rates is often the objective. Therefore, we will need ways to supplement DFT to turn the energetic data into reaction rates. One could talk of moving from an energy representation to a rate constant representation. Together with the thermodynamic feasibility of a reaction, its rate is important when we want to make predictions of activity and selectivity.

We can discuss activity in terms of turnover frequency (TOF), which is effectively the instantaneous reaction rate relative to the concentration of active sites. It could be argued that the most accurate way to define the turnover frequency is as the number of times each active centre completes a catalytic cycle per second. In practice, however, the TOF is often determined as the rate at which reactants are consumed or products released by each active site (as in eqn 23), but may could also be defined relative to *e.g.* catalyst mass or surface area.

$$\mathrm{TOF} = \frac{dN}{dt} = \left(\frac{dn_{\mathrm{product}}}{dt} / n_{\mathrm{catalyst}} \right) \tag{23}$$

An equivalent measure called a "catalytic constant" or "turnover number" is commonly used in the field of enzymatic catalysis.

Chemists may use the Bell–Evans–Polanyi principle (sometimes Brønsted–Evans–Polanyi) to infer the activation energies of elementary reactions. It is a simplified but useful linear relation, based on the observation that more exothermic reactions are likely to proceed through relatively low barriers when compared to other reactions of the same type. In other words, a more negative reaction enthalpy $\Delta_r H$ coincides with a higher reaction rate. Despite its simplicity, it has been shown that the BEP principle is often applicable to catalytic reactions on metal surfaces.[156,157] However, in the following exploration of computational kinetic analysis, the focus is on methods that involve finding transition states (TS)—structures corresponding to saddle points in the PES between the reactants and products. The difference in energy between the reactants and the transition state is the energetic barrier that must be surpassed for the reaction to occur, often called the activation energy (ΔE_a) of the reaction. Frameworks such as transition state theory then provide the mathematical tools to produce rate constants from this energetic information.

There are significant challenges in measuring catalyst behaviour *operando* (during realistic operation) as chemical reactions are often too fast to follow, and the reaction conditions may involve significantly elevated temperatures and pressures. Many *in situ* methods, such as diffuse reflectance infrared Fourier transform spectroscopy (DRIFTS)[55,58,158] and x-ray spectroscopy methods,[49,68] are ubiquitous in characterization of heterogeneous systems. Tunnelling electron microscopy can reach the level of nanostructures or even individual atoms, and has been applied to studying heterogeneous catalysts *ex situ* and occasionally *in situ* with (near) atmospheric pressures and elevated temperatures.[42,159] However, it is rarely an option under fully relevant conditions for CO_2 conversion to methanol, especially due to the high pressures. In addition to problems relating to operating conditions, experimental characterization methods often lack resolu-

tion at the scale where reactions take place. For example, DRIFTS measurements can detect the presence and evolution of surface intermediates but, because of its relatively weak signal-to-noise ratio, it is only reliable for species that retain a sufficient concentration on the surface.[158] While turnover frequencies and apparent activation energies for catalytic processes can be obtained from measurements, insight into elementary reactions taking place between surface intermediates can be limited. With computational modelling, we are able to define the composition, physical state, and operating conditions of the catalyst as required and can obtain atomic-level details of the reactions taking place as well as their intermediates, even those that are short-lived or unstable. Some methods for first-principles kinetic analysis include microkinetic modelling (MKM), kinetic Monte Carlo (kMC) methods, and the energetic span model.

Microkinetic modelling has been used, with great success, as a tool in studying heterogeneous systems. In simple terms, it involves finding the rate constants for each elementary step in the reaction network, typically by applying the results of transition state theory to DFT calculated reaction barriers.[149] Using the calculated rate constants, differential equations can be set up and solved for changes in the pressure or coverage of each reaction intermediate. The numerical methods used to solve the differential equations come with modest computational requirements, meaning it is possible to run the microkinetic analysis on personal computers. However, in order to obtain reliable results, additional entropic corrections often need to be applied to the DFT data which adds a layer of work that needs to be done before the analysis can be started.[149] This is especially true when dealing with adsorption or desorption steps from the gas phase. As a mean-field method, microkinetic modelling only accounts for adsorbate–adsorbate interactions in an averaged way. The coverages of surface species are assumed to be completely uniform across the surface. The approximation would break down if the interactions were particularly strong, but is often adequate for catalyst screening and comparing reaction patwhays.[160,161]

The term Monte Carlo refers to a number of methods used across many fields of study that are centred around random sampling. The origins of using Monte Carlo methods to study the evolution of chemical systems may be traced to the 1970s[162,163] and have since spawned numerous varieties through the pursuit of accuracy and flexibility. More modern implementations are able to describe *e.g.* multisite mechanisms and adsorbate–adsorbate interactions.[162–164] In typical Monte Carlo kinetic analysis, the catalyst surface is represented as a lattice of active sites.[163] A configuration lattice with certain values (intermediate, product, empty site, etc.) in each cell can evolve into another configuration with some rate that can be determined from first principles, similarly to before in the case of MKM. Rates can be included not only for reactions between intermediates, but also surface diffusion, defect formation, or any other process of interest. The method proceeds by picking events and evolving the lattice iteratively with a degree of randomness, leading to a simplified view of how the system is likely to change with time. While kMC relies on fewer assumptions than mean-field methods, it comes with an increased computational cost.[164]

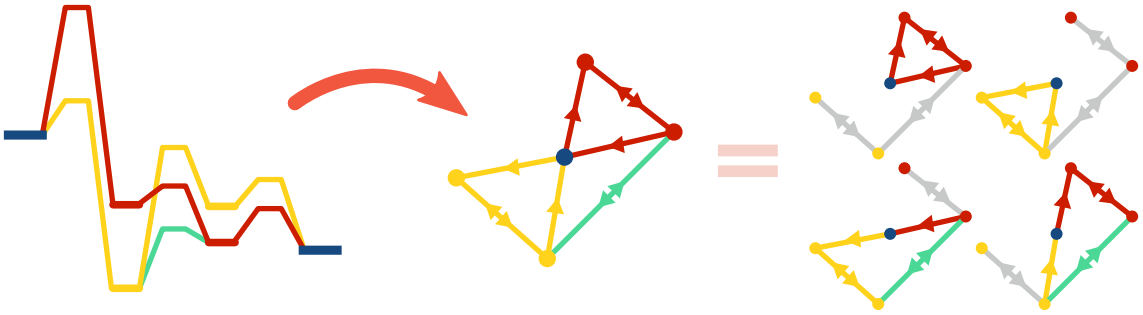

FIGURE 3 Catalytic networks with branching or interconnected pathways (red, yellow, green) can be represented as a graph of nodes (intermediates) connected by edges (transition states). The network can be divided into "mechanisms" which contain one closed cycle but also include all intermediates that are not in the cycle as side branches (light grey). The four mechanisms in this network are shown on the right.

2.4.1 The energetic span model and degrees of turnover control

The energetic span model (ESM) formulated by Kozuch and Shaik[165–167] offers a simplified way of using calculated energies for kinetic analysis. The method allows us to use DFT data without first calculating individual rate constants for sub-reactions, and simplifies the rate equations used to obtain turnover frequencies. Furthermore, the model is simpler for the chemist to set up than many other kinetic models and is not excessively demanding, computationally.

The model is based on Eyring's transition state theory and thus inherits its associated assumptions, namely that the system exists in a quasi-equilibrium between reactants and the transition states following them. Furthermore, the ESM assumes steady-state operation, *i.e.* the forward and backward elementary reactions between surface-bound intermediates are balanced out and thus the rate of change of their amount (coverage) is significant smaller than that of the overall reaction.[168] We also assume that the system quickly reaches a state of thermodynamic equilibrium between the states.

The mathematical model includes the effects of temperature and pressure insomuch as the Gibbs free energies used in the calculations do. The model can be made to include the effects of reagent concentration in the solution (in homogeneous catalysis) or gas-phase by mathematically converting the Gibbs energies to "semi-standard" Gibbs energies (see the original paper by Solel et al.[169] for details.) Nevertheless, the energetic span model is limited in its ability to describe multisite reaction mechanisms or other lateral effects specific to heterogeneous catalyst particles.[170] When utilizing the ESM in paper III, the gas-phase components were introduced when needed in distinct reaction steps and were then consumed in the reactions immediately. Thus, a somewhat significant simplification was made in comparison to the real system where reagents or intermediates may accumulate on the surface.

The situation is somewhat complicated by reaction networks which have alternate, branching, or interconnected pathways. More recent extensions, such

as a graph-theory based implementation[167,171] are more optimal for examining these situations. Figure 3 illustrates another simple situation where pathways are in competition, but some conversion between the paths is also possible. For the purposes of graph-based ESM, the network is divided into "mechanisms" which are defined by exactly one closed catalytic cycle. In the example in Figure 3, a total of four cycles can be found. Intermediates that are not a part of the cycle itself are included in the mechanisms as side branches. Elementary steps (edges) that begin or complete a mechanism can only be traversed in one direction. The turnover frequency of each mechanism can be estimated by summing together exponential terms containing each possible pair of intermediate and transition state energies along with a special delta term.

$$\mathrm{TOF}_n = \frac{k_B T}{h} \frac{1 - e^{\Delta G_r / RT}}{\sum_{i,j} e^{(T_i - I_j + \delta G_{i,j})/RT}}, \tag{24}$$

where k_B is the Boltzmann constant, T is the temperature, h is the Planck constant, ΔG_r is the Gibbs energy of reaction (in this case, of the CTM reaction R1), and T_i and I_j are the Gibbs energies of a given transition state and intermediate, respectively. A summation over all n possible mechanisms in the network, as in eqn 25, gives the TOF of the network as a whole.[167]

$$\mathrm{TOF} = \frac{k_B T}{h} \sum_n \frac{1 - e^{\Delta G_r / RT}}{\sum_{i \in \mathrm{cycle}_n, j} e^{(T_i - I_j + \delta G_{i,j})/RT}} \tag{25}$$

The delta term $\delta G_{i,j}$ here is defined as

$$\delta G_{i,j} = \begin{cases} 0 & \text{if } i > j, \textit{i.e.} \text{ TS follows intermediate} \\ \Delta G_r & \text{if } i \leq j, \textit{i.e.} \text{ TS precedes intermediate,} \end{cases} \tag{26}$$

which arises from the cyclical nature of the reaction. Let us assume that the cycle moves mainly in the forward direction, *i.e.* the TOF is positive. If we encounter the transition state i before intermediate j, the reaction cycle will need to be completed once before the transition state is reached again. In this case the energy difference between the two is offset by the reaction (free) energy ΔG_r. For an example, see Figure 4 where transition state T_1 immediately precedes intermediate I_2. The correct energetic span is calculated relative to T_1 in cycle $n + 1$.

Intermediates in side branches must be taken into account in calculations as they might be stable enough to affect the energetic span. Imagine an extremely stable species present in a side path swinging the thermodynamic equilibrium heavily to the side of said species, effectively poisoning the catalyst. The graph-theory implementation of the ESM can reproduce these effects and address the possible non-linearity of a heterogeneous catalyst cycle. We can simplify the examination of side branches by assuming that transition states in dead-end paths do not contribute to the reaction kinetics. This is reasonable because we have already assumed steady-state operation, *i.e.* that the main path stays in equilibrium with the side branch. In this case, the calculations can simply be completed

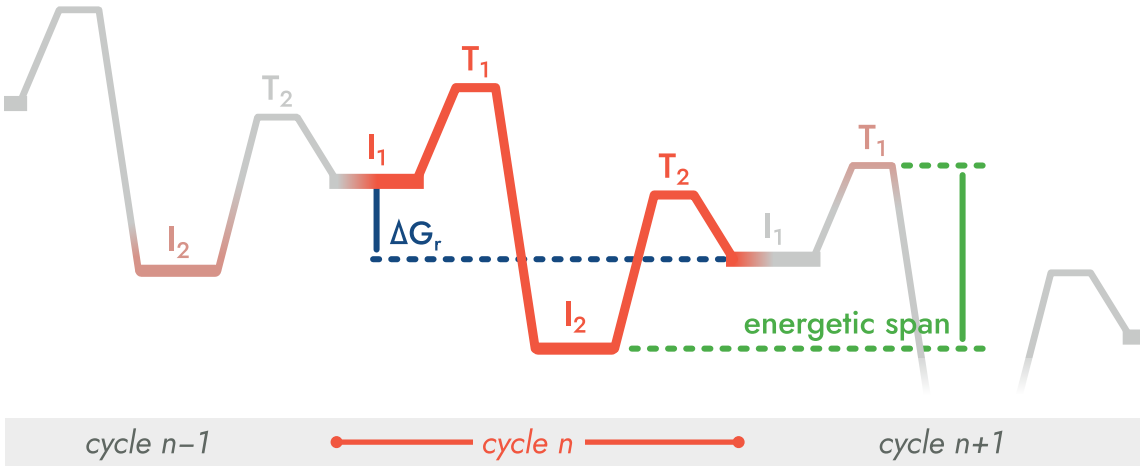

FIGURE 4 Example of a catalytic cycle viewed through the energetic span model. Intermediate I_1 is the starting point/regenerated catalyst of each cycle n. Viewing only one cycle, it could seem that the TOF is limited by the transition state T_2. However, due to the cyclical nature of the process, the I_1 of the next cycle is more TOF-limiting.

as in the case of simple cycles, by treating all intermediates in the branch as being in the position of the branching-off point.

QUANTIFYING INFLUENCES ON REACTION RATES. The concept of the degree of turnover frequency control X_{TOF} is largely similar to the more widely recognized degree of rate control (X_{RC}) that is used to analyse multistep reaction networks.[172–175] Conventionally, the degree of rate control is connected to a specific elementary step i as it is defined using rate constants[172,175]:

$$X_{RC,i} = \left(\frac{\partial r}{\partial k_i}\right)_{k_{i\neq j},K_i} = \left(\frac{\partial \ln r}{\partial \ln k_i}\right)_{k_{i\neq j},K_i} \tag{27}$$

where the rate constants of all other elementary steps ($k_{i\neq j}$) as well as the equilibrium constant of step i (K_i) are kept constant when differentiating. As the theory goes, a X_{RC} approaching 1 is the rate-determining step of the overall reaction. By contrast,† degrees of turnover frequency control are determined separately for intermediates and transition states, and therefore it is possible that the value of X_{TOF} is greatest for two states that are not consecutive. Put in more practical terms, we will not assume that individual elementary steps determine the reaction rate but instead that it is determined by stable intermediates and high–energy transition states regardless of where in the cycle they appear. That is, however, with the caveat apparent in eqn 26. A high-energy transition state appearing before a highly TOF–controlling intermediate may have a less controlling nature in an exothermic cycle because of the offset created by the reaction energy (see Figure 4).

† One could argue that anything rate–controlling is also TOF–controlling and *vice versa*. I make this distinction simply because of the differing mathematical definitions.

$$X_{\mathrm{TOF},T_i,n} = \frac{\sum_j e^{(T_i - I_j + \delta G_{i,j})/RT}}{\sum_{i \in \mathrm{cycle}_n, j} e^{(T_i - I_j + \delta G_{i,j})/RT}} \tag{28}$$

$$X_{\mathrm{TOF},I_j,n} = \frac{\sum_{i \in \mathrm{cycle}_n} e^{(T_i - I_j + \delta G_{i,j})/RT}}{\sum_{i \in \mathrm{cycle}_n, j} e^{(T_i - I_j - \delta G_{i,j})/RT}} \tag{29}$$

Thus, the sum of all X_{TOF} values for transition states add up to 1 and the sum of those for all intermediates sum up to 1.

$$\sum_i X_{\mathrm{TOF},T_i} = \sum_j X_{\mathrm{TOF},I_j} = 1$$

Individual values closer to 1 mean that changing the energy of the state in question would have a bigger impact on the TOF of the entire cycle. Note that there are divergent uses of terminology here, and the result in eqn 28 is also occasionally called the degree of rate control of a transition state.[176,177]

It is commonly the case that a given reaction network is mainly controlled by a single combination of a TOF–determining intermediate (TDI) and a TOF–determining transition state (TDTS), that is, the states both have X_{TOF} values close to 1. In this situation, we can also utilize the so–called energetic span approximation and dismiss all the other states. An equation (eqn 30) can then be constructed for the TOF of the entire reaction cycle that is remarkably simple and reminiscent of the Arrhenius equation.

$$\mathrm{TOF} = \frac{k_B T}{h} e^{-\delta E/RT} \tag{30}$$

where δE is the energetic span

$$\delta E = T_{\mathrm{TDTS}} - I_{\mathrm{TDI}} + \delta G_{\mathrm{TDTS,TDI}} \tag{31}$$

Once again, the delta term $\delta G_{\mathrm{TDTS,TDI}}$ from eqn 26 alludes to the cyclic nature of the reaction. The correct choice of TDTS and TDI is that which maximizes the energetic span δE.

The energetic span model was used in combination with an X_{TOF} analysis in paper III to provide a simplified kinetic model to supplement the energetic values. The Python-based code used to carry out the energetic span analysis was originally developed by Garay-Ruiz,[171,178] and modified by the author for increased speed and computational efficiency with the goal of being able to analyse a more complicated network. A specialized Python script was written by the author for the X_{TOF} analysis.

3 DFT STUDIES ON HETEROGENEOUS CU/ZN/ZRO_2 CATALYSTS FOR CO_2 CONVERSION

A number of models were chosen to model different aspects of the Cu/Zn/ZrO_2 system. When focusing on the interface between the metallic component and the supporting oxide, *i.e.* in papers I and III, we chose to utilize periodic nanorod models that were supported on periodic slabs of zirconia. A nanorod model allows the metal to be periodic in one horizontal direction, which helps avoid particle-in-box type effects that could occur in cluster models and produces less localized states and a DOS that is more representative of metal surfaces.[90] The nanorods were cut from bulk Cu with a (111) facet facing the oxide. Put another way, the rods are built of three one-atom-thick Cu(111) layers. In paper III, some atoms at the interface were replaced with Zn (see Figure 5). This was done in order to include all three components of the CZZ system at the reactive interface. Most previous computational studies on CZZ catalysts have only included one or

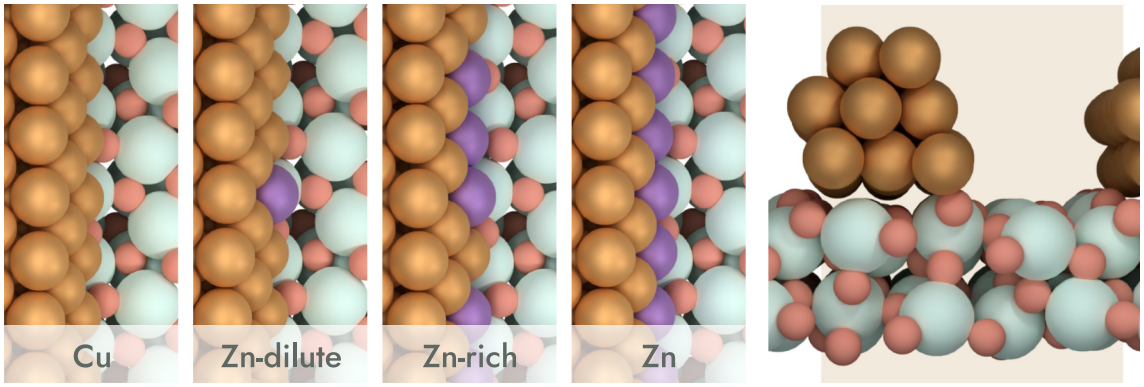

FIGURE 5 Nanorod models used to represent a CuZn interfaces on monoclinic zirconia surfaces. The image on the right shows the thickness of the ZrO_2 slab and the cross-section of a nanorod.

two of the three components, although a handful of ternary ones have been used recently.[73,179] The mixed interfaces in our models let us examine the interplay of all three and represent a suggested case of surface alloying.[37,40,43,76]

The rods were placed on a *m*–$ZrO_2(\bar{1}11)$ surface that was built from two stoichiometric layers. The relatively thin slab was used simply to reduce the computational costs. Based on our tests, the adsorption strength of the nanorod experiences only slight variation when the thickness is increased. However, the calculated adsorption of CO_2 at the interface is slightly weaker because of this simplification.

3.1 Stability of metal–support interface models

For the purposes of this work, it was important that the calculations include the zirconia support in an explicit form, as its exceptional selectivity towards CTM is one of the central questions studied. However, the accuracy of computational results depends on how well the model system describes actual active sites. Therefore, it is important that we do not introduce artificial stabilizing or destabilizing effects that arise from poor model selection or a lack of benchmarking.

In paper I, we chose to examine and assess two candidate models for a Cu nanorod that are geometrically similar to nanorods that have been used for FCC-metals in recent literature.[63,90,180] A top-down view and the cross-sections of the nanorod models chosen are shown in the first two columns of Figure 6. The two nanorod models are both cut from the bulk FCC structure of copper, but in slightly different orientations. Consequently, the oxide–metal interface between zirconia and the bottom of the nanorod features a different Cu facet. One type of rod has a bottom facet where the Cu atoms are arranged in a square grid, corresponding to the (100) plane of an FCC structure. The other has the hexagonal arrangement typical for (111) facets. As a form of shorthand, the two nanorod models in their entirety will be referred to as the (100) and (111) structures, based on their respective termination.

Two phases of zirconia were chosen for the comparison: tetragonal and monoclinic. These are the two phases that are stable under CTM reaction conditions[181–183] while also possessing a regular crystal structure, unlike amorphous zirconia. Of the two, the monoclinic phase is of much lower symmetry than tetragonal, as evident visually by the more irregular look of the *m*–$ZrO_2(\bar{1}11)$ surface. This has a clear significance, as we see that the Cu nanorods—and any other Cu particles—attach to the zirconia surface *via* Cu–O bonds. In the third column of images in Figure 6, we see that the nanorods are aligned so that the bottom layer of Cu atoms are in positions between Zr cations, typically near ZrO_2 lattice oxygens. The placement of Cu directly on Zr top sites is unfavourable but often unavoidable. Shifting the rod perpendicular to its direction can cause up to a 2.2 eV increase in energy per unit cell. However, because of the inherent lattice mismatch and the different geometries of the rod and support, there is actually very little variation in energy when the rod is shifted along its periodic direction. It is also likely that making the nanorod wider would significantly diminish its positional preference, as the irregularity in Cu–O interactions is averaged out.

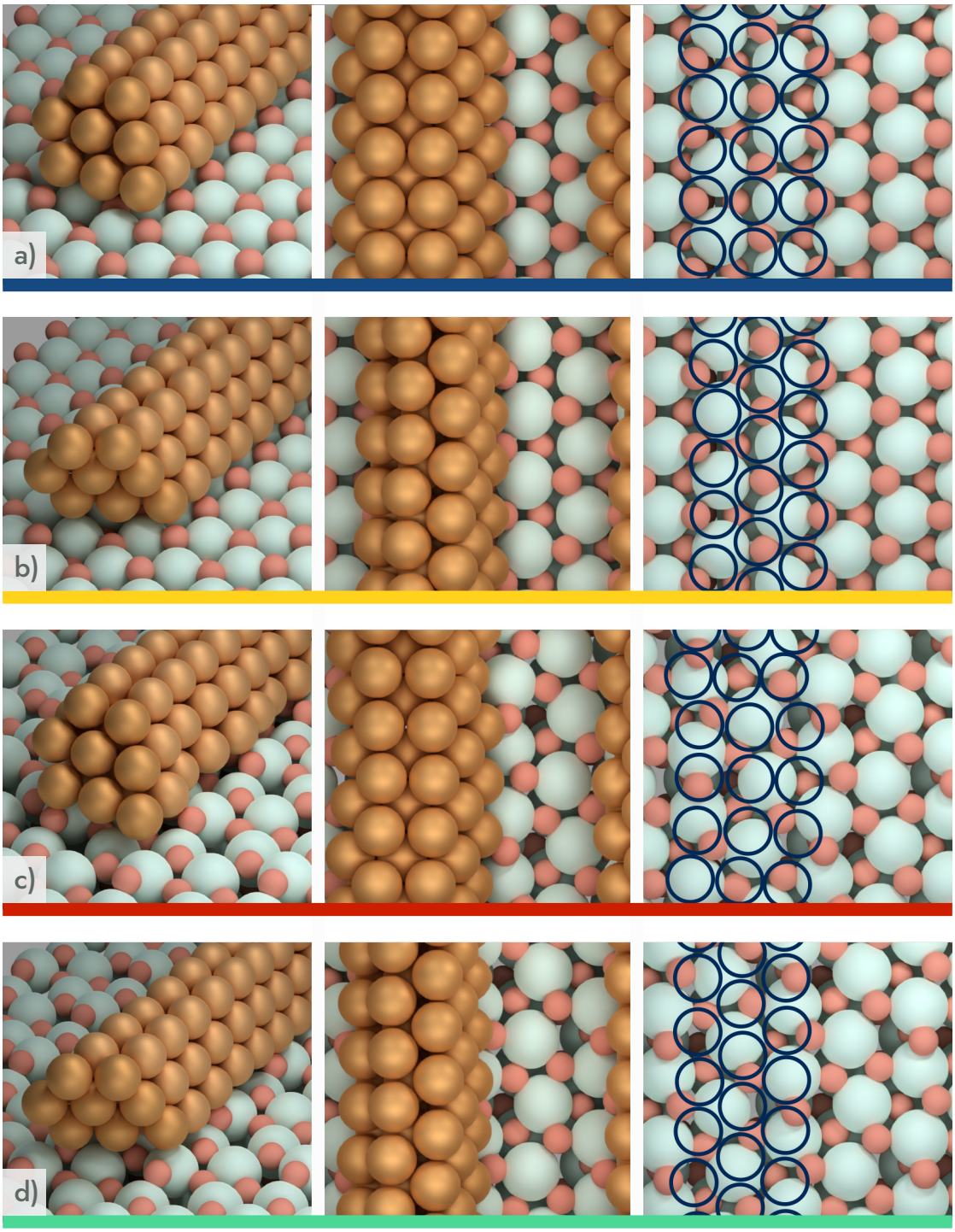

FIGURE 6 Optimized positions for the Cu nanorods used in paper I on tetragonal (a, b) and monoclinic (c, d) zirconia surfaces. a, c) (100) nanorods; b, d) (111) nanorods. The cross-section and a top-down view of each rod is shown. The rightmost images show how the ZrO_2 support aligns with the bottom layer of Cu atoms (marked with dark circles).

TABLE 1 Binding energies of the moderate-strain nanorods (per Cu repeating unit), as well as the best CO_2 adsorption energy found along the interface of said rod and the ZrO_2. Positive strain means that the nanorod is stretched relative to bulk Cu–Cu distance, negative strain equates to compression. Shifts in the Cu d-band $\Delta\varepsilon_d$ caused by interaction with the ZrO_2

interface		strain (%)	$\Delta\varepsilon_d$ (eV)	ΔE_b(rod) (eV/r.u.)	$E_{ads}(CO_2)$ (eV)
t-ZrO_2	(100)	−2.71	−0.40	−1.06	—
		−0.72	−0.33	−1.11	−1.01
		+4.24	−0.40	−0.98	−1.17
	(111)	−2.71	−0.28	−0.97	−0.51
		−0.72	−0.28	−0.91	−0.52
		+4.24	−0.32	−0.84	−0.71
m-ZrO_2	(100)	−1.02	−0.26	−0.74	−1.38
	(111)	−1.02	−0.18	−0.67	−0.44

Combining two (or more) chemical species in DFT calculations where the components are also periodic in the same direction(s) introduces its own problem. It is unlikely that one unit cell is the perfect size to match the lattice constants of all components, and thus there is an inherent strain that comes from the mismatch. In a two-component model, such as a supported nanorod system, the size of the computational cell can be optimized for one but not both. Several combinations of unit cells, which match the ZrO_2 surface exactly but put some strain on the Cu nanorod, were examined to quantify what magnitude of effect this mismatch may have. Some key features of these combinations are summarized in Table 1. It was found that this kind of artificial strain has a non-negligible effect on the stability of the rod model, as well as the adsorption of a CO_2 molecule. More extreme strains than those listed in Table 1 were originally included. However, it was found that they quickly begin causing clear structural deformations in the rod during CO_2 adsorption. This change in effective coordination leads to very unpredictable differences in CO_2 adsorption energies between different Cu sites at the interface, which vary significantly more as the strain was increases. It is difficult to establish an absolute rule for a maximum strain before the rod becomes unstable, but $\pm 5\,\%$ certainly seems to be too high. For these reasons, we will focus on a combination of ZrO_2 slab size and rod size which minimizes the strain caused by their lattice mismatch, despite the need for a slightly larger unit cell and thus more computational resources. In the minimum-strain configurations, the nanorod is compressed by 0.72 % relative to bulk when adsorbed on t–ZrO_2 and by 1.02 % on m–ZrO_2.

In the gas phase, the (111) nanorod is more stable than the (100) nanorod by 0.24 eV per Cu_8 repeating unit. This is not necessarily surprising, as Cu(111) surfaces are generally the most stable copper facets,[42] and all the exposed faces of the (111) rod share this geometry. As a consequence, when we examine the

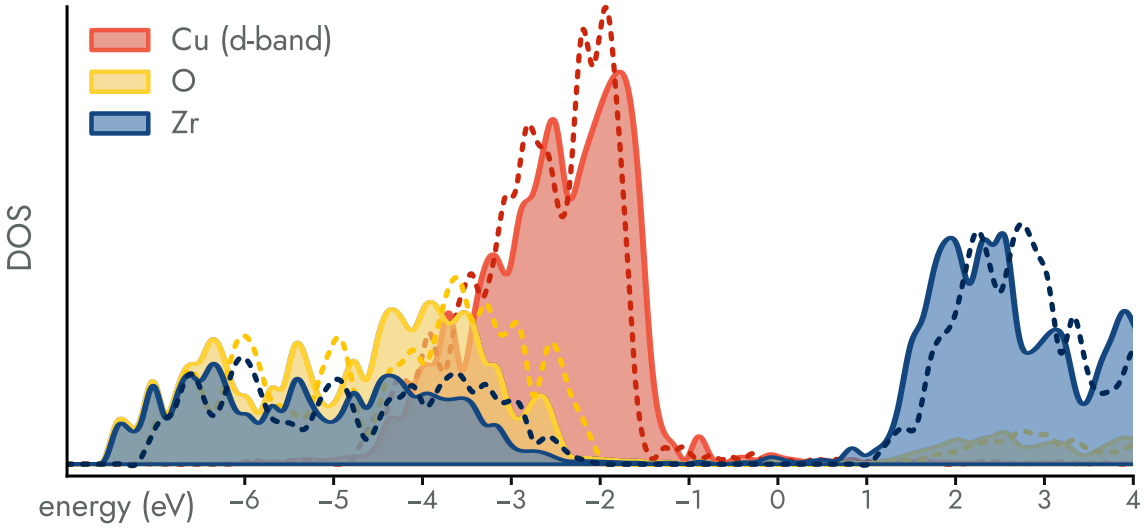

FIGURE 7 The density of states of the minimum-strain (111) rod on t–ZrO_2. Dashed lines correspond to the Cu and ZrO_2 components calculated in separate cells, filled areas show the DOS of the combined system.

binding energy (Table 1) with which the gas-phase rod attaches to the support, we can see that the (100) nanorod is stabilized much more by the interaction with ZrO_2. It would appear that the binding energy is stronger for rods experiencing negative strain. However, it remains somewhat unclear how the stabilization connects to an increasing Cu:ZrO_2 ratio. By analysing changes in the copper d-band centre, a kind of ligand effect can be seen during the interaction of copper and zirconia. Adsorption of the rod onto the support shifts the d-band of the interface atoms ($\Delta\varepsilon_d$) down in energy (see Table 1). However, the shift down is seen only for the Cu atoms on the bottom of the rod, which are in contact with ZrO_2 lattice oxygens. This includes several of the interface atoms and thus the d-band centre of the interface is affected. The trend for the rod as a whole is very different, and it seems that the gap between Cu and Zr states around the Fermi level actually gets narrower, as can be seen in Figure 7. The shift in $\Delta\varepsilon_d$ of the interface atoms is not strongly correlated with strain, especially when structural deformations occur. $\Delta\varepsilon_d$ is slightly smaller for monoclinic zirconia. However, no clear trends are easily obtained between rod stability or CO_2 adsorption strength and the d-band centre or its shift. The exact environment and coordination of the individual interface atoms seem to be more important than differences in specifics of the electron structure, and the interface is too complex to study using these simplifications. The assumptions inherent in the d-band model break down at the metal–oxide interface.

The results from this screening lead to the choice of a slightly larger unit cell in combination with the nanorod systems used in the rest of the work, despite the slightly increased computational cost. Of the two nanorods, the more stable (111) was used so as not to artificially enhance CO_2 adsorption strength. Finally, while the tetragonal support was included in this discussion, the following sections will focus solely on monoclinic zirconia, as did papers II, III, and IV.

3.2 Elementary steps of the CTM process

3.2.1 Carbon dioxide adsorption onto Cu/Zn/ZrO_2

The activated adsorption and its strength was an important metric used throughout papers I, III, and IV. Indeed, Table 1 already showcased the adsorption energies of CO_2 at the most optimal adsorption site along each strained interface. In this context, activated adsorption refers to a situation where the very stable structure of CO_2 is disrupted. This typically manifests as a bending of the CO_2 (a change in the hybridization of the C atom, if you prefer), and it may also include a transfer of electron density to the molecule. Technically, another potential activation could be the direct splitting of the CO_2 molecule into adsorbed CO and O, which has been suggested as a possible mechanism on Cu step or defect sites.[97,184,185] However, this pathway was not included in the model reaction network, as it was found that the resulting intermediates are remarkably unstable at most of the interfaces studied here.

MINIMUM-ENERGY SURFACES. Let us first examine how CO_2 adsorbs on the surface of pure copper, modelled as a Cu(111) slab (Figure 8d). The molecule stays completely linear, as it does in the gas phase. This physisorption is very slightly exothermic with an adsorption energy of -0.21 eV. In the optimized geometry, the distance between the Cu surface and the CO_2 is 3.1 Å, which likely indicates the absence of covalent bonds. The Bader analysis reported in paper IV suggests that the molecule has a very slight charge of ca. $-0.1\,e$, although this small a number may be meaningless due to the inaccuracy of the partitioning method. Regardless, the molecule can be said to stay largely charge neutral when adsorbed. In many computational works on metal surfaces, it is often assumed or implied that CO_2 activation occurs through direct reaction between linear CO_2 and a dissociated hydrogen species on the surface; what could be considered Eley–Rideal-type formation of formate (HCOO),[37,38,68,186] although some could argue that this is not strictly correct if the linear CO_2 is thought to be physisorbed on the surface. Regardless, it may be that activative adsorption of CO_2 is not necessarily required for the formation of methanol. The activation energy of this type of HCOO formation has been reported to be in the order of 0.8 eV to 1.0 eV,[38,68,186] putting it in the same general range as HCOO formation at the interface, discussed later.

The ZrO_2 support itself has the ability to adsorb and activate CO_2. Our calculations, as well as previous studies,[69,70] show that the optimal adsorption geometry is a trigonal structure resembling a carbonate ion (CO_3^{2-}), where the CO_2 attaches to one of the exposed lattice oxygens on the zirconia surface (Figure 8a). One of the O atoms in the adsorbate rests on top of a Zr cation. The most favourable adsorption location is the two-coordinated oxygen found on the m–$ZrO_2(\bar{1}11)$ surface.

NANOPARTICLE–ZIRCONIA INTERFACES. Several experimental and computational studies have pointed to the CO_2 reduction taking place at a metal–

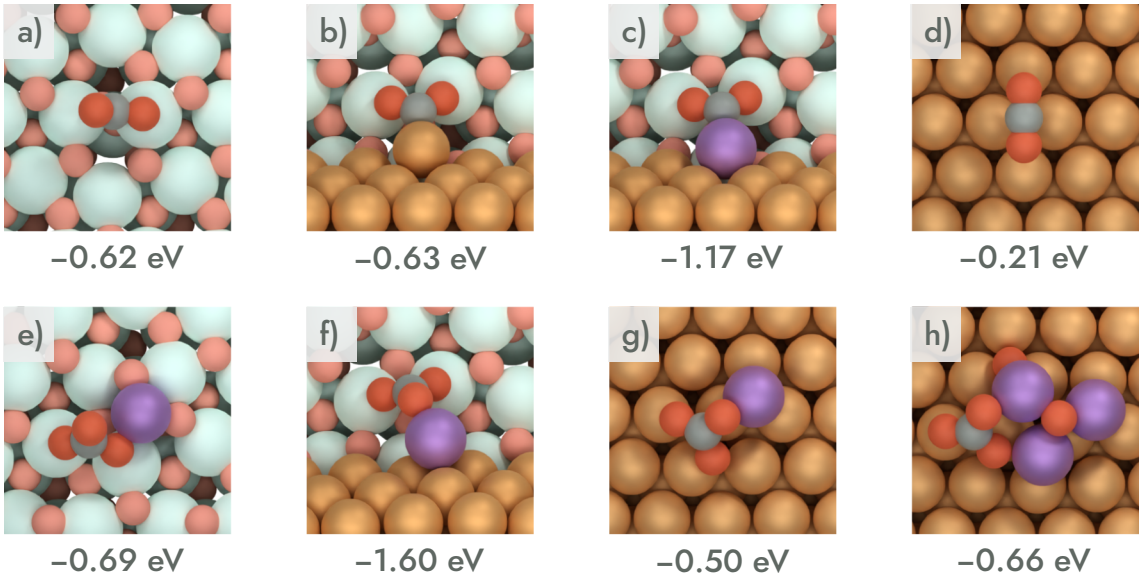

FIGURE 8 CO_2 geometries and adsorption energies (E_{ads}) at several sites relevant to the Cu/ZnO/ZrO_2 system: a) ZrO_2, b) Cu–ZrO_2 interface, c) CuZn–ZrO_2 interface (Zn-dilute), d) Cu(111), e) ZnO/ZrO_2, f) ZnO/Cu–ZrO_2, g) ZnO/Cu(111), h) Zn_3O_3/Cu(111). Note that E_{ads} are calculated using total energies without ZP-corrections.

oxide interface.[35,52,58,67–70] This made the interface between the Cu nanoparticle and the zirconia support the primary interest of the studies presented. It was demonstrated in previous computational studies[69,90] as well as papers I and III that, at the Cu–ZrO_2 interface, a distinctive CO_2 adsorption geometry is favourable. The CO_2 molecule coordinates to an interface Cu atom through its carbon, while its oxygens are placed on two adjacent Zr top sites. In our calculations at the interface of Cu and m–ZrO_2, the adsorption energy was determined to be -0.6 eV and the Cu–C length was observed to be ca. 2.0 Å. Unlike in the case of CO_2 physisorption on Cu(111), there is significant charge transfer from the catalyst to the adsorbate. The charge of the adsorbed $CO_2^{\delta-}$ moiety is ca. $1.2\,e$ at both the Cu interface and the Zn-containing interfaces. The majority of this extra electron density is concentrated on the C atom. Activation of the molecule is also evident from its bent geometry. A top-down view of this geometry can be seen in Figure 8b. Because of the way both oxygens are touching the zirconia surface, we occasionally call this a "bidentate" binding geometry. A "monodentate" version, where a Cu–C bond is formed just the same, but only one oxygen rests on a Zr cation is found mainly in cases where the structure of the interface is more restrictive. The change in coordination has only a minor impact on stability. Similar adsorption modes that are reminiscent of this "monodentate" form have also been reported at Pt–TiO_2 and Rh–ZrO_2 interfaces[47,63] as well as on the edges of reverse ZrO_2/Cu(111) and TiO_2/Cu(111) cluster systems,[55,68] where similar Cu–C bonds are formed with one oxygen coordinating to a Zr/Ti cation.

Figure 8c features a mixed CuZn interface from paper III. The adsorption geometry remains the same, although it seems that the Zn is pulled slightly

farther away from the rod which indicates that the Zn-containing adsorption sites may have enhanced geometric flexibility. The Zn–C distance is ca. 2.1 Å, which is similar to the copper interface. The presence of Zn at the active site increases CO_2 adsorption strength, with E_{ads} ranging between -1.1 and -1.3 eV depending on Zn content, although the effect seems to disappear when a metal-bound hydrogen atom is near the active site, such as during the first hydrogenation reaction to HCOO.

SUB-NANO CLUSTER–ZIRCONIA INTERFACES. In an experimental study,[187] the activity of inverse ZnO/Cu(111) and ZnO/Cu(100) catalysts was attributed to the formation of a ZnO–Cu interface which binds CO_2 and formate. The authors report observing ZnO nanoparticles with properties distinct from ZnO bulk or CuZn alloys. The edges of "graphitic" ZnO layers on the copper surface have also been suggested as potential active sites with calculations showing favourable CO_2 adsorption energies.[93] Similarly, we have shown in paper IV that ZnO monomers and small ZnO clusters are able to bind CO_2, regardless of whether they are located on the ZrO_2 surface, the Cu(111) surface, or the Cu–ZrO_2 interface. The preferred adsorption geometries, shown in Figure 8e–f, are similar in all cases: the CO_2 takes a trigonal, carbonate-like form, where the CO_2 attaches to the monomer/cluster *via* a C–O bond. CO_2 adsorption energies between ZrO_2, ZnO/ZrO_2, ZnO/Cu(111), and Cu–ZrO_2 are very consistent, falling in the range of -0.5 eV to -0.7 eV. Notably, however, adsorption to the ZnO/Cu–ZrO_2 interface (Figure 8f) is the strongest of all modes we have found by a significant margin. The difference can not be explained by charge transfer, as the (Bader) charges of the adsorbed CO_2 molecules are quite consistently around $-0.2\,e$ to $-0.3\,e$ between the different binding locations. As mentioned, the adsorbate is more negative at the metallic interface, but this is not reflected in the E_{ads}. Instead, we suspect that the strong binding at ZnO/Cu–ZrO_2 is largely a consequence of the high flexibility of the interface structure, which significantly reduces strain in the adsorbed CO_2 compared to more geometrically restrictive active sites.

We also performed calculations on mixed monomers (CuZnO), as there is a chance they may be formed under reaction conditions as a result of Cu migration, *e.g. via* Ostwald ripening[188] or similar processes. The mixed monomers also able to bind CO_2 by its oxygen centre with an adsorption energy of -0.46 eV. In this case the adsorption geometry of CO_2 is once again similar to those on ZnO monomers. Larger mixed clusters of the form $Cu_xZn_xO_x$ ($x \geq 2$) create a variety of potential adsorption centres, some of which are able to bind CO_2 and some are not. Again, carbonate geometries can form as a combination of CO_2 and oxygens belonging to the cluster. However, adsorption modes with metal–carbon bonds like those possible at the interfaces and Cu clusters are not found. Some attempts to optimize activated structures succeeded but yielded adsorption structures that were thermoneutral or significantly endothermic.

3.2.2 Supply of dissociated hydrogen

It is generally believed that the dissociative adsorption of molecular hydrogen occurs on the surface of the Cu component.[37,53,58,94–96] Although computational studies have shown that the abundant Cu(111) surface is capable of hydrogen splitting,[96,147] lattice edge and defect sites have been credited with high efficiency for hydrogen dissociation due to increased reactivity brought about by the lower coordination.[95,97] Surface diffusion of dissociated hydrogen on copper particles is also facile, with barriers in the order of 0.15 eV.[189] It is therefore reasonable to assume that hydrogen will be available for reactions at the Cu surface and Cu–ZrO_2 interface. We also considered the dissociative adsorption of H_2 at our CuZn–ZrO_2 interfaces, where both H atoms adsorb on Cu/Zn sites at a nanorod interface. Without further corrections to DFT energies, the homolytic dissociation is endothermic by 0.4 eV with an activation energy of ca. 1.1 eV, the same value determined for dissociation on Cu(111). The interface also presents an option for heterolytic dissociation where, upon dissociation, a hydride–proton pair is created. A H_2 molecule contacting both the metal and the zirconia can split into a hydride on the metal and a proton on an oxide anion. However, this heterolytic dissociation is endothermic by ca. 1.0 eV and has a kinetic barrier of 1.4 eV. It is therefore less feasible than the spillover process, which only has a barrier of 0.8 eV. While the spillover by itself is endothermic by 0.6 eV, the presence of CO_2 or further reaction intermediates stabilizes an adjacent H on the oxide up to the point where it is lower in energy than a rod-bound H.

Our calculations also show that a H_2 molecule may adsorb onto a ZnO monomer on ZrO_2, breaking the H–H bond in the process. In this case, the H_2 splits into a hydride which binds to the Zn, and a proton which forms an O–H bond with the oxygen of the monomer. Relative to the ZP-corrected gas-phase hydrogen molecule, the adsorption energy is a considerable -1.3 eV. Furthermore, a NEB calculation shows that the reaction only needs to cross an activation barrier of 0.5 eV. This suggests that highly dispersed ZnO centres, that may exist *e.g.* after catalyst preparation using ALD, are also able to supply dissociated hydrogen to surface reactions. This may also explain the non-zero activity of Cu-free ZnO/ZrO_2 catalysts.[190,191]

3.2.3 Catalytic pathways and intermediates at Cu(Zn)–ZrO_2 interfaces

There are two main competing pathways that have been proposed for the catalytic conversion of CO_2 to methanol which are presented in Figure 9.[35,52,80] The formate pathway begins with the reaction of CO_2 to form the titular formate intermediate (HCOO). As discussed in the previous section, this could happen either *via* a Langmuir–Hinshelwood or an Eley–Rideal type reaction, depending on if the CO_2 is adsorbed on the surface first. What we will call the reverse water–gas shift pathway involves the conversion of CO_2 to carbon monoxide (CO), which is then hydrogenated to methanol on the same catalyst. The suggested mechanism here begins with the formation of a (hydro)carboxyl intermediate COOH. As

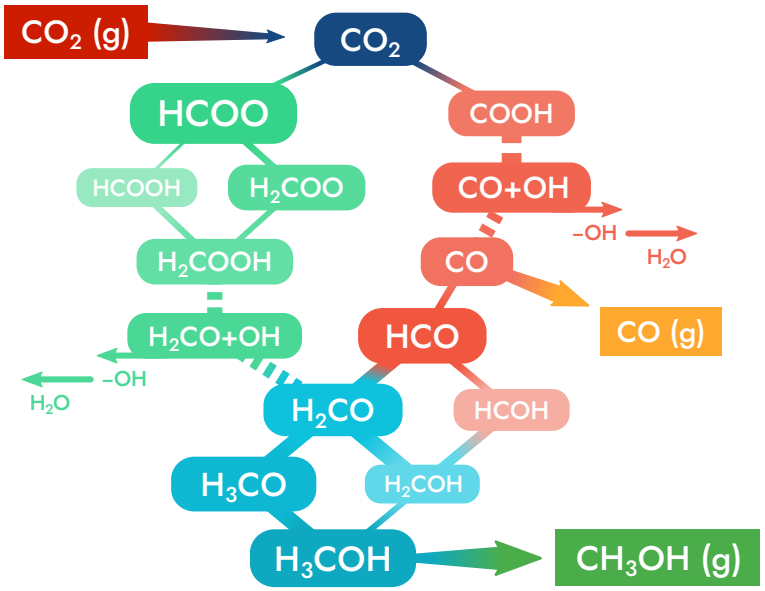

FIGURE 9 Theoretical reaction network for carbon dioxide conversion to methanol. The pathway along the left side (light green) is often called the formate pathway. The reverse water–gas shift pathway through CO formation and hydrogenation is on the right (red-orange). Intermediate species in rounded boxes are adsorbed on the catalyst surface, Solid lines between intermediates imply hydrogen addition. Arrows are points where (de)adsorption may occur.

mentioned, a third mechanism starting with direct CO_2 splitting has been investigated previously[97,184,185] but will not be included here in detail. The system of shorthand for intermediates and transition states in this section is the same as used in paper III.

The reaction network was inspected by modelling the adsorption of the intermediates at the Cu nanorod interface as well as the three Zn-containing interfaces introduced on page 39. Additionally, the transition states for the elementary reactions along the proposed mechanisms were sought using the nudged elastic band method. Unless otherwise specified, the values in the following discussion are of the Zn-dilute interface. Regardless, they are largely representative of all Zn-containing interfaces. Differences between the interfaces are highlighted when relevant. The process of obtaining Gibbs free energies corrections by computational methods was omitted in this study simply due to the large number of structures included. Because the focus here is solely on obtaining a qualitative comparison between the RWGS and formate pathways, and the intermediate steps that we are interested in are mainly surface reactions, the energies produced by DFT are enough for our purposes. However, this omission does affect the adsorption/desorption steps of gas-phase components that occur at the beginning and end of the conversion—namely those of CO_2, H_2, and CH_3OH. By extension, it may also have an impact on the reaction energy. Yet, with the level of theory used here, the reaction energy was determined to be $-0.53\,\mathrm{eV}$, which is in line with the reaction enthalpy of $-0.42\,\mathrm{eV}$ to $-0.52\,\mathrm{eV}$ reported in previous literature.[52,186]

3.2.3.1 Competing reactions for carbon dioxide hydrogenation

As discussed in subsection 3.2.1, CO_2 adsorbs readily at the interface between Cu or CuZn and the ZrO_2 support in a way that involves both components: the carbon atom attaches to the nanorod, while the oxygens rest on Zr cations. Generally, it is believed that the Cu component is responsible for the dissociation of molecular hydrogen.[37,53,58,94–96] Consequently, it can be assumed that the hydrogens are bound to the metal surface as the hydrogenation reactions begin. On the other hand, a hydrogen spillover effect, where hydrogen moves from the metal onto the surface of the support, may be important for catalytic activity.[98,99] From this setting, two options emerge for hydrogen addition (Figure 10): reaction with a Cu-bound H to form a C–H bond and a formate intermediate, or reaction with a ZrO_2-bound H to create an O–H bond and a carboxyl intermediate. This spillover effect was considered when modelling the elementary reactions of the CTM process, especially those where the reactants are not bound to the metal–support interface such as the hydrogenation of the methoxy intermediate.

FORMATE PATHWAY. The reaction to formate has a significant activation energy of 1.2 eV (T_{01} in Figure 10a), which is in line with previous results.[68,69] The activation energy is slightly lower for the Cu interface at 1.0 eV, which would indicate that Cu stabilizes the H atom passing over it more than Zn. This may also be seen in the exothermic energy of the adsorption of the hydrogen at the Cu interface, as seen in Figure 11. During the formation of the HCOO intermediate, the metal–carbon bond is broken, but the adsorbate remains bound to Zr cations through both its oxygens. The reaction is exothermic by 1.2 eV and the resulting formate intermediate is remarkably stable with an adsorption energy of -2.1 eV. Despite this, the formate is readily hydrogenated into a methylenedioxy (H_2COO) intermediate in the vicinity of the interface. Hydrogen from the metal is able to react and form a second C–H bond with an activation barrier of ca. 0.4 eV. Many past studies conducted using metal surface or inverse catalyst models[37,38,48,55,68,192] have concluded that the hydrogenation of the formate proceeds *via* formic acid (HCOOH) and do not report values for H_2COO formation. However, in our calculations on ZrO_2 supported systems, HCOOH formation is clearly the less favourable option with an activation energy in excess of 1.5 eV. The HCOOH intermediate is also ca. 0.8 eV less stable than the H_2COO. This difference in the stabilities can be explained by the presence of Zr–O bonds that stabilize the methylenedioxy structure on ZrO_2, while the copper shows no such effect. At the interface, the metal component is not involved in the adsorption of H_2COO at all. Due to the low kinetic barrier between them, the conversion of HCOO to H_2COO and *vice versa* is likely to be fast, which has also been suggested in a previous computational study.[69] The reaction following the H_2COO intermediate—the creation of a hydroxymethoxy intermediate H_2COOH—also proceeds through a similarly modest barrier of ca. 0.5 eV. This reaction takes place on the zirconia only, as neither its reactants or products are bound to the nanorod and the hydrogen is transferred to the molecule from a ZrO_2 lattice oxygen. On zirconia, H_2COOH readily dissociates into formaldehyde (H_2CO) and a

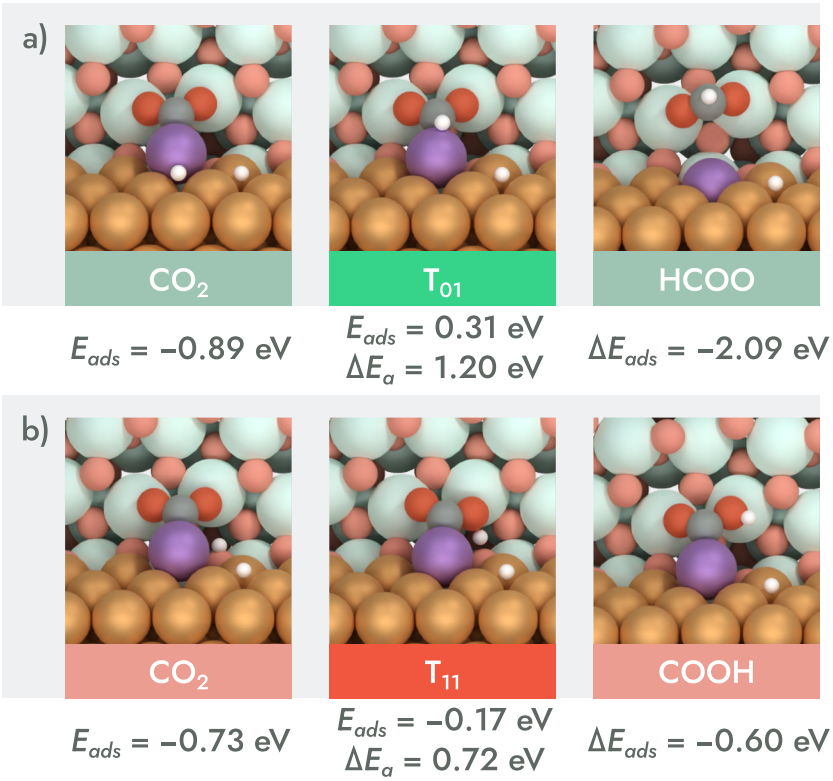

FIGURE 10 Elementary reactions of CO_2 conversion to formate (a) and carboxyl (b) at the Zn-dilute interface. E_{ads} relative to gas-phase CO_2 and H_2, as well as the activation barrier ΔE_a are shown.

Zr-bound hydroxyl group through a barrier of 0.2 eV.

RWGS PATHWAY AND CO HYDROGENATION. In the CO_2 to COOH reaction presented in Figure 10b, the hydrogen is initially bound to a ZrO_2 lattice oxygen at the interface from where it reacts to form a bond with the oxygen of the adsorbate. This reaction is slightly endothermic relative to the adsorbed CO_2, but its activation energy is only 0.7 eV. In a previous study,[69] the COOH intermediate was created starting from a hydrogen that was initially bound to the Cu cluster. However, this lead to a barrier that is significantly higher at 2.0 eV, as was corroborated by our test calculations at the Zn-dilute interface which produces a similar result when the hydrogen is initially placed on the metal.

The formed carboxyl intermediate retains a bent shape similar to the adsorbed CO_2 molecule, where its carbon is bonded to the active metal site and its oxygens remain bound to Zr top sites. The added hydrogen points away from the zirconia surface. The addition of the hydrogen has weakened the C–O bond between the new OH group and the central carbon, and its dissociation becomes facile. At CuZn interfaces, the barrier for this breaking of the adsorbate into CO and OH is only 0.2 eV. Conversely, since the COOH is bound to the interface, a hydrogen could conceivably react from the metal surface to create HCOOH. This option was explored through NEB calculations, but resulted in the spontaneous breaking of the C–O bond during the simulation, as the barrier for this H–C bond formation was in excess of 0.7 eV. It was therefore excluded from the network, as it seems reasonable to expect that COOH breaks into carbon monoxide and a Zr-

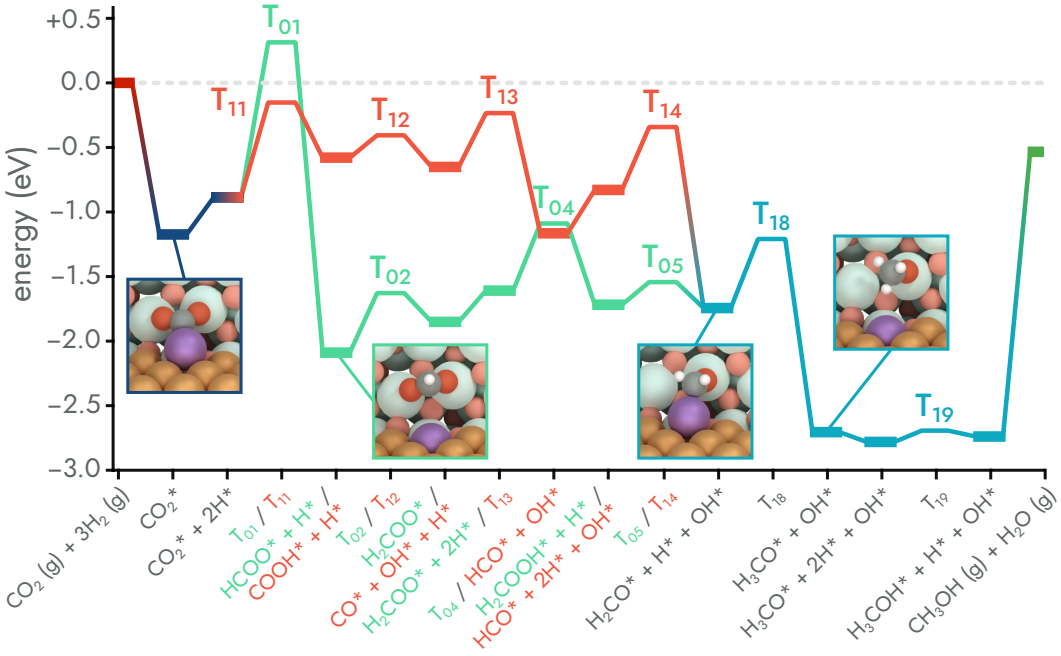

FIGURE 11 Potential energy diagram of the formate (green) and RWGS (red) pathways at the Zn-dilute interface.

bound OH group instead. The CO molecule can be adsorbed on the Cu surface or the Cu–ZrO_2 interface, but is also significantly stabilized by Zr cations and can thus stay adsorbed on the zirconia. In fact, the adsorption energy on both Cu interface sites and Zr sites is similar at ca. −0.5 eV relative to gas-phase CO.* Notably, the Zn centres present at the interface are not able to adsorb a CO molecule. Instead, it moves to an adjacent Cu site.

As the first step of carbon monoxide hydrogenation, CO adsorbed at an interface Cu site forms a bond with a metal-bound H atom to produce a formyl intermediate (HCO). This reaction is exothermic by −0.4 eV with an activation energy of 0.32 eV. We explored COH formation as an alternative but found it to be endothermic by 0.6 eV and hindered by a considerable barrier and thus excluded. HCO hydrogenation to HCOH was left out for the same reasons. Instead, HCO reacts with hydrogen from the metal to form H_2CO with an activation energy of 0.5 eV. Combined, the hydrogenation of CO into H_2CO is exothermic by −1.3 eV.

Figure 11 provides an easy visual comparison between the competing formate and RWGS pathways. It is clear that intermediates belonging to the RWGS process and the hydrogenation of CO to H_2CO are less stable than those along the formate path. On the other hand, the RWGS pathway is free of the high barrier associated with HCOO formation and its energy landscape is much flatter. Therefore, it could be that the formate pathway is limited by its kinetics. Ultimately, it is not immediately apparent which pathway is favoured.

Elementary steps from H_2CO to the release of methanol are shared between the two mechanisms. H_2CO can be hydrogenated to a methoxy intermediate (H_3CO) at the interface, the activation energy of which varies in the order of

* The values in Figures 11 and 12 are relative to gas-phase CO_2 and H_2 and include OH and H on the surface.

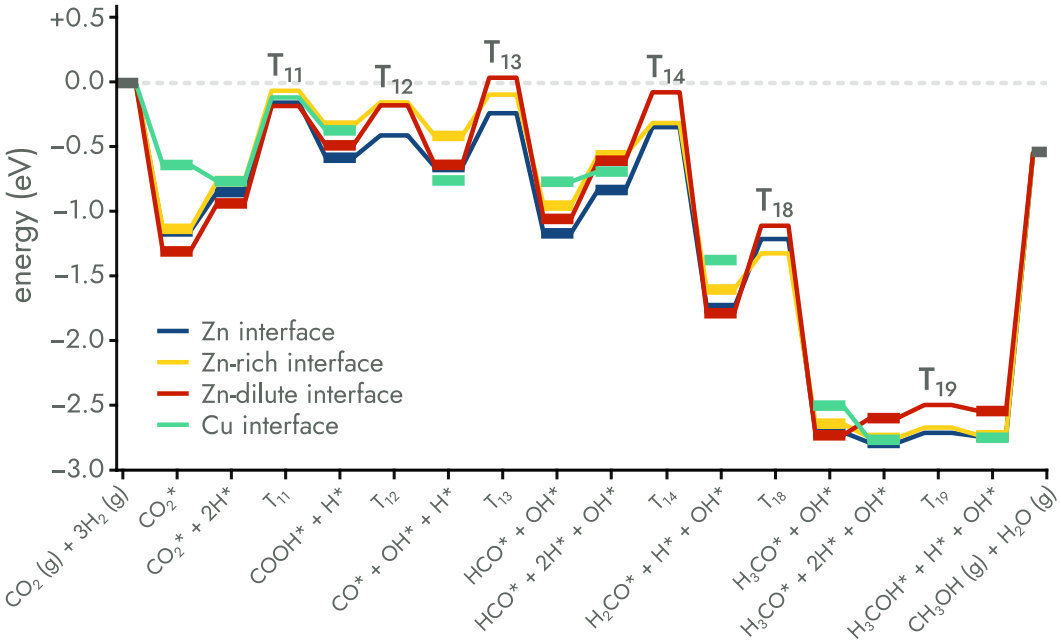

FIGURE 12 Potential energy diagram of the RWGS pathway at all Cu–ZrO_2 and CuZn–ZrO_2 interfaces.

0.4 eV to 0.6 eV depending on the interface. The formation of H_2COH is also possible from hydrogen that has spilled over onto the zirconia, and the activation energy for this is no more than 0.1 eV. However, the formation of the methoxy species from H_2CO is exothermic by 1.0 eV, while the reaction to H_2COH is practically thermoneutral. The situation is essentially reversed for the final step, where H_3CO reacts onward through a negligible barrier and a practically thermoneutral reaction using hydrogen from the zirconia surface, and H_2COH forms methanol over the interface in a very exothermic reaction with an activation energy of 0.5 eV to 0.7 eV. The product, methanol, is adsorbed on the zirconia surface through a Zr–O bond, standing near the interface but without clear bonds to the metal. The molecule is bound to the zirconia quite strongly with an adsorption energy of 1.3 eV. In addition to the desired product, the process creates water which, in our calculations, was left in its dissociated form on the zirconia surface, *i.e.* one hydroxyl on a Zr top site and one hydrogen either forming a terminal OH with a ZrO_2 lattice oxygen or adsorbed on the metal. The energetic cost of removing these as molecular water is relatively high at ca. 0.9 eV, suggesting that they may instead accumulate on the zirconia surface.

INFLUENCE OF ZN CONTENT. As seen in Figure 12, there are several points in the PES where the stability of intermediates differs between the Cu interface and the Zn-containing interfaces. The differences are, as one could expect, most visible in intermediates that are in direct contact with a metal site. While the optimal adsorption locations for the adsorbates are near the interface where they were formed, many intermediates such as HCOO, H_2COO, and H_3CO, do not form clear bonds with the interface. Thus, there is only a very small difference in their relative energies between the Cu interface and Zn-containing ones. For example, a formate intermediate adsorbed to a site next to the interface is only

TABLE 2 Comparison between experimental and DFT calculated formate IR frequencies. DFT-calculated values are given for m–$ZrO_2(\bar{1}11)$, Cu(111), and a ZrO_2-bound ZnO monomer.

	exp. frequency (cm^{-1})			DFT frequency (cm^{-1})		
mode	Cu/Zr	Zn/Cu/Zr	Cu/Zn/Zr	ZrO_2	Cu(111)	ZnO/Zr
ν_s(O–C–O)	1367	1369	1369	1323	1307	1326
ρ(C–H)	1379	1377	1377	1338	1347	1358
ν_{as}(O–C–O)	1569	1575	1575	1532	1507	1535
ν(C–H)	2873	2867	2867	2981	2970	2961

0.1 eV more stable than one standing farther away, free from the influence of the interface. Based on this, it would seem that diffusion of these intermediates across the zirconia surface could be possible, although the kinetic feasibility of this was not examined here. There are also slight differences in the adsorption and activation energies between interfaces of different Zn content. However, the differences are very small and do not seem to form clear trends. They can be explained, in part, by the mismatch of Cu and Zn lattice constants creating a similar straining effect as was described in section 3.1. In this case, the strain of the interface atoms increases with increasing Zn content, leading to more unpredictable behaviour most evident when looking at line for the Zn interface in Figure 12.

3.2.3.2 DFT-assisted identification of surface intermediates

The combined experimental study in paper II was focused on examining Cu/Zn/ZrO_2 catalysts prepared using atomic layer deposition. A series of samples was produced, where the order of Zn addition by ALD and Cu addition by impregnation was varied. This hypothetically leads to configurations where different components end up partially covering each other. As a part of catalyst testing, *in situ* diffuse reflectance infrared Fourier transform spectroscopy (DRIFTS) was used to examine the presence and evolution of surface-bound intermediates such as formates, carboxyls, and formic acid. While the general regions for the IR adsorption peaks of these intermediates are available in literature, a computational estimate of how the peaks are influenced by the surface structure may be useful in identifying the dominant adsorption sites seen during DRIFTS. We used DFT calculations to determine the vibrational frequencies for HCOO, COOH, H_2COO, and HCOOH on a variety of supports, namely m–$ZrO_2(\bar{1}11)$, Cu(111), and Cu(110). A ZnO monomer adsorbed on a zirconia slab was used to model the ZnO/ZrO_2 active site.

After the calcination and reductive activation of the catalysts, alternating mixtures of 10 % CO_2 and H_2, separated by argon flushing, were streamed into the system at a rate of 50 mL/min in a temperature range of 450 K to 550 K. DRIFTS spectra were recorded at each step. Formate species appearing on the surface were detected after adsorption cycles with CO_2 and H_2, suggesting that some hydrogenation is taking place. The positions of DFT-calculated peaks are

relatively consistent with the experimental spectra, although a systematic underestimation of ca. 45 cm^{-1} is evident in the absolute values seen in Table 2. However, the experimental bands ascribed to C–H stretching are at much lower wavenumbers than those determined computationally and peaks in the area of the computed values are typically assigned to ν_{as}(O–C–O) + δ(C–H) combination modes.[193] The experimental values in Table 2 that were determined for ν_s(O–C–O) and ρ(C–H) are no more than 10 cm^{-1} apart, matching best with the gap of 15 cm^{-1} between the respective computational frequencies on ZrO_2. The difference is clearly larger both ZnO/ZrO_2 (22 cm^{-1}) and Cu(111) (40 cm^{-1}), suggesting that the formate binds on the ZrO_2 surface, rather than on Cu or ZnO particles. Other relations between peaks are not sufficiently unique to aid identification. Furthermore, the experimental values do not differ significantly from one sample to another. However, this is consistent with the conclusion that formate is more likely to be adsorbed on the exposed zirconia, rather than either Cu or Zn(O). Furthermore, the presence of (bi)carbonate structures after CO_2 adsorption was confirmed by DRIFTS, confirming adsorption to oxidic active sites.[91,194] However, no further CTM reaction intermediates, such as H_2COO, HCOOH, or H_3CO, were identified in DRIFTS measurements. This could be due to the analysis conditions and alternating gas composition used during the measurements, which do not fully represent reaction conditions and can not sustain the full conversion mechanism.

3.2.4 Examining the relative kinetics at CuZn–ZrO_2 interfaces using the energetic span model and degrees of TOF control

To provide a point of comparison between the formate and RWGS mechanisms, the DFT-calculated energies of intermediates and transition states along the catalytic network depicted in Figure 9 were used as input for an energetic span analysis, which was then run at 500 K. Most unstable reaction intermediates and competing paths with higher activation energies were removed from the network, as illustrated in Figure 13. This excluded *e.g.* the possibility of HCOO hydrogenation through formic acid, as well as the unfavourable HCOH intermediate. Note also that another simplification was made regarding OH groups on the zirconia surface, which were handled differently in the ESM analysis than what is shown in Figures 11 and 12. In the ESM network (Figure 13), the surface hydroxyl and one hydrogen were removed from the surface after the formation of H_2CO, effectively assuming the formation of water. The network was reduced mainly in the interest of performance so that it would be possible to run the analysis on a typical workstation computer within a reasonable timeframe. The network in Figure 13a also includes the possibility of CO desorption, which was excluded for technical reasons relating to the code used for analysis.

The simplified reaction network is broken down into the four cycles listed in Table 3. Two of these can be considered RWGS paths and two of them are formate paths, with the difference being the second-to-last intermediate being either H_3CO of H_2COH. The energetic span analysis suggests that the turnover

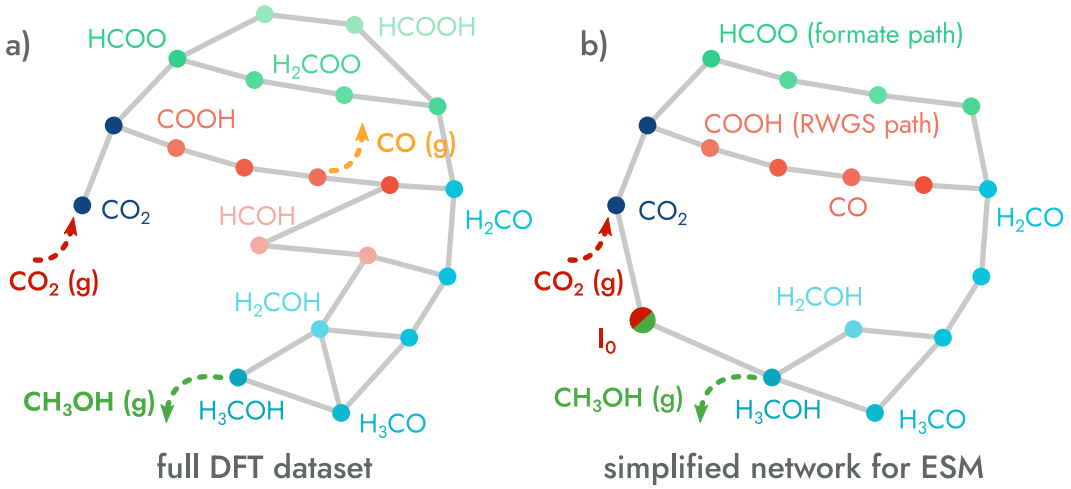

FIGURE 13 a) full network built from intermediates discussed in paper III; b) simplified catalytic network used for the energetic span analysis in paper III. I_0 marks a beginning/end of the catalytic cycle where the all reagents and products are in the gas phase.

TABLE 3 Turnover frequencies and effective energetic span values for several possible pathways of carbon dioxide conversion to methanol at the Zn-dilute interface. TOF values were calculated at 500 K. The key intermediates that identify each cycle are listed (see also Figure 13).

	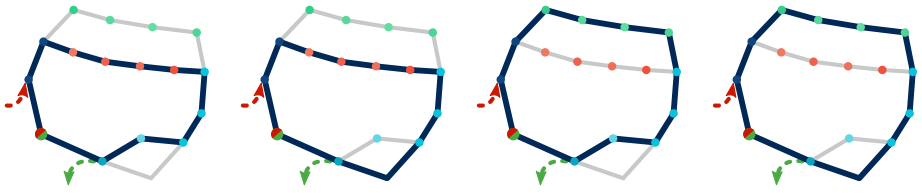			
	cycle 1	cycle 2	cycle 3	cycle 4
	COOH		HCOO	
	H_2COH	H_3CO	H_2COH	H_3CO
δE_{eff} (eV)	2.67	1.89	3.13	2.35
TOF (s^{-1})	4.2×10^{-12}	5.6×10^{-5}	2.7×10^{-16}	3.6×10^{-9}

frequencies of the RWGS pathways are higher than those of the formate paths with the same latter half. The results also clearly show that the methoxy (H_3CO) intermediate is dominant over H_2COH by several orders of magnitude. This is consistent with the difference in their relative stabilities as well as the conclusions of previous computational studies on Cu cluster and surface models.[38,68,69] The most favourable route through the network therefore proceeds through the RWGS pathway and CO hydrogenation at the metal–oxide interface and ends with H_3CO hydrogenation into methanol on the zirconia surface. The predicted turnover frequency for the most optimal path is $5.6 \times 10^{-5}\,\mathrm{s}^{-1}$. The TOFs of all cycles are shown in Table 3.

It is worth discussing the simplification we have made by immediately removing the OH produced during the reaction from the surface. This is an endothermic step on ZrO_2 and ends up raising the energy level by 0.7 eV. If, hypothetically, we were to ignore the desorption and assume that the OH groups accumulate on the surface, we would likely arrive at a higher predicted TOF, as the energetic span is lowered and the cycle becomes more exothermic. It may therefore be that, in reality, some accumulation of the surface species occurs as the reaction is cycled, although the simplified ESM is not able to directly represent it. Additionally, it is known from experiments that it is a significant side product in CTM on Cu/ZrO_2 catalysts.[35,60,68] Indeed, it was also identified as a major product in paper II. The release is perhaps limited by the high pressures that the reaction typically takes place in and the fact that CO adsorption is exothermic. Nevertheless, the model assumes that all CO either reacts forward to HCO or backward to COOH.

For a deeper view of which parts of the conversion process limit the TOF, a degree of turnover frequency control analysis was performed with the same data. Species with $X_{\mathrm{TOF}} > 0.001$ are listed in Table 4. It is quite clear that, because of its high stability, the formate is the most strongly TOF-controlling intermediate. On the other hand, the degrees of TOF-control for transition states in the networks is more nuanced. If we were to look only at the RWGS pathway, we would find that the X_{TOF} for the barrier of methoxy intermediate formation is at unity. The rate of the RWGS path could therefore be described as being controlled entirely by the stability of the formate and the activation energy of methoxy formation from formaldehyde. The rates of formate mechanisms are also influenced greatly by the barrier to form H_3CO. However, in this case the large barrier for CO_2 hydrogenation to formate is also roughly 31 % TOF-controlling.

3.3 Stability and agglomeration of ZnO on Cu/ZrO_2

The existence of atomically dispersed Zn(O) units was suggested in paper II as well as recent experimental studies involving catalysts prepared using ALD[93] and double-nozzle flame spray pyrolysis.[73] This may lead to lone Zn species being present on the surface of the as-prepared catalyst, particularly in cases where

TABLE 4 Degrees of TOF control for certain states of interest in paper III. Only the values for the RWGS and formate mechanisms with the highest TOFs are shown.

intermediate	X_{TOF} (RWGS)	X_{TOF} (form.)
HCOO (formate)	1.00	1.00
transition state		
H_2CO+H–H_3CO	1.00	0.69
CO_2+H–HCOO	—	0.31

Zn was added last and is thus not covered by other components. However, the stability and atomic-level evolution of these species under the calcination steps of catalyst preparation and the highly reductive reaction conditions is unknown. Typically, metallic species tend towards sintering through coalescence, or growth through *e.g.* Ostwald ripening.[188,195–197] We investigated the adsorption geometries and stability of ZnO monomers and sub-nano clusters on the surfaces of monoclinic zirconia and copper, as well as their interface, with the aim of addressing whether Zn/ZnO monomers are stable under reaction conditions of CO_2 CTM or whether larger agglomerates are preferred. Because of this wide range of conditions, we chose to examine both oxidic ZnO monomers and Zn_xO_x clusters as well as cases where "metallic" Zn (reduced metal adatoms/clusters) exists on the catalyst surface. To assist in the examination, we may define the agglomeration energy of a structure AB as:

$$\Delta E_{agg} = \Delta E_f(\mathrm{AB}) - \left[\Delta E_f(\mathrm{A}) + \Delta E_f(\mathrm{B})\right], \tag{32}$$

where A and B are two species combined to form AB. The formation energies ΔE_f here are defined relative to the energy of an isolated ZrO_2 slab and not its elements in their reference states. That is, for a cluster of form Zn_xO_y,

$$\Delta E_f(\mathrm{Zn}_x\mathrm{O}_y/\mathrm{ZrO}_2) = E(\mathrm{Zn}_x\mathrm{O}_y/\mathrm{ZrO}_2) - \left[E(\mathrm{ZrO}_2) + x e^{\mathrm{bulk}}_{\mathrm{Zn}} + y\frac{1}{2}E(\mathrm{O}_2)\right], \tag{33}$$

where $E(\mathrm{ZrO}_2)$ is the DFT energy of the isolated ZrO_2 model, $e^{\mathrm{bulk}}_{\mathrm{Zn}}$ is the energy of a bulk Zn atom and $E(\mathrm{O}_2)$ is the energy of an oxygen molecule determined from eqn 21. This can easily be extended to species of different composition and to different support models.

ZrO_2-SUPPORTED MONOMERS AND CLUSTERS. Zn_xO_y species attach to the ZrO_2 surface through Zn–O and O–Zr bonds, resting beside the binding ZrO_2 lattice oxygen (see Figure 14). The sub-nano clusters studied are quite far from the size range where they would have defined surfaces or any kind of bulk-like structure. The structures are also very different from the optimal conformations of the clusters in the gas phase. It seems then that the optimal geometries are formed from optimal bonding to the *m*–$ZrO_2(\bar{1}11)$ surface which, as already noted, is quite irregular. Recently, Nikolajsen et al.[198] reported the presence of similar amorphous ZnO species that were stable on the zirconia surface. Both the ZnO monomer and sub-nano Zn_xO_y clusters are placed preferentially in contact

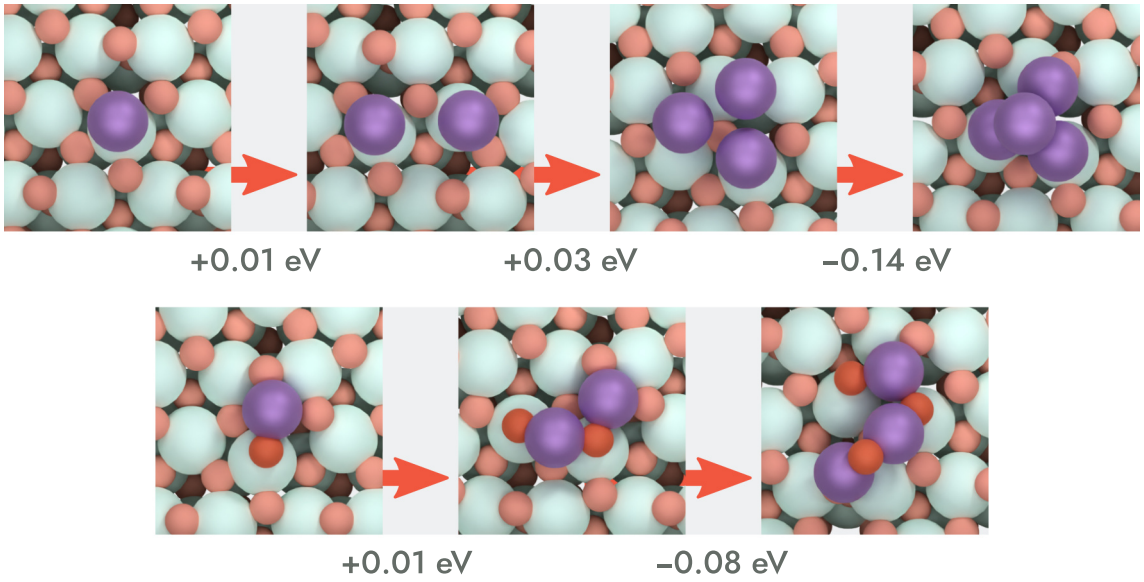

FIGURE 14 Agglomeration energies of Zn_x and stoichiometric Zn_xO_x structures on zirconia from adsorbed atoms/monomers at infinite separation. Purple: Zn, red: O.

with low-coordinated oxygen sites—namely the two-coordinated oxygen that is present on the $(\bar{1}11)$ surface. In fact, the adsorption at this site is 1.5 eV stronger than at the most favourable 3-coordinated site. On an ideal surface, these low-coordination sites are found once per 2.2 nm^2, setting a soft limit for the maximum ZnO monomer coverage. This is comparable with the experimental coverage of 1.9 nm^2 determined in paper II.

Metallic Zn monomers seem to adsorb only weakly to zirconia, and settle ca. 3.5 Å above surface Zr sites during optimization. There is little preference for any specific Zr cation, as the energies vary at most 0.1 eV. We also see, that a Zn adatom has an adhesive energy of only −0.2 eV relative to the gas phase. It can therefore be concluded, that they would not be anchored to the zirconia and, if formed through reduction, will be highly mobile.

Both non-oxidized Zn and oxidic ZnO seem resistant to agglomeration on zirconia, at least initially, and the joining of two fully separated ZnO units is almost thermoneutral (see Figure 14). The formation energies relative to bulk are also much less endothermic for Zn/ZnO species than, for example, the ΔE_f of Cu clusters: ca. 0.7 eV per x for Zn_xO_x *versus* 2.1 eV for Cu_x. This suggests that, while the thermodynamics favour sintering and bulk formation, this potential is lower for Zn-based species on ZrO_2. Similarly to ZnO, Zn adatoms do not show an immediate tendency towards agglomeration. This is also reflected in the Zn–Zn bond lengths of Zn_x-type clusters, which are longer than those in bulk Zn, decreasing slightly as the agglomeration progresses.

CU(111)-SUPPORTED MONOMERS AND CLUSTERS. ZnO monomers are less stable on the Cu(111) surface than they are on zirconia by ca. 0.7 eV. The clusters adsorb in more regular geometries than they do on zirconia, with their oxygens mainly in surface hollow sites (see Figure 15). A previous computational

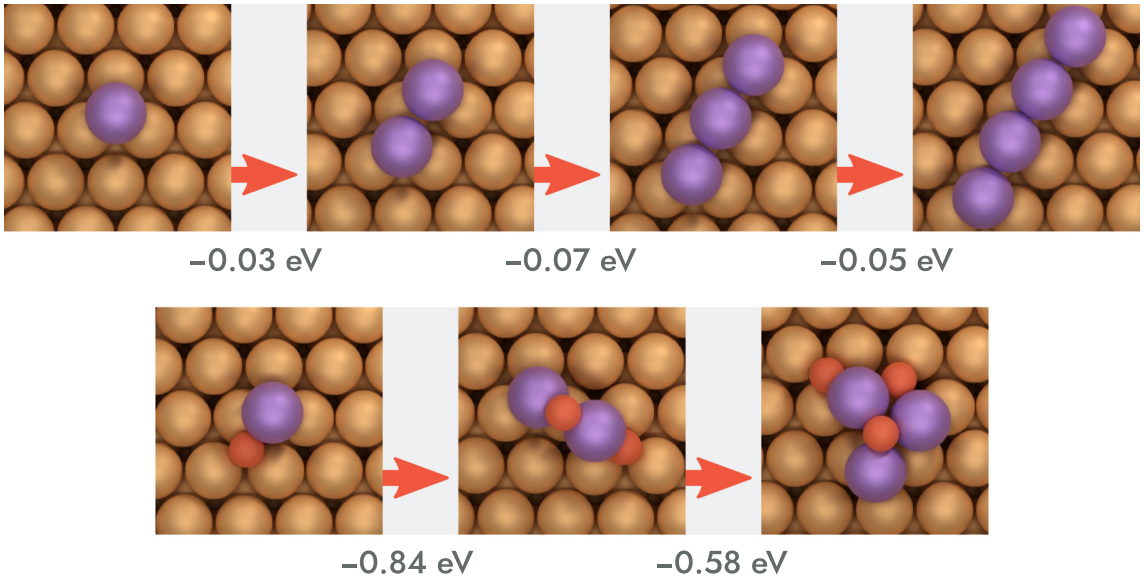

FIGURE 15 Agglomeration energies of Zn_x and stoichiometric Zn_xO_x structures on Cu(111) from adsorbed atoms/monomers at infinite separation. Purple: Zn, red: O.

study[128] examined similar Zn_xO_y clusters on Cu(111) in a higher size range of $3 \geq x \geq 7$ and similarly found the structures to be relatively regular and symmetric. This is, of course, enabled by the high symmetry of the (111) surface. However, the clusters differ slightly from structures that were previously reported for $(ZnO)_x$ in gas phase,[199] where the structures tend to be more cyclical and planar. It is again likely that O–Cu binding guides the geometry.

While the ZnO units adsorb weaker on Cu(111), they show a much clearer tendency towards agglomeration. The E_{agg} values are in the order of 0.6 eV to 0.9 eV per ZnO monomer addition—an order of magnitude higher than values on zirconia. It appears that the agglomeration is closing the gap between the stabilities of Zn_xO_x species on ZrO_2- and Cu(111). While the difference was 0.7 eV for the ZnO monomer, the Zn_3O_3 cluster is only 0.6 eV, or 0.2 eV per ZnO unit, less stable on Cu(111). This likely speaks to the ability of the zirconia to stabilize the ZnO monomer.

Whereas Zn adatoms and Zn_x clusters show no clear binding to zirconia, they are 0.6 eV more stable on the Cu(111) surface per Zn atom. This could suggest a degree of Zn migration onto the Cu surface under highly reductive conditions. The optimal adsorption locations are at Cu(111) hollow sites (FCC), but the energy differences between different cluster geometries are small. The optimal geometries found are the same linear shapes reported in another recent study.[128] While the Zn–Zn distances of ca. 2.7 Å are consistent with inter-atomic bonds, unlike those of ZrO_2 supported clusters, the agglomeration energies are relatively weak (Figure 15).

ZNO AT THE CU–ZRO$_2$ INTERFACE. As we have already demonstrated the importance of the Cu–ZrO_2 interface in the CTM reaction steps, it is reasonable to investigate the behaviour of the oxidic ZnO component at these active sites.

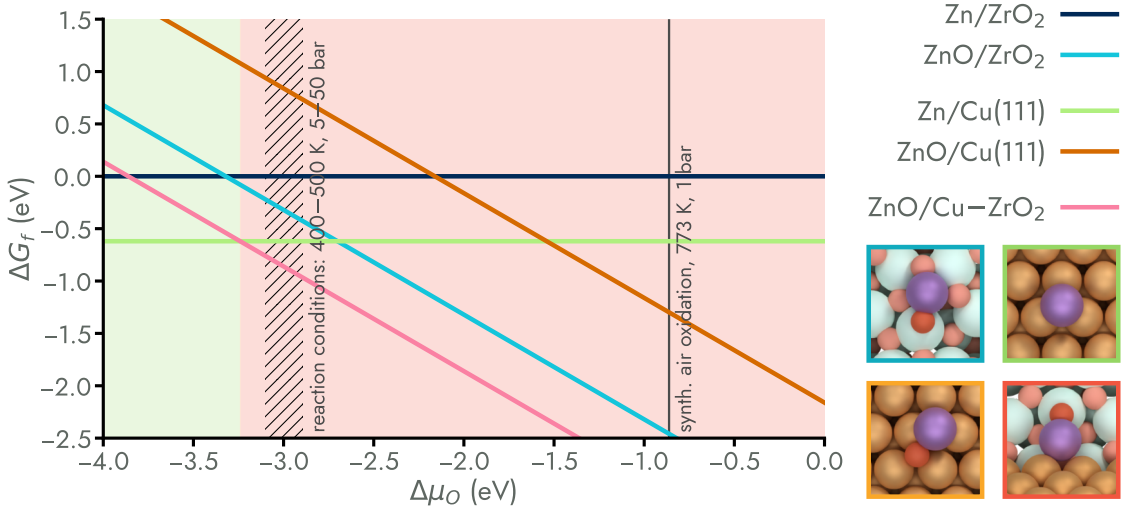

FIGURE 16 Formation energies of Zn and ZnO monomers on ZrO_2, Cu(111), and the Cu–ZrO_2 interface as a function of the chemical potential of oxygen, with Zn on ZrO_2 used as a reference. The background is coloured according to the most stable state in the region. $\Delta\mu_O$ values corresponding to reaction and calcination conditions are marked.

For this examination, only ZnO and Zn_2O_2 were chosen as sufficient representatives. We see that the ZnO monomer binds very strongly at the interface, lowering the energy by 0.5 eV compared to the most favourable adsorption at the two-coordinated ZrO_2 lattice oxygen. The preferred geometry spans the interface, the Zn centre binding the metallic Cu, while the oxygen of the monomer remains on a Zr cation top site, as before (seen in Figure 16, bottom right). Similarly to ZnO species on zirconia, the aggomeration at the interface is not favourable and, in fact, is slightly more endothermic at 0.2 eV. Regardless, the Zn_2O_2 cluster is also 0.9 eV more stable on the interface. Therefore, ZnO deposits on the surface of the catalyst are thermodynamically driven to gather at the interface. Obviously, at higher loadings this would lead to the Cu–ZrO_2 interface being eventually covered by zinc oxide. As discussed in subsection 3.2.1, CO_2 is able to adsorb and be activated on interfacial ZnO. The impact on other intermediates and elementary reaction steps is a potential subject of further research.

3.3.1 Exploring ZnO stability using atomistic thermodynamics

We have seen that there are competing sites for ZnO adsorption, but also that the oxidation state has an effect on their stability. It is then possible that the Zn promoter may exist in different phases in the as-prepared catalyst after oxidative calcination steps than it does during the reaction, which is carried in an atmosphere of CO_2 and hydrogen. In fact, this was one possible origin for the confusion surrounding ZnO. We can provide a prediction of how the atmosphere affects stability in our models through the use of atomistic thermodynamics.

The relative stabilities between both Zn and ZnO on ZrO_2, Cu(111), and the Cu–ZrO_2 interface can be compared by examining their formation energies as a

function of oxygen chemical potential in the way shown in Figure 16. The analysis confirms that, under both calcination and reaction conditions, ZnO adsorbed at the metal–oxide interface is the most stable configuration of the promoter (pink area in Figure 16). It is likely, that ZnO produced during catalyst preparation will migrate to the interface. Similarly, ZnO on the zirconia may migrate to the interface until it is completely covered.

However, when conditions become very reductive, *i.e.* $\Delta\mu_O \leq -3.0$ eV, the energies are very close to each other and the existence of Zn adatoms/alloys on Cu(111) becomes competitive. In fact, the difference between ZnO/Cu–ZrO_2 and Zn/Cu(111) is already relatively small under the range of typical reaction conditions, marked in the figure by hashing. This is also true for the reducibility of larger Cu-supported Zn_xO_y clusters, determined in a previous computational study.[128] Certainly, the formation of CuZn surface alloys under very reductive conditions has been suggested previously.[43,76,86,87] Still, we can conclude that the alloy never becomes the most favourable state. The reduction of ZnO units that may remain bound to ZrO_2 lattice oxygens is similarly an option, as the energy required is in the order of 0.2 eV to 0.5 eV in the range of reaction conditions. A recent experimental study[198] observed partially reduced ZnO_x, where $x \approx 0.98$, showing that the reduction is possible.

It is likely that the migration of ZnO to the interface as well as the exact degree of its reduction are dependent on ZnO loading. After all, a completely opposite effect on ZnO overlayer formation has been suggested for CZA-type catalysts.[37,43,66,84] The relatively low loading in our models is made to reflect highly dispersive methods, such as ALD, which makes comparison with much of the available literature difficult. A careful comparison of the distributions of Cu and Zn on ALD-prepared catalysts, that can be seen in the scanning transmission electron microscope (STEM) images in paper II, shows what appear to be Zn deposits around the perimeters of Cu nanoparticles but not on them. However, this examination is severely limited by the resolution.

4 CONCLUSIONS

Methanol is a promising means of storing renewable energy in a chemical form. As a liquid, it is naturally easier to store and transport than certain other renewable energy sources, such as natural gas and hydrogen. Although methanol is toxic, it degrades naturally and is less harmful to the environment than many alternatives. Furthermore, pure methanol produces no soot and no NO_x or SO_x emissions when burnt. Points of emission, such as power stations may be ideal as centres for CO_2 capture and conversion to methanol, and waste heat can be harnessed in the CTM process. This may provide an effective way to store and balance electricity in the grid, to be used to power households and transit. On the other hand, methanol-burning engines may be adopted in freight transport and aviation, where efforts to electrify have come against significant challenges.

Current catalysts for CO_2 CTM are based on oxide-supported Cu systems, of which Cu/ZrO_2 is especially promising. We have presented density functional theory calculations and additional computational techniques used to examine the structure, stability, and catalytic performance of heterogeneous copper–zirconia systems and Cu/ZrO_2 systems with added Zn promoter. The results offer a look into the interactions between the three components, as well as their roles in the conversion of carbon dioxide into methanol. An emphasis was placed on examining the chemical state and behaviour of the Zn promoter in situations where it is highly dispersed, such as in cases where the catalyst is prepared using the atomic layer deposition method.

Significant consideration was given to the choice of nanorod model used to study the metal–zirconia interface. This was due to the slightly different models used previously in literature giving potentially differing results. Indeed, through the screening and assessment reported in full in paper I, we discovered that effects of strain arising from the choice of computational unit cell can lead to unpredictable destabilization of the model. Additionally, the specific cuts used to make the nanorod model from bulk metal affect its stability and the binding strength of adsorbates at the resulting interface.

There are locations favourable for CO_2 activation to be found on the plain zirconia surface, metal–ZrO_2 interfaces, and around ZnO promoter particles. In

all cases, we observe activation in the form of the adsorbed CO_2 gaining a slightly negative charge. The strength of the adsorption at the interfaces is not easily optimized, as it does not seem to correlate directly with typical descriptors, such as metal *d*-band positions. However, as the CO_2 takes a trigonal, carbonate-like shape when activated, it may be that the most favourable sites are simply those that allow this geometry to form with minimal strain. Therefore, conformational flexibility of the adsorption site may be named as a contributing factor as to why Zn species are advantageous for CTM.

Incorporating Zn into the metal–oxide interface in a metallic form selectively stabilized intermediates that optimally bind to the interface, including CO_2, COOH, and H_2CO. However, carbon monoxide, a key intermediate and product of the RWGS process, does not bind to Zn centres but adsorbs instead on Cu top sites or on ZrO_2 surface cations. Similarly, monomeric ZnO species present at the interface adsorb CO_2 exceptionally strongly. The additional adsorption sites and enhanced binding strength of the zinc component could go some way to explaining its promoting effect on CO_2 conversion.

Our computational results show that the formation of a (hydro)carboxyl intermediate COOH is feasible under the right conditions, whereas previous studies have suggested much larger barriers. Specifically, accounting for a spillover, where the hydrogen dissociated on the surface of the Cu nanoparticle diffuses to the zirconia surface, creates more options for favourable hydrogenation geometries. This further suggests that the metal–support interface is special in its ability to offer diverse sites for elementary reactions in a centralized location.

An *ab initio* thermodynamic examination suggests that the complete reduction of ZnO is unfavourable. Furthermore, ZnO monomers and small Zn_xO_x clusters on the surface of zirconia are able to resist agglomeration to some degree, although ultimately the tendency is to form bulk oxide. On the other hand, ZnO agglomeration on the surface of copper is very favourable, which is consistent with experimental observations of ZnO overlayer growth. Considering that ZnO units of all sizes are less stable on Cu(111) than they are on the zirconia support, and especially at the Cu–ZrO_2 interface, it may be that the zirconia component acts against ZnO migration onto the Cu component.

Many past studies have been dedicated to examining the components of $Cu/Zn/ZrO_2$ using model catalysts. Now future efforts in the field bear the task of integrating this knowledge into a working model of catalyst activity and selectivity. A combination of experimental and theoretical work, focused on realistic active sites is needed, although made challenging by the significant structural and changes the system undergoes under different conditions. Future research may also neede to examine the mechanism of hydrogen spillover on irreducible oxides, such as zirconia, as it is not fully understood. Computational modelling could play a key part in this, as a way to examine the effect on an atomic level. Understanding the effect is of importance to CTM, but may also be advantageous in designing hydrogen storage technologies or other conversions. Certainly, the atomic-level behaviour in heterogeneous systems is likely to hold the key to designing catalysts that provide a sustainable future for everyone.

YHTEENVETO

Metanoli on jo nykypäivänä tärkeä teollinen liuotin ja lähtöaine useille synteettisille materiaaleille, maaleille, liimoille ja lääkeaineille. Viimeisten vuosikymmenien aikana sille on kuitenkin ehdotettu uusia käyttötarkoituksia vastauksena tavoitteisiin vähentää liikenteestä ja teollisuudesta syntyviä päästöjä ja fossiilisten luonnonvarojen kulutusta. Hiilidioksidi, joka on kerätty ilmakehästä tai teollisuuden päästöistä, voidaan vedyn kanssa muuntaa metanoliksi esimerkiksi käyttäen heterogeenisiä metalli–metallioksidikatalyyttejä. Näin voidaan teoriassa myös luoda kestävä hiilikierto, jossa uusiutuvasti tuotettu energia varastoidaan metanolin kemiallisiin sidoksiin, minkä jälkeen se voidaan käyttää tarkoitukseen suunniteltujen moottorien tai polttokennojen energianlähteenä. Koska hiilidioksidi on hyvin vakaa molekyyli, sen aktivointiin ja muuntamiseen muiksi tuotteiksi vaaditaan kuitenkin tehokas katalyytti nopeuttamaan reaktiota ja mahdollistamaan sen toteuttamisen kohtuullisessa paineessa ja lämpötilassa. On myös edullista, että tämä katalyytti pystytään kehittämään valikoivaksi juuri metanolin syntymistä kohtaan ja sivutuotteiden vapautuminen minimoidaan.

Nykyiset teolliset katalyytit perustuvat $Cu/ZnO/Al_2O_3$ katalyytteihin, joita on käytetty metanolin teolliseen tuotantoon häkäpitoisista kaasuista. Näissä katalyyteissä metallinen kupari asettuu metallioksidin pintaan luoden rajapintoja, joissa aktiivisten kohtien uskotaan sijaitsevan. Aiemmat kokeelliset tutkimukset ovat kuitenkin osoittaneet zirkoniumdioksidin toimivan sinkkioksidia parempana kantajana kuparille, kun reaktiokaasuna käytetään hiilimonoksidin sijaan hiilidioksidia, lisäten sekä katalyytin aktiivisuutta, että valikoituvuutta. Sinkkidioksidia voidaan kuitenkin lisätä tähän systeemiin promoottorina aktiivisuuden lisäämiseksi entisestään.

Tässä väitöskirjatyössä tarkasteltiin heterogeenisten kupari–sinkki–zirkoniumdioksidikatalyyttien (CZZ katalyyttien) atomitason rakennetta, stabiilisuutta ja katalyyttistä toimintakykyä käyttäen apuna tiheysfunktionaaliteoriaan (DFT) perustuvia kvanttimekaanisia mallinnusmenetelmiä. Saatuja energia-arvoja käytettiin lähtökohtana reaktiokinetiikan ja katalyyttien termodynaamisen stabiilisuuden matemaattiseen arviointiin mm. energiavälimallia (energetic span model) ja atomistista termodynamiikkaa käyttäen. Tulokset tarjoavat atomitason tietoa $Cu/Zn/ZrO_2$ systeemin kolmen komponentin välisistä vuorovaikutuksista ja niiden rooleista hiilidiokdisin muuntamisessa metanoliksi

Työtä edeltävästä kirjallisuudesta voi löytää useita erilaisia malleja, joilla metallin ja oksidin välistä rajapintaa on kuvattu, mutta joiden rakenteet poikkeavat huomattavasti toistaan ja saattavat siten tuottaa eriäviä tuloksia. Tähän väitöskirjaan kuuluva osajulkaisu I sisältää laajan rakenteiden seulonnan, joka pyrkii havainnollistamaan ja määrällistämään eroja, jotka syntyvät sekä nanosauvamallien geometrian, että laskennallisen yksikkökopin valinnasta. Tulokset osoittavat, että metallinanosauvan ja oksidipinnan yhteensovittamisesta syntyvä jännitys vaikuttaa huomattavasti ja usein ennalta-arvaamattomasti sekä nanosauvamallin sitoutumiseen kantajaan, että hiilidioksidin sitoutumiseen metalli–oksidi

rajapintaan. Myös nanosauvan tarkka rakenne vaikuttaa hiilidioksidin adsorptioenergiaan: laskennallisen mallin vähemmän stabiili kuparirakenne voi johtaa virheellisen voimakkaaseen kiinnittymiseen. Adsorptioenergiat eivät kuitenkaan ole aina johdonmukaisia tyypillisten kuvaajien, kuten siirtymämetallien *d*-vyökeskuksen siirtymien kanssa. Voidaan päätellä, että metallin ja oksidin välinen rajapinta on varsinkin monokliinisen zirkoniumdioksidin tapauksessa liian monimutkainen yksinkertaisten aktiivisuusmallien kuvattavaksi.

Osajulkaisu II käsittelee atomikerroskasvatusmenetelmällä (ALD) valmistettuja $Cu/Zn/ZrO_2$ katalyyttejä sekä kokeellisten karakterisointien ja aktiivisuusmittausten avulla, että laskennallisesti. Tulokset osoittavat kuinka komponenttien kerrostusjärjestys vaikuttaa katalyytin aktiivisuuteen, niiden toimien tehokkaimmin, kun sinkki lisätään viimeisenä. *In situ* infrapunaspektroskopiatulokset osoittavat hiilidioksidin muodostamien karbonaatti/vetykarbonaattivälituotteiden muuntuvan katalyyttien pinnalla formiaattivälituotteeksi (HCOO) vetyilmakehässä. Välituotteiden laskennallista mallinnusta käytettiin apuna infrapunaspektrien tulkitsemisessa.

Aiemmat CZZ systeemiä tarkastelleet laskennalliset tutkimukset ovat keskittyneet pääasiassa yhteen tai kahteen systeemin kolmesta komponentista. Nämä mallit eivät kuitenkaan pysty huomioimaan kaikkien kolmen vaikutusta aktiivisen rajapinnan toimintaan. Osajulkaisu III pyrkivät lisäämään tietoa sinkkipromoottorin vaikutuksesta konversion alkeisreaktioihin. Käytetyt laskennalliset mallit tuotettiin lisäämällä sinkkikomponentti seostamalla julkaisussa I käytettyihin $Cu/m–ZrO_2$ rajapintamalleihin. Tulokset osoittavat, kuinka sinkkikeskukset pystyvät valikoivasti stabiloimaan rajapintaan kiinnittyviä reaktiovälituotteita, joita ovat esim. aktivoitunut CO_2, COOH ja H_2CO (formaldehydi). Kuitenkin CO, joka on yksi konversion sivutuote, kiinnittyy heikommin Zn keskuksiin, selittäen mahdollisesti kokeissa havaitun pienentyneen valikoituvuuden. Laskennallisia tuloksia käytettiin lähtökohtana energiavälimalliin perustuvaan kineettiseen analyysiin, joka viittaa nopeimman reaktiopolun kulkevan käänteisen vesikaasun siirtoreaktion ja hiilimonoksidin vedytyksen kautta. Vedyn siirtyminen katalyyttimetallilta kantajalle tuottaa aktiivisia kohtia, joissa hiilidioksidin muuntuminen hiilimonoksidiksi on helppoa. Toisaalta formiaattivälituotteen muodostumisen suuri aktivaatioenergia hidastaa sen kautta kulkevaa mekanismia.

Osajulkaisu IV käsittelee kupari- ja sinkkimetalleista muodostuneiden monomeerien ja nanoklusterien kasvamista ja hapettumista zirkoniakantajan pinnalla reaktio-olosuhteissa. Tämä malli suunniteltiin vastaamaan tilannetta, jossa katalyytti on valmistettu ALD:llä tai muulla menetelmällä, joka johtaa metallin suureen hajaantuneisuuteen. Klusterien ja kaasumolekyylien DFT-optimoituja rakenteita ja energioita käytettiin atomistiseen termodynaamiseen tarkasteluun, jolla pystyttiin kuvaamaan katalyyttipartikkeleiden stabiiliutta ja aktiivisten keskusten koostumusta reaktio-olosuhteissa. Tulokset osoittavat zirkoniaan kiinnittyneiden sinkkidioksidimonomeerien ja -partikkeleiden pysyvän (osittain) hapettuneessa muodossa myös hyvin pelkistävissä reaktio-olosuhteissa. Ne myös osoittavat jonkin verran kykyä vastustaa kasaantumista zirkoniapinnalla ja metalli–oksidi rajapinnalla, kun taas kuparin pinnalla kasaantumat muodostuvat

helposti. Tämä viittaa oksidikantajan kykyyn stabiloida suuresti hajautunutta promoottoria.

Tämä väitöskirjatyö lisää ymmärrystä kupari–sinkki–zirkoniakatalyytin ja erityisesti sinkkipromoottorin toiminnasta ja kemiallisesta käyttäytymisestä atomistisella tasolla. Yhdessä olemassa olevan kirjallisuuden kanssa, tätä tietoa voidaan käyttää uusien katalyyttien ja niiden nanorakenteiden säätämiseen, jotta ne stabiloivat tehokkaasti metanolin muodostumisen kannalta tärkeitä reaktiopolun osia. Näiden katalyyttien ja konversioprosessin optimointi atomitasolta teolliselle mittakaavalle asti voisi mahdollistaa metanolin käyttämisen tulevaisuuden kestävänä ja hiilineutraalina energialähteenä.

REFERENCES

[1] Basile, A.; Dalena, F., *Methanol : Science and Engineering*; Elsevier: Amsterdam, 2017.

[2] Methanol Institute Renewable Methanol https://www.methanol.org/renewable/ (accessed on 02.09.2024).

[3] Dalena, F.; Senatore, A.; Marino, A.; Gordano, A.; Basile, M.; Basile, A. In Basile, A., Dalena, F., Eds.; Elsevier: 2017; Chapter Methanol Production and Applications: An Overview, pp 3–28.

[4] International Maritime Organization Resolution MEPC.304(72) on the initial IMO Strategy on reduction of GHG emissions from ships https://wwwcdn.imo.org/localresources/en/KnowledgeCentre/IndexofIMOResolutions/MEPCDocuments/MEPC.304(72).pdf (accessed on 11.06.2024).

[5] Kisielewicz, J; Lonsdale, J; Audino, A; Griffa, A; Rahim, S; Dobre, I; Malkun Cure, S; Reinfandt, N; Rao, S; Frizis, I; Eichhammer, W; Kimpeler, S; Rörden, J; Winkler, M; Honegger, M; Fazekas, D; Chatburn, L, *Research and innovation for climate neutrality by 2050: Challenges, opportunities and the path forward*; Publications Office of the European Union: 2024. DOI: 10.2777/459259.

[6] Moller, A. Alcohol, Biomethane and Ammonia are the best-positioned fuels to reach zero net emissions https://www.maersk.com/news/articles/2019/10/24/alcohol-biomethane-and-ammonia-are-the-best-positioned-fuels-to-reach-zero-net-emissions (accessed on 16.08.2024).

[7] Schröder, J.; Winther, K.; Müller-Langer, F.; Baumgarten, W.; Aakko-Saksa, P.; Lindgren, M. *Methanol as Motor Fuel*; IEA Advanced Motor Fuels Technology Collaboration, 2020, https://iea-amf.com/content/projects/map_projects/56 (accessed on 09.06.2024).

[8] Olah, G. A.; Prakash, G. K.; Goeppert, A. *J. Am. Chem. Soc.* **2011**, *133*, 12881. DOI: 10.1021/ja202642y.

[9] Frusteri, F.; Bonura, G.; Cannilla, C.; Drago Ferrante, G.; Aloise, A.; Catizzone, E.; Migliori, M.; Giordano, G. *Appl. Catal. B Environ.* **2015**, *176-177*, 522. DOI: 10.1016/j.apcatb.2015.04.032.

[10] Bilgili, L. *Renew. Sustain. Energy Rev.* **2023**, *182*, 113367. DOI: 10.1016/j.rser.2023.113367.

[11] Rihko-Struckmann, L. K.; Peschel, A.; Hanke-Rauschenbach, R.; Sundmacher, K. *Ind. Eng. Chem. Res.* **2010**, *49*, 11073. DOI: 10.1021/ie100508w.

[12] Baak, J. A.; Pozarlik, A. K.; Arentsen, M. J.; Brem, G. *Energy Convers. Manag.* **2019**, *182*, 530. DOI: 10.1016/j.enconman.2018.12.015.

[13] Brown, T.; Hampp, J. *Joule* **2023**, *7*, 2414. DOI: 10.1016/j.joule.2023.10.001.

[14] St1 St1 is planning a synthetic methanol pilot plant in Lappeenranta, Finland https://www.st1.com/st1-is-planning-a-synthetic-methanol-pilot-plant-in-lappeenranta-finland (accessed on 02.09.2024).

[15] Liquid Wind Accelerating eFuel production in Finland https://www.liquidwind.com/haapavesi (accessed on 02.09.2024).

[16] Roy, S.; Cherevotan, A.; Peter, S. C. *ACS Energy Lett.* **2018**, *3*, 1938. DOI: 10.1021/acsenergylett.8b00740.

[17] Kohl, A. L.; Nielsen, R. B. In *Gas Purification*; Elsevier: 1997, pp 40–186. DOI: 10.1016/b978-088415220-0/50002-1.

[18] MacDowell, N.; Florin, N.; Buchard, A.; Hallett, J.; Galindo, A.; Jackson, G.; Adjiman, C. S.; Williams, C. K.; Shah, N.; Fennell, P. *Energy Environ. Sci.* **2010**, *3*, 1645. DOI: 10.1039/c004106h.

[19] Bolland, O.; Sæther, S. *Energy Convers. Manag.* **1992**, *33*, 467. DOI: 10.1016/0196-8904(92)90045-x.

[20] Oxy-Fuel Gas Turbine, Gas Generator and Reheat Combustor Technology Development and Demonstration, Vol. 3, Turbo Expo: Power for Land, Sea, and Air, Vol. 3, 2010, pp 733–743, DOI: 10.1115/GT2010-23001.

[21] Allam, R. J.; Palmer, M. R.; Brown, G. W.; Fetvedt, J.; Freed, D.; Nomoto, H.; Itoh, M.; Okita, N.; Jones, C. *Energy Procedia* **2013**, *37*, 1135. DOI: 10.1016/J.EGYPRO.2013.05.211.

[22] Palmer, M.; Allam, R.; Brown, G. Apparatus and method for combusting a fuel at high pressure and high temperature, and associated system and device. US-20100300063-A1, 2010.

[23] Allam, R.; Palmer, M.; Brown, G.; Fetvedt, J.; Forrest, B. System and method for high efficiency power generation using a carbon dioxide circulating working fluid. US-20180291805-A1, 2018.

[24] Chan, W.; Morosuk, T.; Li, X.; Li, H. *Energy Convers. Manag.* **2023**, *294*, 117607. DOI: 10.1016/j.enconman.2023.117607.

[25] Goeppert, A.; Czaun, M.; Surya Prakash, G. K.; Olah, G. A. *Energy Environ. Sci.* **2012**, *5*, 7833. DOI: 10.1039/c2ee21586a.

[26] Artz, J.; Müller, T. E.; Thenert, K.; Kleinekorte, J.; Meys, R.; Sternberg, A.; Bardow, A.; Leitner, W. *Chem. Rev.* **2018**, *118*, 434. DOI: 10.1021/acs.chemrev.7b00435.

[27] Aminu, M. D.; Nabavi, S. A.; Rochelle, C. A.; Manovic, V. *Appl. Energy* **2017**, *208*, 1389. DOI: 10.1016/j.apenergy.2017.09.015.

[28] Bai, M.; Zhang, Z.; Fu, X. *Renew. Sustain. Energy Rev.* **2016**, *59*, 920. DOI: 10.1016/j.rser.2016.01.043.

[29] Carroll, A.; Przeslawski, R.; Radke, L.; Black, J.; Picard, K.; Moreau, J.; Haese, R.; Nichol, S. *Cont. Shelf Res.* **2014**, *83*, 116. DOI: 10.1016/j.csr.2013.11.012.

[30] Pires, J.; Martins, F.; Alvim-Ferraz, M.; Simões, M. *Chem. Eng. Res. Des.* **2011**, *89*, 1446. DOI: 10.1016/j.cherd.2011.01.028.

[31] Qazvini, O. T.; Babarao, R.; Telfer, S. G. *Nat. Commun.* **2021**, *12*, DOI: 10.1038/s41467-020-20489-2.

[32] Wang, W.; Chen, D.; Li, F.; Xiao, X.; Xu, Q. *Chem* **2024**, *10*, 86. DOI: https://doi.org/10.1016/j.chempr.2023.09.009.

[33] Service, R. F. *Science* **2004**, *305*, 958. DOI: 10.1126/science.305.5686.958.

[34] Davies, J.; Dolci, F.; Klassek-Bajorek, D.; Ortiz Cebolla, R.; Weidner, E., *Current status of chemical energy storage technologies: trends in research, development and deployment in Europe and the rest of the world*; Publications Office of the European Union: 2020. DOI: 10.2760/280873.

[35] Kattel, S.; Liu, P.; Chen, J. G. *J. Am. Chem. Soc.* **2017**, *139*, 9739. DOI: 10.1021/jacs.7b05362.

[36] Tackett, B. M.; Gomez, E.; Chen, J. G. *Nat. Catal.* **2019**, *2*, 381. DOI: 10.1038/s41929-019-0266-y.

[37] Behrens, M.; Studt, F.; Kasatkin, I.; Kuhl, S.; Havecker, M.; Abild-Pedersen, F.; Zander, S.; Girgsdies, F.; Kurr, P.; Kniep, B.-L.; Tovar, M.; Fischer, R. W.; Nørskov, J. K.; Schlögl, R. *Science* **2012**, *336*, 893. DOI: 10.1126/science.1219831.

[38] Grabow, L. C.; Mavrikakis, M. *ACS Catal.* **2011**, *1*, 365. DOI: 10.1021/cs200055d.

[39] Etim, U. J.; Song, Y.; Zhong, Z. *Front. Energy Res.* **2020**, *8*, DOI: 10.3389/fenrg.2020.545431.

[40] Kuld, S.; Thorhauge, M.; Falsig, H.; Elkjær, C. F.; Helveg, S.; Chorkendorff, I.; Sehested, J. *Science* **2016**, *352*, 969. DOI: 10.1126/science.aaf0718.

[41] Zander, S.; Kunkes, E. L.; Schuster, M. E.; Schumann, J.; Weinberg, G.; Teschner, D.; Jacobsen, N.; Schlögl, R.; Behrens, M. *Angew. Chem. Int. Ed.* **2013**, *52*, 6536. DOI: 10.1002/anie.201301419.

[42] Hansen, P. L.; Wagner, J. B.; Helveg, S.; Rostrup-Nielsen, J. R.; Clausen, B. S.; Topsøe, H. *Science* **2002**, *295*, 2053. DOI: 10.1126/science.1069325.

[43] Grunwaldt, J. D.; Molenbroek, A. M.; Topsøe, N. Y.; Topsøe, H.; Clausen, B. S. *J. Catal.* **2000**, *194*, 452. DOI: 10.1006/jcat.2000.2930.

[44] Zhao, H.; Yu, R.; Ma, S.; Xu, K.; Chen, Y.; Jiang, K.; Fang, Y.; Zhu, C.; Liu, X.; Tang, Y.; Wu, L.; Wu, Y.; Jiang, Q.; He, P.; Liu, Z.; Tan, L. *Nat. Catal.* **2022**, *5*, 818. DOI: 10.1038/s41929-022-00840-0.

[45] Martin, O.; Mondelli, C.; Cervellino, A.; Ferri, D.; Curulla-Ferré, D.; Pérez-Ramírez, J. *Angew. Chemie - Int. Ed.* **2016**, *55*, 11031. DOI: 10.1002/anie.201603204.

[46] Bavykina, A.; Yarulina, I.; Al Abdulghani, A. J.; Gevers, L.; Hedhili, M. N.; Miao, X.; Galilea, A. R.; Pustovarenko, A.; Dikhtiarenko, A.; Cadiau, A.; Aguilar-Tapia, A.; Hazemann, J. L.; Kozlov, S. M.; Oud-Chikh, S.; Cavallo, L.; Gascon, J. *ACS Catal.* **2019**, *9*, 6910. DOI: 10.1021/acscatal.9b01638.

[47] Kattel, S.; Yan, B.; Chen, J. G.; Liu, P. *J. Catal.* **2016**, *343*, 115. DOI: 10.1016/j.jcat.2015.12.019.

[48] Cao, A.; Wang, Z.; Li, H.; Elnabawy, A. O.; Nørskov, J. K. *J. Catal.* **2021**, *400*, 325. DOI: 10.1016/j.jcat.2021.06.020.

[49] Słoczyński, J.; Grabowski, R.; Kozłowska, A.; Olszewski, P.; Stoch, J.; Skrzypek, J.; Lachowska, M. *Appl. Catal. A Gen.* **2004**, *278*, 11. DOI: 10.1016/j.apcata.2004.09.014.

[50] Grabowski, R.; Słoczyński, J.; Śliwa, M.; Mucha, D.; Socha, R. P.; Lachowska, M.; Skrzypek, J. *ACS Catal.* **2011**, *1*, 266. DOI: 10.1021/cs100033v.

[51] Jiang, X.; Nie, X.; Guo, X.; Song, C.; Chen, J. G. *Chem. Rev.* **2020**, *120*, 7984. DOI: 10.1021/acs.chemrev.9b00723.

[52] Scotti, N.; Bossola, F.; Zaccheria, F.; Ravasio, N. *Catalysts* **2020**, *10*, 168. DOI: 10.3390/catal10020168.

[53] Li, K.; Chen, J. G. *ACS Catal.* **2019**, *9*, 7840. DOI: 10.1021/acscatal.9b01943.

[54] Fulham, G. J.; Wu, X.; Liu, W.; Marek, E. J. *Chem. Eng. J.* **2024**, *480*, 147732. DOI: 10.1016/j.cej.2023.147732.

[55] Kattel, S.; Yan, B.; Yang, Y.; Chen, J. G.; Liu, P. *J. Am. Chem. Soc.* **2016**, *138*, 12440. DOI: 10.1021/jacs.6b05791.

[56] Witoon, T.; Chalorngtham, J.; Dumrongbunditkul, P.; Chareonpanich, M.; Limtrakul, J. *Chem. Eng. J.* **2016**, *293*, 327. DOI: 10.1016/j.cej.2016.02.069.

[57] Abbas, I.; Kim, H.; Shin, C.-H.; Yoon, S.; Jung, K.-D. *Appl. Catal. B Environ.* **2019**, *258*, 117971. DOI: 10.1016/j.apcatb.2019.117971.

[58] Wang, Y.; Kattel, S.; Gao, W.; Li, K.; Liu, P.; Chen, J. G.; Wang, H. *Nat. Commun.* **2019**, *10*, 1166. DOI: 10.1038/s41467-019-09072-6.

[59] Arena, F.; Barbera, K.; Italiano, G.; Bonura, G.; Spadaro, L.; Frusteri, F. *J. Catal.* **2007**, *249*, 185. DOI: 10.1016/j.jcat.2007.04.003.

[60] Nitta, Y.; Suwata, O.; Ikeda, Y.; Okamoto, Y.; Imanaka, T. *Catal. Lett.* **1994**, *26*, 345. DOI: 10.1007/BF00810608.

[61] Burch, R.; Golunski, S. E.; Spencer, M. S. *J. Chem. Soc. Faraday Trans.* **1990**, *86*, 2683. DOI: 10.1039/ft9908602683.

[62] Zhao, Z.-J.; Li, Z.; Cui, Y.; Zhu, H.; Schneider, W. F.; Delgass, W. N.; Ribeiro, F.; Greeley, J. *J. Catal.* **2017**, *345*, 157. DOI: 10.1016/j.jcat.2016.11.008.

[63] Kauppinen, M. M.; Melander, M. M.; Bazhenov, A. S.; Honkala, K. *ACS Catal.* **2018**, *8*, 11633. DOI: 10.1021/acscatal.8b02596.

[64] Wu, Y. Y.; Mashayekhi, N. A.; Kung, H. H. *Catal. Sci. Technol.* **2013**, *3*, 2881. DOI: 10.1039/c3cy00243h.

[65] Green, I. X.; Tang, W.; Neurock, M.; Yates, J. T. *Science* **2011**, *333*, 736. DOI: 10.1126/science.1207272.

[66] Lunkenbein, T.; Schumann, J.; Behrens, M.; Schlögl, R.; Willinger, M. G. *Angew. Chemie - Int. Ed.* **2015**, *54*, 4544. DOI: 10.1002/anie.201411581.

[67] Zabilskiy, M.; Sushkevich, V. L.; Palagin, D.; Newton, M. A.; Krumeich, F.; van Bokhoven, J. A. *Nat. Commun.* **2020**, *11*, 2409. DOI: 10.1038/s41467-020-16342-1.

[68] Kattel, S.; Ramírez, P. J.; Chen, J. G.; Rodriguez, J. A.; Liu, P. *Science* **2017**, *355*, 1296. DOI: 10.1126/science.aal3573.

[69] Larmier, K.; Liao, W.-C.; Tada, S.; Lam, E.; Verel, R.; Bansode, A.; Urakawa, A.; Comas-Vives, A.; Copéret, C. *Angew. Chem. Int. Ed.* **2017**, *56*, 2318. DOI: 10.1002/anie.201610166.

[70] Tang, Q.-L.; Hong, Q.-J.; Liu, Z.-P. *J. Catal.* **2009**, *263*, 114. DOI: 10.1016/j.jcat.2009.01.017.

[71] Dong, X.; Li, F.; Zhao, N.; Xiao, F.; Wang, J.; Tan, Y. *Appl. Catal. B: Environ.* **2016**, *191*, 8. DOI: 10.1016/j.apcatb.2016.03.014.

[72] Zhan, H.; Shi, X.; Tang, B.; Wang, G.; Ma, B.; Liu, W. *Catal. Commun.* **2021**, *149*, 106264. DOI: 10.1016/j.catcom.2020.106264.

[73] Yang, M.; Yu, J.; Zimina, A.; Sarma, B. B.; Pandit, L.; Grunwaldt, J. D.; Zhang, L.; Xu, H.; Sun, J. *Angew. Chem. Int. Ed.* **2023**, *62*, e202216803. DOI: 10.1002/anie.202216803.

[74] Huang, C.; Chen, S.; Fei, X.; Liu, D.; Zhang, Y. *Catalysts* **2015**, *5*, 1846. DOI: 10.3390/catal5041846.

[75] Ro, I.; Liu, Y.; Ball, M. R.; Jackson, D. H.; Chada, J. P.; Sener, C.; Kuech, T. F.; Madon, R. J.; Huber, G. W.; Dumesic, J. A. *ACS Catal.* **2016**, *6*, 7040. DOI: 10.1021/acscatal.6b01805.

[76] Kuld, S.; Conradsen, C.; Moses, P. G.; Chorkendorff, I.; Sehested, J. *Angew. Chemie Int. Ed.* **2014**, *53*, 5941. DOI: 10.1002/anie.201311073.

[77] Samson, K.; Sliwa, M.; Socha, R. P.; Góra-Marek, K.; Mucha, D.; Rutkowska-Zbik, D.; Paul, J. F.; Ruggiero-Mikoajczyk, M.; Grabowski, R.; Soczyński, J. *ACS Catal.* **2014**, *4*, 3730. DOI: 10.1021/cs500979c.

[78] Laudenschleger, D.; Ruland, H.; Muhler, M. *Nat. Commun.* **2020**, *11*, DOI: 10.1038/s41467-020-17631-5.

[79] Beck, A.; Zabilskiy, M.; Newton, M. A.; Safonova, O.; Willinger, M. G.; van Bokhoven, J. A. *Nat. Catal.* **2021**, *4*, 488. DOI: 10.1038/s41929-021-00625-x.

[80] Liu, X.; Wang, H.; Lu, J. *J. Catal.* **2024**, 115561. DOI: 10.1016/j.jcat.2024.115561.

[81] Nakamura, J.; Fujitani, T.; Kuld, S.; Helveg, S.; Chorkendorff, I.; Sehested, J. *Science* **2017**, *357*, eaan8074. DOI: 10.1126/science.aan8074.

[82] Kattel, S.; Ramírez, P. J.; Chen, J. G.; Rodriguez, J. A.; Liu, P. *Science* **2017**, *357*, eaan8210. DOI: 10.1126/science.aan8210.

[83] Beck, A.; Huang, X.; Artiglia, L.; Zabilskiy, M.; Wang, X. *Nat. Commun.* **2020**, *11*, 3220. DOI: 10.1038/s41467-020-17070-2.

[84] Claeyssens, F.; Freeman, C. L.; Allan, N. L.; Sun, Y.; Ashfold, M. N. R.; Harding, J. H. *J. Mater. Chem.* **2005**, *15*, 139. DOI: 10.1039/B414111C.

[85] Frei, E.; Gaur, A.; Lichtenberg, H.; Zwiener, L.; Scherzer, M.; Girgsdies, F.; Lunkenbein, T.; Schlögl, R. *ChemCatChem* **2020**, *12*, 4029. DOI: 10.1002/cctc.202000777.

[86] Topsøe, N. Y.; Topsøe, H. *Top. Catal.* **1999**, *8*, 267. DOI: 10.1023/a:1019133832569.

[87] Amann, P.; Klötzer, B.; Degerman, D.; Köpfle, N.; Götsch, T.; Lömker, P.; Rameshan, C.; Ploner, K.; Bikaljevic, D.; Wang, H.-Y.; Soldemo, M.; Shipilin, M.; Goodwin, C. M.; Gladh, J.; Halldin Stenlid, J.; Börner, M.; Schlueter, C.; Nilsson, A. *Science* **2022**, *376*, 603. DOI: 10.1126/science.abj7747.

[88] Zabilskiy, M.; Sushkevich, V. L.; Newton, M. A.; Van Bokhoven, J. A. *ACS Catal.* **2020**, *10*, 14240. DOI: 10.1021/acscatal.0c03661.

[89] Nakamura, J.; Choi, Y.; Fujitani, T. *Top. Catal.* **2003**, *22*, 277. DOI: 10.1023/A:1023588322846.

[90] Polierer, S.; Jelic, J.; Pitter, S.; Studt, F. *J. Phys. Chem. C* **2019**, *123*, 26904. DOI: 10.1021/acs.jpcc.9b06500.

[91] Korhonen, S. T.; Calatayud, M.; Krause, A. O. I. *J. Phys. Chem. C* **2008**, *112*, 16096. DOI: 10.1021/jp803353v.

[92] Kordus, D.; Widrinna, S.; Timoshenko, J.; Lopez Luna, M.; Rettenmaier, C.; Chee, S. W.; Ortega, E.; Karslioglu, O.; Kühl, S.; Roldan Cuenya, B. *J. Am. Chem. Soc.* **2024**, *146*, 8677. DOI: 10.1021/jacs.4c01077.

[93] Liu, X.; Luo, J.; Wang, H.; Huang, L.; Wang, S.; Li, S.; Sun, Z.; Sun, F.; Jiang, Z.; Wei, S.; Li, W.-X.; Lu, J. *Angew. Chem. Int. Ed.* **2022**, *61*, e202202330. DOI: 10.1002/anie.202202330.

[94] Fornero, E. L.; Bonivardi, A. L.; Baltanás, M. A. *J. Catal.* **2015**, *330*, 302. DOI: 10.1016/j.jcat.2015.07.025.

[95] Campbell, J. M.; Campbell, C. T. *Surf. Sci.* **1991**, *259*, 1. DOI: 10.1016/0039-6028(91)90519-X.

[96] Sakong, S.; Groß, A. *Surf. Sci.* **2003**, *525*, 107. DOI: 10.1016/s0039-6028(02)02550-5.

[97] Hagman, B.; Posada-Borbón, A.; Schaefer, A.; Shipilin, M.; Zhang, C.; Merte, L. R.; Hellman, A.; Lundgren, E.; Grönbeck, H.; Gustafson, J. *J. Am. Chem. Soc.* **2018**, *140*, 12974. DOI: 10.1021/jacs.8b07906.

[98] Jung, K.-D.; Bell, A. T. *J. Catal.* **2000**, *193*, 207. DOI: 10.1006/jcat.2000.2881.

[99] Wang, Y. H.; Gao, W. G.; Wang, H.; Zheng, Y. E.; Na, W.; Li, K. Z. *RSC Adv.* **2017**, *7*, 8709. DOI: 10.1039/C6RA28305E.

[100] Shen, H.; Li, H.; Yang, Z.; Li, C. *Green Energy Environ.* **2022**, *7*, 1161. DOI: 10.1016/j.gee.2022.01.013.

[101] Prins, R. *Chem. Rev.* **2012**, *112*, 2714. DOI: 10.1021/cr200346z.

[102] Prins, R.; Palfi, V. K.; Reiher, M. *J. Phys. Chem. C* **2012**, *116*, 14274. DOI: 10.1021/jp212274y.

[103] Bettahar, M. M. *Catal. Rev.* **2022**, *64*, 87. DOI: 10.1080/01614940.2020.1787771.

[104] Chen, H. Y. T.; Tosoni, S.; Pacchioni, G. *ACS Catal.* **2015**, *5*, 5486. DOI: 10.1021/acscatal.5b01093.

[105] Parr, R. G.; Yang, W., *Density-functional theory of atoms in molecules*; Oxford University Press: New York, 1989.

[106] Robertson, J.; Xiong, K.; Clark, S. J. *Phys. Stat. Sol. b* **2006**, *243*, 2054. DOI: 10.1002/pssb.200666802.

[107] Ernzerhof, M.; Perdew, J. P.; Burke, K. *Int. J. Quantum Chem.* **1997**, *64*, 285. DOI: 10.1002/(SICI)1097-461X(1997)64:3<285::AID-QUA2>3.0.CO;2-S.

[108] Dandu, N. K.; Adeyiga, O.; Panthi, D.; Bird, S. A.; Odoh, S. O. *J. Comput. Chem.* **2018**, *39*, 2667. DOI: 10.1002/jcc.25714.

[109] Capelle, K. *Braz. J. Phys.* **2006**, *36*, 1318. DOI: 10.1590/S0103-97332006000700035.

[110] Mori-Sánchez, P.; Cohen, A. J.; Yang, W. *Phys. Rev. Lett.* **2008**, *100*, 146401. DOI: 10.1103/PhysRevLett.100.146401.

[111] Wellendorff, J.; Lundgaard, K. T.; Møgelhøj, A.; Petzold, V.; Landis, D. D.; Nørskov, J. K.; Bligaard, T.; Jacobsen, K. W. *Phys. Rev. B* **2012**, *85*, 235149. DOI: 10.1103/PhysRevB.85.235149.

[112] Perdew, J. P.; Zunger, A. *Phys. Rev. B* **1981**, *23*, 5048. DOI: 10.1103/PhysRevB.23.5048.

[113] Dudarev, S. L.; Botton, G. A.; Savrasov, S. Y.; Humphreys, C. J.; Sutton, A. P. *Phys. Rev. B* **1998**, *57*, 1505. DOI: 10.1103/PhysRevB.57.1505.

[114] Korpelin, V.; Melander, M. M.; Honkala, K. *J. Phys. Chem. C* **2022**, *126*, 933. DOI: 10.1021/acs.jpcc.1c08979.

[115] Kim, H.; Yu, N.-K.; Tian, N.; Medford, A. J. *J. Phys. Chem. C* **2024**, *128*, 11159. DOI: 10.1021/acs.jpcc.4c01497.

[116] Grimme, S. *J. Comp. Chem.* **2004**, *25*, 1463. DOI: 10.1002/jcc.20078.

[117] Dion, M.; Rydberg, H.; Schröder, E.; Langreth, D. C.; Lundqvist, B. I. *Phys. Rev. Lett.* **2004**, *92*, 246401. DOI: 10.1103/PhysRevLett.92.246401.

[118] Tkatchenko, A.; Scheffler, M. *Phys. Rev. Lett.* **2009**, *102*, 073005. DOI: 10.1103/PhysRevLett.102.073005.

[119] Blöchl, P. E. *Phys. Rev. B* **1994**, *50*, 17953. DOI: 10.1103/PhysRevB.50.17953.

[120] Enkovaara, J.; Rostgaard, C.; Mortensen, J. J.; Chen, J.; Dułak, M; Ferrighi, L.; Gavnholt, J.; Glinsvad, C; Haikola, V.; Hansen, H. A.; Kristoffersen, H. H.; Kuisma, M.; Larsen, A. H.; Lehtovaara, L.; Ljungberg, M.; Lopez-Acevedo, O.; Moses, P. G.; Ojanen, J.; Olsen, T.; Petzold, V.; Romero, N. A.; Stausholm-Møller, J; Strange, M.; Tritsaris, G. A.; Vanin, M.; Walter, M.; Hammer, B.; Häkkinen, H.; Madsen, G. K. H.; Nieminen, R. M.; Nørskov, J. K.; Puska, M.; Rantala, T. T.; Schiøtz, J; Thygesen, K. S.; Jacobsen, K. W. *J. Phys. Condens Matter* **2010**, *22*, 253202. DOI: 10.1088/0953-8984/22/25/253202.

[121] Mortensen, J. J.; Larsen, A. H.; Kuisma, M.; Ivanov, A. V.; Taghizadeh, A.; Peterson, A.; Haldar, A.; Dohn, A. O.; Schäfer, C.; Jónsson, E. Ö.; Hermes, E. D.; Nilsson, F. A.; Kastlunger, G.; Levi, G.; Jónsson, H.; Häkkinen, H.; Fojt, J.; Kangsabanik, J.; Sødequist, J.; Lehtomäki, J.; Heske, J.; Enkovaara, J.; Winther, K. T.; Dulak, M.; Melander, M. M.; Ovesen, M.; Louhivuori, M.; Walter, M.; Gjerding, M.; Lopez-Acevedo, O.; Erhart, P.; Warmbier, R.; Würdemann, R.; Kaappa, S.; Latini, S.; Boland, T. M.; Bligaard, T.; Skovhus, T.; Susi, T.; Maxson, T.; Rossi, T.; Chen, X.; Schmerwitz, Y. L. A.; Schiøtz, J.; Olsen, T.; Jacobsen, K. W.; Thygesen, K. S. *J. Chem. Phys.* **2024**, *160*, 092503. DOI: 10.1063/5.0182685.

[122] Hjorth Larsen, A.; Jørgen Mortensen, J.; Blomqvist, J.; Castelli, I. E.; Christensen, R.; Dułak, M.; Friis, J.; Groves, M. N.; Hammer, B.; Hargus, C.; Hermes, E. D.; Jennings, P. C.; Bjerre Jensen, P.; Kermode, J.; Kitchin, J. R.; Leonhard Kolsbjerg, E.; Kubal, J.; Kaasbjerg, K.; Lysgaard, S.; Bergmann Maronsson, J.; Maxson, T.; Olsen, T.; Pastewka, L.; Peterson, A.; Rostgaard, C.; Schiøtz, J.; Schütt, O.; Strange, M.; Thygesen, K. S.; Vegge, T.; Vilhelmsen, L.; Walter, M.; Zeng, Z.; Jacobsen, K. W. *J. Phys. Condens. Matter* **2017**, *29*, 273002. DOI: 10.1088/1361-648X/aa680e.

[123] Bitzek, E.; Koskinen, P.; Gähler, F.; Moseler, M.; Gumbsch, P. *Phys. Rev. Lett.* **2006**, *97*, 170201. DOI: 10.1103/PhysRevLett.97.170201.

[124] Wales, D. J.; Doye, J. P. K. *J. Phys. Chem. A* **1997**, *101*, 5111. DOI: 10.1021/jp970984n.

[125] Vilhelmsen, L. B.; Hammer, B. *J. Chem. Phys.* **2014**, *141*, 044711. DOI: 10.1063/1.4886337.

[126] Deaven, D. M.; Ho, K. M. *Phys. Rev. Lett.* **1995**, *75*, 288. DOI: 10.1103/PhysRevLett.75.288.

[127] Goedecker, S. *J. Chem. Phys.* **2004**, *120*, 9911. DOI: 10.1063/1.1724816.

[128] Reichenbach, T.; Walter, M.; Moseler, M.; Hammer, B.; Bruix, A. *J. Phys. Chem. C* **2019**, *123*, 30903. DOI: 10.1021/acs.jpcc.9b07715.

[129] Reichenbach, T.; Mondal, K.; Jäger, M.; Vent-Schmidt, T.; Himmel, D.; Dybbert, V.; Bruix, A.; Krossing, I.; Walter, M.; Moseler, M. *J. Catal.* **2018**, *360*, 168. DOI: 10.1016/j.jcat.2018.01.035.

[130] Chen, M.; Straatsma, T. P.; Fang, Z.; Dixon, D. A. *J. Phys. Chem. C* **2016**, *120*, 20400. DOI: 10.1021/acs.jpcc.6b06730.

[131] Lloyd, L. D.; Johnston, R. L.; Salhi, S. *J. Comp. Chem.* **2005**, *26*, 1069. DOI: 10.1002/jcc.20247.

[132] Ji, M.; Wang, C.-Z.; Ho, K.-M. *Phys. Chem. Chem. Phys.* **2010**, *12*, 11617. DOI: 10.1039/C004096G.

[133] Schönborn, S. E.; Goedecker, S.; Roy, S.; Oganov, A. R. *J. Chem. Phys.* **2009**, *130*, 144108. DOI: 10.1063/1.3097197.

[134] Peterson, A. A. *Top. Catal.* **2013**, *57*, 40. DOI: 10.1007/s11244-013-0161-8.

[135] Henkelman, G.; Jónsson, H. *J. Chem. Phys* **2000**, *113*, 9978. DOI: 10.1063/1.1323224.

[136] Henkelman, G.; Uberuaga, B. P.; Jónsson, H. *J. Chem. Phys.* **2000**, *113*, 9901. DOI: 10.1063/1.1329672.

[137] Pederson, M.; Quong, A.; Broughton, J.; Feldman, J. *Comput. Mater. Sci.* **1994**, *2*, 536. DOI: 10.1016/0927-0256(94)90084-1.

[138] Porezag, D.; Pederson, M. R. *Phys. Rev. B* **1996**, *54*, 7830. DOI: 10.1103/physrevb.54.7830.

[139] Frederiksen, T.; Paulsson, M.; Brandbyge, M.; Jauho, A.-P. *Phys. Rev. B* **2007**, *75*, 205413. DOI: 10.1103/PhysRevB.75.205413.

[140] Szabo, A.; Ostlund, N. S., *Modern quantum chemistry: an introduction to advanced electronic structure theory*; Dover publications: New York, 1996.

[141] Fonseca Guerra, C.; Handgraaf, J.-W.; Baerends, E. J.; Bickelhaupt, F. M. *J. Comp. Chem.* **2003**, *25*, 189. DOI: 10.1002/jcc.10351.

[142] Ertural, C.; Steinberg, S.; Dronskowski, R. *RSC Adv.* **2019**, *9*, 29821. DOI: 10.1039/c9ra05190b.

[143] Bader, R. F. W., *Atoms in molecules: a quantum theory*; Clarendon Press: Oxford, 1990.

[144] Popelier, P. L. A. *Theor. Chem. Acc.* **2001**, *105*, 393. DOI: 10.1007/s002140000224.

[145] De Proft, F.; Van Alsenoy, C.; Peeters, A.; Langenaeker, W.; Geerlings, P. *J. Comp. Chem.* **2002**, *23*, 1198. DOI: 10.1002/jcc.10067.

[146] Tang, W; Sanville, E; Henkelman, G *J. Phys. Cond. Matt.* **2009**, *21*, 084204. DOI: 10.1088/0953-8984/21/8/084204.

[147] Hammer, B.; Nørskov, J. K. *Surf. Sci.* **1995**, *343*, 211. DOI: 10.1016/0039-6028(96)80007-0.

[148] Hammer, B.; Nørskov, J. K. *Adv. Catal.* **2000**, *45*, 71. DOI: 10.1016/S0360-0564(02)45013-4.

[149] *Chemical Bonding at Surfaces and Intermediates*; Nilsson, A., Pettersson, L., Nørskov, J., Eds.; Elsevier: Amsterdam, 2008.

[150] Mavrikakis, M.; Hammer, B.; Nørskov, J. K. *Phys. Rev. Lett.* **1998**, *81*, 2819. DOI: 10.1103/PhysRevLett.81.2819.

[151] Miller, S. D.; Kitchin, J. R. *Surf. Sci.* **2009**, *603*, 794. DOI: 10.1016/j.susc.2009.01.021.

[152] Chase, M.; Davies, C.; Downey, J.; Frurip, D.; McDonald, R.; Syverud, A., *NIST JANAF thermochemical tables*; National Institute of Standards and Technology, Gaithersburg: 1986. DOI: 10.18434/T42S31, https://janaf.nist.gov/ (accessed on 16.10.2023).

[153] Sargeant, E.; Illas, F.; Rodríguez, P.; Calle-Vallejo, F. *J. Electroanal. Chem.* **2021**, *896*, 115178. DOI: 10.1016/j.jelechem.2021.115178.

[154] Almeida, M. O.; Kolb, M. J.; Lanza, M. R. V.; Illas, F.; Calle-Vallejo, F. *ChemElectroChem* **2022**, *9*, e202200210. DOI: 10.1002/celc.202200210.

[155] Montemore, M. M.; van Spronsen, M. A.; Madix, R. J.; Friend, C. M. *Chem. Rev.* **2018**, *118*, 2816. DOI: 10.1021/acs.chemrev.7b00217.

[156] Tang, M. T.; Liu, X.; Ji, Y.; Nørskov, J. K.; Chan, K. *J. Phys. Chem. C* **2020**, *124*, 28083. DOI: 10.1021/acs.jpcc.0c08310.

[157] Cheng, Y.-L.; Hsieh, C.-T.; Ho, Y.-S.; Shen, M.-H.; Chao, T.-H.; Cheng, M.-J. *Phys. Chem. Chem. Phys.* **2022**, *24*, 2476. DOI: 10.1039/d1cp05723e.

[158] Zaera, F. *Chem. Soc. Rev.* **2014**, *43*, 7624. DOI: 10.1039/C3CS60374A.

[159] Hendriksen, B. L. M.; Bobaru, S. C.; Frenken, J. W. M. *Top. Catal.* **2005**, *36*, 43. DOI: 10.1007/s11244-005-7861-7.

[160] Nørskov, J. K.; Bligaard, T.; Rossmeisl, J.; Christensen, C. H. *Nat. Chem.* **2009**, *1*, 37. DOI: 10.1038/nchem.121, (accessed on 04.09.2024).

[161] Li, Q.; García-Muelas, R.; López, N. *Nature Communications* **2018**, *9*, 526. DOI: 10.1038/s41467-018-02884-y, (accessed on 04.09.2024).

[162] Stamatakis, M.; Vlachos, D. G. *J. Chem. Phys.* **2011**, *134*, DOI: 10.1063/1.3596751.

[163] Lukkien, J. J.; Segers, J. P.; Hilbers, P. A.; Gelten, R. J.; Jansen, A. P. *Phys. Rev. E* **1998**, *58*, 2598. DOI: 10.1103/PhysRevE.58.2598.

[164] Pineda, M.; Stamatakis, M. *J. Chem. Phys.* **2017**, *147*, DOI: 10.1063/1.4991690.

[165] Kozuch, S.; Shaik, S. *Acc. Chem. Res.* **2011**, *44*, 101. DOI: 10.1021/ar1000956.

[166] Kozuch, S.; Shaik, S. *J. Phys. Chem. A* **2008**, *112*, 6032. DOI: 10.1021/jp8004772.

[167] Kozuch, S. *ACS Catal.* **2015**, *5*, 5242. DOI: 10.1021/acscatal.5b00694.

[168] IUPAC Compendium of Chemical Terminology, DOI: 10.1351/goldbook, http://goldbook.iupac.org (accessed on 28.05.2024).

[169] Solel, E.; Tarannam, N.; Kozuch, S. *Chem. Commun.* **2019**, *55*, 5306. DOI: 10.1039/C9CC00754G.

[170] Falivene, L.; Kozlov, S. M.; Cavallo, L. *ACS Catal.* **2018**, *8*, 5637. DOI: 10.1021/acscatal.8b00042.

[171] Garay-Ruiz, D.; Bo, C. *ACS Catal.* **2020**, *10*, 12627. DOI: 10.1021/acscatal.0c02332.

[172] Campbell, C. T. *Top. Catal.* **1994**, *1*, 353. DOI: 10.1007/BF01492288.

[173] Campbell, C. T. *J. Catal.* **2001**, *204*, 520. DOI: 10.1006/jcat.2001.3396.

[174] Campbell, C. T. *ACS Catal.* **2017**, *7*, 2770. DOI: 10.1021/acscatal.7b00115.

[175] Stegelmann, C.; Andreasen, A.; Campbell, C. T. *J. Am. Chem. Soc* **2009**, *131*, 8077. DOI: 10.1021/ja9000097.

[176] Cohen, M.; Vlachos, D. G. *Ind. Eng. Chem. Res.* **2022**, *61*, 5117. DOI: 10.1021/acs.iecr.2c00390.

[177] Cohen, M.; Vlachos, D. G. *Ind. Eng. Chem. Res.* **2023**, *62*, 2191. DOI: 10.1021/acs.iecr.2c01991.

[178] Garay-Ruiz, D. gTOFfee: applying the energy span model to reaction networks https://gitlab.com/dgarayr/gtoffee (accessed on 28.02.2022).

[179] Dharmalingam, B. C.; Koushik V, A.; Mureddu, M.; Atzori, L.; Lai, S.; Pettinau, A.; Kaisare, N. S.; Aghalayam, P.; Varghese, J. J. *Appl. Catal. B: Environ.* **2023**, *332*, 122743. DOI: 10.1016/j.apcatb.2023.122743.

[180] Mehta, P.; Greeley, J.; Delgass, W. N.; Schneider, W. F. *ACS Catal.* **2017**, *7*, 4707. DOI: 10.1021/acscatal.7b00979.

[181] Rühle, M. *Adv. Mater.* **1997**, *9*, 195. DOI: 10.1002/adma.19970090304.

[182] Jung, K. T.; Bell, A. T. *Catal. Lett.* **2002**, *80*, 63. DOI: 10.1023/A:1015326726898.

[183] Jung, K. T.; Bell, A. T. *J. Mol. Catal. A Chem.* **2000**, *163*, 27. DOI: 10.1016/S1381-1169(00)00397-6.

[184] Posada-Borbón, A.; Hagman, B.; Schaefer, A.; Zhang, C.; Shipilin, M.; Hellman, A.; Gustafson, J.; Grönbeck, H. *Surf. Sci.* **2018**, *675*, 64. DOI: 10.1016/j.susc.2018.04.015.

[185] Eren, B.; Weatherup, R. S.; Liakakos, N.; Somorjai, G. A.; Salmeron, M. *J. Am. Chem. Soc.* **2016**, *138*, 8207. DOI: 10.1021/jacs.6b04039.

[186] Studt, F.; Behrens, M.; Kunkes, E. L.; Thomas, N.; Zander, S.; Tarasov, A.; Schumann, J.; Frei, E.; Varley, J. B.; Abild-Pedersen, F.; Nørskov, J. K.; Schlögl, R. *ChemCatChem* **2015**, *7*, 1105. DOI: 10.1002/cctc.201500123.

[187] Palomino, R. M.; Ramírez, P. J.; Liu, Z.; Hamlyn, R.; Waluyo, I.; Mahapatra, M.; Orozco, I.; Hunt, A.; Simonovis, J. P.; Senanayake, S. D.; Rodriguez, J. A. *J. Phys. Chem. B* **2018**, *122*, 794. DOI: 10.1021/acs.jpcb.7b06901.

[188] Ouyang, R.; Liu, J.-X.; Li, W.-X. *J. Am. Chem. Soc.* **2013**, *135*, 1760. DOI: 10.1021/ja3087054.

[189] Greeley, J.; Mavrikakis, M. *J. Phys. Chem. B* **2005**, *109*, 3460. DOI: 10.1021/jp046540q.

[190] Wang, J.; Li, G.; Li, Z.; Tang, C.; Feng, Z.; An, H.; Liu, H.; Liu, T.; Li, C. *Sci. Adv.* **2017**, *3*, e1701290. DOI: 10.1126/sciadv.1701290.

[191] Cheng, K.; Gu, B.; Liu, X.; Kang, J.; Zhang, Q.; Wang, Y. *Angew. Chem. Int. Ed.* **2016**, *128*, 4803. DOI: 10.1002/anie.201601208.

[192] Kauppinen, M.; Posada-Borbón, A.; Grönbeck, H. *J. Phys. Chem. C* **2022**, *126*, 15235. DOI: 10.1021/acs.jpcc.2c05715.

[193] Rhodes, M; Pokrovski, K; Bell, A *J. Catal.* **2005**, *233*, 210. DOI: 10.1016/j.jcat.2005.04.027.

[194] Kouva, S.; Andersin, J.; Honkala, K.; Lehtonen, J.; Lefferts, L.; Kanervo, J. *Phys. Chem. Chem. Phys.* **2014**, *16*, 20650. DOI: 10.1039/c4cp02742f.

[195] Bartholomew, C. H. *Appl. Catal. A Gen.* **2001**, *212*, 17. DOI: 10.1016/S0926-860X(00)00843-7.

[196] Dietze, E. M.; Abild-Pedersen, F.; Plessow, P. N. *J. Phys. Chem. C* **2018**, *122*, 26563. DOI: 10.1021/acs.jpcc.8b09303.

[197] Hu, S.; Li, W.-X. X. *Science* **2021**, *374*, 1360. DOI: 10.1126/science.abi9828.

[198] Nikolajsen, M.; Grivel, J.-C.; Gaur, A.; Hansen, L.; Baumgarten, L.; Schjødt, N.; Mentzel, U.; Grunwaldt, J.-D.; Sehested, J.; Christensen, J.; Høj, M. *J. Catal.* **2024**, *431*, 115389. DOI: 10.1016/j.jcat.2024.115389.

[199] Wang, B.; Nagase, S.; Zhao, J.; Wang, G. *J. Phys. Chem. C* **2007**, *111*, 4956. DOI: 10.1021/jp066548v.

ORIGINAL PAPERS

I

INFLUENCE OF A CU-ZIRCONIA INTERFACE STRUCTURE ON CO_2 ADSORPTION AND ACTIVATION

by

Gell, L.; Lempelto, A.; Kiljunen, T.; Honkala, K.

J. Chem. Phys. 2021, 154, 214707

https://doi.org/10.1063/5.0049293

The Journal of Chemical Physics ARTICLE scitation.org/journal/jcp

Influence of a Cu–zirconia interface structure on CO_2 adsorption and activation

Cite as: J. Chem. Phys. 154, 214707 (2021); doi: 10.1063/5.0049293
Submitted: 3 March 2021 • Accepted: 17 May 2021 •
Published Online: 3 June 2021

Lars Gell, Aku Lempelto, Toni Kiljunen, and Karoliina Honkala[a)]

AFFILIATIONS

Department of Chemistry, Nanoscience Center, University of Jyväskylä, P.O. Box 35 (YN), Jyväskylä FI-40014, Finland

[a)]Author to whom correspondence should be addressed: karoliina.honkala@jyu.fi

ABSTRACT

CO_2 adsorption and activation on a catalyst are key elementary steps for CO_2 conversion to various valuable products. In the present computational study, we screened different Cu–ZrO_2 interface structures and analyzed the influence of the interface structure on CO_2 binding strength using density functional theory calculations. Our results demonstrate that a Cu nanorod favors one position on both tetragonal and monoclinic ZrO_2 surfaces, where the bottom Cu atoms are placed close to the lattice oxygens. In agreement with previous calculations, we find that CO_2 prefers a bent bidentate configuration at the Cu–ZrO_2 interface and the molecule is clearly activated being negatively charged. Straining of the Cu nanorod influences CO_2 adsorption energy but does not change the preferred nanorod position on zirconia. Altogether, our results highlight that CO_2 adsorption and activation depend sensitively on the chemical composition and atomic structure of the interface used in the calculations. This structure sensitivity may potentially impact further catalytic steps and the overall computed reactivity profile.

I. INTRODUCTION

Chemical transformations of CO_2 into fuels and platform chemicals have been identified as a highly promising approach to alleviate anthropogenic CO_2, providing a waste-value approach to upgrade CO_2 into building block and value-added products for chemical industry.[1–3] Due to the highly oxidized state, thermodynamic stability, and unreactive nature of CO_2, economical, active, and selective catalysts are mandatory and the chemical conversion and the economical utilization of CO_2 are notable scientific and technical challenges.[1]

Numerous experimental and computational studies have shown that CO_2 reduction takes place at the metal–oxide interface,[4–10] which is also an active domain for many other industrially important catalytic reactions,[11] such as the water–gas shift reaction[12,13] and CO oxidation[14,15] just to mention but a few. These reactions have been reported to take place over a variety of metal–oxide interfaces with diverse chemical nature and composition, e.g., Au–TiO_2,[15–17] Cu–ZnO,[4,9] Rh–ZrO_2,[13,18] FeO–Pt,[19] Pd–Co_3O_4,[20,21] Pt–SiO_2,[22,23] and others.[24] As the experimental characterization of interface structures at the atomic level is demanding, density functional theory (DFT) modeling is extensively used to obtain microscopic information about chemical and structural properties of interfaces[4,13,15,17,25,26] and to establish structure–performance relationships.[25] While the catalyst models used in DFT calculations must be firmly based on real catalytic systems, simplifications are mandatory to reduce the computational burden. The key feature of a catalyst to be captured by the model is an active site. Typically, the employed models vary depending on the chemical composition and nature of the active site. For metal-only active sites, periodic surface slab models are commonly used,[27–30] whereas active sites consisting of the metal–oxide interface are often represented by oxide-supported metal clusters[8,31–34] or infinitely long nanorods.[13,15,25,26]

Among the possible chemical transformations, CO_2 conversion to methanol is particularly interesting due to the potential of methanol as a future energy carrier.[2,35] While Cu/ZnO/Al_2O_3 catalysts are commonly used in industry to produce methanol from CO and they have also successfully been applied to CO_2 reduction to methanol,[2,5,36,37] ZrO_2 supported or promoted Cu catalysts have been identified as promising alternatives due to their higher selectivities and turn over frequencies toward methanol.[5,6,38–40] Recent studies indicate that a reaction mechanism and selectivity are determined by the adsorption energies of key reaction intermediates.[5,8,26,31] Two central reaction steps, namely, H_2 dissociation[41,42] and CO_2

activation, are strongly associated with the Cu–ZrO_2 interface.[5,38,43] The reaction is inferred to be structure sensitive to Cu, and the synergy between Cu and support oxides is responsible for enhanced reactivity.[4,5,44–48] In calculations, however, adsorption characteristics may sensitively depend on a constructed catalyst model, and small differences between relatively similar active sites may introduce large variations in adsorption energies as shown, e.g., for CO adsorption on zirconia supported metal clusters.[33] Computationally, CO_2 conversion to methanol has recently been studied employing a Cu_{38} cluster model supported on a m-$ZrO_2(\bar{1}11)$ surface[8] and a Cu nanorod model, which is composed of three layers of stacked Cu(100) facets on t-$ZrO_2(101)$.[26] A similar nanorod model was also used for a Au–MgO interface to address a water–gas shift reaction.[12] In another computational study, the catalytic properties of various metal–MgO interfaces were considered using rods that also consist of (100) terminated slices but cut in a different orientation to better match the symmetry of MgO(100).[25] CO_2 reduction on SiO_2 and TiO_2 supported Pt was, in turn, investigated using a Pt_{25} cluster, also composed of stacked (100) facets and exposing (111) microfacets toward the interface.[31] A differently shaped Rh nanorod, terminated by (111) facets on each side, was employed for a water–gas shift reaction on ZrO_2,[13] and a similar model was used for Au–TiO_2 to address CO oxidation[15] and low temperature H_2 oxidation.[49] As one would expect, the symmetry and periodicity of the underlying support oxide naturally influence the interface and must therefore be considered. For highly symmetric oxide surfaces, such as MgO(100), the orientation of a deposited nanorod has a vanishingly small impact on the interface. For less symmetric oxides, the position and orientation of the nanorod can substantially change the interface structure. For example, a monoclinic $ZrO_2(\bar{1}11)$ surface displays a less symmetric crystal structure than a tetragonal $ZrO_2(101)$ surface. One more feature that may affect interface reactivity is strain effects,[25] which together with defects in catalytic metal particles have been suggested to have a significant impact on catalytic efficiency.[25,50,51] This is hardly surprising as it is well established from the numerous studies that straining of metal surfaces changes their reactivity observed as shifts in d-band centers.[30,52] Artificial strain effects may emerge in the construction of atomic models for metal–oxide interfaces because the lattice mismatch between the metal and oxide will introduce strain along the nanorod as it has to meet the periodicity set for the support surface.

In this study, we focus on CO_2 adsorption and activation on various Cu–ZrO_2 interface structures to shed light on the influence of the interface properties on CO_2 binding. Specifically, we considered two Cu nanorod models with different geometries and both tetragonal [t-$ZrO_2(101)$] and monoclinic [m-$ZrO_2(\bar{1}11)$] zirconia surfaces. A comprehensive screening of nanorod positions was performed on oxide, and CO_2 characteristics were analyzed for differently strained interfaces. The adsorption process was broken down to distinct electronic contributions, and they were used to attempt to establish general trends between the interface structure and its ability to adsorb and activate CO_2.

II. COMPUTATIONAL METHODS

All density functional theory (DFT) calculations were carried out using the Bayesian error estimation functional with van der Waals correlation (BEEF-vdW)[53] in the projector-augmented wave (PAW)[54] formalism as implemented in the GPAW[55] package. The core electrons of all elements were described by PAW setups in the frozen-core approximation. A maximum spacing of 0.18 Å was used for the real-space grid basis, and the reciprocal space was sampled at the Γ point. Periodic boundary conditions were used in two directions. A Hubbard U correction[56] of 2.0 eV was applied to the d-orbitals of the zirconium atoms. The geometry optimizations were performed using the BFGS algorithm as implemented in the Atomic Simulation Environment (ASE).[57] The computed electronic structures were analyzed by the Bader partitioning method[58] using the code written by Tang *et al.*[59] to obtain the distribution of partial charges on individual atoms. The search for transition states was carried out using the climbing image nudged elastic band (NEB)[60,61] method. The density of states (see Figs. S7 and S8, for example) was analyzed to locate the d-band centers for the purpose of investigating their importance to the reactivity of the Cu nanorods according to the d-band model.[62]

The interface models were built by placing a Cu nanorod over the most stable facets of monoclinic and tetragonal zirconia surfaces, m-$ZrO_2(\bar{1}11)$ and t-$ZrO_2(101)$, as supports (see Fig. 1 for an overview). We adopted two Cu nanorod models, similar to those that have been used in previous publications,[13,25,26] to be used in the present study. Both models have an equal number of atoms, and they display a (111) facet toward the reactive Cu–zirconia interface. The nanorod structures differ by the facet via which they are attached to the zirconia support. The bottom interface is either a (100) facet or a (111) facet; hence, we will here call them the (100) and (111) models, respectively. As shown in Fig. 1 and Fig. S1, the (100) model has a more gently sloping reactive interface than the (111) model. Under the reaction conditions of CO_2 conversion to methanol, the most commonly exposed Cu surfaces are (111) and (100) of which (111) is slightly more stable.[63]

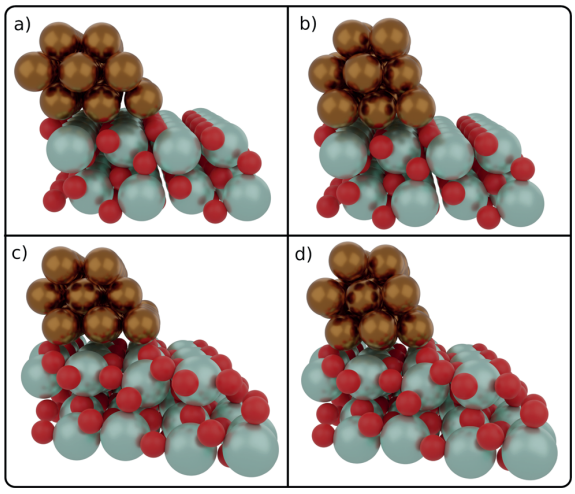

FIG. 1. The optimized minimum energy structures of a Cu nanorod on tetragonal or monoclinic zirconia supports. (a) (100)/t-ZrO_2, (b) (111)/t-ZrO_2, (c) (100)/m-ZrO_2, and (d) (111)/m-ZrO_2.

A. Model system screening

Figure 1 illustrates the catalytic model systems for both nanorod models and supports. Screening of the rod position was carried out by displacing the nanorods in two directions on the support: along and perpendicular to the nanorod, while keeping the orientation fixed. To scan the surface, we used a grid of 0.7 Å steps along the nanorod axis and 1.1 or 1.5 Å steps perpendicular to the nanorod for t-ZrO_2 or m-ZrO_2, respectively. The CO_2 binding was studied by attaching the molecule to one of the bottom-row Cu atoms at the reactive interface.

The oxide support was described by a slab model, the thickness of which was set to two stoichiometric layers. This approximation is necessary to reduce the computational burden, especially in the larger cells (see below). We consider the two-layer model sufficient to reveal general trends when comparing the nanorod models and justified since in preliminary evaluations with two to four layers, the Cu–zirconia binding energy showed only minor variation. We also determined that the d-band centers of the interfacial copper atoms varied insignificantly between different slab thicknesses. However, the CO_2 adsorption energy depends on slab thickness and test calculations showed that a thicker slab would enhance the binding. In geometry optimizations, the bottom layer of the zirconia slab was kept frozen at its initial bulk geometry, while the top zirconia layer, the Cu nanorod, and the possible CO_2 adsorbate were allowed to relax until the maximum residual force was reduced below 0.02 eV $Å^{-1}$.

B. Strain of the nanorod

With the present DFT model, we obtain a bulk Cu lattice constant of 3.69 Å, which leads to 2.61 Å nearest-neighbor Cu–Cu distance prior to modifications. Nanorods were created by repeating periodic Cu_8 minimum nanorod units having a length of one atom. Our computationally determined zirconia lattice constants can be found in Table S1. To explore possible implications of the artificial strain on the metal–oxide interface, we studied five different nanorod lengths on tetragonal ZrO_2 and three on monoclinic ZrO_2 surfaces; see Table S2 and Fig. S2 for details on the computational cells.

Because the calculations have to be periodic along the length of the rod, the Cu–Cu distance modified in that direction was always adjusted accordingly to meet the periodicity of the given surface unit cell. We define the strain as positive when the nanorod is stretched and negative when it is compressed relative to the computationally optimized bulk Cu lattice constant. The nanorods illustrated in Fig. 1 are those with the lowest strains, with the t-ZrO_2 support producing a −0.72% and m-ZrO_2 a −1.02% strain. Overall, the strain varies from −7.3% to +8.1% between the different surface models investigated.

C. Energy decomposition

The energy decomposition was set to characterize different contributions in the adsorption of CO_2 at the catalytic sites. First, the adsorption energy of CO_2 was computed from the total energies as

$$\Delta E_{ads} = E_{CO_2/Cu/ZrO_2} - E_{Cu/ZrO_2} - E_{CO_2}, \quad (1)$$

where $E_{CO_2/Cu/ZrO_2}$ stands for the full system, E_{Cu/ZrO_2} stands for the bare ZrO_2-supported Cu nanorod, and E_{CO_2} stands for gas-phase (linear, inactivated) CO_2. The gas-phase reference was computed in a large non-periodic cell. We will use the adsorption energy difference $\Delta\Delta E_{ads}$ to compare the different interface model systems. Then, to exclude the contribution of atomic relaxations from the above CO_2–Cu/ZrO_2 bond strength, we computed the total electronic interaction energy as

$$\Delta E_{el}^{tot} = E_{CO_2/Cu/ZrO_2} - E^*_{Cu/ZrO_2} - E^*_{CO_2}. \quad (2)$$

Here, asterisks stand for reference configurations, where all the atomic positions were fixed to those optimized for the full system. The adsorption and electronic interaction energies in Eqs. (1) and (2) thus differ by an energy penalty required by the deformation of the catalyst and the CO_2 molecule upon adsorption. Again, for comparison, we define $\Delta\Delta E_{el}^{tot}$ to assess the difference between the models.

The electronic interaction energies between the CO_2 molecule and the catalyst components Cu and ZrO_2 were separated according to

$$\Delta E_{el}^{Cu} = E^*_{CO_2/Cu} - E^*_{Cu} - E^*_{CO_2}, \quad (3)$$

$$\Delta E_{el}^{Zr} = E^*_{CO_2/ZrO_2} - E^*_{ZrO_2} - E^*_{CO_2}. \quad (4)$$

Again, the atomic coordinates of CO_2 and the isolated Cu nanorod and ZrO_2 were fixed to those optimized for the full system. Summing Eqs. (3) and (4) together accounts for the pairwise contributions to the three-body interaction in Eq. (2). Finally, to account for the missing contribution to the total electronic interaction, we define an excess energy

$$\Delta E_{exc} = \Delta E_{el}^{tot} - \Delta E_{el}^{Cu} - \Delta E_{el}^{Zr}, \quad (5)$$

which describes the change in electronic interaction energy due to the synergy effect of the metal–oxide interface.

III. RESULTS AND DISCUSSION

A. Binding of the minimum-strain Cu nanorods on ZrO_2 supports

To evaluate how the structure and position of a nanorod on a zirconia support influence the catalytic properties of the formed interface, we carefully analyzed the binding of the two nanorods by screening their positions on zirconia. The heat maps given in Fig. 2 show how the binding energy of a nanorod depends on its position on the surface. Specifically, we plot the relative energies of both (100) and (111) models with respect to their most stable structures on both tetragonal [Figs. 2(a) and 2(b)] and monoclinic [Figs. 2(c) and 2(d)] supports. We find that the variation of the nanorod position along its length has only a minor influence on the binding energy, whereas moving the nanorod in the perpendicular direction across the zirconia surface introduces substantial energy changes. On t-ZrO_2, the energy difference between the most stable and the least stable nanorod position is 1.4 eV for the (100) model and 2.0 eV for the (111) model. On m-ZrO_2, the corresponding value is 2.2 eV for both models.

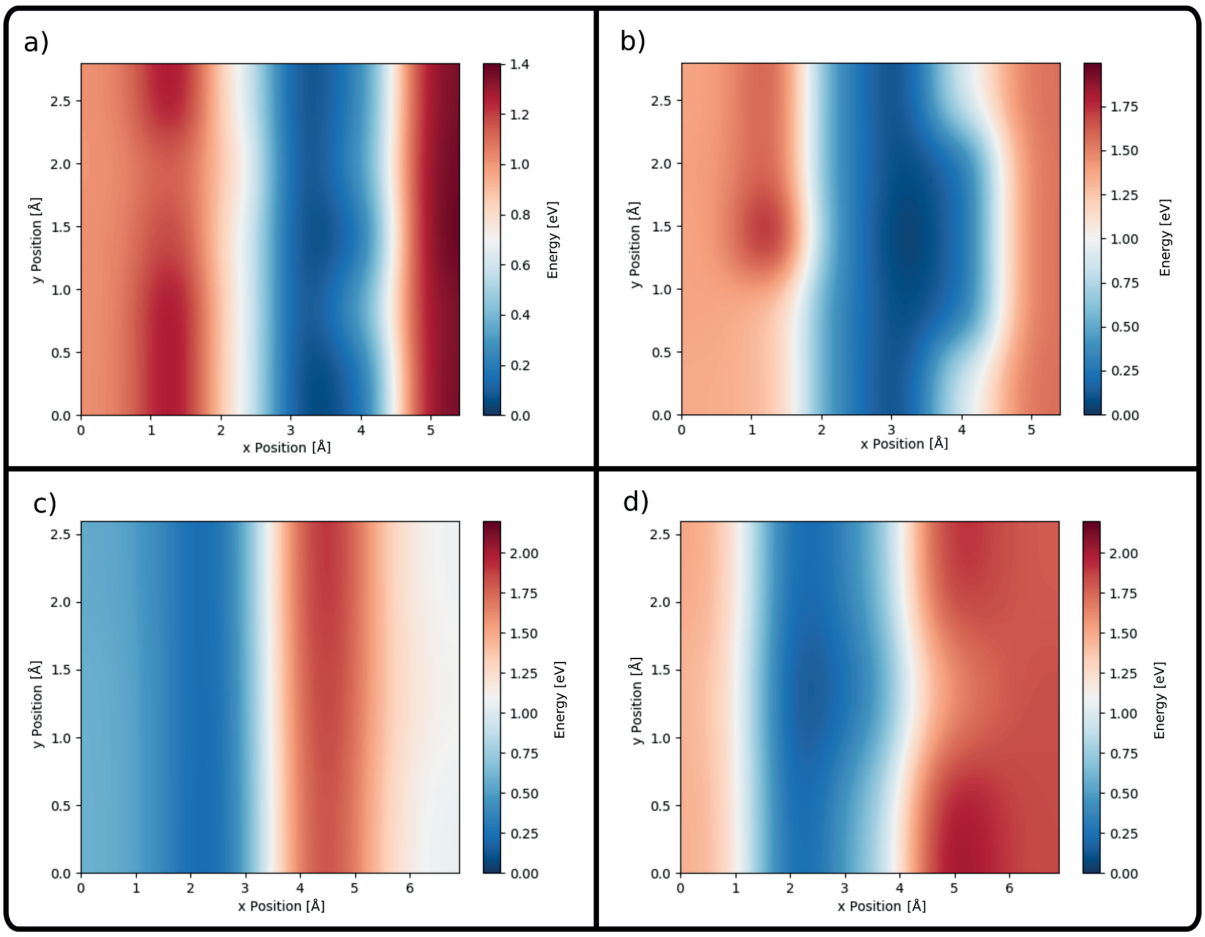

FIG. 2. Variation of the binding energy of a Cu nanorod across the studied zirconia surfaces: (a) (100)/*t*-ZrO_2, (b) (111)/*t*-ZrO_2, (c) (100)/*m*-ZrO_2, and (d) (111)/*m*-ZrO_2. The nanorods are oriented along the *y* axis (vertical). The position range along the *x* axis covers the surface cell length, whereas the y-range is limited to the nearest-neighbor Cu–Cu distance along the rod length.

We ascribe the large positional effect on the energy to the strong interaction between the bottom Cu atoms and the surface O anions. Figure 1 and Fig. S3 display the most energetically favorable interface structures for the (100) and (111) models on both tetragonal zirconia and monoclinic zirconia. Careful visual inspection of several interface structures indicates that the edge Cu atoms are attracted to surface oxygens and they avoid the positions directly above the Zr atoms. The interaction leads to the charge transfer of ≈0.4–0.5 electrons from the rod to zirconia according to the Bader charge analysis. We anticipate that the positional effect, manifested in energy corrugation, would decrease with increasing nanorod width. The heat maps in Fig. 2 show that the favorable binding zone for Cu nanorods on zirconia is very narrow. Thus, wider nanorods would always spread out over unfavorable areas of zirconia as well, which weakens the overall binding to the underlying support. The fact that the relative energy increases steeply in heat maps when Cu atoms move to Zr top sites may also have implications for binding characteristics of larger Cu nanoparticles on zirconia. Interface structures where the Cu edge atoms reside on Zr top sites should statistically appear less often as they are energetically costly, and thus, nanoparticles would prefer to create interfaces similar to those shown in Fig. 1 and Fig. S3. (For a top view of the binding interface, see Fig. S4.)

A more detailed comparison of energies of the two models shows that the (111) model is more stable than the (100) model. On *t*-ZrO_2, the relative stability of the models differs by 0.11 eV/nanorod unit, while on *m*-ZrO_2, the difference is as large as 0.32 eV. In the gas-phase, the (111) model is 0.33 eV/nanorod

unit more stable than the (100) model. However, as this energy difference decreases on the tetragonal zirconia surface, it implies that the interaction with the support, particularly, stabilizes the (100) Cu nanorod. We link the surface-specific stabilization effect to the Cu–O distances, which are shorter on tetragonal zirconia than on monoclinic zirconia; see Figs. S5(a) and S6. The relative stabilities of (100) and (111) nanorods on zirconia surfaces are 0.37 and 0.24 eV/nanorod unit, respectively, and they further demonstrate the ability of the tetragonal surface to better stabilize Cu than the monoclinic surface. Even when considering the adsorption of a single Cu atom, we see that adsorption is about 0.3 eV more exothermic on tetragonal zirconia. These are in line with a previous experimental study,[39] which reports stronger Cu–ZrO_2 interactions on tetragonal zirconia than on monoclinic. The comparison between the adsorption energies of Cu rods normalized to the surface area and the surface energies of relevant Cu and ZrO_2 surfaces shows that on monoclinic zirconia, the normalized adsorption energies are roughly half of the surface energy of m-$ZrO_2(\bar{1}01)$ and ca. one third of the surface energies of Cu surfaces; see Table S6. To gain more detailed understanding of the energy variation seen in the heat map plots and to link the binding energy to the microscopic structure, we plotted the energy change with respect to the most stable (111)-ZrO_2 structure vs the average minimum Cu–O distance between the bottom Cu atoms and topmost surface anions for different nanorod positions over both surfaces. Figures S5(a) and S6 clearly display that the (111) model is more stable than the (100) model, and for both nanorod models, the shorter distance corresponds to the more stable structure. Furthermore, the average distance of the entire Cu nanorod (bottom) from zirconia is 2.5 Å on t-ZrO_2 and 3.1 Å on m-ZrO_2. The shorter average C–O distances and shorter nanorod–oxide distance can be explained with more exposed and symmetrically located lattice oxygens on the tetragonal surface. The optimization of bottom Cu atom positions with respect to surface oxygens is more challenging on the monoclinic surface owing to the larger asymmetry of the surface and the fact that the surface anions are located deeper in the topmost surface layer. Additionally, we note that structural deformations in Cu nanorods originating from the interaction with the zirconia support show no correlation with the relative energy of the system, as can be seen in Fig. S5(b).

B. Strain effects on nanorod binding

A less optimal oxide surface cell size in calculations can introduce artificial strain effects on the nanorod, and these, in turn, can influence the computed adsorption characteristics. Therefore, we analyzed strain effects more closely; for computational details, see Table S2. First, the position of the differently strained nanorods was screened over both zirconia surfaces. We find that the preferred nanorod positions are almost identical to those given in Fig. 1 and Figs. S3 and S4 for the ideal interfaces, and thus, we limit our study on the most stable nanorod positions. In particular, we aim to understand changes in nanorod binding energies due to strain and elucidate the difference between the tetragonal and monoclinic ZrO_2 surfaces with special emphasis on the tetragonal surface.

The last column in Table I shows that the total binding energy (ΔE_b) is more exothermic for the (100) model and the tetragonal surface than for the (111) model and the monoclinic surface, but it follows no obvious trend. To understand the origin of this variation better, the thermodynamic cycle (see Fig. 3) was devised to analyze the different components. The cycle divides the Cu–ZrO_2 binding energy into four contributions. The first three steps constitute the changes in the gas-phase nanorod, and the last one measures the pure electronic interaction with zirconia. Step 1 describes the change for the optimization of interatomic Cu–Cu distances, whereas step 2 gives the energy change originating from strain

TABLE I. Nanorod binding energies (in eV) at each stage of the thermodynamic cycle shown in Fig. 3. ΔE_b stands for binding energy of a nanorod to the zirconia surface and step 5 in the thermodynamic cycle. To facilitate comparison, the energies are divided by the number of rod units in the corresponding cell.

ZrO_2	Nanorod	Strain (%)	Step 1	Step 2	Step 3	Step 4	ΔE_b
t-ZrO_2	(100)	−7.34	−0.034	+0.159	−0.363	−1.069	−1.306
		−2.71	−0.034	+0.002	−0.005	−1.025	−1.061
		−0.72	−0.034	+0.021	+0.007	−1.108	−1.113
		+4.24	−0.034	+0.220	+0.014	−1.183	−0.983
		+8.10	−0.034	+0.456	+0.055	−1.256	−0.779
	(111)	−7.34	−0.012	+0.205	−0.199	−0.871	−0.877
		−2.71	−0.012	+0.003	+0.035	−0.994	−0.968
		−0.72	−0.012	+0.008	+0.102	−1.010	−0.912
		+4.24	−0.012	+0.168	+0.045	−1.039	−0.838
		+8.10	−0.012	+0.390	+0.120	−1.136	−0.638
m-ZrO_2	(100)	−1.02	−0.019	+0.008	+0.067	−0.787	−0.741
	(111)	−4.02	−0.012	+0.035	+0.002	−0.714	−0.579
		−1.02	−0.012	+0.001	+0.009	−0.743	−0.673
		+5.57	−0.012	+0.225	+0.072	−0.898	−0.667

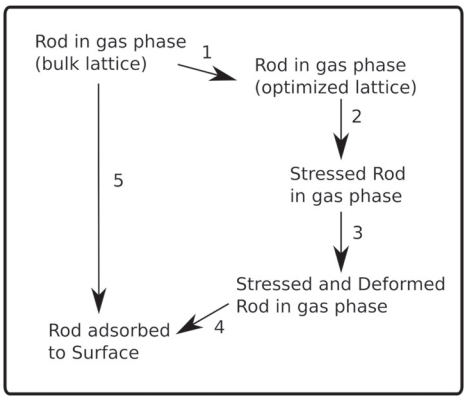

FIG. 3. A thermodynamic cycle for the binding energy decomposition of a Cu nanorod on ZrO_2.

effects, and step 3 represents the energy change due to structure deformation arising from the interaction between the nanorod and zirconia. The remaining contribution, step 4, defines the pure electronic binding interaction between the deformed Cu nanorod and zirconia.

The energy changes accompanying the thermodynamic steps are collected in Table I. Overall, the contributions from steps 1–3 are small compared to step 4, which dominates. The slight energy decrease seen in step 1 for all the models indicates that the Cu bulk lattice constant is not optimal for the gas-phase nanorod. In fact, the Cu–Cu distance decreases from the bulk value of 2.61 Å to 2.58 Å for both nanorod models on *m*-ZrO2$_2$ and to 2.55 (2.57) Å for the (100) model [(111) model] on *t*-ZrO2$_2$. Other minor variations in Cu–Cu distances and energies in step 1 originate from the differences in the computational cell shapes. As expected, increasing strain leads to a positive (endothermic) energy change in step 2 as mainly also does nanorod deformation in step 3. While irregularities introduced by the support make it difficult to predict clear trends, the larger strain is accompanied by stronger deformation and this is especially clear for the two most strained (100) rods.

Cu nanorod binding energy on zirconia is dominated by electronic interaction (step 4), which is more exothermic for *t*-ZrO_2 than for *m*-ZrO_2 resulting most likely from the shorter Cu–O distance as also suggested for the minimum-strain interfaces. As illustrated in Fig. S9, the introduced strain correlates well with the electronic interaction energy, where the compression of the nanorod decreases the electronic interaction between Cu and zirconia, while the expansion of the nanorod enhances it. No clear correlation is seen when attempting to link binding energies to strain. Multiple factors may contribute to this, the main reason being the irregular structural deformations during structure optimization. The *d*-band-center analysis supports the stronger interaction between Cu and tetragonal zirconia as the shifts in the *d*-band center are larger for tetragonal than for monoclinic surfaces. The net shift, see Table S3, is to lower energies, and it is dominated by the "ligand" effect introduced by the oxide, whereas the "strain" effect, including deformation, constitutes minor contribution.

C. CO_2 adsorption and activation

In order to estimate the significance of an interface site to CO_2 adsorption and activation, we conducted a thorough screening of the available sites for the structures explored in Sec. III A. In agreement with previous calculations,[8,26] we find that CO_2 adsorbs preferably in a bent configuration for the minimum-strain interface structures, as shown in Figs. 4 and 5. Our results also demonstrate that adsorption energies depend sensitively on the nanorod model and the interface structure.

Figure 4 displays the minimum-strain Cu–*t*-ZrO_2 interface for which the most exothermic CO_2 adsorption energies were computed to be −1.01 and −0.52 eV for the (100) and (111) models, respectively. CO_2 adsorption to Cu–*m*-ZrO_2 is an activated process to Cu–*m*-$ZrO_2(\bar{1}11)$ with the activation energy of 0.38 eV with respect to physisorbed CO_2 computed with the NEB. The adsorption energies for other interfacial sites along these interfaces can be found in Table S4. A previous DFT study[26] reports as large as −1.78 eV adsorption energy for CO_2 with the (100) model. We associate the large difference with two factors: first, a +0.41 eV gas-phase correction was applied to CO_2[26] and second, to the fact that the employed interface model has substantial, 5.08%, strain, which strongly impacts CO_2 adsorption, as discussed below. Figure 5 illustrates the CO_2 adsorption on the Cu–*m*-ZrO_2 interface, where the computed CO_2 adsorption energies are −1.38 eV for the (100) nanorod and −0.44 eV for the (111) nanorod. For a Cu_{38}–*m*-$ZrO_2(\bar{1}11)$ interface, the CO_2 absorption energy is −1.86 eV[8] being substantially more exothermic than what we found in this work. This time, the observed adsorption energy difference is attributed, on one hand, to the different exchange and correlation functional and, on the other hand, to the 38-atom cluster geometry. In another computational work, an adsorption energy of −0.69 eV was reported for a slightly thinner (111)-type Cu nanorod on a stepped *m*-$ZrO_2(\bar{2}12)$ surface,[7] where CO_2 is at the interface but binds only to the Cu atoms.

The most stable CO_2 adsorption geometries are structurally similar for both zirconia surfaces and nanorod models. CO_2 prefers a bidendate geometry, i.e., it binds to Cu via the carbon atom and has both oxygen atoms pointing down toward the support cations with the O–C–O angle being close to 120°. A substantial deviation from the linear gas-phase structure and a slight, 0.14 Å, elongation of the C–O bonds clearly indicate CO_2 activation. This is further supported by the Bader charge analysis, showing that the CO_2 molecule gains 1.2 $|e|$ upon adsorption to the Cu–ZrO_2 interfaces, as seen in Table S7, which is in line with the previously reported value.[8] The angle and charge of adsorbed CO_2 are similar to those of gas-phase formic acid for which the calculated O–C–O angle is 125° and the charge of the COO skeleton is −1.26 $|e|$. After CO_2 adsorption, the nanorod is charged positively by around 1.3 $|e|$ (see Table S7). The anionic behavior of the CO_2 molecule reflects reductive activation due to the metal contacts. Interaction between CO_2 and the interface introduces structural deformations to the Cu nanorods. While in the case of the *t*-ZrO_2 surface, the distortion of the Cu edge is minor, on *m*-ZrO_2, CO_2 clearly pulls out one Cu atom from both the nanorods; see Fig. 5.

Table II summarizes the energy contributions defined in Eqs. (1)–(5) and displays the origin of the variation of CO_2 adsorption energies from one minimum-strain interface to the other. We

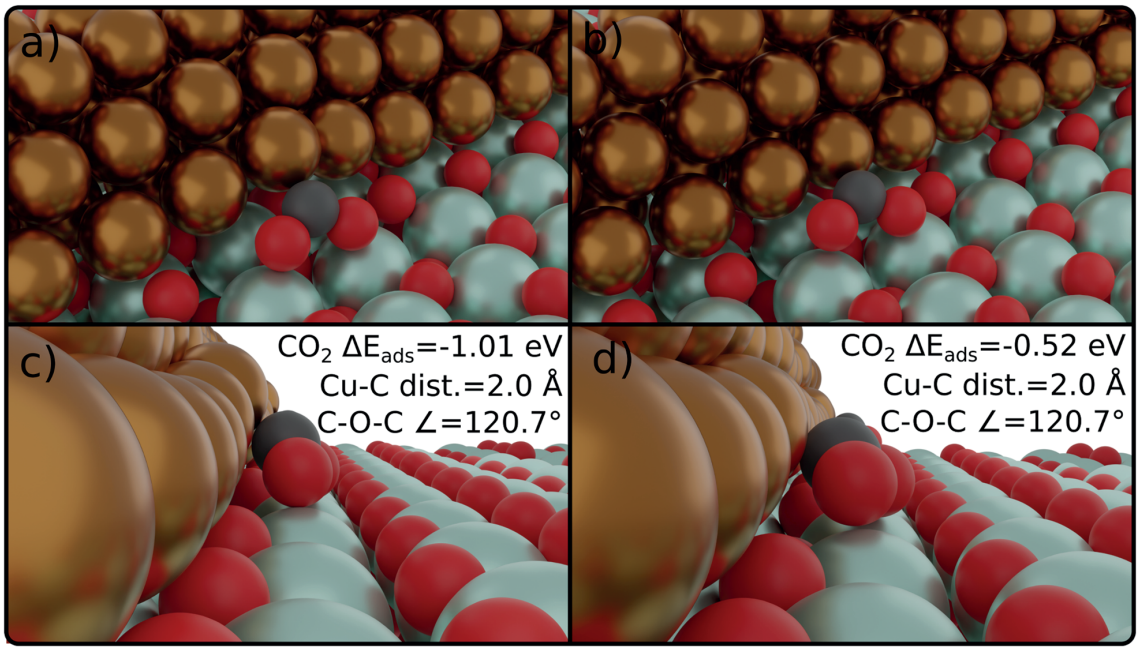

FIG. 4. Front and side views of the most stable CO_2 adsorption geometry at the minimum-strain Cu–*t*-ZrO_2 interfaces for the (100) model [(a) and (c)] and the (111) model [(b) and (d)].

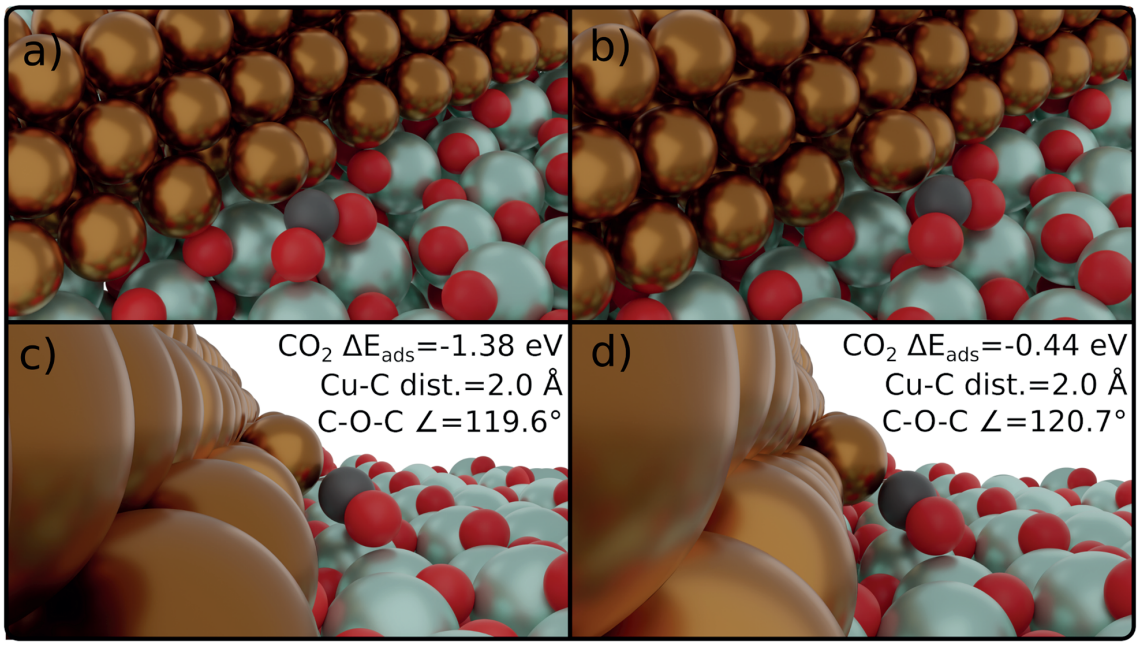

FIG. 5. Front and side views of the most stable CO_2 adsorption geometry at the minimum-strain Cu–*m*-ZrO_2 interfaces for the (100) model [(a) and (c)] and the (111) model [(b) and (d)].

TABLE II. CO_2 adsorption energies (ΔE_{ads}) and electronic interaction energies (ΔE_{el}^{tot}, ΔE_{el}^{Cu}, ΔE_{el}^{Zr}, and ΔE_{exc}), defined in Eqs. (2)–(5) for different models and strain values. All the energy values are given in eV.

ZrO_2	Nanorod	Strain (%)	ΔE_{ads}	ΔE_{el}^{tot}	ΔE_{el}^{Cu}	ΔE_{el}^{Zr}	ΔE_{exc}
t-ZrO_2	(100)	−0.72	−1.01	−6.30	−2.49	−1.76	−2.05
		+4.24	−1.17	−6.39	−2.86	−1.63	−1.89
	(111)	−7.34	−1.91	−6.02	−2.34	−1.55	−2.13
		−2.71	−0.51	−5.84	−2.38	−1.85	−1.60
		−0.72	−0.52	−5.55	−2.58	−1.50	−1.47
		+4.24	−0.71	−5.98	−2.49	−1.63	−1.87
		+8.10	−1.33	−6.27	−2.17	−1.39	−2.71
m-ZrO_2	(100)	−1.02	−1.38	−6.06	−2.13	−1.63	−2.30
	(111)	−4.02	−0.89	−5.79	−1.88	−1.72	−2.18
		−1.02	−0.44	−5.57	−1.78	−1.62	−2.18
		+5.57	−1.34	−5.81	−2.69	−1.70	−1.42

first focus on electronic interaction energies, which exclude all the structural deformations. For example, the adsorption energy difference ($\Delta\Delta E_{ads}$) between the (100) and (111) models is 0.49 eV for the tetragonal surface, whereas the pure electronic, aka binding, interaction energy difference, $\Delta\Delta E_{el}^{tot}$, shows a larger, 0.75 eV, value. Interestingly, for the monoclinic surface, $\Delta\Delta E_{ads}$ is larger than $\Delta\Delta E_{el}^{tot}$ (0.9 vs 0.5 eV). The opposite behavior is ascribed to non-identical atomic relaxations for different CO_2-interface systems. The deformation energies vary heavily from one system to the other, where the bending of the CO_2 molecules is the dominant contribution. However, the differences in deformation penalties between rods of different structures are not consistent with the differences in adsorption energies. In general, we attribute the observed adsorption energy differences to different electronic interaction energies, which are clearly more exothermic for the (100) model on both tetragonal zirconia and monoclinic zirconia. The interaction energies from the CO_2–Cu and CO_2–ZrO_2 subsystems, which measure the binding between CO_2 and metal and CO_2 and oxide, do not indicate that one nanorod model or zirconia crystal structure is favored over the other. The substantial synergy between Cu and zirconia is demonstrated by the exothermic values of ΔE_{exc} for all the studied system. This is reflected by larger charge transfer to CO_2 at the interface compared to the individual CO_2–Cu and CO_2–ZrO_2 subsystems, as can be seen in Table S7

Next, a CO_2 adsorption site at the (111)–ZrO_2 interface is further explored by moving the nanorod across the oxide surfaces. Figure 6 displays the heat maps summarizing the energy variation with respect to the most stable adsorption structure at the interface. The plots show that for many nanorod positions, CO_2 does not either adsorb at all or adsorption is energetically very unfavorable. In order to interpret the heat map information, we analyzed the calculated CO_2 adsorption structures. For a favorable CO_2 adsorption, it seems to be crucial to have lattice Zr cations sufficiently close to the Cu edge to ensure that the oxygens of the CO_2 molecule can interact with them. The nanorod positions, where surface anions are closer to the Cu edge than the Zr cations, lead to unfavorable CO_2 adsorption due to repulsive interactions between the oxygen atoms and anions. The central role of the zirconia support is further highlighted by the fact that, without the support, CO_2 only physisorbs maintaining a linear structure on a Cu(111) surface and on our (111) and (100) nanorods. This agrees well with the previous DFT results, which also demonstrate CO_2 physisorption on Cu(111) and Cu(533) surfaces.[28,37]

CO_2 adsorption on the bare zirconia surface leads to carbonate (CO_3) formation with the lattice oxygen. We find this process exothermic by −0.57 eV on *t*-ZrO_2 and by −0.59 eV on *m*-ZrO_2. In the case of a (111) model, the carbonate formation is thermodynamically slightly more favorable than CO_2 adsorption at the interface, which makes these two simultaneous reactions competing. On the other hand, CO_2 adsorption at the interface is clearly preferred to carbonate formation for the (100) model. Previously computed[64] carbonate formation energy on the same monoclinic zirconia surface is about −1.13 eV, which is substantially more exothermic than the value reported here. We ascribe this energy difference to the different exchange and correlation functional and to the thicker zirconia slab, not computationally feasible for the present screening study. Note that under the reaction conditions, zirconia is partially covered by OH groups, which are known to react with CO_2 to create an extremely stable formate species.[6,13,64,65]

We close the discussion on CO_2 adsorption and activation by considering that at the strained metal–oxide interfaces. Similar to the minimum-strained nanorods, CO_2 is activated via electron transfer and the molecule adopts a bent adsorption configuration. The bidentate binding is preferred, while monodentate geometries also appear at slightly higher energies. CO_2 adsorption energies and the electronic interaction energy components for the strained interfaces are presented in Table II. While the data do not allow to make comprehensive conclusions for all the interfaces, we can say that for the (111) model, the straining and compressing of the nanorod lead to more exothermic electronic interaction energies. However, one has

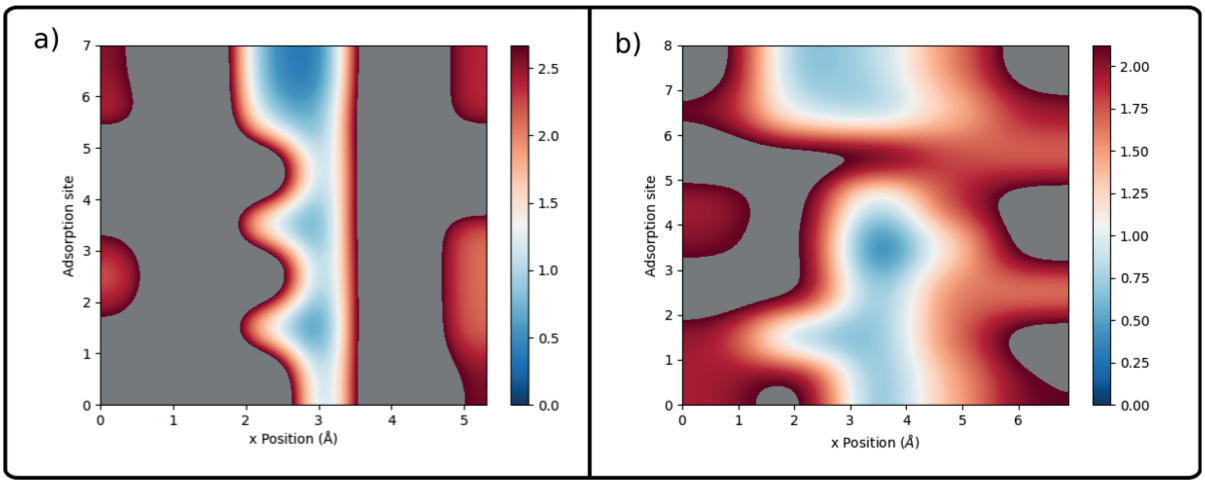

FIG. 6. Heat maps for CO_2 adsorption upon varying the position of the (111) nanorod across the (a) *t*-ZrO_2 and (b) *m*-ZrO_2 surfaces. The nanorod lies parallel to the vertical axis and is moved along the horizontal axis. The energy difference is given with respect to the most stable adsorption structure. The vertical axis numbers represent Cu edge atoms to which CO_2 was attempted to bind. Gray color corresponds to the nanorod positions, which do not bind or activate CO_2.

to be careful with the nanorods exposed to larger (± > 7%) strain as they experienced significant structural deformations during the atomic structure optimization, which reduced the atomic coordination number of some Cu atoms, typically those interacting with the C atom leading to enhanced CO_2 adsorption. Therefore, these systems are largely omitted from the detailed discussion. In general, adsorption and total electronic interaction energies do not correlate. This means that adsorption energy difference and total electronic interaction energy difference, $\Delta\Delta E_{ads}$ and $\Delta\Delta E_{el}^{tot}$, differ for a considered system pair. Again, this can be attributed to diverse deformations of the nanorod and the molecule, giving system-specific positive deformation energies. In addition, we see for all the systems strong synergy between the metal and oxide, which is reflected by exothermic values of ΔE_{exc} and highlights the unique nature of the interface. Table II also shows that interfaces built from the (100) nanorod give more exothermic CO_2 adsorption energies than its (111) counterpart.

In order to understand the variation of CO_2 adsorption energy from one system to the other, we performed *d*-band-center analysis separately to each step in the thermodynamic cycle. The formation of a metal–oxide interface has been considered as a two-step process,[25] including the "strain" and "ligand" contributions similar to bimetallic systems.[66] The "strain" effects include both changes in Cu–Cu distances along the nanorod and structural deformation of the nanorod due to interaction with zirconia, whereas the ligand effect describes the electronic interactions between Cu and zirconia. The first three steps in the thermodynamic cycle contribute to the shift of the *d*-band center due to strain effects $\Delta\epsilon_d^{strain}$, while the shift of the *d*-band center for step 4 ($\Delta\epsilon_d^{ligand}$) measures the change resulting from the ligand effect. The overall impact of the support on the Cu nanorod is a clear shift of a *d*-band center to lower energies for all the models; see Table S3 for explicit numerical values. The ligand effects clearly dominate, and the negative value of $\Delta\epsilon_d^{ligand}$ for all the interface models highlights that binding interaction between Cu and zirconia shifts the *d*-band center to lower energies. The contribution of the strain effects to the shift of the *d*-band center is negligible, being positive for some interfaces and negative for some others. Table S3 shows that CO_2 adsorption energies cannot be rationalized with the shift of the *d*-band center as no correlation can be established between the adsorption energy and the total shift in the *d*-band center. We believe that the complex metal–oxide interaction effects at the interface together with structural deformations, especially in the case of the less stable (100) rod, make the *d*-band model insufficient to explain CO_2 adsorption energies.

Altogether, our DFT results highlight that CO_2 adsorption and activation depend sensitively on the atomic structure and composition, making only few site geometries favorable for CO_2. Moreover, care must be taken when building computational interface models as artificial strain enhances CO_2 adsorption, and similar effects might be present for reaction intermediates as well, let alone that the possible strain effects may affect the activation barriers for elementary steps taking place at the interface. Structure sensitivity of CO_2 adsorption suggests that not all the Cu–ZrO_2 interfaces at real-world catalytic systems are active toward CO_2 chemistry. This is because supported nanoparticles present various interface sites with different compositions and atomic structures, and their direct structural optimization is infeasible.

IV. CONCLUSIONS

We have investigated the properties of a Cu–ZrO_2 interface and its ability to adsorb and activate CO_2 using density functional theory calculations. Specifically, two Cu nanorod models were explored on *m*-$ZrO_2(\bar{1}11)$ and *t*-$ZrO_2(101)$ surfaces. We observed that the (111)

nanorod model is always more stable than the (100) one regardless of whether it is supported by zirconia or not. Tetragonal ZrO_2 stabilizes both nanorod models more than monoclinic ZrO_2, which is likely due to the more exposed oxygen anions of the t-ZrO_2(101) surface. Our calculations demonstrate that the stability of the nanorod depends sensitively on its local chemical environment on ZrO_2 and results from the fact that Cu atoms avoid the interaction with surface cations and prefer to minimize a Cu-anion nearest-neighbor distance. Compression along the nanorod enhances binding to zirconia, while tension of the nanorod weakens the interaction with the studied oxide surfaces.

Our results demonstrate that the employed Cu–ZrO_2 interface model significantly impacts the adsorption characteristics of the CO_2 molecule. In general, the interfaces built using the (100) nanorod adsorb CO_2 more strongly compared to the interfaces created with the (111) nanorods. The activation of CO_2 is seen as clearly negative Bader charge originating from the synergy between Cu and ZrO_2 and a bent adsorption configuration. Applying strain to the nanorod enhances electronic interaction with CO_2, which is not always reflected in more exothermic adsorption energies due to structural deformation effects. The excess interaction energy originating from the synergy between the metal and the support is strongly exothermic for the all studied systems, highlighting the importance of the metal–oxide interface. Furthermore, depending on how the nanorod is positioned on ZrO_2, CO_2 might not adsorb at the interface at all.

Overall, not only the chemical composition but also the diverse structural features of an interface can impact the adsorption characteristics of reacting molecules and, consequently, the computed activity and selectivity profiles. Therefore, when building computational models for catalytic reactions taking place at the metal–oxide interface, care should be taken in constructing interfaces and identifying interfacial active sites.

SUPPLEMENTARY MATERIAL

See the supplementary material for details on the construction and the structure of the atomic models, density of states plots, and the d-band shifts for the thermodynamic cycle.

ACKNOWLEDGMENTS

This work was funded by the Academy of Finland under Project Nos. 329977 and 307623 and the University of Jyväskylä. The electronic structure calculations were made possible by the computational resources provided by the CSC—IT Center for Science, Espoo, Finland (https://www.csc.fi/en/), and the Finnish Grid and Cloud Infrastructure.

DATA AVAILABILITY

The data that support the findings of this study are available from the corresponding author upon reasonable request.

REFERENCES

[1]S. Roy, A. Cherevotan, and S. C. Peter, ACS Energy Lett. **3**, 1938 (2018).
[2]B. M. Tackett, E. Gomez, and J. G. Chen, Nat. Catal. **2**, 381 (2019).
[3]R. P. Ye, J. Ding, W. Gong, M. D. Argyle, Q. Zhong, Y. Wang, C. K. Russell, Z. Xu, A. G. Russell, Q. Li, M. Fan, and Y. G. Yao, Nat. Commun. **10**, 5698 (2019).
[4]S. Kattel, P. J. Ramírez, J. G. Chen, J. A. Rodriguez, and P. Liu, Science **355**, 1296 (2017).
[5]S. Kattel, P. Liu, and J. G. Chen, J. Am. Chem. Soc. **139**, 9739 (2017).
[6]N. Scotti, F. Bossola, F. Zaccheria, and N. Ravasio, Catalysts **10**, 168 (2020).
[7]Q.-L. Tang, Q.-J. Hong, and Z.-P. Liu, J. Catal. **263**, 114 (2009).
[8]K. Larmier, W.-C. Liao, S. Tada, E. Lam, R. Verel, A. Bansode, A. Urakawa, A. Comas-Vives, and C. Copéret, Angew. Chem., Int. Ed. **56**, 2318 (2017).
[9]M. Zabilskiy, V. L. Sushkevich, D. Palagin, M. A. Newton, F. Krumeich, and J. A. van Bokhoven, Nat. Commun. **11**, 2409 (2020).
[10]Y. Wang, S. Kattel, W. Gao, K. Li, P. Liu, J. G. Chen, and H. Wang, Nat. Commun. **10**, 1166 (2019).
[11]Q. Fu and T. Wagner, Surf. Sci. Rep. **62**, 431 (2007).
[12]Z.-J. Zhao, Z. Li, Y. Cui, H. Zhu, W. F. Schneider, W. N. Delgass, F. Ribeiro, and J. Greeley, J. Catal. **345**, 157 (2017).
[13]M. M. Kauppinen, M. M. Melander, A. S. Bazhenov, and K. Honkala, ACS Catal. **8**, 11633 (2018).
[14]Y. Y. Wu, N. A. Mashayekhi, and H. H. Kung, Catal. Sci. Technol. **3**, 2881 (2013).
[15]I. X. Green, W. Tang, M. Neurock, and J. T. Yates, Science **333**, 736 (2011).
[16]M. Boronat and A. Corma, Dalton Trans. **39**, 8538 (2010).
[17]P. Schlexer, D. Widmann, R. J. Behm, and G. Pacchioni, ACS Catal. **8**, 6513 (2018).
[18]H. Tao, C. Choi, L.-X. Ding, Z. Jiang, Z. Han, M. Jia, Q. Fan, Y. Gao, H. Wang, A. W. Robertson, S. Hong, Y. Jung, S. Liu, and Z. Sun, Chem **5**, 204 (2019).
[19]Q. Fu, W.-X. Li, Y. Yao, H. Liu, H.-Y. Su, D. Ma, X.-K. Gu, L. Chen, Z. Wang, H. Zhang, B. Wang, and X. Bao, Science **328**, 1141 (2010).
[20]J.-Y. Luo, M. Meng, X. Li, X.-G. Li, Y.-Q. Zha, T.-D. Hu, Y.-N. Xie, and J. Zhang, J. Catal. **254**, 310 (2008).
[21]J. Shen, R. E. Hayes, and N. Semagina, Catal. Today **360**, 435 (2021).
[22]N. T. S. Phan, M. Van Der Sluys, and C. W. Jones, Adv. Synth. Catal. **348**, 609 (2006).
[23]V. Polshettiwar, C. Len, and A. Fihri, Coord. Chem. Rev. **253**, 2599 (2009).
[24]Z.-c. Zhang, B. Xu, and X. Wang, Chem. Soc. Rev. **43**, 7870 (2014).
[25]P. Mehta, J. Greeley, W. N. Delgass, and W. F. Schneider, ACS Catal. **7**, 4707 (2017).
[26]S. Polierer, J. Jelic, S. Pitter, and F. Studt, J. Phys. Chem. C **123**, 26904 (2019).
[27]J. K. Nørskov, T. Bligaard, J. Rossmeisl, and C. H. Christensen, Nat. Chem. **1**, 37 (2009).
[28]D. Kopač, B. Likozar, and M. Huš, Appl. Surf. Sci. **497**, 143783 (2019).
[29]I. A. Pašti and S. V. Mentus, Electrochim. Acta **55**, 1995 (2010).
[30]M. Mavrikakis, B. Hammer, and J. K. Nørskov, Phys. Rev. Lett. **81**, 2819 (1998).
[31]S. Kattel, B. Yan, J. G. Chen, and P. Liu, J. Catal. **343**, 115 (2016).
[32]M. M. Kauppinen, V. Korpelin, A. M. Verma, M. M. Melander, and K. Honkala, J. Chem. Phys. **151**, 164302 (2019).
[33]A. S. Bazhenov and K. Honkala, J. Phys. Chem. C **123**, 7209 (2019).
[34]Y. Yang, J. Evans, J. A. Rodriguez, M. G. White, and P. Liu, Phys. Chem. Chem. Phys. **12**, 9909 (2010).
[35]G. A. Olah, Angew. Chem., Int. Ed. **52**, 104 (2013).
[36]M. Behrens, F. Studt, I. Kasatkin, S. Kuhl, M. Havecker, F. Abild-Pedersen, S. Zander, F. Girgsdies, P. Kurr, B.-L. Kniep, M. Tovar, R. W. Fischer, J. K. Norskov, and R. Schlögl, Science **336**, 893 (2012).
[37]L. C. Grabow and M. Mavrikakis, ACS Catal. **1**, 365 (2011).
[38]S. Kattel, B. Yan, Y. Yang, J. G. Chen, and P. Liu, J. Am. Chem. Soc. **138**, 12440 (2016).
[39]T. Witoon, J. Chalorngtham, P. Dumrongbunditkul, M. Chareonpanich, and J. Limtrakul, Chem. Eng. J. **293**, 327 (2016).
[40]Y. Nitta, O. Suwata, Y. Ikeda, Y. Okamoto, and T. Imanaka, Catal. Lett. **26**, 345 (1994).
[41]K.-D. Jung and A. T. Bell, J. Catal. **193**, 207 (2000).
[42]I. A. Fisher and A. T. Bell, J. Catal. **178**, 153 (1998).
[43]I. A. Fisher, H. C. Woo, and A. T. Bell, Catal. Lett. **44**, 11 (1997).

[44]F. Arena, G. Italiano, K. Barbera, S. Bordiga, G. Bonura, L. Spadaro, and F. Frusteri, Appl. Catal., A **350**, 16 (2008).
[45]F. Arena, G. Mezzatesta, G. Zafarana, G. Trunfio, F. Frusteri, and L. Spadaro, J. Catal. **300**, 141 (2013).
[46]J.-D. Grunwaldt, A. M. Molenbroek, N.-Y. Topsøe, H. Topsøe, and B. S. Clausen, J. Catal. **194**, 452 (2000).
[47]A. Le Valant, C. Comminges, C. Tisseraud, C. Canaff, L. Pinard, and Y. Pouilloux, J. Catal. **324**, 41 (2015).
[48]J. Zhong, X. Yang, Z. Wu, B. Liang, Y. Huang, and T. Zhang, Chem. Soc. Rev. **49**, 1385 (2020).
[49]I. X. Green, W. Tang, M. Neurock, and J. T. Yates, Jr., Angew. Chem., Int. Ed. **50**, 10186 (2011).
[50]I. Kasatkin, P. Kurr, B. Kniep, A. Trunschke, and R. Schlögl, Angew. Chem., Int. Ed. **46**, 7324 (2007).
[51]M. M. Günter, T. Ressler, B. Bems, C. Büscher, T. Genger, O. Hinrichsen, M. Muhler, and R. Schlögl, Catal. Lett. **71**, 37 (2001).
[52]S. Sakong and A. Groß, Surf. Sci. **525**, 107 (2003).
[53]J. Wellendorff, K. T. Lundgaard, A. Møgelhøj, V. Petzold, D. D. Landis, J. K. Nørskov, T. Bligaard, and K. W. Jacobsen, Phys. Rev. B **85**, 235149 (2012).
[54]P. E. Blöchl, Phys. Rev. B **50**, 17953 (1994).
[55]J. Enkovaara, C. Rostgaard, J. J. Mortensen, J. Chen, M. Dułak, L. Ferrighi, J. Gavnholt, C. Glinsvad, V. Haikola, H. A. Hansen, H. H. Kristoffersen, M. Kuisma, A. H. Larsen, L. Lehtovaara, M. Ljungberg, O. Lopez-Acevedo, P. G. Moses, J. Ojanen, T. Olsen, V. Petzold, N. A. Romero, J. Stausholm-Møller, M. Strange, G. A. Tritsaris, M. Vanin, M. Walter, B. Hammer, H. Häkkinen, G. K. H. Madsen, R. M. Nieminen, J. K. Nørskov, M. Puska, T. T. Rantala, J. Schiøtz, K. S. Thygesen, and K. W. Jacobsen, J. Phys.: Condens. Matter **22**, 253202 (2010).
[56]S. L. Dudarev, G. A. Botton, S. Y. Savrasov, C. J. Humphreys, and A. P. Sutton, Phys. Rev. B **57**, 1505 (1998).
[57]A. H. Larsen, J. J. Mortensen, J. Blomqvist, I. E. Castelli, R. Christensen, M. Dułak, J. Friis, M. N. Groves, B. Hammer, C. Hargus, E. D. Hermes, P. C. Jennings, P. B. Jensen, J. Kermode, J. R. Kitchin, E. L. Kolsbjerg, J. Kubal, K. Kaasbjerg, S. Lysgaard, J. B. Maronsson, T. Maxson, T. Olsen, L. Pastewka, A. Peterson, C. Rostgaard, J. Schiøtz, O. Schütt, M. Strange, K. S. Thygesen, T. Vegge, L. Vilhelmsen, M. Walter, Z. Zeng, and K. W. Jacobsen, J. Phys.: Condens. Matter **29**, 273002 (2017).
[58]R. F. W. Bader, in *Atoms in Molecules: A Quantum Theory*, International Series of Monographs on Chemistry, edited by R. F. W. Bader (Oxford University Press, Oxford, 1990).
[59]W. Tang, E. Sanville, and G. Henkelman, J. Phys.: Condens. Matter **21**, 084204 (2009).
[60]G. Henkelman, B. P. Uberuaga, and H. Jónsson, J. Chem. Phys. **113**, 9901 (2000).
[61]G. Henkelman and H. Jónsson, J. Chem. Phys. **113**, 9978 (2000).
[62]B. Hammer and J. K. Nørskov, Surf. Sci. **343**, 211 (1995).
[63]P. L. Hansen, J. B. Wagner, S. Helveg, J. R. Rostrup-Nielsen, B. S. Clausen, and H. Topsøe, Science **295**, 2053 (2002).
[64]S. Kouva, J. Andersin, K. Honkala, J. Lehtonen, L. Lefferts, and J. Kanervo, Phys. Chem. Chem. Phys. **16**, 20650 (2014).
[65]A. S. Bazhenov and K. Honkala, Top. Catal. **60**, 382 (2017).
[66]J. R. Kitchin, J. K. Nørskov, M. A. Barteau, and J. G. Chen, Phys. Rev. Lett. **93**, 156801 (2004).

II

EFFECT OF ATOMIC LAYER DEPOSITED ZINC PROMOTER ON THE ACTIVITY OF COPPER-ON-ZIRCONIA CATALYSTS IN THE HYDROGENATION OF CARBON DIOXIDE TO METHANOL

by

Arandia, A.; Yim, J.; Warraich, H.; Leppäkangas, E.; Bes, R.; Lempelto, A.; Gell, L.; Jiang, H.; Meinander, K.; Viinikainen, T.; Huotari, S.; Honkala, K.; Puurunen, R.

Appl. Catal. B Environ. 2023, 321, 122046

https://doi.org/10.1016/j.apcatb.2022.122046

Applied Catalysis B: Environmental 321 (2023) 122046

Contents lists available at ScienceDirect

Applied Catalysis B: Environmental

journal homepage: www.elsevier.com/locate/apcatb

Effect of atomic layer deposited zinc promoter on the activity of copper-on-zirconia catalysts in the hydrogenation of carbon dioxide to methanol

Aitor Arandia [a,*], Jihong Yim [a], Hassaan Warraich [a], Emilia Leppäkangas [a], René Bes [b,c], Aku Lempelto [d], Lars Gell [d], Hua Jiang [e], Kristoffer Meinander [f], Tiia Viinikainen [a], Simo Huotari [b], Karoliina Honkala [d], Riikka L. Puurunen [a]

[a] Department of Chemical and Metallurgical Engineering, School of Chemical Engineering, Aalto University, Kemistintie 1, P.O. Box 16100, FI-00076 Aalto, Espoo, Finland
[b] Department of Physics, University of Helsinki, P.O. Box 64, FI-00014 Helsinki, Finland
[c] Helsinki Institute of Physics, P.O. Box 64, FI-00014 Helsinki, Finland
[d] Department of Chemistry, Nanoscience Center, University of Jyväskylä, P.O. Box 35, FI-40014 Jyväskylä, Finland
[e] Department of Applied Physics, Aalto University, P. O. Box 13500, FI-00076 Aalto, Espoo, Finland
[f] Department of Bioproducts and Biosystems, School of Chemical Engineering, Aalto University, P. O. Box 16300, FI-00076 Aalto, Espoo, Finland

ARTICLE INFO

Keywords:
Carbon dioxide
Hydrogenation
Methanol
Atomic layer deposition
Copper
Zinc oxide

ABSTRACT

The development of active catalysts for carbon dioxide (CO_2) hydrogenation to methanol is intimately related to the creation of effective metal-oxide interfaces. In this work, we investigated how the order of addition of copper and zinc on zirconia influences the catalytic properties, the catalytic activity and selectivity toward methanol. Regarding the carbon dioxide conversion and methanol production, the catalysts on which the promoter (zinc) was atomically deposited after copper impregnation (i.e., $ZnO/Cu/ZrO_2$ and $ZnO/Cu/ZnO/ZrO_2$) were superior catalysts compared to the reverse copper-after-zinc catalyst ($Cu/ZnO/ZrO_2$). Temperature-programmed experiments and in situ diffuse reflectance infrared Fourier transform-spectroscopy (DRIFTS) experiments allowed us to elucidate the benefits of the zinc-after-copper pair to store CO_2 as carbonate species and further convert them into formate species, key intermediates in the formation of methanol. This research provides insights into the potential of atomic layer deposition in the development of tailored heterogeneous catalysts for efficient CO_2 valorization to methanol.

1. Introduction

Worldwide, there is a great desire to develop technologies for the efficient capture and conversion of carbon dioxide to fuels and chemicals, such as methanol [1–3]. Methanol is a carrier of carbon and hydrogen [4,5] and, as an energy carrier, it can be used directly as a fuel in direct methanol fuel cells (DMFCs) and internal combustion engines (ICEs) [6,7]. Additionally, methanol can be used in the production of high value-added chemicals (e.g. formaldehyde, methyl tert-butyl ether and acetic acid) and as a feedstock to produce hydrocarbons (such as alkanes, olefins or aromatics) and inherently fuels [6–8].

Traditionally, Cu/ZnO-based catalysts have been employed in the industrial production of methanol from the syngas stream ($CO/CO_2/H_2$) generated in the steam reforming of natural gas [9–11]. The mechanism of methanol formation from CO/CO_2 has been under debate for decades [12,13]. Since CO is the predominant carbon-containing molecule in syngas [2,12] and Cu is an outstanding metal for CO_2 reduction to CO (through reverse water-gas shift, $CO_2 + H_2 \rightleftharpoons CO + H_2O$), CO has been considered the primary carbon source in methanol production for decades ($CO + 2\,H_2 \rightleftharpoons CH_3OH$) [10,12]. It was in the late 1980 s when the use of ^{14}C-labeled isotopes provided evidence to suggest CO_2 as the main carbon source in the methanol production ($CO_2 + 3\,H_2 \rightleftharpoons CH_3OH + H_2O$) from $CO_2/CO/H_2$ mixtures [14]. Since then, many studies have been driven in the same direction [10,12,15–17], and currently, CO_2 is perceived as the major reactant under industrial conditions. However, as Grabow and Mavrikakis suggested based on density functional theory

* Corresponding author.
E-mail address: aitor.arandiagutierrez@aalto.fi (A. Arandia).

https://doi.org/10.1016/j.apcatb.2022.122046
Received 31 May 2022; Received in revised form 30 September 2022; Accepted 3 October 2022
Available online 6 October 2022

(DFT) calculations and microkinetic modeling [12], under typical methanol production conditions, both CO and CO_2 hydrogenation routes can coexist.

In addition to the active discussion about the carbon source, the knowledge gained regarding the nature of the active sites in the CO_2-to-methanol (CTM) process has grown exponentially in recent decades [18–20]. CO_2 is a stable molecule and greatest difficulties in achieving great methanol selectivity in CO_2 hydrogenation are related to kinetic limitations [21]. Therefore, a molecular understanding of the key aspects that govern the activity and selectivity of a catalyst is crucial. Overall, over copper-based catalysts, the CO_2 hydrogenation to methanol reaction has been described as a structure-sensitive reaction in which not all of the surface atoms have the same role and activity [15, 18,22]. For copper-zinc oxide (Cu-ZnO) binary systems, copper is responsible for the adsorption, dissociation and spillover of atomic hydrogen (H*) [23], while zinc oxide enhances the dispersion of Cu nanoparticles and facilitates the adsorption of CO_2 [24]. The Cu-ZnO interface and surroundings have been described as the most active sites responsible for the activity wherein the intermediate species (e.g. carbonates and formates) are further hydrogenated to methanol [11, 25–27]. Lately, ZrO_2-based catalysts are emerging as active [18,28,29] and cost-effective solutions for the efficient synthesis of methanol [30] and a few experimental studies have explored the synergistic interactions of Cu/ZnO/ZrO_2 catalysts and the active interplay toward methanol production [10,18,31,32]. Alone on ZrO_2, both Cu [28,33] and ZnO [34,35] can also display some activity in the hydrogenation of intermediate species to methanol. Also, the ZrO_2/Cu inverse configuration has shown excellent properties for an efficient methanol synthesis from CO_2 [36,37].

In recent years, more investigations have described not only the synergistic effect of binary Cu/ZnO catalysts but also the effects of the locations of both the active metal (Cu) and promoter (ZnO) on methanol production from CO_2 [19,38,39]. The formation of ZnO particles or reduced Zn on the Cu surface have been found to improve the Cu dispersion and eventually, the accessible Cu surface area [11,19,25,39]. Experimental and computational studies on CO_2 hydrogenation to methanol have pointed out that the formation of ZnO aggregates on top of Cu particles promoted methanol production which may be related to the increase in the number of active ZnO-Cu pairs [19,38]. Palomino et al. [38] experimentally demonstrated that ZnO added on top of Cu (100) and (111) surfaces yields a superior methanol production compared to the inverse copper-added-on-top-of-zinc oxide catalyst. Moreover, the highest production of methanol was observed at a relatively low surface coverage (θ_{Zn}) of 0.15–0.20 monolayer (ML) and similar values of $\theta_{Zn} \approx 0.20$ ML were reported by Nakamura and coworkers for ZnO over polycrystalline copper [40], and Kattel and collaborators over Cu(111) substrates [19]. By a combination of experimental, and DFT calculations and modeling based on thermodynamics, Kuld and coworkers [41] found the highest methanol turnover frequency (TOF) at a surface coverage of $\theta_{Zn} \approx 0.47$ ML, with the TOF being greater when using larger Cu particles.

The above examples highlight the potential of and interest in synthesizing and testing zinc-on-top-of-copper catalysts with ZnO surface coverages of approximately $\theta_{Zn} \approx 0.1$–0.2 ML. An atomic-scale synthesis technique, such as atomic layer deposition (ALD), is an efficient technique to reach this range of surface coverage. The ALD technique is based on the sequential use of self-terminating gas–solid reactions and can offer accurate atomic level control of the deposited metal concentrations [42,43]. To modify metal oxide interfaces, single atoms can be uniformly distributed on high surface area supports by ALD [43–45]. The first studies in atomic-scale synthesis (by ALD) toward CTM reaction have already been reported (e.g. ZrO_2-ALD on Cu/SiO_2 [46] and Ni-ALD on Cu nanoparticles on γ-Al_2O_3 [47]), bringing out the benefits of this technique to enhance the catalyst activity, selectivity and stability. In a recent publication, Saedy and coworkers [48] applied preferential chemical vapor deposition (PCVD) and incipient wetness impregnation in the synthesis of ZnO/Cu/Al_2O_3 catalysts for the CTM reaction. Zinc oxide introduced by the PCVD method on a prereduced copper phase resulted in a more active and selective catalyst compared to the impregnated catalyst [48]. By means of various diffraction, spectroscopic and microscopy characterization techniques, the investigators demonstrated a more efficient production of active/selective ZnO/Cu interfaces compared to the more traditional impregnation method [48]. Furthermore, the authors suggested that the inverse ZnO/Cu interface may result in a more active system than the conventional Cu/ZnO interface [48]. In a recent research [49], ZnO was added by ALD (323 K, diethylzinc as a precursor) on copper hydroxide nanowires and the size of ZnO was tuned from isolated species to nanoparticles by increasing the number of ZnO cycles from 1 to 20. The maximum methanol production rate was found after 3 cycles.

In this work, we focused on studying the catalytic performance of diverse copper-zinc oxide on zirconia catalysts for the hydrogenation of carbon dioxide to methanol. Atomic layer deposition (ALD) and incipient wetness impregnation were applied for the incorporation of Zn and Cu into the catalyst, respectively. Zn was deposited by ALD in one ALD cycle, which in practice should correspond to atomically dispersed ZnO species covering 10–20% of the surface (0.1–0.2 ML). By alternating the order in which Cu and Zn were attached to the catalyst, we created different metal-oxide configurations. A combination of various characterization techniques, such as diffuse reflectance infrared Fourier transform spectroscopy (DRIFTS), hydrogen temperature programmed reduction (H_2-TPR), carbon dioxide temperature programmed desorption (CO_2-TPD), X-ray photoelectron and absorption spectroscopy (XPS and XAS) and scanning transmission electron microscopy-energy-dispersive X-ray spectroscopy (STEM-EDS), DFT calculations and catalytic tests, led us to identify the most active configuration. We expect that the findings of this research shall enhance the understanding of the elemental features in the zinc oxide/copper/zirconia system and help to consider the location of zinc oxide (promoter) and copper (metal) as a crucial parameter to produce active sites for the efficient hydrogenation of carbon dioxide to methanol.

2. Experimental

2.1. Preparation of copper-zinc on zirconia samples

In total, five samples were synthesized: ZnO/ZrO_2, Cu/ZrO_2, ZnO/Cu/ZrO_2, Cu/ZnO/ZrO_2 and ZnO/Cu/ZnO/ZrO_2. The self-made samples were prepared following two different methods, depending on which metal was incorporated into the porous structure of the support (monoclinic zirconia, ZrO_2). Thus, Cu was added by incipient wetness impregnation (IWI), while Zn was added by atomic layer deposition (ALD). Monoclinic zirconia, provided by Saint-Gobain NorPro as cylindrical pellets (length 5 mm, diameter 3 mm) was used as a support material (surface area of 70 $m^2\ g^{-1}$). Prior to its utilization, ZrO_2 was crushed and sieved to a particle size of 250–420 μm and calcined in a muffle furnace (Nabertherm P330) in ambient air at 873 K for 5 h (10 K min^{-1}) to remove possible surface impurities. Cu nitrate trihydrate, Cu$(NO_3)_2$0.3 H_2O (CAS: 10031–43–3, Sigma Aldrich, 99–104% purity) and Zn acetylacetonate, Zn$(C_5H_7O_2)_2$0.3 H_2O (Zn$(acac)_2$, CAS: 14024–63–6, Volatec) were used as copper and zinc precursors, respectively. The targeted areal number density for Cu and Zn was 2 atoms/nm^2 (Zn/Cu atomic ratio of one). The Cu and Zn loadings in wt% measured by ICP–OES are shown in Table 1, and a scheme that shows the sequence of samples prepared is shown in Fig. 1.

For the impregnation of Cu by IWI, either on ZrO_2 or ZnO/ZrO_2, the corresponding amount of Cu precursor was dissolved in the exact amount of deionized water needed to fill the pore volume of the support. The water uptake capacity of the support (≈ 0.3 mL g^{-1}) was experimentally estimated by adding deionized water drop by drop to a known amount of dried support (393 K, 24 h). Approximately 3–5 drops of the Cu nitrate solution were added at a time to an Erlenmeyer flask

Table 1
List of samples containing the metal loadings of Cu and Zn measured by ICP–OES, the corresponding areal number density of Cu and Zn (metal atoms per nm^2), the amount of CO_2 desorbed determined by CO_2-TPD at 323 K and the number of reduction peaks and temperature at the maximum height of the peak determined by H_2-TPR.

		ICP–OES				CO_2-TPD			H_2-TPR
Sample	Code	Cu metal loading, wt%	Zn metal loading, wt%	Cu nm^{-2}	Zn nm^{-2}	μmol CO_2 $(g_{cat})^{-1}$	molecules CO_2 Zn^{-1}	molecules CO_2 nm^{-2}	Number of reduction peaks (temperature in K)
ZrO_2	Zr	n.a.	n.a.	n.a.	n.a.	95	n.a.	0.8	n.a.
ZnO/ZrO_2	Zn/Zr	n.a.	1.4	n.a.	1.9	96	0.45	0.8	n.a.
Cu/ZrO_2	Cu/Zr	1.3	n.a.	1.7	n.a.	63	n.a.	0.5	3 (405, 418, 477)
$ZnO/Cu/ZrO_2$	Zn/Cu/Zr	1.1	1.1	1.5	1.5	115	0.67	1.0	1 (418)
$Cu/ZnO/ZrO_2$	Cu/Zn/Zr	1.2	1.2	1.6	1.6	85	0.45	0.7	2 (448, 500)
$ZnO/Cu/ZnO/ZrO_2$	Zn/Cu/Zn/Zr	1.2	2.3	1.6	3.1	109	0.30	0.9	3 (431, 440, 475)

Fig. 1. Scheme of the samples synthesized and the sequence in which they were prepared. The calcination temperatures in each case were chosen for the effective removal of nitrates and $(acac)_2$ ligands, while minimizing the sintering of copper.

containing the dried support. Next, the partially wet support was first gently mixed, and then the flask was shaken for 2–3 min to ensure an even distribution of the solution. After adding the final drops of the solution, the slightly damp material was aged for 5 h at room temperature and dried overnight at 393 K in an oven under static air. Finally, the dried material was calcined at 673 K for 2 h (5 K min^{-1}) in a tube furnace with a constant flow of 100 mL min^{-1} of synthetic air (AGA 99.999% purity, 20% O_2, 80% N_2).

The deposition of Zn on ZrO_2 by ALD started by treating the calcined support in a flow-type fixed bed F-120 ALD reactor (ASM Microchemistry) at 523 K for 10 h to remove moisture before the actual ALD process. Then, the solid zinc acetylacetonate reactant was vaporized at 393 K in flowing nitrogen and reacted to the pretreated ZrO_2 support by one cycle of the ALD process for 3 h at 473 K and a pressure of ca. 3 mbar. Reactant-originated acetylacetonate ligands were removed by oxidative treatment in a tube furnace in synthetic air flow (100 mL min^{-1}) at 773 K for 2 h (5 K min^{-1}). The same procedure was followed when Zn was deposited on ZrO_2, Cu/ZrO_2 and $Cu/Zn/ZrO_2$. Fig. 2 shows a conceptual scheme with the configurations of the various copper-zinc-zirconia catalysts that were synthesized and tested in this research.

2.2. Catalyst characterization

The metal content of the catalysts was determined by inductively coupled plasma atomic emission spectroscopy (ICP–OES). Samples (ca 0.100 mg) were weighed in Teflon vessels, and a mixture of nitric acid (HNO_3, 65%, 2.5 mL) and hydrochloric acid (HCl, 37%, 7.5 mL) was added. Vessels were closed and placed in a microwave oven (Milestene, Ethos) and heated (1 h, 200 °C). After cooling, the samples were diluted with MQ-grade water, and the Cu- and Zn-contents were determined with an F-AAS instrument (Varian 220 F) using an air-acetylene burner.

The surface area and cumulative pore volume of zirconia were obtained by nitrogen physisorption isotherm (liquid nitrogen, 77 K) in a Thermo Scientific Surfer equipment. The support sample was weighted to a quartz glass burette (ca. 200 mg) and degassed at 573 K for 3 h. Specific surface area was calculated from the isotherm according to the Brunauer-Emmett-Teller (BET) method [50]. The cumulative pore

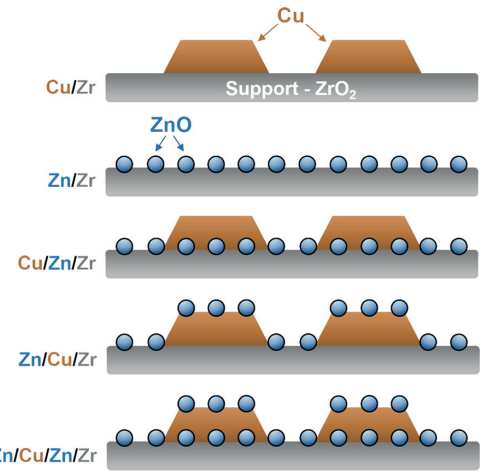

Fig. 2. Conceptual scheme of the various sample configurations prepared in this work.

volume was calculated based on the Barrett-Joyner-Halenda (BJH) method [51].

The phase/crystallinity of the support was studied by X-ray diffraction that was carried out on a ground sample in a PANanalytical X'Pert Pro MPD Alpha 1 device equipped with Cu Kα1 radiation (45 kV and 40 mA). The X-ray scanning range was from 10° to 100° (2θ) with a step size of 0.0131° and a time per step of 51 s. The results are shown in the supporting information (Fig. S1). The characteristic monoclinic phase (JCPDS 37–1484) was identified with main reflections at 24.5°, 28.3°, 31.5°, 34.2°, 35.4°, 40.8°, 49.3°, 50.2°, 54.1° and 55.5°.

The reducibility of the metal oxides was studied by hydrogen temperature-programmed reduction. The experiments were performed using an Altamira AMI-200 characterization system with a thermal conductivity detector (TCD) connected to an OmniStarTM mass spectrometer (MS) produced by Pfeiffer Vacuum. A total of 150 mg of sample was placed in a U-shaped quartz reactor and treated in constant He flow (AGA 99.999% purity) at 473 K for 60 min and cooled back to 303 K. The sample was then heated from 303 to 873 K or 1173 K in 2% H_2/Ar (AGA 99.999% purity) with a heating ramp of 5 K min^{-1}. The TPR measurement of ZrO_2 and ZnO/ZrO_2 was performed up to 1173 K, while 873 K was used as the maximum temperature for the Cu-containing samples. The TPR results are qualitative (given as arbitrary units) and the areas under the peaks cannot be compared with each other. The total gas flow was set at 50 mL min^{-1} (STP conditions) during the whole measurement.

Similarly, carbon dioxide desorption was studied by CO_2 temperature-programmed desorption. The experiments were performed using an Altamira AMI-200 characterization system with a TCD connected to an OmniStarTM MS produced by Pfeiffer Vacuum. A total of 150 mg of sample was placed in a U-shaped quartz reactor, treated in He flow at 473 K for 60 min, and cooled back to 303 K. Then, the sample was activated by heating the solid from 303 to 623 K in 2% H_2/Ar with a heating ramp of 10 K min^{-1} and 60 min hold time. The sample was then cooled to 323 K in He flow and maintained at that temperature for 30 min. Thereafter, the reduced sample was exposed to a constant flow of 10% CO_2/He (AGA 99.999% purity) for 30 min at 323 K and flushed for 60 min at the same temperature in He flow to remove the physisorbed CO_2. Finally, the sample was heated from 323 to 1073 K in He flow to desorb the chemisorbed CO_2. The possible desorbed products were continuously monitored during the experiment by mass spectrometry. The amount of CO_2 desorbed for each measurement was quantified by using calcium carbonate ($CaCO_3$) as an internal standard. About 4 mg of $CaCO_3$ was mixed with the sample and decomposed during the desorption step into CO_2 (g) and CaO (s) in the range of 800–950 K. The total gas flow was set at 50 mL min^{-1} (STP conditions) for all measurements.

The electronic structure of the samples was studied by high-energy-resolution fluorescence-detected X-ray absorption spectroscopy (HERFD-XAS). The experiments were performed at the ID20 beamline of the European Synchrotron Radiation Facility (ESRF, Grenoble, France) [52,53]. The beam was monochromated by a combination of a Si(111) premonochromator and a Si(311) channel-cut monochromator. The spectrometer was a von Hamos spectrometer based on three Si(333) crystal analyzers.

X-ray photoelectron spectroscopy (XPS) was used to study the surface composition of the reduced samples (623 K for 30 min, 2% H_2/Ar, transfer to XPS was done through air). The measurements were performed with a Kratos AXIS Ultra DLD X-ray photoelectron spectrometer using a monochromated AlKα X-ray source (1486.7 eV) run at 100 W. A pass energy of 80 eV and a step size of 1.0 eV were used for the survey spectra, while a pass energy of 20 eV and a step size of 0.1 eV were used for the high-resolution spectra. Photoelectrons were collected at a 90° take-off angle under ultra-high vacuum conditions, with a base pressure typically below 1×10^{-9} Torr. The diameter of the beam spot from the X-ray was 1 mm, and the area of analysis for these measurements was 300 μm x 700 μm. Both survey and high-resolution spectra were collected from three different spots on each sample surface in order to check for homogeneity and surface charge effects. All spectra were charge-corrected relative to the position of C-C bonding of adventitious carbon at 284.8 eV.

Scanning transmission electron microscopy high-angle annular dark-field (STEM-HAADF) images were acquired for the prereduced samples (623 K, 60 min, 50 mL min^{-1} of 2% H_2/Ar, STP conditions) by a JEOL JEM-2200FS double aberration corrected, high-resolution microscope, operated at 200 kV acceleration voltage. The chemical elemental mapping analysis was conducted with an X-ray energy-dispersive spectroscopy (EDS) detector. The samples were drop-casted using acetone onto a gold grid coated with an ultrathin holey carbon film.

The evolution of the surface species during the cyclic CO_2-H_2 adsorption was measured by diffuse reflectance infrared Fourier transform spectroscopy (DRIFTS) carried out in a Nicolet Nexus FTIR spectrometer with a high temperature/pressure Spectra-Tech reactor chamber equipped with a dome and ZnSe windows. The gas flow leaving the chamber was monitored with an OmniStar GSD 301 spectrometer by Pfeiffer Vacuum. The scans were collected from 4000 to 600 cm^{-1} at a scan resolution of 4 cm^{-1}. Prior to the experiment, a background spectrum was acquired under room conditions using an aluminum mirror in constant Ar flow. Approximately 20 mg of crushed sample powder was placed in the sample holder, heated from room temperature to 673 K in a constant flow of 10% O_2/N_2/Ar (synthetic air: AGA 99.999% purity, 20% O_2, 80% N_2; Ar: AGA 99.9999% purity) and kept there for 60 min to remove possible surface impurities. The temperature was then decreased to 623 K in the same atmosphere, and the gas was switched to 10% H_2/Ar (H_2: AGA 99.999% purity; Ar: AGA 99.9999% purity) and kept for 60 min to activate the metal oxides. The catalyst was then cooled to the desired reaction temperature, either 450, 500 or 550 K, and flushed with Ar for 30 min. The cyclic adsorption of CO_2-H_2 consisted of three consecutive full cycles of the following sequence: i) CO_2 adsorption for 12 min under flowing 10% CO_2/He (AGA 99.999% purity), ii) switching to Ar flow for 12 min, iii) switching to H_2 adsorption for 12 min under flowing 10% H_2/Ar and, iv) switching to Ar flow for 12 min. During each step within each cycle, a spectrum (100 scans, approximately 2 min) was recorded at 0, 5 and 10 min to monitor the surface of the catalyst with respect to time on stream. The total gas flow was set at 50 mL min^{-1} (STP conditions) during the whole experiment. A summary of the experimental conditions (timing, gases, flow rates, and temperatures) used for DRIFTS experiments is depicted in Fig. 3.

2.3. Computational methods

To assist infrared band identification, density functional theory (DFT) calculations were performed using the BEEF–vdW exchange–correlation functional [54] as implemented in the GPAW [55] software. The monoclinic zirconia was described by a two-layer-thick slab model, built from a 3 × 2 m-ZrO_2(111) supercell with periodic boundary conditions used in the lateral directions. The final cell measurements were 20.67 × 14.79 × 24.0 Å with angles of 90°/90°/116.5°. Cu(111) and stepped Cu(110) surfaces were modeled as three-layer periodic slabs, where the bottom layers were kept fixed in their bulk geometry in unit cells of 4 × 4 and 3 × 4, respectively. The core electrons of all elements were described by projector-augmented wave (PAW) [56] setups in the frozen-core approximation. A real–space grid basis was used with a maximum grid spacing of 0.2 Å. Periodic boundary conditions were used in two directions and the reciprocal space was sampled at the Γ point. A Hubbard U correction [57] of 2.0 eV was applied to the d–orbitals of the zirconium atoms. The atomic structures were optimized using the Fast Inertial Relaxation Engine (FIRE) algorithm as implemented in the Atomic Simulation Environment (ASE) [58,59] package until the maximum residual force was below 0.005 eV $Å^{-1}$. Vibrational frequencies for modes involving adsorbate and binding catalyst surface atoms were determined using the Frederiksen method [60]. The frequencies of the combined modes were obtained by adding up the frequencies of their individual contributions.

2.4. Activity tests in a continuous flow reactor

The catalytic performance was evaluated in a high-pressure continuous-flow fixed-bed equipped with a stainless-steel tube reactor with a mesh placed in the midsection of the reactor. One gram of calcined catalyst, sieved to 0.25–0.42 mm, was loaded in the reactor. Prior to the catalytic reaction, the catalyst was activated by in situ reduction at 623 K for 60 min with a constant flow of 10% H_2/N_2 (v/v; H_2: AGA 99.999% purity, N_2: AGA 99.999% purity). Activity tests were conducted at 450, 500 and 550 K with a total pressure of 3.0 MPa and a gas hourly space velocity (GHSV) of 7500 h^{-1} (STP conditions: 273.15 K and 1 bar). The reaction mixture was composed of H_2/CO_2/N_2 (~ 71/23/6, v/v/v; H_2: AGA 99.999% purity; CO_2, AGA: 99.995%; N_2: AGA 99.999% purity). The volumetric flows were 6.3 L h^{-1} of H_2, 2 L h^{-1} of CO_2 and 0.6 L h^{-1} of N_2 (STP conditions) and the volume of catalyst used per experiment was approximately 1.2 10^{-3} L. For each catalyst, the reaction temperature was increased in steps of 50 K. Initially, the reactor temperature was stabilized at 450 K and kept there for 90 min. Next, the temperature was increased to 500 K (10 K min^{-1}), stabilized, and kept there for another 90 min. Finally, the procedure was repeated for the highest temperature of 550 K. Thus, the data depicted in this manuscript were collected after 90 min under each operating condition. The unreacted gases and reaction products were continuously monitored

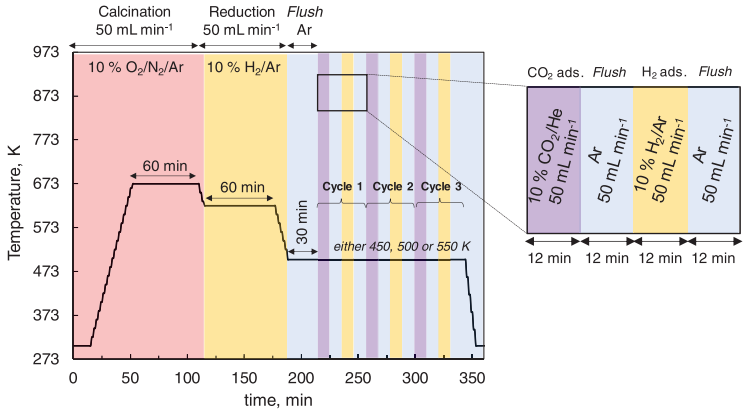

Fig. 3. Summary of the timing and experimental conditions used for the DRIFTS experiments. Heating and cooling ramps are estimates.

in an Agilent 490 Micro Gas Chromatograph (microGC) fitted with a thermal conductivity detector (TCD) and equipped with two columns: a) MS-5 molecular sieve for permanent gases H_2, N_2, CH_4 and CO and, b) PoraPLOT U for CO_2, CH_3OH and H_2O. The CO_2 conversion (X_{CO2}, Eq. 1) and product selectivity ($_{Si}$, Eq. 2) were calculated by internal normalization standard with N_2. The CO_2 conversion, the selectivity of CH_3OH, CO and CH_4 and the space-time yield of CH_3OH (STY_{CH3OH}, mmol h^{-1} g_{cat}^{-1}, Eq. 3) were calculated according to the following formulas:

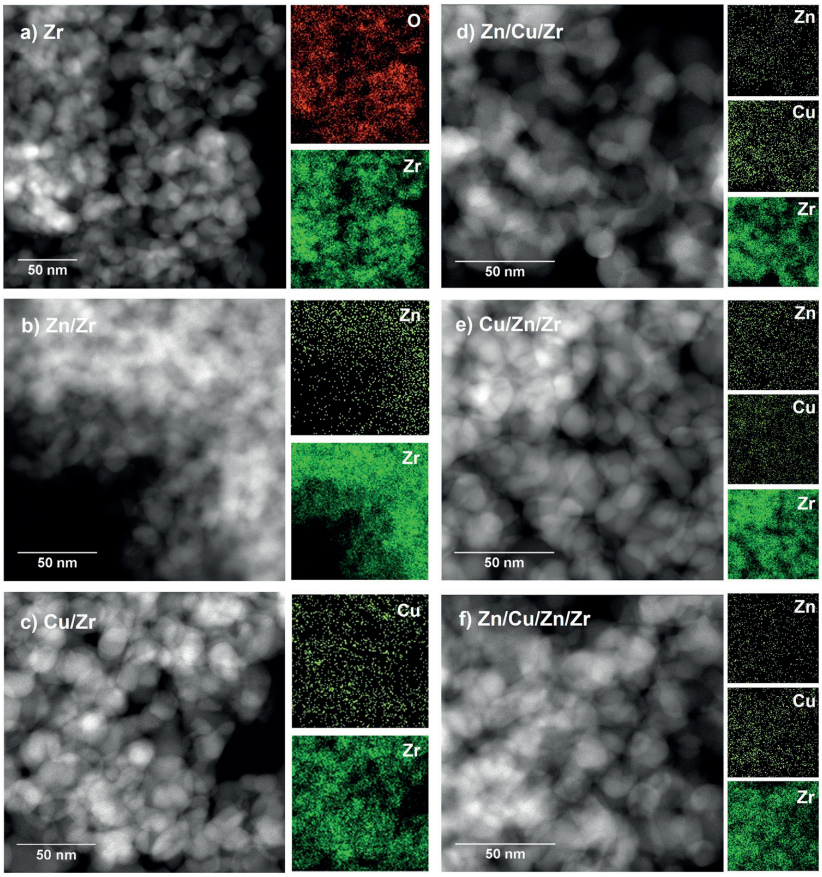

Fig. 4. STEM-HAADF images and energy-dispersive X-ray spectroscopy (EDS) mapping of different elements for Zr (a) and prereduced Zn/Zr (b), Cu/Zr (c), Zn/Cu/Zr (d), Cu/Zn/Zr (e) and Zn/Cu/Zn/Zr (f) samples.

$$X_{CO_2}(\%) = \frac{F_{CO2,in} - F_{CO2,out}}{F_{CO2,in}} * 100\% \quad (1)$$

$$S_i(\%) = \frac{F_{i,out}}{F_{CH3OH,out} + F_{CO,out} + F_{CH4,out}} * 100\% \quad (2)$$

$$STY_{CH_3OH}(\text{mmol h}^{-1}\text{g}_{cat}^{-1}) = \frac{F_{CO2,in} * X_{CO_2} * S_{CH_3OH}}{m_{cat}} \quad (3)$$

where F_{CO2} and F_i are the molar flow rates of CO_2 or products (CH_3OH, CO and CH_4) and m_{cat} is the mass of catalyst in grams.

3. Results and discussion

3.1. Characterization of fresh catalysts

The list of samples (support and self-made catalysts), the corresponding sample code used throughout the manuscript, the Cu and Zn metal loadings measured by ICP–OES and the Cu and Zn areal number density, the amount of CO_2 desorbed in the CO_2-TPD experiments and

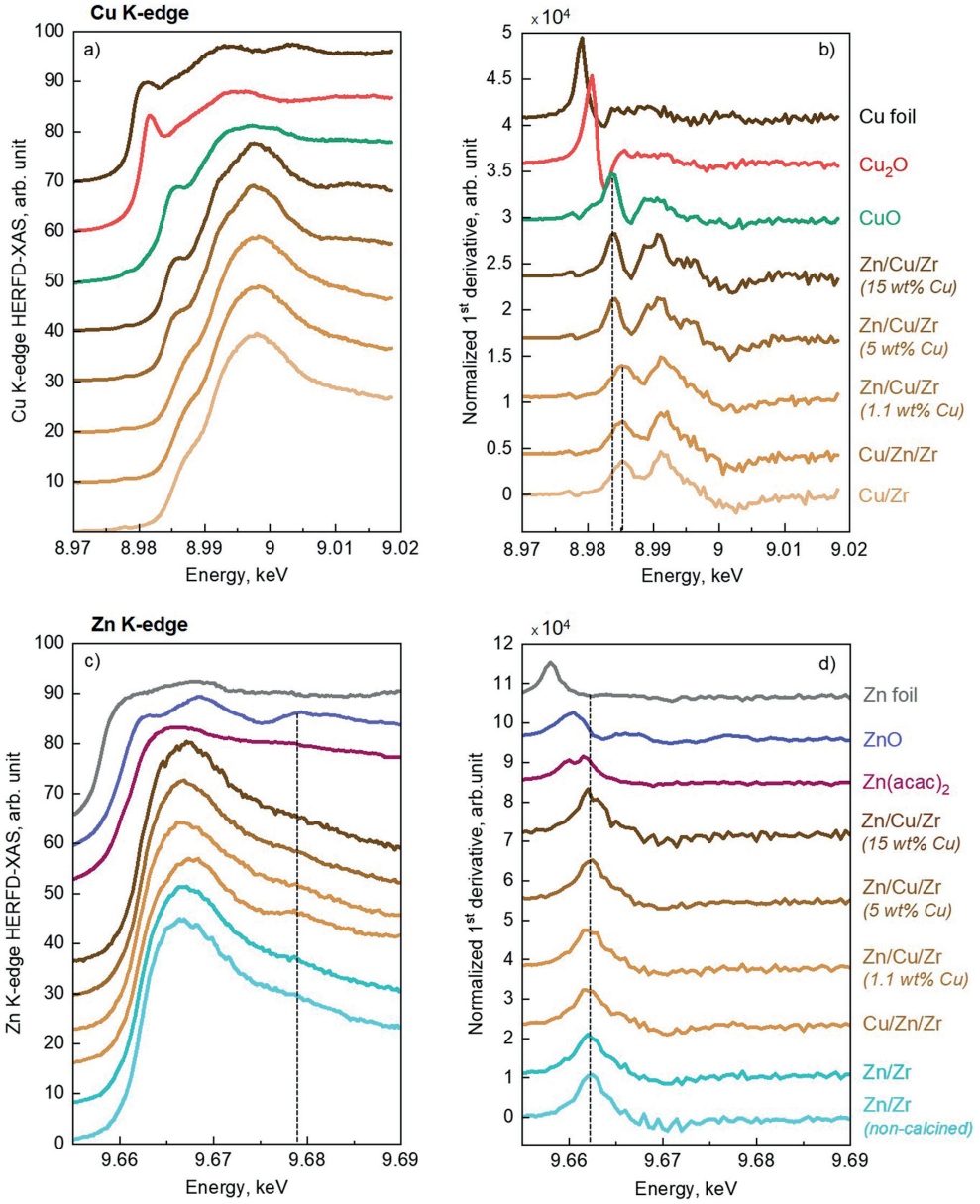

Fig. 5. Cu K-edge HERFD-XAS (a) and normalized first derivative (b) and, Zn K-edge HERFD-XAS (c) and normalized first derivative (d) for the self-made Cu-Zn on ZrO_2 samples. Cu foil, Cu_2O, CuO, Zn foil, ZnO and $Zn(acac)_2$ spectra were included as references.

the number of reduction peaks (for Cu-species) and temperature at the maximum height of the peak determined by H_2-TPR are listed in Table 1.

The STEM-HAADF images and EDS mapping of elements for the support and self-made samples are depicted in Fig. 4. Based on the results, the elements mapped for each sample seem to be evenly distributed throughout the samples and no high concentration spots were detected in any of the samples. The estimation of the Cu and Zn particle size distributions was impossible due to the poor contrast between Cu, Zn and Zr.

Also, the percentage of a monolayer of ZnO (% ML) was estimated as a ratio between the areal number density of ZnO in each sample (Zn atoms per nm^2, calculated from the Zn metal loadings measured by ICP–OES) and the average areal number density of Zn in one bulk ZnO monolayer obtained through equation reported elsewhere [42] (12.0 nm^{-2}, from ZnO density = 5.61 g cm^{-3}). According to these calculations, one Zn-ALD cycle (Zn/Zr, Cu/Zn/Zr and Zn/Cu/Zr samples) yielded approximately 15% of a bulk ZnO ML equivalent.

3.2. X-ray absorption spectroscopy (XAS)

The electronic structure (oxidation states) of copper and zinc was investigated by high-energy-resolution fluorescence-detected X-ray absorption spectroscopy (HERFD-XAS). The Cu and Zn absorbance at the Cu and Zn K-edges are depicted in Fig. 5 for the various catalysts and references (Cu foil, Cu_2O, CuO, Zn foil, ZnO and $Zn(acac)_2$). Along with the samples prepared and reported in Table 1, two more samples were prepared and analyzed: Zn/Cu/Zr (5 wt% Cu) and Zn/Cu/Zr (15 wt% Cu). These samples were synthesized to observe a possible effect of the Cu loading on the electronic structure of Cu and Zn. All the samples analyzed by HERFD-XAS were studied after the calcination treatment detailed under Section 2.1 (673 K or 773 K when Cu or Zn were added last, respectively), except a Zn/Zr sample that was also studied before the calcination step, i.e., after the Zn-ALD cycle.

Analyzing the Cu K-edge HERFD-XAS and first derivative (relative to incident energy) spectra (Fig. 5a-b) of the Zn/Cu/Zr samples with various Cu loadings, the spectra of the samples with 5 wt% and 15 wt% Cu were similar to that of CuO, which indicated a clearer presence of bulk CuO when increasing the Cu content. The characteristic edge transition for CuO can be observed at ca. 8.984 keV [32]. The rest of the samples (Zn/Cu/Zr with 1.1 wt% Cu, Cu/Zn/Zr and Cu/Zr) showed the absence of the first main shoulder that caused an apparent shift of the first peak of the derivative spectrum toward higher energies (Fig. 5b). The shoulder in CuO stems from 1 s to 4p transitions with a charge transfer from the ligand (1s13d10 _L_ final state, with _L_ denoting a ligand hole) [61,62]. This ligand effect decreases from CuO to the catalysts and it is typically absent in tetrahedral Cu(II) complexes [63]. The local coordination in bulk CuO is nearly square planar while the difference in the catalysts indicates a different local coordination in the surface-dominated Cu species. Thus, the pre-edge intensity (at 8.979 eV) decreases from CuO to the catalysts, indicating more likely an octahedral coordination in our samples, where the pre-edge is dipole-forbidden. However, the absence of the characteristic Cu^{1+} 1 s-4p transition feature at ca. 8.98 keV [63] indicates the absence of Cu_2O in any of the samples. Thus, it can be concluded that the Cu valence state seemed to be Cu^{2+} for all the catalysts.

For the Zn K-edge (Fig. 5c-d), the HERFD-XAS spectra and 1st derivative were very similar for all the samples, which suggests that the chemical environment for Zn is not significantly influenced either by the order in which Cu and Zn were added to the catalyst or by the Cu loading. Comparing the HERFD-XAS spectra of the samples with the ZnO (wurtzite) reference, there were significant differences; however, the presence of the Zn^{2+} oxidation state can be assumed. The peak at 9.679 eV present on ZnO reference, assigned to multiple scattering on atomic neighbors beyond the first shell [64], was not visible in any of the samples (except for a small peak observed on the Cu/Zn/Zr sample) which evidenced the presence of atomically dispersed ZnO species. It was computationally [64] and experimentally [49] demonstrated that ZnO XANES features are developed while increasing the number of ZnO atomic shells and, consequently, the ZnO cluster size. To the best of our understanding, it was expected that Zn was atomically dispersed as lone ZnO units with an oxidation state of Zn^{2+}.

3.3. X-ray photoelectron spectroscopy (XPS)

To complement the bulk structural-chemical information obtained by HERFD-XAS, the surface composition was analyzed by XPS. The samples were reduced ex situ and momentarily exposed to the atmosphere during the preparation before the analysis.

The elemental composition and the relative amount of the diverse zinc components are included in Table 2. The survey spectra of the samples in the range of 0–1200 eV are included in Fig. S2 and the high-resolution XPS spectra of the Zn 2p and Cu 2p regions are depicted in Fig. 6. As expected, all samples exhibited zirconium and oxygen, the relative amount of which decreased when adding other components (Table 2). The surface concentration of copper and zinc content measured by XPS varied between 2–4 and 3–7 at%, respectively, for the samples. The Zn/Cu atomic ratio was close to two for the samples with one ALD cycle of Zn and Cu by impregnation. Compared to the bulk atomic ratio of about one (see Table 1), the observed Zn/Cu ratio is consistent with zinc located on the surface and copper somewhat clustered. Addition of zinc on Cu/Zr decreased the surface concentration of copper, as expected (from 3.0 to 1.9 at% for Zn/Cu/Zr). According to XPS, the Cu/Zn/Zr sample had a higher surface concentration of both copper and zinc than the inverse Zn/Cu/Zr. While the reason for this observation is not fully clear, we speculate that it may have to do with the details of impregnation (zinc oxide is amphoteric [65] and the impregnation solution was acidic; part of the zinc may have dissolved and migrated to the outer surface during drying). Addition of zinc on Cu/Zn/Zr again decreased the surface concentration of copper (from 4.0 to 2.8 at% on Zn/Cu/Zn/Zr).

Taking a closer look at the high resolution XPS results, the Zn $2p_{3/2}$ region (Fig. 6a) could be deconvoluted to three different species of Zn^{2+}. These correspond to ZnO-like species (1021.5 eV) and Zn mixed state denoted *a* (1023.1 eV) and Zn mixed state denoted *b* (1024.4 eV). The presence of metallic zinc can be discarded due to the absence of a peak at a slightly lower binding energy (at ~ 1021 eV [66]). The highest fraction of zinc in ZnO-like species was in the Zn/Cu/Zr sample (over 85%). The Cu $2p_{3/2}$ region (Fig. 6b) showed the presence of Cu metal (Cu^0) and Cu^{2+} in all Cu-containing samples. Although the samples had been reduced before the XPS measurements, sample transfer through air to XPS had evidently been sufficient to oxidize part of the Cu^0 to Cu^{2+}.

Table 2
XPS-measured relative surface concentration of elements and relative amount of the different components of zinc.

Sample	Element, at%[a]					Zn/Cu ratio	Components of zinc, %	
	Zr 3d	Zn 2p	Cu 2p	O 1 s	C 1 s		ZnO	Zn mixed state *a* + *b*
Zr	31.9	0.0	0.0	53.7	12.6	–	0.00	0.00
Zn/Zr	30.6	2.9	0.0	52.8	12.5	–	69.8	27.4 + 2.8
Cu/Zr	30.9	0.0	3.0	51.6	13.6	–	0.00	0.00
Zn/Cu/Zr	28.3	3.6	1.9	51.2	14.3	1.9	86.7	12.5 + 0.8
Cu/Zn/Zr	23.1	7.1	4.0	50.1	15.3	1.8	72.3	22.2 + 5.5
Zn/Cu/Zn/Zr	25.3	7.0	2.8	49.4	14.9	2.5	73.0	21.8 + 5.2

[a] The remaining percentage in the elemental composition up to 100% corresponds to a small contamination of fluorine.

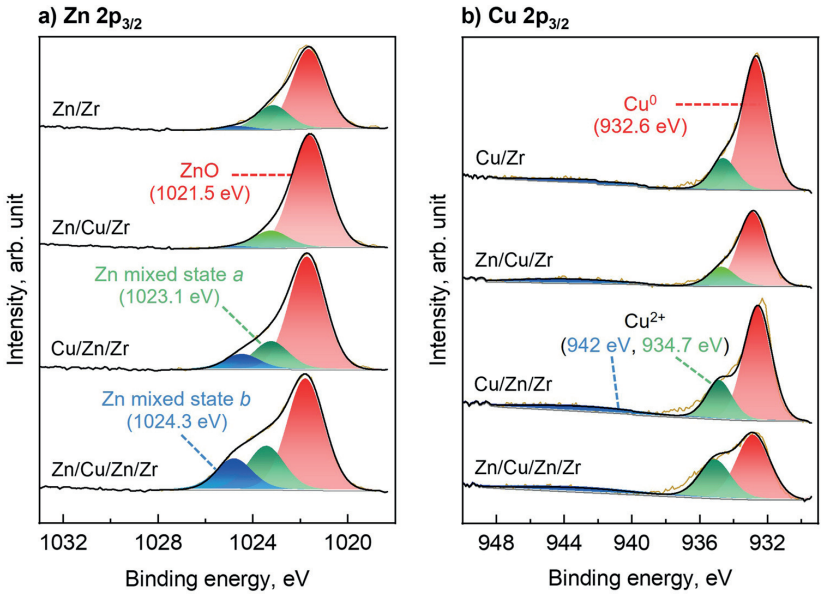

Fig. 6. High-resolution XPS spectra of the Zn 2p (a) and Cu 2p (b) regions for the self-made Cu-Zn on zirconia samples.

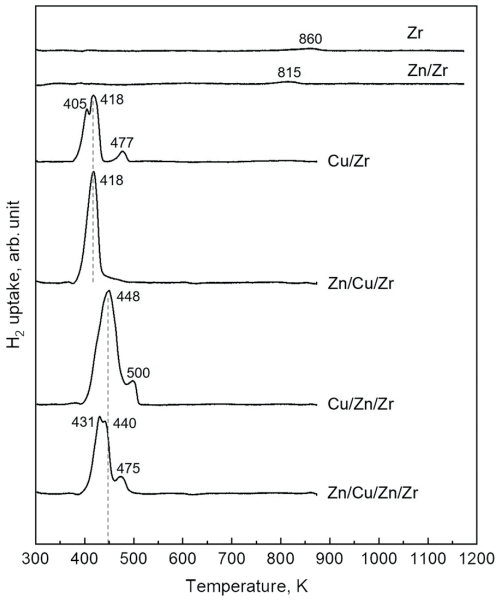

Fig. 7. Temperature-programmed reduction (H_2-TPR) profiles of zirconia support (Zr) and self-made Cu-Zn on zirconia samples. The samples are described in Table 1.

3.4. Temperature-programmed experiments

The reducibility of CuO was studied by H_2-TPR (hydrogen temperature-programmed reduction). The results are shown in Fig. 7. The reduction profiles for Zr and Zn/Zr samples are also shown in Fig. 7 as a reference. The Zr sample showed a very small and broad reduction peak with a maximum at 860 K that can be related to the formation of surface oxygen vacancies on the support [67,68]. On the Zn/Zr sample, a single reduction peak was found at 815 K, which can be associated with the partial reduction of the support and/or with the partial reduction of ZnO to metallic Zn [69,70].

The Cu-containing samples showed various reduction peaks in the range of 360–510 K, depending on the order in which Cu and Zn were incorporated into the support. Reduction of CuO in the Cu/Zr sample generated up to three reduction peaks: two overlapping peaks with maxima at 405 and 418 K and a third peak with a maximum at 477 K. The double reduction peak at relatively low temperatures (frequently named the α and β peaks [71–74]) has been previously reported in samples with relatively low CuO loadings of approximately 5 wt%. In accordance with these authors, well-dispersed Cu^{2+} species are first reduced to Cu^{+} (α-peak) and subsequently to Cu^{0} (β-peak). The third peak at higher temperature can be assigned to the reduction of more poorly dispersed bulk-like CuO particles or CuO particles with a stronger metal-support interaction [72,73,75].

The deposition of Zn on top of Cu/Zr (Zn/Cu/Zr sample) led to a partial improvement in the reducibility of CuO. The previously reported α and β peaks in the Cu/Zr sample merged into a single reduction peak at 418 K, while the reduction at 477 K in Cu/Zr shifted to a lower temperature. This latter observation suggests that the addition of Zn after Cu improved the dispersion of bulk CuO particles [19,76]. Surprisingly, when zinc was added by ALD before copper impregnation (Cu/Zn/Zr sample), higher reduction temperatures than in the Zn/Cu/Zr sample were observed with two reduction peaks at ca. 448 and 500 K, the latter presumably generated by the reduction of larger CuO particles. The positive effect of zinc addition after copper impregnation on the reducibility of bulk CuO is also observable in the Zn/Cu/Zn/Zr sample with a shift of the peak maximum from 500 to 475 K.

The CO_2-TPD (carbon dioxide temperature-programmed desorption) profiles of pure Zr and the self-made Cu-Zn on Zr samples are displayed in Fig. 8. Up to four different desorption peaks or desorption domains can be identified. The first two peaks (at ca. 380 and 445 K) can be assigned to weakly basic sites with different gas–solid interactions, while peaks at approximately 565 and 700 K can be attributed to moderate and strong basic sites, respectively [77,78]. Accordingly, the

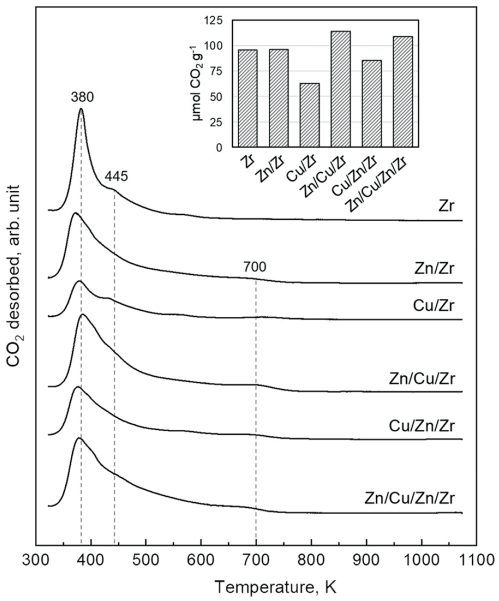

Fig. 8. Temperature-programmed desorption (CO_2-TPD) profiles of zirconia (Zr) support and self-made Cu-Zn on zirconia samples. The bar chart in the upper right corner shows the amount of CO_2 desorbed per gram of catalyst calculated with an internal standard ($CaCO_3$). The samples are described in Table 1.

desorption profile of pure Zr showed the presence of a significant amount of desorbed CO_2 in the range of 340–600 K with a main desorption peak at 380 K (most likely bicarbonate species on surface -OH groups) and a less significant and broader peak at 445 K. The addition of Cu and/or Zn resulted in the appearance of new desorption peaks at higher temperatures while the main peak at approximately 380 K became broader and less intense.

The amount of desorbed CO_2 (Table 1) followed the order (from higher to lower): Zn/Cu/Zr > Zn/Cu/Zn/Zr > Zn/Zr > Zr > Cu/Zn/Zr > Cu/Zr ranging from 115 to 63 μmol of CO_2 per gram of catalyst. In general, ZnO played an important role for the adsorption of CO_2, especially when it was introduced after copper. The deposition of ZnO on Cu/Zr sample (Zn/Cu/Zr sample) increased the total amount of adsorbed CO_2 from 63 to 115 μmol CO_2 g_{cat}^{-1} (~80% higher) while the deposition of ZnO on Cu/Zn/Zr (Zn/Cu/Zn/Zr sample) increased the adsorbed CO_2 from 85 to 109 μmol CO_2 g_{cat}^{-1} (~30% higher). This trend shows the benefits of the zinc-after-copper pair in promoting the adsorption capacity of the catalyst and the advantages of adding the Zn atoms after Cu. When the results were expressed as molecules of CO_2 per Zn atom (Table 1), Zn/Cu/Zr was still a superior catalyst (0.67 molecules of CO_2 per Zn atom); however, the Zn/Cu/Zn/Zr sample performed worse, turning out to be the catalyst with the lowest capacity among the Zn-containing catalysts (0.3 molecules of CO_2 per Zn atom). These results showed that Zn has an essential role in the adsorption of CO_2 but the amount of CO_2 and the Zn loading are not linearly correlated, the Zn/Cu/Zr being the preferred configuration to maximize the amount of adsorbed CO_2.

3.5. Evaluation of CO_2 and H_2 adsorption by DRIFTS

To understand the CO_2 and H_2 adsorption of Cu and Zn on ZrO_2, the surface species were monitored during three consecutive adsorption cycles of CO_2 and H_2 by in situ DRIFTS. To follow the catalyst surface with the experiment, representative spectra of the first and third cycles of adsorption are depicted in Fig. 9 in the fingerprint region (1700–1200 cm^{-1}). The results are shown for the studied catalysts at three temperatures (450, 500 and 550 K). The selected spectra in Fig. 9 show the surface species after either 5 or 10 min of a certain gas flow (CO_2, H_2 or Ar). In the supplementary material (Figs. S3-S7), monitoring with respect to time on stream (first five minutes of exposure to CO_2 and H_2) of the surface species during the first cycle of CO_2 and H_2 adsorption is displayed. An example of the evolution of several MS signals during the DRIFTS experiment carried out at 500 K with the Zn/Cu/Zr sample is displayed in Fig. S8.

The cyclic adsorption on the Zr sample (Fig. 9a) was considered to serve as a reference for the CO_2 and H_2 adsorption capabilities of the support material at various temperatures. After 10 min of CO_2 flow, the surface showed the presence of bicarbonate species, HCO_3 at ca. 1625, 1427 and 1220 cm^{-1} and bidentate carbonates CO_3^{2-} at ca. 1560–1530, and 1330 cm^{-1}, with the band positions exhibiting good agreement with the literature [79–82]. According to the literature, the presence of terminal -OH groups is required for the formation of bicarbonate species, while carbonates (either monodentate, bidentate or polydentate) require the presence of coordinately unsaturated (c.u.s.) Zr^{4+} and O^{2-} sites [79,80,82]. Experimentally, the highest intensity for bicarbonate species was observed at the lowest temperature (450 K), and the intensity decreased with increasing temperature, especially from 450 to 500 K. In contrast, the intensity of bidentate carbonate species was not significantly affected by the temperature of the experiment. The spectrum after one minute of CO_2 flow (Fig. S3) did not differ from the spectrum after 10 min, which indicated a rapid saturation of the surface with carbonate and bicarbonate species. After switching the gas flow from CO_2 to Ar, bicarbonate species vanished almost completely during 10 min of Ar purge. At 450 K, vibrational bands at ca. 1564 and 1330 cm^{-1} corresponding to bidentate carbonate species remained slightly visible, which suggested a stronger adsorption of these species to ZrO_2 compared to bicarbonate species. A similar observation was made by Kouva and coworkers [79] when studying the adsorption of CO_2 on ZrO_2 by DRIFTS in the range of 373–673 K. Both the first and third cycles of adsorption yielded comparable spectra with no apparent accumulation of any species throughout the experiment.

The incorporation of Zn atoms onto ZrO_2 by ALD (Zn/Zr sample, Fig. 9b) clearly modified the CO_2 adsorption capacity of ZrO_2. After 10 min of CO_2 exposure (either during the first or third cycle of adsorption), a crowded carbonate region (1600–1300 cm^{-1}) was observed. The vibrational band at 1220 cm^{-1} during the CO_2 flow indicated the presence of bicarbonate species, most likely on unsaturated Zr or Zn sites [83,84]. After 10 min of Ar purge after the first cycle of CO_2 adsorption, the spectra still displayed a busy carbonate region, indicating that Zn or the Zn-ZrO_2 interface can store CO_2-related species (especially carbonates at ca. 1535 cm^{-1}) with a greater adsorption strength than ZrO_2. The switch from Ar to H_2 flow led to the formation of new species such as formates (*$HCOO^-$) located at ca. 2966, 2873 (Fig. S4), 1575, 1379 and 1365 cm^{-1} (Fig. 9b), while the intensity of carbonate species (at ca. 1535 cm^{-1}) decreased in parallel. The formation of formate species was already visible after 1 min of H_2 flow (Fig. S4), which indicated a speedy hydrogenation of carbonates to formates on a Zn/Zr sample. In addition, more formates were clearly detected with increasing experimental temperature and number of adsorption cycles. This indicated: i) the ability of the Zn or Zn-ZrO_2 interface to accumulate carbonates during the CO_2 flow and to further convert them to formates, and ii) the high stability of formates on the Zn/Zr sample even at high temperature since they did not disappear or further react between cycles.

The computational and experimentally observed infrared vibrational frequencies for formate species are displayed in Table 3. The frequencies for formate species were computed on different model systems such as m-ZrO_2 (111), ZnO/m-ZrO_2 (111), Cu (111), and Cu (110). The model surfaces used in DFT calculations are displayed in Fig. S9. Additionally, the computed IR frequencies for possible intermediates, such as formic

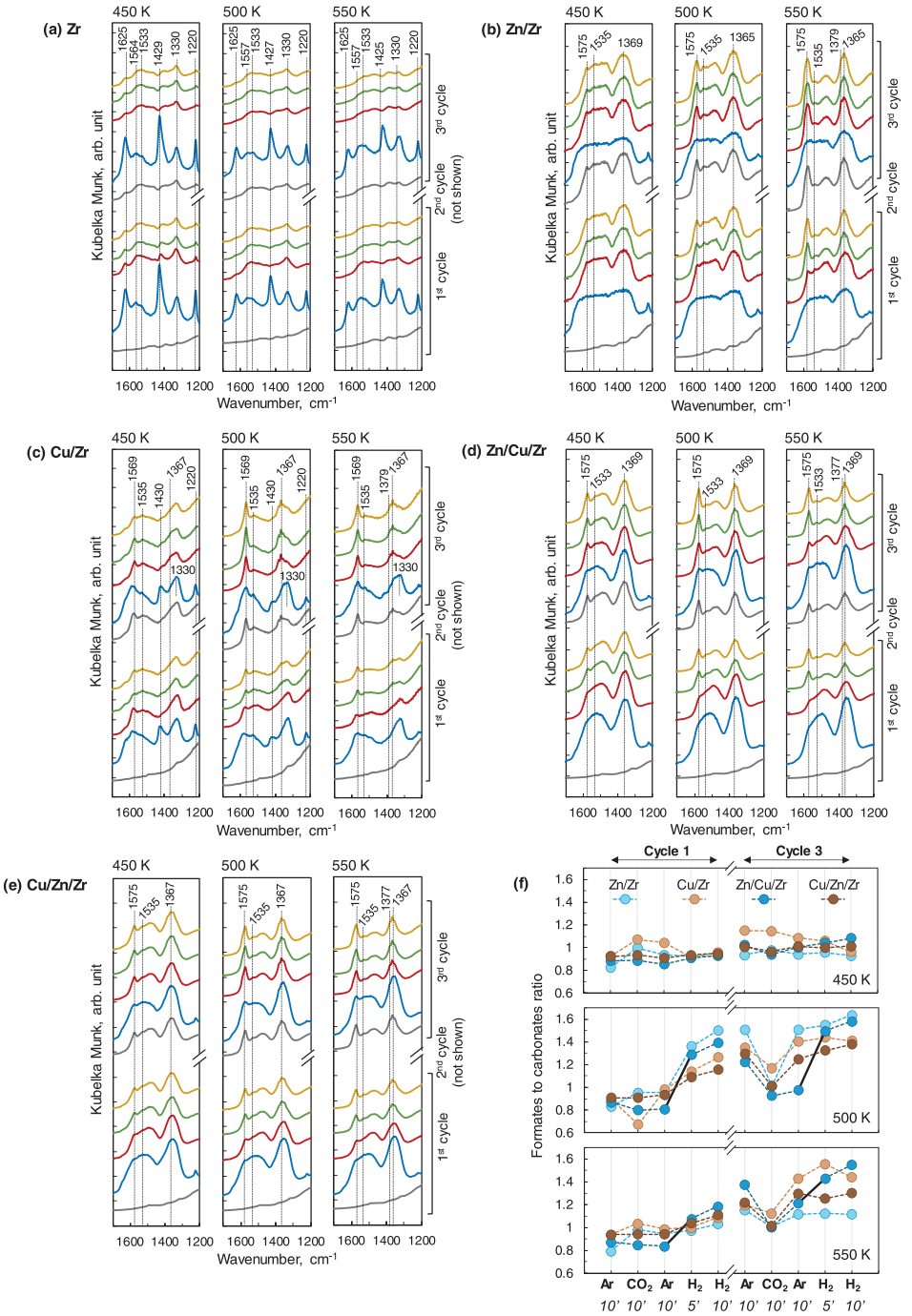

Fig. 9. DRIFT spectra of surface species in the 1700–1200 cm^{-1} (fingerprint) region during the 1st and 3rd cyclic adsorption of CO_2-H_2 with Ar purge in between for (a) Zr, (b) Zn/Zr, (c) Cu/Zr, (d) Zn/Cu/Zr and (e) Cu/Zn/Zr samples. Color coding: in Ar flow before switching to CO_2 flow (gray), after 10 min of CO_2 flow (blue), after 10 min Ar flow before switching to H_2 flow (red), after 5 min of H_2 flow (green), after 10 min of H_2 flow (yellow). (f) Formates (ca. 1575 cm^{-1}) to carbonate (ca. 1335 cm^{-1}) intensity ratio for each catalyst and different temperatures. Experimental conditions: 0.1 MPa; 450, 500 and 550 K; 50 mL min^{-1} (STP conditions) of: Ar during Ar purge; 10% CO_2/He during CO_2 flow; 10% H_2/Ar during H_2 flow. The results for the 1st and 3rd cycle of adsorption are presented.

Table 3
Comparison between experimental and DFT calculated infrared vibrational frequencies (in cm^{-1}) for formate species. Formates were calculated for m-ZrO_2, ZnO/m-ZrO_2, Cu (111) and Cu (110) systems.

Assignment	Experimental IR frequencies (cm^{-1})	Calculated IR frequencies (cm^{-1})			
		m-ZrO_2	ZnO/ m-ZrO_2	Cu (111)	Cu (110)
OCO-symmetric, υ_s(O-C-O)	Zn/Zr: 1365–1369 Cu/Zr: 1367 Zn/Cu/Zr: 1369 Cu/Zn/Zr: 1367	1323	1326	1307	1315
CH swing, bending δ(C-H)	Zn/Zr: 1379 Cu/Zr: 1379 Zn/Cu/Zr: 1377 Cu/Zn/Zr: 1377	1338	1358	1347	1358
OCO-asymmetric, υ_{as}(O-C-O)	Zn/Zr: 1575 Cu/Zr: 1569 Zn/Cu/Zr: 1575 Cu/Zn/Zr: 1575	1532	1535	1507	1524
CH strech, υ(C-H)	Zn/Zr: 2869 Cu/Zr: 2873 Zn/Cu/Zr: 2867 Cu/Zn/Zr: 2869	2981	2961	2970	2953

acid *HCOOH, carboxyl *COOH and dioxymethylene *H_2COO, which are intermediate species in methanol formation [19,85], are given in Figs. S10-S13. According to the DFT calculations, formate species produced four different bands on ZnO/ZrO_2 in the 3000–1200 cm^{-1} region that correspond to different functional groups and types of vibration. The bands were located at 1326, 1358, 1535 and 2961 cm^{-1}, and they correspond to symmetric stretch υ_s(O-C-O), bending δ(C-H), asymmetric stretch υ_{as}(O-C-O) and stretching υ(C-H), respectively. The experimental band at ca. 2970 cm^{-1} can be attributed to the combination of C-H bending and asymmetric O-C-O stretching modes [86].

The first cycle of CO_2 adsorption over the Cu/Zr sample (Fig. 9c) led to a less crowded fingerprint region compared to Zn/Zr sample. As for the Zr sample, the main species detected were bicarbonates (at ca. 1625, 1430 and 1220 cm^{-1}) and bidentate carbonates (at ca. 1557 and 1330 cm^{-1}): the bicarbonates were rapidly removed after 10 min of Ar purge. Additionally, according to the band observed at 1535 cm^{-1}, carbonates were present on the catalyst surface. Similar to the Zn/Zr sample (Fig. 9b), formates were formed during exposure to H_2; however, the position of the band of the O-C-O asymmetric vibration differed (1575 cm^{-1} on the Zn/Zr sample and 1569 cm^{-1} on the Cu/Zr sample). A lower IR frequency for formate species on Cu (111 and 110) compared to that on a Zn/Zr sample was also predicted by DFT calculations (Cu (111) vs. ZnO/m-ZrO_2, Table 3). After three consecutive cycles of CO_2 and H_2 adsorption, formates reached the highest intensity at 500 K, followed by 550 and 450 K. During the 3rd cycle of H_2 flow on the Cu/Zr sample, the intensity of formate species slightly decreased from 5 to 10 min on stream, which evidenced the strong adsorption of formate species on the Cu/Zr sample. Herein, by using a combined experimental and computational (DFT calculations) approach, Larmier and coworkers [85] found that on a Cu/ZrO_2 catalyst, formate species exhibit a low Gibbs free energy, which dictates their strong adsorption on the catalyst surface.

With Zn/Cu/Zr (Fig. 9d) and Cu/Zn/Zr (Fig. 9e) samples, the detected species and the discussed trends with respect to temperature and CO_2 and H_2 cycles displayed a combination of the results observed based on Zn/Zr and Cu/Zr samples. Thus, mainly due to the presence of Zn in both Zn/Cu/Zr and Cu/Zn/Zr samples, the fingerprint region was highly occupied by CO_2-related species after exposing the catalysts to CO_2. Formate was the main species detected after completing the cycles of adsorption of CO_2 and H_2, and no further hydrogenated species were observed (such as formic acid, *HCOOH, dioxymethylene, *H_2COO or methoxy, *H_3CO).

Based on the DRIFTS results discussed above, carbonates were present on all samples, and formate was the prevalent hydrogenated species in the selected experimental conditions. To compare the ability of each catalyst to hydrogenate carbonates into formates, a "formates to carbonates intensity ratio" was calculated and followed throughout the first to third cycles of adsorption for the various temperatures (Fig. 9f). Bands at 1535–1533 and 1575–1569 cm^{-1} were chosen as representative frequencies for carbonates and formates, respectively. Comparing the evolution of the ratio by temperature, clear trends could be observed at 500 and 550 K, while at 450 K, the ratio remained roughly constant at ca. 1 throughout cycles, which indicated a poor reduction of carbonates to formates at this temperature. At 500 and 550 K, the ratio was approximately 1.5 and 1.3, respectively, which pointed out the positive effect of temperature in the transformation of carbonates to formates. In all cases, the increase of the ratio originated from the concurrent decrease in the intensity of carbonate and the increase in the intensity of formate. At 500 K, the Zn/Zr sample yielded the highest ratios at the end of each cycle which indicated the crucial role of the ZnO-ZrO_2 interface to form formate from carbonate. Especially outstanding was the increase of the ratio for the Zn/Cu/Zr sample at 500 and 550 K when hydrogen was introduced into the system (increase highlighted with solid black in lines in Fig. 9f). This behavior revealed the good ability of the Zn/Cu/Zr configuration in the hydrogenation of carbonate to formate. In addition, the Zn/Cu/Zr was the unique sample that exhibited a rising ratio during H_2 flow under any condition. This indicated that the Zn/Cu/Zr configuration was able to remain active in the transformation of carbonate to formate during the 10 min of H_2 flow, presumably due to a greater ability to keep CO_2 adsorbed, as observed in Fig. 8.

3.6. Catalytic performance evaluation

The catalytic performance of Cu-Zn on zirconia catalysts is illustrated in Fig. 10 for the three selected reaction temperatures: 450, 500 and 550 K. Fig. 10a shows the CO_2 conversion, Fig. 10b-c show the production of CH_3OH expressed as the space-time yield in $mmol_{CH3OH}\ g_{cat}^{-1}\ h^{-1}$ and in $mmol_{CH3OH}\ g_{Cu}^{-1}\ h^{-1}$, respectively, and Fig. 10d shows the product selectivity for CH_3OH, CO and CH_4. Among the three reaction temperatures tested, all the catalysts showed activity at 500 and 550 K, while there was no measurable activity at 450 K. Greater CO_2 conversion values were achieved for all the samples with increasing reaction temperature. The CO_2 conversion values attained with both Cu- and Zn-containing samples, i.e., Zn/Cu/Zn/Zr, Zn/Cu/Zr and Cu/Zn/Zr, were higher than those achieved with Zn/Zr, Cu/Zr and Zr samples, which evidenced the importance of the Cu-Zn interactions in the CO_2 hydrogenation reaction in accordance with the literature [18,19,87]. Interestingly, the addition of Zn on top of Cu (Zn/Cu/Zr and Zn/Cu/Zn/Zr samples) promoted CO_2 conversion, and the most remarkable improvement occurred at 550 K, with conversion values of approximately 9% for Zn/Cu/ZrO_2 and 6.5% for Zn/Cu/Zn/ZrO_2. Under the same operating conditions, the other samples (Cu/Zn/Zr, Cu/Zr and Zn/Zr) yielded CO_2 conversion values between 2% and 4%.

Regarding the product selectivity (Fig. 10d), temperature had a remarkable effect on the product distribution. At 500 K, the prevailing product was methanol with all catalyst combinations (except on the Zr sample, which only produced CO). Thus, the highest CH_3OH selectivity was achieved at 500 K with Zn/Cu/Zn/Zr sample (close to 80%) followed by Zn/Cu/Zr (71%) and Cu/Zn/Zr (68%) samples. The selectivity toward CO increased significantly when increasing the temperature from 500 to 550 K, according to the endothermicity of the reverse-WGS reaction ($\Delta H^{\circ}_{298k} = +41\ kJ\ mol^{-1}$) [88]. Advantageously, the Zn/Cu/Zr sample did not produce any methane under any of the conditions, in contrast to the Zn/Cu/Zn/Zr and Cu/Zn/Zr samples that produced methane at both 500 and 550 K with selectivities around 3–6%.

In terms of methanol production (Fig. 10b-c), the most efficient catalysts were Zn/Cu/Zn/Zr and Zn/Cu/Zr, with similar production rates at 500 K (~ 1.9 $mmol_{CH3OH}\ g_{cat}^{-1}\ h^{-1}$) and 550 K (~

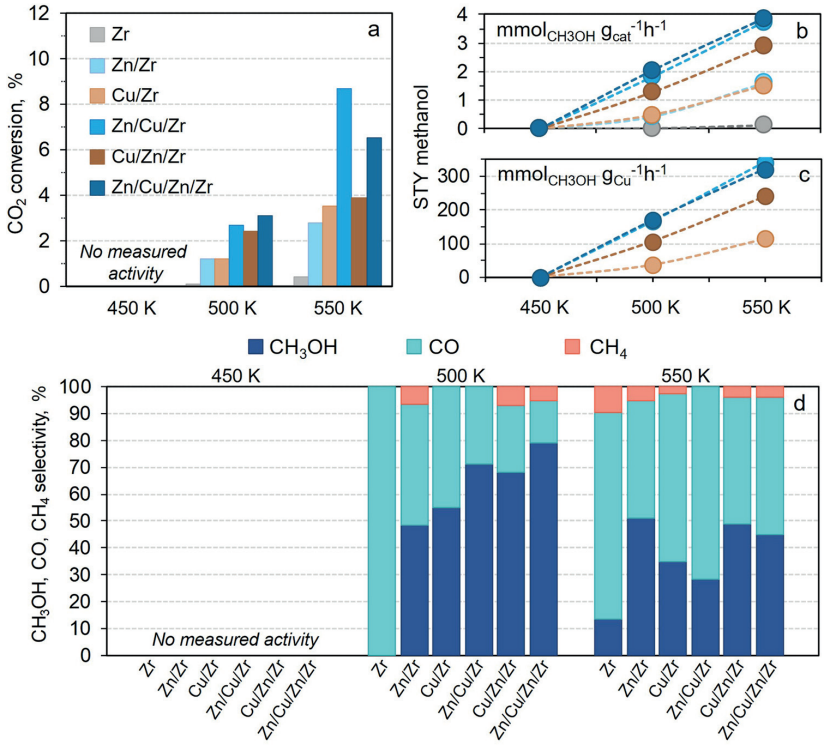

Fig. 10. CO_2 conversion (a), CH_3OH space-time yield in $mmol_{CH3OH}\ g_{cat}^{-1}h^{-1}$(b), CH_3OH space-time yield in $mmol_{CH3OH}\ g_{Cu}^{-1}h^{-1}$ (c), and CH_3OH, CO and CH_4 selectivity (d) for each catalyst. Experimental conditions: 3.0 MPa; 450, 500 and 550 K; reaction mixture composed of $H_2/CO_2/N_2$ (71/23/6, v/v/v); gas hourly space velocity (GHSV) of 7500 h^{-1}. The data were collected after 90 min under the given operating conditions.

3.8 $mmol_{CH3OH}\ g_{cat}^{-1}\ h^{-1}$). For Cu/Zn/Zr sample, the methanol production was lower (1.3 and 2.9 $mmol_{CH3OH}\ g_{cat}^{-1}\ h^{-1}$ at 500 and 550 K, respectively). Moreover, Zn/Cu/Zr and Zn/Cu/Zn/Zr samples showed a space-time yield of methanol approximately three times higher than that achieved with Cu/Zr and Zn/Zr samples. When the methanol production was referred to in terms of grams of copper (Fig. 10c), the Zn/Cu/Zr sample produced 165 and 340 $mmol_{CH3OH}\ g_{Cu}^{-1}\ h^{-1}$ at 500 and 550 K (similar rates were attained with the Zn/Cu/Zn/Zr sample), while the Cu/Zn/Zr sample produced 107 and 241 $mmol_{CH3OH}\ g_{Cu}^{-1}\ h^{-1}$ under the same operating conditions. Therefore, the activity results highlight the potential interest of adding Zn by atomic layer deposition after Cu to promote methanol production catalysis.

3.7. On the impact of zinc promoter produced by ALD on carbon dioxide hydrogenation to methanol

The presence of zinc oxide overlayers on top of copper particles in industrial-type $Cu/ZnO/Al_2O_3$ catalysts during the hydrogenation of carbon oxides to methanol has been demonstrated in diverse studies during the last decade [11,89,90]. Schott *et al.* [91] reported the unique properties of ZnO layers on the surface of copper particles due to the partial reduction of ZnO to a less strongly oxidized $Zn^{\delta+}$ state under the reducing conditions of methanol synthesis. Similarly, Behrens and collaborators [11] demonstrated that the Cu-ZnO synergy lies in their strong metal support interaction leading to partial coverage of the copper surface with ZnO_x under reducing (activation) conditions. Thus, ZnO nanoparticles dispersed on top of copper are special entities that could show particular physico-chemical properties not observed for bulk oxides [38,89,92].

As previously described in the introduction there seems to be agreement among scholars in setting the optimal coverage of copper particles by ZnO_x for a higher catalytic activity at relatively low values of 15–20% monolayer (ML) [19,38,40]. Nevertheless, higher coverages ($\theta_{Zn} = 0.47$) have also been reported as optimal values [41]. Although this difference is not fully understood, all of these studies agree that larger coverages of ZnO may negatively affect the catalyst activity in terms of methanol production [19,38,40,41]. Furthermore, the computational studies carried out by Kuld and coworkers [41] predicted a greater TOF of methanol for ZnO particles smaller than 7 nm, sizes that can be easily accomplished by ALD. Based on our results, we observed that zinc added by one ALD cycle yielded ~15% ML of ZnO, while we speculate that Cu formed larger structures from nanoparticles to small clusters. Based on this remark, the addition of copper by impregnation after zinc ALD might have disabled some of the ZnO species and prevented their assistance in any further reaction. This speculation is supported by the similar methanol production rates observed for Zn/Cu/Zr and Zn/Cu/Zn/Zr samples.

To place these arguments and calculations on a more solid basis, we have compared the results included in this manuscript with the results reported in the literature for earlier studies (Table 4). In our work, with the Zn/Cu/Zr sample, we report rates of 165 and 340 $mmol_{CH3OH}\ g_{Cu}^{-1}h^{-1}$ at 500 and 550 K, respectively, while 169 and 321 $mmol_{CH3OH}\ g_{Cu}^{-1}h^{-1}$ were produced with the Zn/Cu/Zn/Zr sample under the same temperature conditions. Recently, Saedy *et al.* [48] accomplished a methanol productivity of ~ 56 $mmol_{CH3OH}\ g_{Cu}^{-1}h^{-1}$ at 523 K and 3.0 MPa with a $ZnO/Cu/Al_2O_3$ catalyst (Zn added by PCVD) and a Zn/Cu atomic ratio of 0.5. Higher Zn/Cu atomic ratios (up to 1.64) did not significantly affect the production of methanol. It is also important

Table 4
Summary table comparing the areal number density (Zn atoms nm^{-1}), % monolayer of ZnO, experimental conditions (pressure and temperature), CO_2 conversion, methanol selectivity and space-time yield of methanol ($mmol_{CH3OH}\ g_{Cu}^{-1}h^{-1}$) of the Zn-Cu-containing samples presented in this work and other literature values for similar studies. A H_2/CO_2 molar ratio of approximately 3 was used in all the studies reported in this table.

Catalyst	Synthesis method	Areal number density, Zn atoms nm^{-1}	% of monolayer (ML) of ZnO	P, MPa	T, K	X_{CO2}, %	S_{CH3OH}, %	STY, $mmol_{CH3OH}\ g_{Cu}^{-1}h^{-1}$	Ref.
Zn/Zr sample	ALD	1.9	16%	3.0	500 550	1.2% 2.8%	48.5% 51%	n.a.	Present work
Cu/Zr sample	IWI	n.a.	n.a.	3.0	500 550	1.2% 3.5%	55% 35%	37 115	Present work
Cu/Zn/Zr sample	ALD	1.6	14%	3.0	500 550	2.4% 3.9%	68% 49%	107 241	Present work
Zn/Cu/Zr sample	ALD	1.5	13%	3.0	500 550	2.7% 8.7%	71% 28.5%	165 340	Present work
Zn/Cu/Zn/Zr sample	ALD	3.1	27%	3.0	500 550	3.1% 6.5%	79% 45%	169 321	Present work
$ZnO/Cu/Al_2O_3$	PCVD (zinc deposition time, 2 h)	~1.2	~10%	3.0	523	ca. 1.2%	ca. 65%	56	Saedy *et al.* [48]
$ZnO/Cu/Al_2O_3$	PCVD (zinc deposition time, 9 h)	~4.4	~37%	3.0	523	ca. 1.3%	ca. 60%	ca. 55	Saedy *et al.* [48]
$ZnO/Cu/SiO_2$	ALD	~0.6	~5%	4.0	523	–	10.1%	10.6	Gao *et al.* [27]

to highlight that we achieved a similar areal number density and % of ML of ZnO for the Zn/Cu/Zr sample to those reported by Saedy *et al.* (~ 1.5 Zn atoms/nm^2, ~ 13% ML). In a similar study, Gao *et al.* [27] synthesized ALD ZnO-coated Cu/SiO_2 catalysts with various exposure times and ALD cycles and tested them in the hydrogenation of carbon dioxide. Among the prepared catalysts, the most active catalyst (exposure time of 30 s to the Zn precursor and one ALD cycle) was more selective toward carbon monoxide (96 $mmol_{CO}\ g_{Cu}^{-1}h^{-1}$) than toward methanol (10.6 $mmol_{CH3OH}\ g_{Cu}^{-1}h^{-1}$) at 523 K and 4.0 MPa. However, for that particular $ZnO/Cu/SiO_2$ catalyst, the areal number density was significantly lower than the value that we report in our manuscript (~ 0.6 Zn atoms/nm^2, ~ 5% ML).

In general, the data included in Table 4 highlight the good performance of the catalysts prepared and tested in the present work for carbon dioxide hydrogenation to methanol. It is worth mentioning that this level of activity was achieved with relatively low Cu and Zn metal loadings (~1–2 wt%) which led to considerably high methanol production rates when they were expressed per gram of copper. This range of metal contents seemed to be relatively efficient to achieve a good and even distribution of both copper and zinc and to produce a significant amount of active ZnO-Cu sites. As a future challenge, it would be worth investigating whether it is viable to obtain similar methanol production rates per gram of copper with higher metal contents. In this context, atomic layer deposition (ALD) can be an outstanding synthesis method for the scale up of catalysts toward higher metal loadings.

4. Conclusions

Tuning the interaction of zinc and copper must be considered an important parameter to control the catalytic performance toward methanol formation. In this work, by alternating the order in which metal (copper) and promoter (zinc) were added to the catalyst, a series of catalysts with various metal-promoter-support configurations were synthesized. The order in which the zinc promoter was introduced onto the catalyst by atomic layer deposition (ALD) compared to the active copper metal by impregnation affected the catalytic activity. Zinc ALD after copper impregnation (zinc-on-copper) yielded higher CO_2 conversion and methanol production rates than copper-on-zinc, although the overall copper and zinc loadings were similar. Advantageously, unlike the other catalysts, the zinc-on-copper zirconia catalyst (Zn/Cu/Zr sample) did not produce any methane with high methanol production rates under the tested operating conditions.

Infrared studies of cyclic adsorption of CO_2 and H_2 revealed that zinc ALD on impregnated copper accumulated carbonates and bicarbonates (CO_3^{2-}, HCO_3^-) exceptionally well during the carbon dioxide feed and transformed them into formate species (*HCOO) during the hydrogen feed. Together with the higher CO_2 conversion and methanol production rate achieved with the Zn/Cu/Zr sample, this suggests that the catalytic activity to some extent relies on the ability of the catalyst to transform carbonates to formates. The DFT calculations accurately predicted the band position for formate species on different model surfaces (i.e, ZnO/ZrO_2, Cu(111) and Cu(110)) compared to the experimental bands observed by DRIFTS. The formate pathway was the favored mechanistic route of carbon dioxide hydrogenation to methanol under the selected experimental conditions. In addition, the CO_2 temperature programmed desorption analyses showed the great capacity of the zinc-copper on zirconia catalyst for the adsorption of CO_2. When evaluating the molecules of CO_2 adsorbed per atom of zinc, the zinc-on-copper configuration adsorbed more CO_2 molecules than the copper-on-zinc configuration (0.67 versus 0.45 molecules CO_2 per zinc atom). Additionally, according to TPR studies, the zinc deposited after copper impregnation improved the homogeneity of copper oxide species and the reducibility of the bulk CuO.

Overall, this work provides insight into the significance of the zinc oxide/copper/zirconia interactions for selective hydrogenation of carbon dioxide to methanol and highlights the potential of atomic layer deposition (ALD) in the synthesis of atomically dispersed metal catalysts for an efficient methanol synthesis.

CRediT authorship contribution statement

Aitor Arandia: Conceptualization, Investigation, Methodology, Formal analysis, Validation, Visualization, Supervision, Writing – original draft, Writing – review & editing. **Jihong Yim**: Investigation, Methodology, Formal analysis, Validation, Writing – review & editing. **Hassaan Warraich**: Investigation, Formal analysis, Methodology. **Emilia Leppäkangas**: Investigation, Methodology. **René Bes**: Investigation, Formal analysis, Writing – review & editing. **Aku Lempelto**: Investigation, Software, Formal analysis, Visualization, Writing – review & editing. **Lars Gell**: Investigation, Software, Formal analysis, Visualization, Writing – review & editing. **Hua Jiang:** Investigation. **Kristoffer Meinander**: Investigation, Formal analysis, Visualization, Writing – review & editing. **Tiia Viinikainen**: Methodology, Writing – review & editing. **Karoliina Honkala**: Conceptualization, Writing – review & editing, Funding acquisition. **Simo Huotari**: Investigation, Formal analysis, Visualization, Writing – review & editing. **Riikka L. Puurunen**: Conceptualization, Methodology, Resources, Writing – review & editing, Supervision, Project administration, Funding acquisition.

Declaration of Competing Interest

The authors declare that they have no known competing financial interests or personal relationships that could have appeared to influence the work reported in this paper.

Data Availability

Data will be made available on request.

Acknowledgements

The work at Aalto University has been financially supported by the Academy of Finland (COOLCAT consortium, decision no. 329977 and 329978; ALDI consortium, decision no. 331082). This work made use of Aalto University Bioeconomy, OtaNano and RawMatters infrastructure. Hannu Revitzer (Aalto University) is thanked for the ICP-OES analysis, Aalto workshop people (especially Seppo Jääskeläinen) for working on the reactor modifications. The DFT calculations were made possible by computational resources provided by the CSC — IT Center for Science, Espoo, Finland (https://www.csc.fi/en/) and computer capacity from the Finnish Grid and Cloud Infrastructure (urn:nbn:fi:research-infras-2016072533). The University of Helsinki acknowledges support from Academy of Finland (project 295696) as well as ESRF for beamtime and Blanka Detlefs and Christoph Sahle for expert support. Preliminary XANES measurements were performed using the Helsinki Center for X-ray Spectroscopy Hel-XAS instrument under the proposal number 2021–0011.

Appendix A. Supporting information

Supplementary data associated with this article can be found in the online version at doi:10.1016/j.apcatb.2022.122046.

References

[1] T.A. Atsbha, T. Yoon, P. Seongho, C.J. Lee, A review on the catalytic conversion of CO_2 using H2 for synthesis of CO, methanol, and hydrocarbons, J. CO_2 Util. 44 (2021), 101413, https://doi.org/10.1016/j.jcou.2020.101413.
[2] J. Zhong, X. Yang, Z. Wu, B. Liang, Y. Huang, T. Zhang, State of the art and perspectives in heterogeneous catalysis of CO_2 hydrogenation to methanol, Chem. Soc. Rev. 49 (2020) 1385–1413, https://doi.org/10.1039/c9cs00614a.
[3] S. Roy, A. Cherevotan, S.C. Peter, Thermochemical CO_2 hydrogenation to single carbon products: scientific and technological challenges, ACS Energy Lett. 3 (2018) 1938–1966, https://doi.org/10.1021/acsenergylett.8b00740.
[4] J. Andersson, A. Krüger, S. Grönkvist, Methanol as a carrier of hydrogen and carbon in fossil-free production of direct reduced iron, Energy Convers. Manag. X. 7 (2020), 100051, https://doi.org/10.1016/j.ecmx.2020.100051.
[5] O.Y.H. Elsernagawy, A. Hoadley, J. Patel, T. Bhatelia, S. Lim, N. Haque, C. Li, Thermo-economic analysis of reverse water-gas shift process with different temperatures for green methanol production as a hydrogen carrier, J. CO_2 Util. 41 (2020) 101280–101289, https://doi.org/10.1016/j.jcou.2020.101280.
[6] S.S. Araya, V. Liso, X. Cui, N. Li, J. Zhu, S.L. Sahlin, S.H. Jensen, M.P. Nielsen, S. K. Kær, A review of the methanol economy: the fuel cell route, Energies 13 (2020) 596–627, https://doi.org/10.3390/en13030596.
[7] S. Verhelst, J.W. Turner, L. Sileghem, J. Vancoillie, Methanol as a fuel for internal combustion engines, Prog. Energy Combust. Sci. 70 (2019) 43–88, https://doi.org/10.1016/j.pecs.2018.10.001.
[8] T. Li, T. Shoinkhorova, J. Gascon, J. Ruiz-Martinez, Aromatics production via methanol-mediated transformation routes, ACS Catal. 11 (2021) 7780–7819, https://doi.org/10.1021/acscatal.1c01422.
[9] S. Ren, X. Fan, Z. Shang, W.R. Shoemaker, L. Ma, T. Wu, S. Li, N.B. Klinghoffer, M. Yu, X. Liang, Enhanced catalytic performance of Zr modified CuO/ZnO/Al2O3 catalyst for methanol and DME synthesis via CO_2 hydrogenation, J. CO_2 Util. 36 (2020) 82–95, https://doi.org/10.1016/j.jcou.2019.11.013.
[10] I. Abbas, H. Kim, C.H. Shin, S. Yoon, K.D. Jung, Differences in bifunctionality of ZnO and ZrO2 in Cu/ZnO/ZrO2/Al2O3 catalysts in hydrogenation of carbon oxides for methanol synthesis, Appl. Catal. B Environ. 258 (2019) 117971–117981, https://doi.org/10.1016/j.apcatb.2019.117971.
[11] M. Behrens, F. Studt, I. Kasatkin, S. Kühl, M. Hävecker, F. Abild-pedersen, S. Zander, F. Girgsdies, P. Kurr, B.-L. Kniep, M. Tovar, R.W. Fischer, J.K. Nørskov, R. Schlögl, The Active Site of Methanol Synthesis over Cu/ZnO/Al2O3 Industrial Catalysts, Science 336 (2012) 893–897, https://doi.org/10.1126/science.1219831.
[12] L.C. Grabow, M. Mavrikakis, Mechanism of methanol synthesis on cu through CO_2 and CO hydrogenation, ACS Catal. 1 (2011) 365–384, https://doi.org/10.1021/cs200055d.
[13] S.G. Jadhav, P.D. Vaidya, B.M. Bhanage, J.B. Joshi, Catalytic carbon dioxide hydrogenation to methanol: a review of recent studies, Chem. Eng. Res. Des. 92 (2014) 2557–2567, https://doi.org/10.1016/j.cherd.2014.03.005.
[14] G.C. Chinchen, P.J. Denny, D.G. Parker, M.S. Spencer, D.A. Whan, Mechanism of methanol synthesis from CO_2/CO/H2 mixtures over copper/zinc oxide/alumina catalysts: use of 14C-labelled reactants, Appl. Catal. 30 (1987) 333–338, https://doi.org/10.1016/S0166-9834(00)84123-8.
[15] J. Zhu, Y. Su, J. Chai, V. Muravev, N. Kosinov, E.J.M. Hensen, Mechanism and nature of active sites for methanol synthesis from CO/CO2on Cu/CeO2, ACS Catal. 10 (2020) 11532–11544, https://doi.org/10.1021/acscatal.0c02909.
[16] J. Skrzypek, M. Lachowska, H. Moroz, Kinetics of methanol synthesis over commercial copper/zinc oxide/alumina catalysts, Chem. Eng. Sci. 46 (1991) 2809–2813, https://doi.org/10.1016/0009-2509(91)85150-V.
[17] U.J. Etim, Y. Song, Z. Zhong, Improving the Cu/ZnO-based catalysts for carbon dioxide hydrogenation to methanol, and the use of methanol as a renewable energy storage media, Front. Earth Sci. 8 (2020) 1–26, https://doi.org/10.3389/fenrg.2020.545431.
[18] Y. Wang, S. Kattel, W. Gao, K. Li, P. Liu, J.G. Chen, H. Wang, Exploring the ternary interactions in Cu–ZnO–ZrO2 catalysts for efficient CO_2 hydrogenation to methanol, Nat. Commun. 10 (2019) 1166, https://doi.org/10.1038/s41467-019-09072-6.
[19] S. Kattel, P.J. Ramírez, J.G. Chen, J.A. Rodriguez, P. Liu, Active sites for CO_2 hydrogenation to methanol on Cu/ZnO catalysts, Science 355 (2017) 1296–1299, https://doi.org/10.1126/science.aal3573.
[20] D. Laudenschleger, H. Ruland, M. Muhler, Identifying the nature of the active sites in methanol synthesis over Cu/ZnO/Al2O3 catalysts, Nat. Commun. 11 (2020) 3898, https://doi.org/10.1038/s41467-020-17631-5.
[21] Y. Lu, Z. Zhang, H. Wang, Y. Wang, Toward efficient single-atom catalysts for renewable fuels and chemicals production from biomass and CO_2, Appl. Catal. B Environ. 292 (2021) 120162–120199, https://doi.org/10.1016/j.apcatb.2021.120162.
[22] A.O. Elnabawy, J. Schumann, P. Bothra, A. Cao, J.K. Nørskov, The Challenge of CO hydrogenation to methanol: fundamental limitations imposed by linear scaling relations, Top. Catal. 63 (2020) 635–648, https://doi.org/10.1007/s11244-020-01283-2.
[23] B. Hu, Y. Yin, G. Liu, S. Chen, X. Hong, S.C.E. Tsang, Hydrogen spillover enabled active Cu sites for methanol synthesis from CO_2 hydrogenation over Pd doped CuZn catalysts, J. Catal. 359 (2018) 17–26, https://doi.org/10.1016/j.jcat.2017.12.029.
[24] J. Toyir, P.R. De la Piscina, J.L.G. Fierro, N. Homs, Catalytic performance for CO_2 conversion to methanol of gallium-promoted copper-based catalysts: influence of metallic precursors, Appl. Catal. B Environ. 34 (2001) 255–266, https://doi.org/10.1016/S0926-3373(01)00203-X.
[25] L. Martínez-Suarez, N. Siemer, J. Frenzel, D. Marx, Reaction network of methanol synthesis over Cu/ZnO nanocatalysts, ACS Catal. 5 (2015) 4201–4218, https://doi.org/10.1021/acscatal.5b00442.
[26] Y. Sun, C. Huang, L. Chen, Y. Zhang, M. Fu, J. Wu, D. Ye, Active site structure study of Cu/Plate ZnO model catalysts for CO_2 hydrogenation to methanol under the real reaction conditions, J. CO_2 Util. 37 (2020) 55–64, https://doi.org/10.1016/j.jcou.2019.11.029.
[27] J. Gao, P.E. Boahene, Y. Hu, A. Dalai, H. Wang, Atomic layer deposition ZnO over-coated Cu/SiO2 catalysts for methanol synthesis from CO_2 hydrogenation, Catalysts 9 (2019) 922–938, https://doi.org/10.3390/catal9110922.
[28] T. Witoon, J. Chalorngtham, P. Dumrongbunditkul, M. Chareonpanich, J. Limtrakul, CO_2 hydrogenation to methanol over Cu/ZrO2 catalysts: Effects of zirconia phases, Chem. Eng. J. 293 (2016) 327–336, https://doi.org/10.1016/j.cej.2016.02.069.
[29] K. Li, J.G. Chen, CO_2 hydrogenation to methanol over ZrO2-containing catalysts: insights into ZrO2 induced synergy, ACS Catal. 9 (2019) 7840–7861, https://doi.org/10.1021/acscatal.9b01943.
[30] X. Jiang, X. Nie, X. Guo, C. Song, J.G. Chen, Recent advances in carbon dioxide hydrogenation to methanol via heterogeneous catalysis, Chem. Rev. 120 (2020) 7984–8034, https://doi.org/10.1021/acs.chemrev.9b00723.
[31] F. Arena, K. Barbera, G. Italiano, G. Bonura, L. Spadaro, F. Frusteri, Synthesis, characterization and activity pattern of Cu-ZnO/ZrO2 catalysts in the hydrogenation of carbon dioxide to methanol, J. Catal. 249 (2007) 185–194, https://doi.org/10.1016/j.jcat.2007.04.003.
[32] S. Velu, K. Suzuki, C.S. Gopinath, H. Yoshida, T. Hattori, XPS, XANES and EXAFS investigations of CuO/ZnO/Al2O3/ZrO2 mixed oxide catalysts, Phys. Chem. Chem. Phys. 4 (2002) 1990–1999, https://doi.org/10.1039/b109766k.
[33] W. Wang, Z. Qu, L. Song, Q. Fu, CO_2 hydrogenation to methanol over Cu/CeO2 and Cu/ZrO2 catalysts: Tuning methanol selectivity via metal-support interaction, J. Energy Chem. 40 (2020) 22–30, https://doi.org/10.1016/j.jechem.2019.03.001.
[34] J. Wang, G. Li, Z. Li, C. Tang, Z. Feng, H. An, H. Liu, T. Liu, C. Li, A highly selective and stable ZnO-ZrO2 solid solution catalyst for CO_2 hydrogenation to methanol, Sci. Adv. 3 (2017) 1–11, https://doi.org/10.1126/sciadv.1701290.
[35] Z. Han, C. Tang, F. Sha, S. Tang, J. Wang, C. Li, CO_2 hydrogenation to methanol on ZnO-ZrO2 solid solution catalysts with ordered mesoporous structure, J. Catal. 396 (2021) 242–250, https://doi.org/10.1016/j.jcat.2021.02.024.
[36] N. Rui, R. Shi, R.A. Gutiérrez, R. Rosales, J. Kang, M. Mahapatra, P.J. Ramírez, S. D. Senanayake, J.A. Rodriguez, CO_2 hydrogenation on ZrO2/Cu(111) surfaces: production of methane and methanol, Ind. Eng. Chem. Res. 60 (2021) 18900–18906, https://doi.org/10.1021/acs.iecr.1c03229.

[37] C. Wu, L. Lin, J. Liu, J. Zhang, F. Zhang, T. Zhou, N. Rui, S. Yao, Y. Deng, F. Yang, W. Xu, J. Luo, Y. Zhao, B. Yan, X.D. Wen, J.A. Rodriguez, D. Ma, Inverse ZrO2/Cu as a highly efficient methanol synthesis catalyst from CO_2 hydrogenation, Nat. Commun. 11 (2020) 5767–5776, https://doi.org/10.1038/s41467-020-19634-8.

[38] R.M. Palomino, P.J. Ramírez, Z. Liu, R. Hamlyn, I. Waluyo, M. Mahapatra, I. Orozco, A. Hunt, J.P. Simonovis, S.D. Senanayake, J.A. Rodriguez, Hydrogenation of CO_2 on ZnO/Cu(100) and ZnO/Cu(111) catalysts: role of copper structure and metal-oxide interface in methanol synthesis, J. Phys. Chem. B. 122 (2018) 794–800, https://doi.org/10.1021/acs.jpcb.7b06901.

[39] F. Liao, Y. Huang, J. Ge, W. Zheng, K. Tedsree, P. Collier, X. Hong, S.C. Tsang, Morphology-dependent interactions of ZnO with Cu nanoparticles at the materials' interface in selective hydrogenation of CO_2 to CH 3OH, Angew. Chem. Int. Ed. 50 (2011) 2162–2165, https://doi.org/10.1002/anie.201007108.

[40] J. Nakamura, I. Nakamura, T. Uchijima, T. Watanabe, T. Fujitani, Model studies of methanol synthesis on copper catalysts, Stud. Surf. Sci. Catal. 101 B (1996) 1389–1399, https://doi.org/10.1016/s0167-2991(96)80351-x.

[41] S. Kuld, M. Thorhauge, H. Falsig, C.F. Elkjær, S. Helveg, I. Chorkendorff, J. Sehested, Quantifying the promotion of Cu catalysts by ZnO for methanol synthesis, Sci. (80-.) 352 (2016) 969–974, https://doi.org/10.1126/science.aaf0718.

[42] J.R. van Ommen, A. Goulas, R.L. Puurunen, Atomic layer deposition, kirk-othmer encycl, Chem. Technol. (2021) 1–42, https://doi.org/10.1002/0471238961.koe00059.

[43] B. Zhang, Y. Qin, Interface tailoring of heterogeneous catalysts by atomic layer deposition, ACS Catal. 8 (2018) 10064–10081, https://doi.org/10.1021/acscatal.8b02659.

[44] B.J. Oneill, D.H.K. Jackson, J. Lee, C. Canlas, P.C. Stair, C.L. Marshall, J.W. Elam, T.F. Kuech, J.A. Dumesic, G.W. Huber, Catalyst design with atomic layer deposition, ACS Catal. 5 (2015) 1804–1825, https://doi.org/10.1021/cs501862h.

[45] J.A. Singh, N. Yang, S.F. Bent, Nanoengineering heterogeneous catalysts by atomic layer deposition, Annu. Rev. Chem. Biomol. Eng. 8 (2017) 41–62, https://doi.org/10.1146/annurev-chembioeng-060816-101547.

[46] I. Ro, Y. Liu, M.R. Ball, D.H.K. Jackson, J.P. Chada, C. Sener, T.F. Kuech, R. J. Madon, G.W. Huber, J.A. Dumesic, Role of the Cu-ZrO2 interfacial sites for conversion of ethanol to ethyl acetate and synthesis of methanol from CO_2 and H2, ACS Catal. 6 (2016) 7040–7050, https://doi.org/10.1021/acscatal.6b01805.

[47] F. Zhao, M. Gong, K. Cao, Y. Zhang, J. Li, R. Chen, Atomic layer deposition of Ni on Cu nanoparticles for methanol synthesis from CO_2 hydrogenation, ChemCatChem 9 (2017) 3772–3778, https://doi.org/10.1002/cctc.201700622.

[48] S. Saedy, M.A. Newton, M. Zabilskiy, J.H. Lee, F. Krumeich, M. Ranocchiari, J. van Bokhoven, Copper-zinc oxide interface as a methanol-selective structure in Cu-ZnO catalyst during catalytic hydrogenation of carbon dioxide to methanol, Catal. Sci. Technol. 12 (2022) 2703–2716, https://doi.org/10.1039/d2cy00224h.

[49] X. Liu, J. Luo, H. Wang, L. Huang, S. Wang, S. Li, Z. Sun, F. Sun, Z. Jiang, S. Wei, W. X. Li, J. Lu, In situ spectroscopic characterization and theoretical calculations identify partially reduced ZnO1−x/Cu interfaces for methanol synthesis from CO_2, Angew. Chem. Int. Ed. 61 (2022), https://doi.org/10.1002/anie.202202330.

[50] S. Brunauer, P.H. Emmett, E. Teller, Adsorption of gases in multimolecular layers, J. Am. Chem. Soc. 60 (1938) 309–319, https://doi.org/10.1021/ja01269a023.

[51] P.P. Halenda, E.P. Barrett, L.G. Joyner, The determination of pore volume and area distributions in porous substances. I. Computations from nitrogen isotherms, J. Am. Chem. Soc. 73 (1951) 373–380, https://doi.org/10.1021/ja01145a126.

[52] S. Huotari, C.J. Sahle, C. Henriquet, A. Al-Zein, K. Martel, L. Simonelli, R. Verbeni, H. Gonzalez, M.C. Lagier, C. Ponchut, M. Moretti Sala, M. Krisch, G. Monaco, A large-solid-angle X-ray Raman scattering spectrometer at ID20 of the European Synchrotron Radiation Facility, J. Synchrotron Radiat. 24 (2017) 521–530, https://doi.org/10.1107/S1600577516020579.

[53] M.M. Sala, K. Martel, C. Henriquet, A. Al Zein, L. Simonelli, C.J. Sahle, H. Gonzalez, M.C. Lagier, C. Ponchut, S. Huotari, R. Verbeni, M. Krisch, G. Monaco, A high-energy-resolution resonant inelastic X-ray scattering spectrometer at ID20 of the European Synchrotron Radiation Facility, J. Synchrotron Radiat. 25 (2018) 580–591, https://doi.org/10.1107/S1600577518001200.

[54] J. Wellendorff, K.T. Lundgaard, A. Møgelhøj, V. Petzold, D.D. Landis, J.K. Nørskov, T. Bligaard, K.W. Jacobsen, Density functionals for surface science: Exchange-correlation model development with Bayesian error estimation, Phys. Rev. B. 85 (2012) 32–34, https://doi.org/10.1103/PhysRevB.85.235149.

[55] J. Enkovaara, C. Rostgaard, J.J. Mortensen, J. Chen, M. Dułak, L. Ferrighi, J. Gavnholt, C. Glinsvad, V. Haikola, H.A. Hansen, H.H. Kristoffersen, M. Kuisma, A.H. Larsen, L. Lehtovaara, M. Ljungberg, O. Lopez-Acevedo, P.G. Moses, J. Ojanen, T. Olsen, V. Petzold, N.A. Romero, J. Stausholm-Møller, M. Strange, G. A. Tritsaris, M. Vanin, M. Walter, B. Hammer, H. Häkkinen, G.K.H. Madsen, R. M. Nieminen, J.K. Nørskov, M. Puska, T.T. Rantala, J. Schiøtz, K.S. Thygesen, K. W. Jacobsen, Electronic structure calculations with GPAW: A real-space implementation of the projector augmented-wave method, J. Phys. Condens. Matter 22 (2010) 253303–253325, https://doi.org/10.1088/0953-8984/22/25/253202.

[56] P.E. Blöchl, Projector augmented-wave method, Phys. Rev. B 50 (1994) 17953–17979, https://doi.org/10.1103/PhysRevB.50.17953.

[57] S. Dudarev, G. Botton, Electron-energy-loss spectra and the structural stability of nickel oxide: An LSDA+U study, Phys. Rev. B - Condens. Matter Mater. Phys. 57 (1998) 1505–1509, https://doi.org/10.1103/PhysRevB.57.1505.

[58] E. Bitzek, P. Koskinen, F. Gähler, M. Moseler, P. Gumbsch, Structural relaxation made simple, Phys. Rev. Lett. 97 (2006) 1–4, https://doi.org/10.1103/PhysRevLett.97.170201.

[59] A. Hjorth Larsen, J. JØrgen Mortensen, J. Blomqvist, I.E. Castelli, R. Christensen, M. Dułak, J. Friis, M.N. Groves, B. Hammer, C. Hargus, E.D. Hermes, P.C. Jennings, P. Bjerre Jensen, J. Kermode, J.R. Kitchin, E. Leonhard Kolsbjerg, J. Kubal, K. Kaasbjerg, S. Lysgaard, J. Bergmann Maronsson, T. Maxson, T. Olsen, L. Pastewka, A. Peterson, C. Rostgaard, J. SchiØtz, O. Schütt, M. Strange, K. S. Thygesen, T. Vegge, L. Vilhelmsen, M. Walter, Z. Zeng, K.W. Jacobsen, The atomic simulation environment - a python library for working with atoms, J. Phys. Condens. Matter 29 (2017) 273002–273032, https://doi.org/10.1088/1361-648X/aa680e.

[60] T. Frederiksen, M. Paulsson, M. Brandbyge, A.P. Jauho, Inelastic transport theory from first principles: methodology and application to nanoscale devices, Phys. Rev. B - Condens. Matter Mater. Phys. 75 (2007) 1–22, https://doi.org/10.1103/PhysRevB.75.205413.

[61] R.A. Bair, W.A. Goddard, Ab initio studies of the x-ray absorption edge in copper complexes. I. Atomic Cu2+ and Cu(ii)Cl2, Phys. Rev. B. 22 (1980) 2767–2776, https://doi.org/10.1103/PhysRevB.22.2767.

[62] G. Döring, C. Sternemann, A. Kaprolat, A. Mattila, K. Hämäläinen, W. Schülke, Shake-up valence excitations in CuO by resonant inelastic x-ray scattering, Phys. Rev. B - Condens. Matter Mater. Phys. 70 (2004) 1–15, https://doi.org/10.1103/PhysRevB.70.085115.

[63] M.M.R. Bhuiyan, S.D. Lin, T.C. Hsiao, Effect of calcination on Cu-Zn-loaded hydrotalcite catalysts for C-C bond formation derived from methanol, Catal. Today 226 (2014) 150–159, https://doi.org/10.1016/j.cattod.2013.10.053.

[64] A. Dadlani, S. Acharya, O. Trejo, D. Nordlund, M. Peron, J. Razavi, F. Berto, F. B. Prinz, J. Torgersen, Revealing the bonding environment of Zn in ALD Zn(O,S) buffer layers through X-ray absorption spectroscopy, ACS Appl. Mater. Interfaces 9 (2017) 39105–39109, https://doi.org/10.1021/acsami.7b06728.

[65] A. Montebelli, C.G. Visconti, G. Groppi, E. Tronconi, S. Kohler, H.J. Venvik, R. Myrstad, Washcoating and chemical testing of a commercial Cu/ZnO/Al2O3 catalyst for the methanol synthesis over copper open-cell foams, Appl. Catal. A Gen. 481 (2014) 96–103, https://doi.org/10.1016/j.apcata.2014.05.005.

[66] E. Diler, B. Lescop, S. Rioual, G. Nguyen Vien, D. Thierry, B. Rouvellou, Initial formation of corrosion products on pure zinc and MgZn2 examinated by XPS, Corros. Sci. 79 (2014) 83–88, https://doi.org/10.1016/j.corsci.2013.10.029.

[67] A.R. Puigdollers, P. Schlexer, S. Tosoni, G. Pacchioni, Increasing oxide reducibility: The role of metal/oxide interfaces in the formation of oxygen vacancies, ACS Catal. 7 (2017) 6493–6513, https://doi.org/10.1021/acscatal.7b01913.

[68] D. Eder, R. Kramer, The stoichiometry of hydrogen reduced zirconia and its influence on catalytic activity - part 1: volumetric and conductivity studies, Phys. Chem. Chem. Phys. 4 (2002) 795–801, https://doi.org/10.1039/b109887j.

[69] W. Donphai, N. Piriyawate, T. Witoon, P. Jantaratana, V. Varabuntoonvit, M. Chareonpanich, Effect of magnetic field on CO_2 conversion over Cu-ZnO/ZrO2 catalyst in hydrogenation reaction, J. CO_2 Util. 16 (2016) 204–211, https://doi.org/10.1016/j.jcou.2016.07.007.

[70] L. Zhao, Y. Zhang, S. Bi, Q. Liu, Metal-organic framework-derived CeO2-ZnO catalysts for C3H6-SCR of NO: An: in situ DRIFTS study, RSC Adv. 9 (2019) 19236–19242, https://doi.org/10.1039/c9ra03103k.

[71] R.X. Zhou, X.Y. Jiang, J.X. Mao, X.M. Zheng, Oxidation of carbon monoxide catalyzed by copper-zirconium composite oxides, Appl. Catal. A Gen. 162 (1997) 213–222, https://doi.org/10.1016/S0926-860X(97)00099-9.

[72] G. Águila, F. Gracia, J. Cortés, P. Araya, Effect of copper species and the presence of reaction products on the activity of methane oxidation on supported CuO catalysts, Appl. Catal. B Environ. 77 (2008) 325–338, https://doi.org/10.1016/j.apcatb.2007.08.002.

[73] K.V.R. Chary, G.V. Sagar, C.S. Srikanth, V.V. Rao, Characterization and catalytic functionalities of copper oxide catalysts supported on zirconia, J. Phys. Chem. B. 111 (2007) 543–550, https://doi.org/10.1021/jp063335x.

[74] C.Z. Yao, L.C. Wang, Y.M. Liu, G.S. Wu, Y. Cao, W.L. Dai, H.Y. He, K.N. Fan, Effect of preparation method on the hydrogen production from methanol steam reforming over binary Cu/ZrO2 catalysts, Appl. Catal. A Gen. 297 (2006) 151–158, https://doi.org/10.1016/j.apcata.2005.09.002.

[75] A.G. Sato, D.P. Volanti, D.M. Meira, S. Damyanova, E. Longo, J.M.C. Bueno, Effect of the ZrO2 phase on the structure and behavior of supported Cu catalysts for ethanol conversion, J. Catal. 307 (2013) 1–17, https://doi.org/10.1016/j.jcat.2013.06.022.

[76] Y. Yao, X. Wu, O.Y. Gutiérrez, J. Ji, P. Jin, S. Wang, Y. Xu, Y. Zhao, S. Wang, X. Ma, J.A. Lercher, Roles of Cu+ and Cu0 sites in liquid-phase hydrogenation of esters on core-shell CuZnx@C catalysts, Appl. Catal. B Environ. 267 (2020) 118698–118708, https://doi.org/10.1016/j.apcatb.2020.118698.

[77] C. Huang, S. Chen, X. Fei, D. Liu, Y. Zhang, Catalytic hydrogenation of CO_2 to methanol: Study of synergistic effect on adsorption properties of CO_2 and H2 in CuO/ZnO/ZrO2 system, Catalysts 5 (2015) 1846–1861, https://doi.org/10.3390/catal5041846.

[78] H. Zhan, X. Shi, B. Tang, G. Wang, B. Ma, W. Liu, The performance of Cu/Zn/Zr catalysts of different Zr/(Cu+Zn) ratio for CO_2 hydrogenation to methanol, Catal. Commun. 149 (2021) 106264–106268, https://doi.org/10.1016/j.catcom.2020.106264.

[79] S. Kouva, J. Andersin, K. Honkala, J. Lehtonen, L. Lefferts, J. Kanervo, Water and carbon oxides on monoclinic zirconia: experimental and computational insights, Phys. Chem. Chem. Phys. 16 (2014) 20650–20664, https://doi.org/10.1039/c4cp02742f.

[80] S.T. Korhonen, M. Calatayud, A. Outi, I. Krause, Structure and stability of formates and carbonates on monoclinic zirconia: a combined study by density functional theory and infrared spectroscopy, J. Phys. Chem. C 112 (2008) 16096–16102, https://doi.org/10.1021/jp803353v.

[81] S.P. Kočk, Eva Maria, Michaela Kogler, Thomas Bielz, Bernhard Klötzer, In situ FT-IR spectroscopic study of CO_2 and CO adsorption on Y2O3, ZrO2, and yttria-

stabilized ZrO2, J. Phys. Chem. C. 117 (2013) 17666–17673, https://doi.org/10.1021/jp405625x.
[82] B. Bachiller-Baeza, I. Rodriguez-Ramos, A. Guerrero-Ruiz, Interaction of carbon dioxide with the surface of zirconia polymorphs, Langmuir 14 (1998) 3556–3564, https://doi.org/10.1021/la970856q.
[83] B. An, J. Zhang, K. Cheng, P. Ji, C. Wang, W. Lin, Confinement of ultrasmall Cu/ZnOx nanoparticles in metal-organic frameworks for selective methanol synthesis from catalytic hydrogenation of CO_2, J. Am. Chem. Soc. 139 (2017) 3834–3840, https://doi.org/10.1021/jacs.7b00058.
[84] X. Dong, F. Li, N. Zhao, F. Xiao, J. Wang, Y. Tan, CO_2 hydrogenation to methanol over Cu/ZnO/ZrO2 catalysts prepared by precipitation-reduction method, Appl. Catal. B Environ. 191 (2016) 8–17, https://doi.org/10.1016/j.apcatb.2016.03.014.
[85] K. Larmier, W.C. Liao, S. Tada, E. Lam, R. Verel, A. Bansode, A. Urakawa, A. Comas-Vives, C. Copéret, CO_2-to-methanol hydrogenation on zirconia-supported copper nanoparticles: reaction intermediates and the role of the metal–support interface, Angew. Chem. Int. Ed. 56 (2017) 2318–2323, https://doi.org/10.1002/anie.201610166.
[86] S. Kattel, B. Yan, Y. Yang, J.G. Chen, P. Liu, Optimizing binding energies of key intermediates for CO_2 hydrogenation to methanol over oxide-supported copper, J. Am. Chem. Soc. 138 (2016) 12440–12450, https://doi.org/10.1021/jacs.6b05791.
[87] A. Le Valant, C. Comminges, C. Tisseraud, C. Canaff, L. Pinard, Y. Pouilloux, The Cu-ZnO synergy in methanol synthesis from CO_2, Part 1: Origin of active site explained by experimental studies and a sphere contact quantification model on Cu + ZnO mechanical mixtures, J. Catal. 324 (2015) 41–49, https://doi.org/10.1016/j.jcat.2015.01.021.
[88] C. Peinado, D. Liuzzi, A. Sanchís, L. Pascual, M.A. Peña, J. Boon, S. Rojas, In situ conditioning of CO_2-rich syngas during the synthesis of methanol, Catalysts 11 (2021), https://doi.org/10.3390/catal11050534.
[89] T. Lunkenbein, J. Schumann, M. Behrens, R. Schlögl, M.G. Willinger, Formation of a ZnO overlayer in industrial Cu/ZnO/Al2O3 catalysts induced by strong metal-support interactions, Angew. Chem. - Int. Ed. 54 (2015) 4544–4548, https://doi.org/10.1002/anie.201411581.
[90] S. Zander, E.L. Kunkes, M.E. Schuster, J. Schumann, G. Weinberg, D. Teschner, N. Jacobsen, R. Schlögl, M. Behrens, The role of the oxide component in the development of copper composite catalysts for methanol synthesis, Angew. Chem. Int. Ed. 52 (2013) 6536–6540, https://doi.org/10.1002/anie.201301419.
[91] V. Schott, H. Oberhofer, A. Birkner, M. Xu, Y. Wang, M. Muhler, K. Reuter, C. Wöll, Chemical activity of thin oxide layers: strong interactions with the support yield a new thin-film phase of zno, Angew. Chem. Int. Ed. 52 (2013) 11925–11929, https://doi.org/10.1002/anie.201302315.
[92] J.A. Rodriguez, P. Liu, D.J. Stacchiola, S.D. Senanayake, M.G. White, J.G. Chen, Hydrogenation of CO_2 to methanol: importance of metal-oxide and metal-carbide interfaces in the activation of CO_2, ACS Catal. 5 (2015) 6696–6706, https://doi.org/10.1021/acscatal.5b01755.

III

EXPLORING CO_2 HYDROGENATION TO METHANOL AT A CUZN-ZRO_2 INTERFACE VIA DFT CALCULATIONS

by

Lempelto, A.; Gell, L.; Kiljunen, T.; Honkala, K.

Catal. Sci. Technol. 2023, 13, 4387

https://doi.org/10.1039/d3cy00549f

Catalysis Science & Technology

ROYAL SOCIETY OF CHEMISTRY

PAPER

View Article Online
View Journal

Cite this: DOI: 10.1039/d3cy00549f

Exploring CO_2 hydrogenation to methanol at a CuZn–ZrO_2 interface *via* DFT calculations†

Aku Lempelto, Lars Gell, Toni Kiljunen and Karoliina Honkala *

Multi-component heterogeneous catalysts are among the top candidates for converting greenhouse gases into valuable compounds. Combinations of Cu, Zn, and ZrO_2 (CZZ) have emerged as promisingly efficient catalysts for CO_2 hydrogenation to methanol. To explore the catalytic mechanism, density functional theory (DFT) calculations and the energetic span model (ESM) were used to study CO_2 conversion routes to methanol on CuZn–ZrO_2 interfaces with a varying Zn content. Our results demonstrate that the presence of Zn sites at the interface improves CO_2 binding. However, the adsorption and activation energies are insensitive to Zn concentration. The calculations also show that the hydrogenation of adsorbate oxygen atoms at the interface is kinetically more favourable and requires hydrogen spillover from the metal to the zirconia. This leads to barriers that are lower than those reported on interface or metal-only sites in previous literature. While DFT calculations alone are unable to identify which one of the competing pathways is more favourable, the ESM model predicts that the carboxyl pathway has a higher turnover frequency than the formate route. Our findings also show the importance of considering effects such as hydrogen spillover which take place at a metal-oxide interface when modelling complex catalytic environments.

Received 20th April 2023,
Accepted 20th June 2023

DOI: 10.1039/d3cy00549f

rsc.li/catalysis

1 Introduction

Transforming CO_2 into value-added products such as methanol, hydrocarbon fuels, and other platform chemicals has gained attention as an attractive approach to reduce the negative impact carbon dioxide has on the climate.[1–4] Using renewable energy and sustainable hydrogen would allow us to establish a circular economy based on carbon recycling.[1,2,5–8] However, due to the stable nature of CO_2, highly active, selective, and deactivation-resistant catalysts are required to make large-scale adaptation feasible.[5] Various catalytic systems with different combinations of active metal and supporting metal oxide have been prepared and characterised to maximise catalytic activity and selectivity for CO_2 conversion to methanol (CTM):[3,9–18]

$$CO_2(g) + 3H_2(g) \rightarrow CH_3OH(g) + H_2O(g). \quad (R1)$$

Oxide-supported Cu nanoparticles have been extensively studied for catalysing CTM due to their promising methanol selectivity, which can be upwards of 60%.[3,19] Several experimental[3,20–24] and computational[3,21,23–26] studies have associated the catalytic activity with active sites at the metal-oxide interface. The type of oxide support can substantially influence the activity and selectivity of the catalyst.[3,4,24] Common choices for suitable oxides include zinc oxide ZnO, zirconia ZrO_2, titania TiO_2, and alumina Al_2O_3. For example, the ternary system of Cu/ZnO/Al_2O_3 is already an industrially established CTM catalyst, but it displays relatively low conversion, typically below 20%, leading to efforts to develop more selective catalysts in addition to the continuous search for increased activity.[3,6,9,27] To this end, zirconia (ZrO_2) has been suggested as an alternative oxide support due to increased turnover rates and selectivity of ZrO_2-supported Cu.[3,24] Additionally, zirconia has been reported to offer enhanced thermal and mechanical stability and to prevent Cu particles from sintering and thus to hinder the deactivation of the catalyst.[3,24,28–33] Adding ZnO as another oxide into Cu/ZrO_2 has demonstrated higher methanol production rates and total conversion percentages than either Cu/ZnO or Cu/ZrO_2, often reaching a 20% conversion whereas a lower 5 to 10 percent conversion is typical for binary systems.[3,4,30,34]

The precise function of ZnO in Cu/ZnO/ZrO_2 (CZZ) is still under debate.[33] The ZnO component is suggested to be able to temporarily store hydrogen,[33] and it may also act as an additional structural modifier, enhancing Cu dispersion and

Department of Chemistry, University of Jyväskylä, Nanoscience Center, P.O. Box 35, FI-40014, Finland. E-mail: karoliina.honkala@jyu.fi

† Electronic supplementary information (ESI) available: See ESI for the structures and energies of all adsorbed intermediates, potential energy diagrams, and details of the ESM analysis. See DOI: https://doi.org/10.1039/d3cy00549f

increasing its surface area.[30] The actual oxidation state of Zn and the mechanism of catalytic promoting remain somewhat controversial,[3,9–11,13,20,22,23,35–39] and the question of whether or not a CuZn-alloy is involved as the active phase remains open. It is known that the strong interaction between the components may lead to partial ZnO coverage of a Cu surface.[11,20] Under certain conditions the ZnO component can partially reduce into metallic Zn which has two possible outcomes: either forming oxygen vacancies or creating surface alloys of Cu and Zn.[9,10,13,40,41] The CuZn alloys formed at defect and edge sites of metal particles can then be partially reduced by the adsorbates and serve as the active sites of Cu/ZnO catalysts.[9] Based on a combination of *in situ* analyses, it has been determined that the extent of the alloying varies largely based on the exact temperatures, the presence of CO_2 or other gaseous species *i.e.* the reducing quality of the conditions.[13,22,23,41,42] Therefore the significance of the alloying remains controversial. A bulk alloy may oxidise and separate into Cu and oxidised Zn,[22] or simply lose its ability to act as an efficient catalyst.[42] Instead, an oxidised phase of Zn in the form of Zn formates has been suggested to be the active intermediate species that lead to methanol formation.[22,36] While the discussion is often centered around bulk alloying, the presence of metallic Zn impurities or dilute alloys at the metal-oxide interface acting as the active sites demand investigation.

In computational studies, a pristine Cu facet such as Cu(111) or Cu(211) has typically been chosen as the model to represent the Cu-containing catalyst system.[9,27,43] While simple to work with, these models obviously omit the effects of the supporting oxide. For example, when CO_2 is electronically activated upon adsorption, it takes a bent shape with an O–C–O angle of 123°, as if sp^2 hybridised. However, both at and stepped Cu surfaces bind CO_2 only in a linear fashion even though physisorption energies as large as −0.56 eV and −0.71 eV have been reported on Cu(111)[9,27,43,44] and Cu(211),[9,45,46] respectively. On the other hand, the copper-oxide interface has been reported to activate CO_2, which bends upon adsorption and the adsorption energy varies in the range of −0.4–1.8 eV, depending on the specific structure of the interface.[25,44,47] Therefore, binary systems where a metal cluster or nanorod is supported on an oxide slab are a common alternative to a purely metallic model.[25,44,47,48] In a recent study combining experiments and calculations, a single Cu atom catalyst on ZrO_2 was found to promote CTM with near 100% selectivity whereas additional active sites at larger Cu clusters and particles were shown to diminish this efficiency.[14]

As the precise role of the Zn promoter in CTM is unsettled,[35,41] the choice of how it should be included in computational models has varied. The density functional theory (DFT) studies on CZZ catalysts conducted so far have only considered one or two of the three components. For example, a CZZ system was recently modelled[21] by depositing a small ZrO_2 cluster on a ZnO($11\bar{2}0$) surface to better understand the catalytic behavior on oxide interfaces. Very recently, an inverse $ZrZn_2O_3$/Cu(111) system was used to model ZrO_2/Cu and ZnO/Cu interfaces.[49] Purely metallic Cu or CuZn models have also been used to mimic active sites at facets and edges of nanoparticles.[9,23,27,46,50] Even though a CuZn(211) surface is unable to activate CO_2 and the intermediates bound to it are thermodynamically less stable than the gas-phase reagents,[9] the hydrogenation intermediates are nevertheless more strongly bound to an alloyed CuZn surface than to a pure Cu surface.[9]

While the reaction mechanism of CTM has been studied for a variety of catalyst compositions, the views are not unanimous on the identity of the key intermediates, the main reaction pathway, and an active catalyst domain.[3,19,24] Generally, the plausible pathways have been narrowed down to two competing ones: one converting CO_2 to a formate (HCOO) which then reacts onwards to methanol, and the other, where CO_2 first breaks down to carbon monoxide (CO) through a reverse water–gas shift (RWGS) reaction and then hydrogenates to methanol *via* a formaldehyde intermediate. Different interpretations of computational and experimental results have led to differing opinions on the dominant reaction route. For example, a formate species bound to the zirconia surface has been both computationally and experimentally determined to be highly stable and could be considered a strong thermodynamic sink.[25,28,44,48] Therefore, formates have been suggested to accumulate at the zirconia and poison the active sites rather than acting as key intermediates in CTM. However, the barrier for HCOO conversion to dioxymethylene (H_2COO) has been computed to be only 0.66 eV on a ZrO_2/ZnO interface.[21] This finding is supported by *in situ* diffuse reflectance infrared spectroscopy measurements, which have shown that the CZZ system can quickly convert formate to a methoxy (CH_3O) species.[21,25]

Another key feature for a hydrogenation catalyst is the ability to efficiently dissociate molecular hydrogen, which, in a Cu-based system, is assumed to be take place on the metal component, where hydrogen readily adsorbs dissociatively.[4,9,21,51–53] Hydrogen spillover from the metal to the ZrO_2 surface may take place and promote a zirconia-bound hydrogen to participate in the CTM reactions.[51,54,55] However, the efficiency and mechanism of the spillover on irreducible oxides, such as zirconia, has been a subject of debate[56–58] and the importance of the kinetic control of the spillover step is unclear.

In this work, we employ DFT calculations to examine the intermediate and transition states for the branched reaction network of CO_2 CTM by first discussing the reactant properties at the interface using supported CuZn nanorod models, then outlining the formate and RWGS route specifics, combining them to form the products, and finally evaluating the kinetic aspects of the catalytic cycle. We model the active interface by constructing mixed CuZn structures with varying concentration of Zn atoms at the Cu-monoclinic $ZrO_2(\bar{1}11)$ interface mimicking a diluted interface nanoalloy. The energetic span model is used to identify rate-controlling intermediates and to draw a simplified comparison between the optimal kinetics of competing mechanisms.

2 Computational methods

DFT calculations were carried out using the BEEF-vdW exchange–correlation functional[59] in the projector-augmented wave (PAW)[60] formalism as implemented in the GPAW[61] package. The core electrons of all elements were described in the frozen-core approximation. A maximum spacing of 0.20 Å was used for the real-space grid basis, and the reciprocal space was sampled at the Γ point. A Hubbard U correction[62] of 2.0 eV, determined using a self-consistent linear response method detailed in ref. 63, was applied to the d-orbitals of the zirconium atoms. A higher value of 4 eV is common in literature[64–67] but the difference is not unusual as the value of the U parameter is very sensitive to the specific DFT implementation used. The geometry optimisations were performed using the fast inertial relaxation engine (FIRE) algorithm as implemented in the atomic simulation environment (ASE).[68,69] During optimisations, the bottom layer of the ZrO_2 slab was kept frozen in its initial bulk geometry. All other atoms were allowed to relax until the maximum residual force was reduced below 0.02 eV Å^{-1}. The transition state searches were carried out using the climbing image nudged elastic band (CI-NEB)[70,71] method where the maximum residual force was set to 0.05 eV Å^{-1} which keeps the computational cost feasible. Hydrogenation reactions were carried out such that the H atom was initially placed either on the metal side of the interface or on the oxide side, close to the molecule to be hydrogenated. The transition states were confirmed by calculating the vibrational modes using the Frederiksen method[72] and verifying that only one mode with an imaginary frequency exists along the reaction coordinate. Partial charges on atoms were analysed with the Bader method[73] using code written by Tang *et al.*[74]

For the metal-oxide interface, we utilise the oxide-supported metal nanorod concept consisting of a Cu rod with some edge Cu atoms replaced with Zn atoms at different concentrations (see Fig. 1 for the structures and denominations). The Cu–(m-$ZrO_2(\bar{1}11)$) interface model was adopted from our previous study,[47] where the length of the nanorod is eight atoms and the thickness three atomic layers. A (111) plane is exposed towards the interface. The zirconia surface is described by a two-layer-thick slab model, built from a 3 × 2 m-$ZrO_2(\bar{1}11)$ supercell with periodic boundary conditions in the horizontal directions. While a Cu rod was found to be more stable on a tetragonal zirconia surface,[47] the monoclinic variety is thermodynamically favoured under reaction conditions[75] and has shown activity towards CO_2 activation and CTM in experiments.[34,76] Three different Zn concentrations were examined by replacing every fourth Cu atom, 3/4 of Cu atoms, or all Cu atoms on the nanorod edge with Zn. These models were named the Zn-dilute, the Zn-rich, and the Zn interface, respectively. This represents situations where Zn centres are dispersed to a varying degree, such as the case where atomic layer deposition has been used to prepare the catalyst.[34] In this instance we have chosen to place the Zn centers along the active interface instead of a more homogeneous alloying with Cu, allowing the use of a pure Cu interface model as a reference, assisting interpretation.

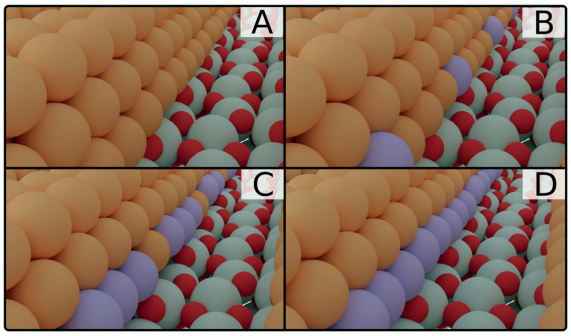

Fig. 1 The four metal/ZrO_2 interface systems with varying amounts of Zn in the Cu nanorod. A: Cu interface, B: Zn-dilute interface, C: Zn-rich interface, D: Zn interface. Red: O, white: H, dark grey: C, purple: Zn, turquoise: Zr, orange: Cu.

The simulation cell measures 20.67 × 14.79 × 24.0 in Å with angles of 90°/90°/116.5°. This unit cell size results in a minor compressive strain of −1.02% for the Cu atoms along the direction of the nanorod.[47] For the Zn interface, the strain is −4.2% as a result of the longer, 2.69 Å, Zn–Zn bulk distance. The strains experienced by the other interfaces are less clearly defined but are likely between the −1.02% of Cu and −4.2% of the Zn interface. A strain of this magnitude at the Cu interface[47] was found to enhance CO_2 binding by up to 0.4 eV. On the other hand, a computed lattice constant of 2.91 Å has been reported for a bulk β-CuZn,[77] corresponding to a shorter Cu–Zn distance of 2.52 Å. This could mean that the compressive strain of the Zn-dilute interface is slightly lower than that of the Cu interface. All three doped interfaces have a Zn atom at the site that binds CO_2 and many further reaction intermediates the strongest, so that they all measure the impact of Zn against the performance of the pure Cu interface. The relative strength of the adsorption at this site is likely due to a lower coordination caused by the interaction between the nanoparticle and the oxide. The models represent cases where the Zn atoms exist as single atom centers dispersed at the metallic interface or as more conjugated assemblies that span several Zn centers. The energy ΔE_{def} by which CO_2 adsorption deforms the interface was calculated as

$$\Delta E_{\mathrm{def}} = E^{*}_{\mathrm{CuZn/ZrO_2}} - E_{\mathrm{CuZn/ZrO_2}}, \quad (1)$$

where $E^{*}_{\mathrm{CuZn/ZrO_2}}$ is the energy of a CuZn/ZrO_2 configuration after removal of CO_2 from an optimised adsorption geometry and $E_{\mathrm{CuZn/ZrO_2}}$ is the energy of the optimal interface without any adsorbate.

A graph theory-based energetic span model[78,79] (ESM) for complex reaction networks was utilised to assess the catalytic cycles. By summing together pairs of intermediate and

transition state energies, it is possible to estimate turnover frequency of each mechanism,

$$\mathrm{TOF}_n = \frac{k_\mathrm{B}T}{h}\frac{1-\mathrm{e}^{\Delta G_\mathrm{r}/RT}}{\sum_{i,j}\mathrm{e}^{\left(T_i-I_j+\delta G_{i,j}\right)/RT}} \quad (2)$$

where k_B is the Boltzmann constant, T is the temperature, h is the Planck constant, ΔG_r is the Gibbs energy of reaction, and T_i and I_j are the Gibbs energies of a given transition state and intermediate, respectively. Furthermore, a summation over all n possible mechanisms in the network gives an estimate of the total TOF.[79]

$$\mathrm{TOF} = \frac{k_\mathrm{B}T}{h}\sum_n \frac{1-\mathrm{e}^{\Delta G_\mathrm{r}/RT}}{\sum_{i\in\mathrm{cycle}_n,j}\mathrm{e}^{\left(T_i-I_j+\delta G_{i,j}\right)/RT}} \quad (3)$$

The delta term $\delta G_{i,j}$ is defined as:[79]

$$\delta G_{i,j} = \begin{cases} 0 & \text{if } i > j, \ \textit{i.e.} \text{ TS follows intermediate} \\ \Delta G_\mathrm{r} & \text{if } i \le j, \ \textit{i.e.} \text{ TS precedes intermediate} \end{cases} \quad (4)$$

The degree of turnover frequency control X_TOF is defined for intermediates and transition states according to eqn (5) and (6) (see ESI† section S3).

$$X_{\mathrm{TOF},T_i,n} = \frac{\sum_j \mathrm{e}^{\left(T_i-I_j+\delta G_{i,j}\right)/RT}}{\sum_{i\in\mathrm{cycle}_n,j}\mathrm{e}^{\left(T_i-I_j+\delta G_{i,j}\right)/RT}} \quad (5)$$

$$X_{\mathrm{TOF},I_j,n} = \frac{\sum_{i\in\mathrm{cycle}_n}\mathrm{e}^{\left(T_i-I_j+\delta G_{i,j}\right)/RT}}{\sum_{i\in\mathrm{cycle}_n,j}\mathrm{e}^{\left(T_i-I_j-\delta G_{i,j}\right)/RT}} \quad (6)$$

The concept is similar to that of the degree of rate control. A value closer to 1 indicates that changes in the state's energy will affect the TOF more than the energies of states with X_TOF values close to 0. However, while the degree of rate control is often determined for elementary steps, here we define the degrees of TOF control separately for intermediates and transition states. This way the values of X_TOF can be maximal for two states that are not part of the same elementary step. We can show the direct influence of the energy of each intermediate of transition state as:

$$\text{Effect of } T_i \text{ on TOF} = \frac{\partial \mathrm{TOF}}{\partial T_i} \quad (7)$$

$$\text{Effect of } I_j \text{ on TOF} = \frac{\partial \mathrm{TOF}}{\partial I_j} \quad (8)$$

which was estimated by using $\partial T_i = \partial I_j = -0.001$ eV. The DFT-computed adsorption and transition state energies were used as input. While the difference between free energies and DFT energies for gas-phase species can be in the order of 0.6 eV, we assume that the catalytic turnover frequencies (TOF) and the degree of TOF control values (X_TOF) can be compared between different reaction pathways that mainly take place on the surface, even though no free energy corrections were included. The TOF values were computed at a temperature of 500 K, which corresponds to experimental reaction conditions.[80]

The ESM analysis was originally developed for studying homogeneous catalysis[78] but it has also been successfully applied for heterogeneous systems including CO_2 hydrogenation to methanol on Cu(111).[81] The basic assumptions of the ESM include that: (i) Eyring's transition state theory is valid, (ii) a steady-state regime is applicable, and (iii) the intermediates undergo fast relaxation to the thermodynamic equilibrium described by the Boltzmann distribution.[78] While the reaction kinetics for heterogeneous catalyst systems is often studied *via* microkinetic modelling or kinetic Monte Carlo simulations,[23,26–28,48,49,82] the ESM offers a simplified way to estimate which pathway is optimal. We used the gTOFfee software,[81,83] which was slightly modified to improve the performance for the present reaction network. Additionally, an extension was made to the code for calculating the degrees of TOF control, see ESI† for details.

3 Results and discussion

3.1 CO_2 and H_2 activation

The CO_2 adsorption properties of the interfaces were determined first since the CO_2 reduction pathways start with the adsorption of the reactants on the catalyst surface. All the interface atoms were first considered as potential sites for the CO_2 adsorption. Subsequent hydrogenation steps are then performed for the most stable CO_2 adsorption geometry, which is similar to the one for the Cu interface.[47] CO_2 binds to the CuZn–ZrO_2 interface in a conformation where the carbon atom resides on top of a Zn atom (C–Zn bond length 2.1 Å) and the two oxygen atoms bind on two Zr cations close to the interface (see Fig. S6†). Upon adsorption, CO_2 takes a bent shape, which resembles a carbonate anion[25,47] and indicates the activation of the molecule with a partial charge of $1.3|e|$.[47] The interaction of CO_2 with the CuZn–ZrO_2 interface leads to a local deformation of the rod such that the metal atom in contact with the C atom is pulled out from the (111) plane.

The CO_2 adsorption is exothermic by −1.17 eV, −1.13 eV, and −1.30 eV at the Zn-dilute, Zn-rich and Zn interfaces, respectively. The Cu interface exhibits significantly weaker binding with an adsorption energy of −0.64 eV.[47] The difference can be rationalised by examining the energy penalty of deformation ΔE_def, calculated using eqn (1), which is +1.7 eV for the Cu interface and +1.1 eV for the Zn-dilute interface. The ΔE_def is consistent with the difference in adsorption energies: the stronger binding at the Zn-containing interface is due to smaller deformation energy. No energy penalty is seen for the Zn-rich and Zn interfaces, as their intrinsic strain already favours a deformed structure. CO_2 adsorption at the Zn-rich interface is a kinetically activated process with a barrier of 0.16 eV, which is 0.22 eV lower than the barrier computed for the Cu interface.[47] Similarly to the more negative adsorption energies, the lower barrier is likely due to the increased mobility of the Zn. Adsorption of CO_2 on the low-coordinated oxygen atoms of the ZrO_2 surface, without the involvement of the interface, is

also possible in a trigonal carbonate-like geometry where the carbon atom of the CO_2 binds the lattice oxygen and one of its oxygens rests on a Zr cation. With an adsorption energy of −0.59 eV, this binding is likely in competition with the adsorption at the interface. In addition to adsorption, we considered dissociative adsorption of CO_2 into CO and O, as studied previously.[84–86] However, the reaction is endothermic with a barrier of 1.7 eV, see ESI† section 1.1 for details, and therefore this pathway was omitted from further evaluation.

The dissociative adsorption of H_2 was considered at the CuZn–ZrO_2 interface at various positions. The dissociation can be homolytic, where both H atoms adsorb on Cu/Zn sites on the rod and have similar small charges of *ca.* −0.3 e, regardless of if they are in the vicinity of a Zn site. Alternatively, it can happen across the interface either homolytically, where one H binds on the surface of the rod and the other on top of a Zr, or heterolytically, where a hydride binds to the surface of the metal rod and a proton to an oxide anion. These sites are illustrated in Fig. S7.† Hydrides and protons on the zirconia have charges of −0.6 e and +0.6 e, respectively. The heterolytic dissociation is endothermic by *ca.* +1 eV and has a kinetic barrier of 1.4 eV, while the homolytic path on the rod is endothermic only by +0.4 eV with a slightly smaller activation energy of 1.1 eV. The spillover of hydrogen from the metal to the oxide surface is endothermic by *ca.* +0.6 eV depending slightly on the interface site. The kinetic barrier for hydride migration from the metal to the Zr on-top site of the oxide is 0.8 eV. However, the presence of CO_2 or further reaction intermediates can stabilise the oxide-bound H, up to the point where it becomes thermodynamically favourable compared to the metal-bound H atom.

3.2 The formate and RWGS routes

The two most commonly proposed CTM reaction mechanisms are considered here: the formate pathway with intermediates labeled F_i, and the RWGS pathway with labels R_i, Fig. 2 displaying the detailed reaction network. The elementary steps along the formate and RWGS pathways were examined at both the Zn-dilute and Zn-rich interfaces, as well as examining selected steps at the Zn interface. We highlight the differences between the systems when they are relevant but in many cases they behave very similarly. In these situations, we use the Zn-dilute interface as an example. The computed adsorption and activation energies for all interfaces are summarised in the ESI† in Table S2 and the corresponding atomic structures are shown in Fig. S8–S13.†

CO_2 to HCOO. Formate, HCOO, is formed across the interface from co-adsorbed CO_2 and H. The CO_2 is initially in its most stable geometry and the hydrogen is positioned on the metal, close to the reaction site. The diffusion of the hydrogen from its optimal geometry on surface of the Cu particle is not included in the calculations. Formate (F_{01}) binds on the ZrO_2 *via* O–Zr bonds and, unlike the CO_2, interacts only with the support as demonstrated by the long

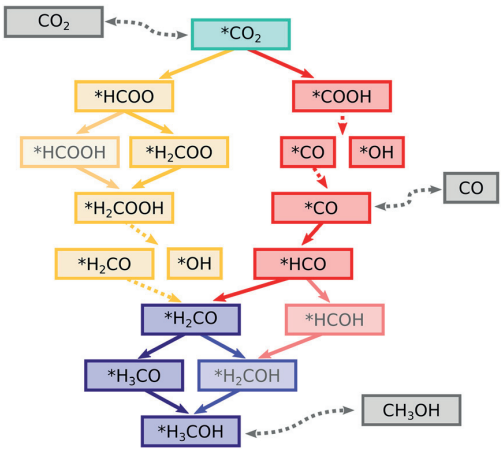

Fig. 2 The CO_2 the two most common reaction routes for the CTM reaction network. The formate route is given in yellow whereas the RWGS route is displayed in pink. Solid lines imply hydrogenation and dashed lines stand for dissociation or ad-/desorption of the intermediate. Less favourable intermediates/paths are more faintly coloured.

Zn–C distance of 3.8 Å. The reaction is exothermic by −1.2 eV and the activation energy is +1.2 eV. The energies are similar across the interface models (see Table S2†). Fig. 3 shows the atomic geometries for the initial, final, and transition states. At the transition state (TS_{01}), the hydrogen atom has migrated from the Cu–Cu bridge geometry to a Zn-top position while the C atom is still in contact with the Zn atom with a mildly elongated C–Zn bond length of 2.2 Å. The activation and reaction energies at CuZn interfaces are not significantly different compared to a Cu interface (Table S2†). The slightly lower activation energy of +1.0 eV at the Cu interface is likely due to the Cu–H interaction at the transition state being stronger than that between Zn and H. The binding geometries of CO_2 and HCOO as well as reaction energies for formate formation are similar to those reported in literature for a variety of different interfaces, *i.e.*, Cu clusters or rods on zirconia,[25,44] zirconia clusters on Cu(111),[28] and other metal–zirconia interfaces.[48] The differences can be rationalised by the structural similarities of the interfaces. In all cases, the reaction energy varies only from −0.6 to −0.7 eV. Previously reported activation energies are in the order of +0.7 eV (ref. 25 and 48) with the exception

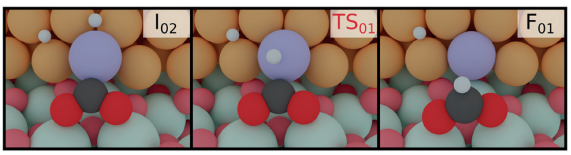

Fig. 3 Initial, transition and final state geometries for formate formation at the Zn-dilute interface. Light red: lattice O, dark red: adsorbate O, white: H, dark grey: C, purple: Zn, turquoise: Zr, orange: Cu.

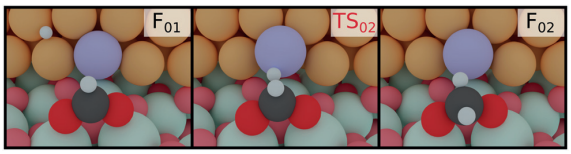

Fig. 4 Initial, transition and final state geometries for HCOO hydrogenation to H_2COO, at the Zn-dilute interface. Light red: lattice O, dark red: adsorbate O, white: H, dark grey: C, purple: Zn, turquoise: Zr, orange: Cu.

of the inverse ZrO_2 cluster on Cu(111) model[28] where the barrier was reported to be only +0.14 eV.

HCOO to H_2COO. The next reaction step in the formate route is formate hydrogenation to a dioxymethylene species (H_2COO). In this step, the hydrogen again reacts with the carbon from the metal side. To this end, the HCOO has to still be relatively close to the interface. This reaction is shown in Fig. 4. The reaction is endothermic by +0.2 eV with activation energies around +0.5 eV. In the transition state (TS_{02}), the C–H distance is around 1.5 Å, which is shorter compared to the 2.0 Å observed during formate formation (TS_{01}). The activation energies are comparable to the value of +0.5 eV that was previously computed at a Cu–$ZrO_2(\bar{2}12)$ interface.[26] The transition state geometry is also similar with a C–H distance of 1.58 Å. A study of a zirconia-supported Cu_{38} cluster reported a slightly higher barrier of *ca.* +0.7 eV (ref. 25) still suggesting a fast interconversion between the HCOO and H_2COO. Interestingly, at a model ZrO_2/ZnO interface,[21] the reaction energy for H_2COO formation is exothermic by −1.27 eV, but the activation energy of +0.66 eV is close to our values. Low activation energies reported for Cu/ZnO, Cu/ZrO_2, and ZnO/ZrO_2 interfaces are in strong contrast to the high activation energies on bare Cu surfaces. For example, the barrier on a Cu(111) surface has been reported to be 1.59 eV[27] or 0.97 eV.[43] On a stepped Cu(533) surface, the activation energy was determined to be 1.42 eV. Consequently, several computational studies[9,23,27,28,45,46] on metal surfaces and inverse oxide-on-metal models have suggested that HCOO hydrogenation leads to formic acid (HCOOH) instead. In these cases, an oxygen atom of the adsorbate and the reacting H are connected to the same component, *e.g.* the metal surface. Thus it is sensible that the formation of an O–H bond to create formic acid is more facile than the reaction with the carbon atom of the formate, which points away from the surface. We find, however, that on CuZn/ZrO_2 the reaction to HCOOH is thermodynamically and kinetically significantly less favourable than the reaction to H_2COO with an activation energy that is over 1 eV higher, as apparent in Fig. S2 and S4 (see ESI† section 1.2 for the full discussion). The difference can be explained simply by the fact that the structure of a metal-oxide interface is able to bring the reacting H and the carbon centre of the HCOO species closer together to create a more favourable pathway.

H_2COO reduction to H_2COOH and splitting into H_2CO. During the conversion of H_2COO to a hydroxymethoxy species (H_2COOH), both the H_2COO and the H_2COOH intermediates stay on the zirconia, attached by their oxygens to Zr top positions but disconnected from the interface. The reacting H atom is initially bound to a zirconia lattice oxygen near the dioxymethylene intermediate. The reaction of H_2COO to H_2COOH is exothermic in the range of −0.1 eV to −0.5 eV with moderate activation energies of *ca.* 0.5 eV at the mixed interfaces. Previous computational studies[21,25] on cluster systems (ZrO_2 on ZnO, Cu_{38} on ZrO_2) have found comparable activation energies for this step but reported the reaction to be slightly endothermic, likely due to a stabilising effect of the zirconia surface.

The next step on is the dissociation of H_2COOH into hydroxyl (OH) and formaldehyde (H_2CO). This reaction shows significant energetic variation depending on the interface, being practically thermoneutral at the Zn-dilute and Zn interfaces, and slightly endothermic by +0.2 eV at the Zn-rich interface. At the Cu interface, the reaction is more endothermic by ∼+0.4 eV, due to the weaker adsorption of the formaldehyde. The activation barriers are in the order of +0.2 to +0.5 eV. A previous study[80] found the reaction and activation energies on a Zn-decorated Cu(211) surface to be similarly slightly endothermic with a low barrier. When the C–O bond is broken, the OH part remains bound to a Zr-top site whereas the H_2CO (F_{06}), while still attached to an oxide cation *via* its oxygen, tilts toward the nearby interface and binds to a Zn *via* its C atom. The resulting C–Zn distance of 2.17 Å is similar to that of activated CO_2. The Zn atom is again slightly pulled out from the ideal position and there is no significant energy difference regarding which of the two neighbouring Zr atoms the oxygen atom binds to. Alternatively, H_2COOH may hydrogenate to methanediol H_2-COHOH (F_{07}). However, we found the activation energy of +0.9 eV to be clearly higher than that of the dissociation. Therefore, the pathway was not considered further.

The full potential energy diagram of CTM through the formate mechanism is shown in Fig. 5. The final steps from H_2CO to methanol are shared between both the formate and the RWGS route.

CO_2 to COOH. The RWGS route begins with the formation and subsequent dissociation of a carboxyl intermediate (COOH) at the metal-oxide interface. Starting from the adsorbed CO_2 and dissociated H, the reacting H atom must be spilled from the metal to the oxide surface, from where it reacts with an oxygen atom of the CO_2 molecule (see Fig. 6). Attempts to make the H react directly from the metallic component to the CO_2 oxygen were not successful. The resulting COOH intermediate (R_{01}) binds to the metal *via* the C atom and to the oxide *via* both O atoms the same way as CO_2 does. This is in contrast to the formate, which detaches from the interface. The formation of COOH at the CuZn interfaces is endothermic by approximately 0.4 eV, and has a moderate +0.7 eV barrier (see ESI,† Table S2, TS_{11} onward). In contrast, the reaction barrier is 1.8 eV for a CuZn-bound H,

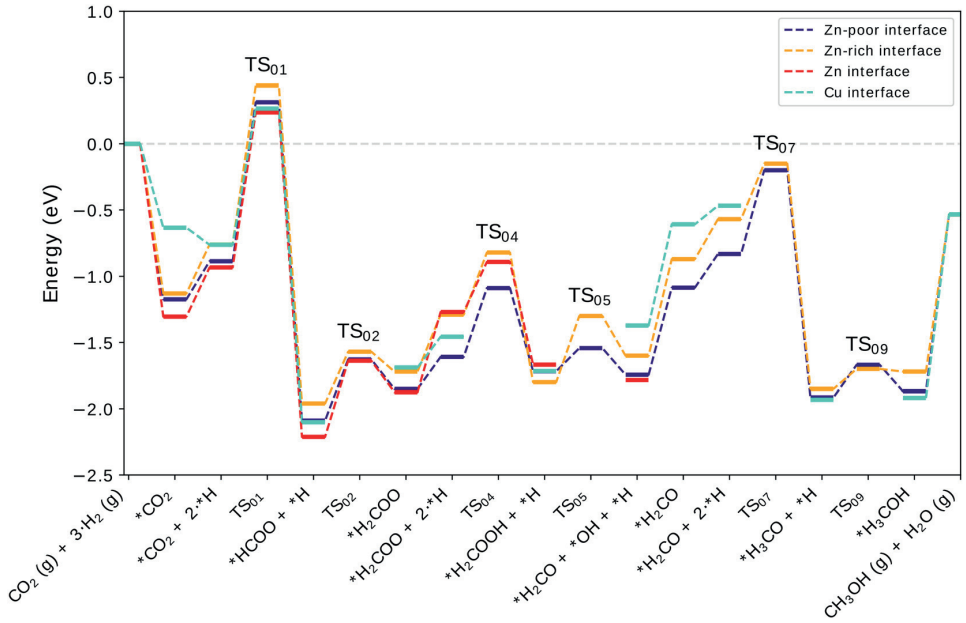

Fig. 5 Potential energy diagrams of the formate route for CO_2 hydrogenation to methanol. Dissociative adsorption steps of hydrogens are not included as they are assumed to be available.

which would severely hinder the RWGS mechanism. Employing the oxide-bound H also minimises the distance that the H atom needs to move to form the new O–H bond.

The COOH is thermodynamically less stable by *ca.* 1.5 eV compared to the HCOO intermediate but the activation energy for COOH formation is 0.5 eV lower. A similar 1.4 eV difference in adsorption was found at a Cu_{38}/ZrO_2 interface.[25] However, in that case the H reacted directly from the Cu_{38} cluster which corresponds to an activation energy of around +2 eV which is 1.2 eV higher than that of the formate formation. These activation energies and their differences are in line with our results but the case where H reacts from the oxide was not previously included.

COOH dissociation. The COOH species dissociates into carbon monoxide (CO) and an OH group that end up bound to adjacent Zr atoms (see R_{02} in Fig. S9–S13†). In the transition state, the CO is bound to a Zr cation *via* its O atom while having a 2.2 Å C–Zn distance and a 1.8 Å C–OH distance. After the reaction is complete, the CO can stay physisorbed on the zirconia surface at a C–Zr distance of 2.8 Å or diffuse to bind at the interface. In both cases the CO adsorption energy is very similar and in the order of −0.5 eV. Bader analysis gives the OH group a charge of ≃0.7 e, pointing to it having an anionic character, while the CO adsorbed at the interface is neutral. The COOH splitting reaction is exothermic by ≃0.1 eV and its activation energy is *ca.* 0.2 eV at the mixed interfaces. At the Cu interface, the reaction energy increases to −0.4 eV due to the CO binding more strongly to Cu than to Zn. A previous study on Cu(111)[27] shows a +0.42 eV activation energy for the dissociation of COOH, while the reaction energy remains slightly exothermic by −0.14 eV.

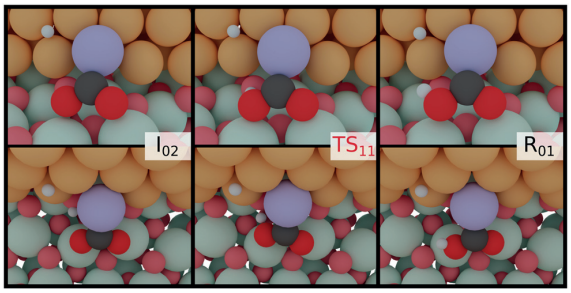

Fig. 6 CO_2 hydrogenation to COOH at the Zn-dilute interface. Light red: lattice O, dark red: adsorbate O, white: H, dark grey: C, purple: Zn, turquoise: Zr, orange: Cu.

CO to HCO. To produce a formyl (HCO) intermediate, a H atom moves in from the metal component to the C atom of a CO adsorbed at the interface (TS_{13} and R_{03} in Fig. S9–S13†). During the reaction, the C–Zn distance shortens to ∼2.1 Å, from the initial values ranging between 2.5 Å at the Zn-rich interface and 4.1 Å at the Zn-dilute. The reaction is exothermic by −0.4 eV, on average, and is accompanied by barriers ranging from 0.32 eV at the Zn-rich interface to 0.67 eV at the Zn interface. We note that these results were obtained in the presence of a bystander OH. We explored COH formation as an alternative but found it endothermic by +0.65 eV—that is—more than 1 eV less stable compared to HCO. Therefore this option was not explored further.

In some previous studies, the formation of HCO has had a different character compared to our $CuZn/ZrO_2$ results.

Namely, on a Cu(111) surface,[27] the reaction is endothermic by +0.78 eV and has an activation energy of almost +1 eV. Furthermore, on an inverse ZnO/Cu model, the reaction is endothermic by +0.39 eV and the barrier is +0.88 eV.[23] These differences point to HCO adsorbing less strongly to Cu surfaces, and to the stabilising effect of the interface.

HCO to H_2CO. We start the reaction of HCO hydrogenation to H_2CO from a position where the molecule is connected to the interface *via* a C–Zn bond its oxygen rests on a Zr cation. Once again, the H preferably reacts from the metal side of the interface to the C atom rather than from the oxide. Both the intermediates and the transition state (TS_{14}) keep contact to the metal *via* a C–Zn bond while the OH group, if kept in the vicinity, remains a spectator. The reaction is exothermic by −0.9 eV to −1.2 eV on CuZn interfaces. At the Cu interface, the reaction energy is −0.7 eV, due to the slightly weaker binding of HCO compared to the CuZn interfaces. The reaction has an activation energy of +0.3–0.5 eV. This is close to the inverse ZnO/Cu model,[23] where the activation energy is +0.25 eV. The other reaction that HCO could participate in is the formation of hydroxymethylene (HCOH, R_{06}), which we found to be endothermic with a 0.9 eV kinetic barrier (visible in Fig. S5†), similar to the results on Cu(111).[27] See section 1.3 in ESI† for full discussion. The full potential energy diagram of the RWGS route for the Zn-dilute interface is shown in Fig. 7.

3.3 Formaldehyde hydrogenation to methanol

The formate and RWGS pathways discussed above merge after the formation of formaldehyde (H_2CO). This species is stable, as the adsorption energy of H_2CO relative to formaldehyde in the gas phase is −1.4 eV. Next, we address two different ways to progress from H_2CO onward by considering the options of removing and keeping the ZrO_2-bound OH group produced during the previous reaction steps. This is done to investigate the influence of OH on reaction energetics, as it could have a co-catalysing effect *via* hydrogen bonds or due to its Lewis acidity. The removal of the OH from the zirconia can take place *via* H_2O formation and desorption, which is endothermic by +0.7 eV on average. A previous study[48] showed no kinetic barriers for the dissociative adsorption of water on ZrO_2 and therefore its desorption likely does not have a kinetic barrier either. For brevity, these two routes are shown in the PES diagrams of the previously discussed formate and RWGS pathways. The case where OH has been removed is shown in the diagram of the formate route (Fig. 5) whereas the OH is kept on the surface at the end of the RWGS path in Fig. 7.

H_2CO to H_3CO. Formaldehyde preferably adsorbs at the interface with its carbon attached to the Zn site and the oxygen on a Zr top site. The hydrogens of the H_2CO are bent away from the interface leaving the carbon with an sp^3-like geometry which shows that the formaldehyde is electronically activated. The reacting H is again sitting on the metal component.

Upon hydrogenation to methoxy (H_3CO), the bond between the product and the metal at the interface is broken and the methoxy binds solely to ZrO_2 *via* its O atom. The reaction is exothermic by −1 eV and requires an activation energy of 0.4–0.6 eV. In this case, the influence of the ZrO_2-bound OH is rather insignificant as the reaction and

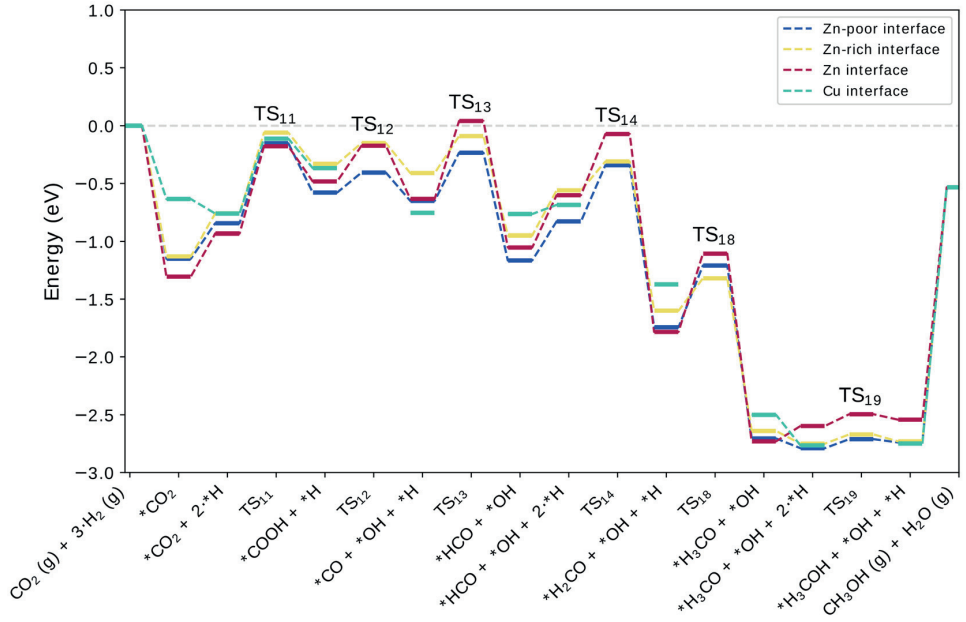

Fig. 7 Potential energy diagrams of the RWGS path. States from H_2CO forward include an OH on the zirconia surface.

activation energies are similar to those without OH. In previous studies, the reaction was practically thermoneutral on Cu(111)[27] and exothermic by −0.67 eV on an inverse ZnO/Cu system.[23] The kinetic barriers at the CuZn interfaces are higher than those found on the Cu(111) and inverse ZnO/Cu surfaces where in both cases an activation energy ~+0.2 eV was reported. This may simply be due to more favourable adsorption and transition state geometries. We also studied the alternative pathway forward *via* the formation and hydrogenation of hydroxymethyl (H_2COH) but found that it is significantly less favourable due to its relative instability and high activation barriers as seen in Fig. S2–S5.† Discussion of this pathway can be found in the ESI† section 1.3.

H_3CO to H_3COH. In the final step of both pathways, the reacting hydrogen transfers from the support oxide to the methoxy to form methanol. The reaction energy is practically thermoneutral and in all cases there is likely a fast interconversion between the methoxy and methanol species. The influence of surface OH on the reaction barrier is minor as the activation energy is *ca.* 0.1 eV with OH present and only a slightly higher ~0.2 eV without (TS_{19} *vs.* TS_{09}). The methanol product binds solely to the ZrO_2 surface, on a Zr top site *via* its oxygen atom. The desorption of methanol into the gas phase does not have an activation barrier but requires a desorption energy of ~1.3 eV. Alternatively, methanol can decompose into a methyl (H_3C) and an OH species with an activation energy quite close to the desorption energy. However, the splitting is clearly endothermic at most interfaces and thus unlikely, although small amounts of methane are observed in experiments.[3,34] A complete discussion of the splitting can be found in section 1.4 of the ESI.† The desorption of both methanol and water is endothermic by +2.2 eV, which leads to an overall reaction energy of −0.53 eV for the completed reaction cycle. Because of the stability of dissociated water on the zirconia surface, some of it will accumulate on the surface as the reaction cycles.

3.4 Potential energy landscape

Fig. 8 shows the potential energy profiles for the formate and RWGS pathways. At the Zn-dilute interface, the formate pathway exhibits lower energies and thus appears thermodynamically more stable as compared to the RWGS pathway. However, accessibility of the formate pathway is limited by the major barrier (TS_{01}) for HCOO formation which is energetically well in line with previous computational studies that have considered CuZn surfaces or Cu cluster models.[23,25] Despite the strong binding of formate, it does not severely poison the CuZn/ZrO_2 interface. This is because it readily reacts onward to H_2COO with a barrier around +0.4 eV. After a further hydrogenation to H_2COOH, the reaction proceeds *via* decomposition into H_2CO and a surface-bound OH group, which is removed to the gas phase as water. According to activation energies, the formation of H_2COH is favoured over H_3CO. However, the activation

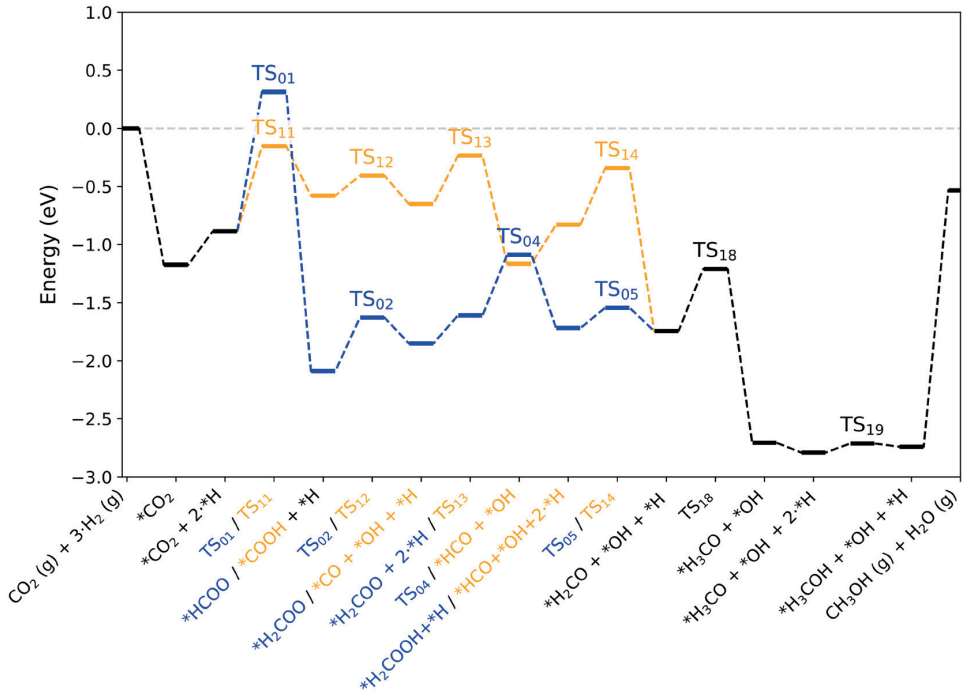

Fig. 8 Potential energy diagram of both the formate and the RWGS paths (Zn-dilute interface). States from H_2CO forward include an OH on the zirconia surface.

energy required for the final hydrogenation step from H_2COH to methanol is considerably larger than that from methoxy, which in turn favours the path through the H_3CO intermediate. Therefore, the methoxy intermediate is likely the dominant one, similar to what previous computational studies have suggested on both cluster and surface models.[23,25,27] In general, intermediates along the formate pathway tend to be slightly more stable at the Zn interface than the Zn-dilute and the Zn-rich interfaces (see Fig. 5). Overall, the variation in energy is modest with the largest difference being 0.25 eV in the case of the formate species.

Along the RWGS pathway, the activation energies are in general lower than those of the formate route. The carboxyl intermediate readily dissociates into OH and CO. At the interface, CO prefers to bind to a Cu site over a geometrically equivalent Zn site and can easily diffuse to a neighbouring Cu or even onto the ZrO_2 surface with no energy penalty. CO converts to HCO and H_2CO at a low energy cost. From this point, the reactions proceed similarly to the formate pathway. Again, the nearly non-existent barrier from H_3CO to methanol would suggest that the methoxy intermediate is dominant over H_2COH. In the case of the RWGS pathway, we often see the Zn-dilute interface with the most stable intermediates. The largest difference occurs for the COOH species with 0.27 eV energy difference between the Zn-dilute and Zn-rich interface. A possible explanation for these small trends between different Zn concentrations could lie in the increased mobility of Zn atoms going from Zn-dilute to the full-Zn interface.

The CuZn interfaces bind several intermediates stronger than the Cu interface does, including CO_2, COOH, HCO, HCOH, H_2CO, and H_2COH. The commonality between these intermediates is that they are bound at the interface, connected to the metal component *via* a Zn–C bond, and most of them are found along the RWGS pathway. Zn centers bind these adsorbates, on average, 0.4 eV stronger than geometrically equivalent adsorption sites at the Cu interface. The important exception to this is carbon monoxide, CO, which is adsorbed 0.1 to 0.3 eV stronger to Cu sites. We also note that a hydrogen placed in the immediate vicinity of the Zn center weakens the adsorption of all aforementioned intermediates and brings the adsorption energies roughly 0.3 eV closer to those at the Cu interface. Intermediates that preferably bind to the support are largely unaffected by the presence of Zn and its concentration.

3.5 Energetic span analysis

The results given by the energetic span model allow us to compare the competing formate and RWGS mechanisms. We note that the predicted turnover frequencies are unlikely directly comparable to experimental numbers.[78,79,81] They are, however, representative of the relative kinetics of the two pathways. The analysis was done separately for the Zn-dilute and Zn-rich interfaces. The relative energies in Table S2 were used as inputs and the model was run at 500 K. To obtain reliable results and to avoid problems with coverage effects, we limit the ESM analysis to competing pathways with the same number of atoms. Therefore the model can not be used to assess if the presence of OH groups speeds up latter reaction steps and they are left out of the following discussion. The endothermicity of the CO production and release also prevents its examination using the computational code of Garay-Ruiz and Bo[81] as an endothermic (endergonic) cycle would lead to a negative TOF.[78,79] Nevertheless, CO is observed in most real-world CTM systems.[3,19] The production of CO is likely controlled, to some extent, by its endothermic nature and the fact that typical reaction conditions include high pressures.

In the terminology of the ESM, the formate and RWGS pathways are competing catalytic cycles. Both pathways are combined and presented as a network graph in Fig. 9a), labelling each intermediate state as a node and each transition state as a line. Starting from the left by adsorption of CO_2, the network is simplified and categorised by ignoring side branches or processes such as CO desorption. The four cycles given in Fig. 9b) feature the mechanisms with the highest turnover frequencies. The analogous Fig. S14 in the ESI† represents the Zn-rich interface. Cycles 1 and 2 follow the RWGS pathway, while Cycles 3 and 4 progress along the

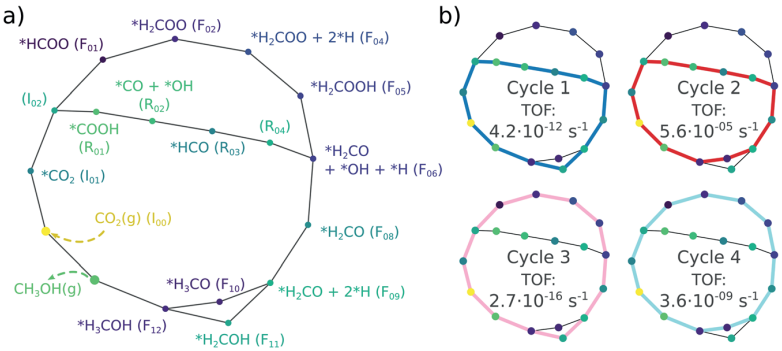

Fig. 9 a) The simplified network used in the energetic span analysis. b) The catalytic cycles in the simplified network with their corresponding turnover frequencies on the Zn-dilute interface.

formate route. Furthermore, cycles 1 and 3 progress *via* the H_2COH intermediate while cycles 2 and 4 go through the formation of H_3CO instead.

Cycle 2, *i.e.* the RWGS route with methanol formed from H_3CO, yields the highest TOF of the four cycles. Accordingly, the energetic span is lowest, being 1.89 eV at the Zn-dilute interface and 1.81 eV at the Zn-rich. The corresponding calculated turnover frequencies are 5.6×10^{-5} s^{-1} and 2.9×10^{-4} s^{-1}, respectively, showing a relatively high degree of sensitivity to the change in δE. The next highest TOF belongs to cycle 4 representing the formate/H_3CO pathway where the effective energetic span is 0.48 eV higher. Cycles 1 and 3 which go through H_2COH have to pass a very high transition state, which becomes TOF-determining, and thus have significantly higher energetic spans and lower turnover frequencies.

A degree of turnover frequency control X_{TOF} analysis (detailed in the ESI† section 3) confirms that the formate acts as a thermodynamic sink. The X_{TOF} for HCOO is practically 1 in all unique cycles of the network (Fig. 9), indicating a large degree of turnover frequency control. Near the calculated formate energy, its effect on the TOF of cycle 2 (eqn (8)) is 1.2×10^{-3} s^{-1} eV^{-1}. Note that, as described earlier, the presence of Zn sites at the interface does not affect the stability of the formate. Assigning the TOF-limiting transition states depends on the cycle. The transition state from H_2COH to CH_3OH (TS_{10}), present only in cycles 1 and 3, has the highest degree of TOF control owing to its significantly high activation energy. In cycles 2 and 4 the transition state from H_2CO to H_3CO (TS_{07}) takes dominance. In cycle 4, corresponding to a formate mechanism, the TS_{01} from CO_2 to HCOO also has some TOF-controlling character with a $X_{TOF}^{(TS_{01})}$ of 0.32. The influence of TS_{10} on cycle 1 (eqn (7)) is -9.0×10^{-11} s^{-1} eV^{-1} and the influence of TS_{07} on cycle 2 is -1.2×10^{-3} s^{-1} eV^{-1} near the calculated energies. Interestingly, all these elementary steps take place at the interface. Based on the energetic span analysis, we can conclude that the RWGS pathway is more favourable compared to the formate pathway, and that the last steps clearly involve the methoxy intermediate.

4 Conclusions

We have employed DFT calculations to obtain a thermodynamic and kinetic view of CO_2 hydrogenation to methanol using a Cu/Zn/ZrO_2 catalyst. To this end, we constructed a mixed CuZn/ZrO_2 interface model using Cu nanorods with a varying Zn concentration at the interface. Our results show that intermediates binding to metal atoms at the interface adsorb stronger to Zn sites than to geometrically equivalent Cu sites. Enhanced binding is visible for all the studied Zn configurations and most pronounced on the interface where the Zn solute is the most dispersed. CO is the one exception to this trend as it preferentially binds to Cu sites. The addition of Zn at the interface has minimal effect on intermediates that do not bind to the metallic component, including some key intermediates such as the formate and methoxy species. Comparison between the four considered interface models shows that the reaction steps are not very sensitive to the concentration and arrangement of Zn at the interface. Zinc centers are active regardless of the identity of their surrounding atoms.

A graph-based energetic span analysis can provide estimates for turnover frequencies to compare the competing mechanisms. Analysing the catalytic cycle as a whole allows us to identify the TOF-determining intermediates and transition states. The results support the RWGS route being the main CTM pathway. This can be explained by smaller reaction barriers along the RWGS mechanisms. Considering hydrogen spillover from the metal component to the support oxide is necessary as it facilitates the protonation of the surface-bound oxygen atoms of the intermediates. By including spillover, the barriers for the formation of several intermediates, notably carboxyl (COOH), become much lower than previously reported making the RWGS route more accessible.

Incorporating a Zn promoter into the interface structure selectively stabilises some intermediates, highlighting the importance of the effort to identify key intermediates and transition states. As Zn binds H less strongly, the role of the Cu is in hydrogen dissociation, storage, and spillover as well as enhancing CO binding. An increased understanding of promoter–adsorbate interactions allows tailoring of catalyst properties to influence adsorbate binding, which is important for selectivity and yield.

Conflicts of interest

The authors have no conflicts to declare.

Acknowledgements

The work was funded by Academy of Finland (project 329977). The electronic structure calculations were made possible by computational resources provided by the CSC – IT Center for Science, Espoo, Finland (**https://www.csc.fi/en/**) and computer capacity from the Finnish Grid and Cloud Infrastructure (urn:nbn:fi:research-infras-2016072533). Dr Minttu Kauppinen is acknowledged for carefully reading the manuscript.

References

1 G. A. Olah, G. K. S. Prakash and A. Goeppert, *J. Am. Chem. Soc.*, 2011, **133**, 12881–12898.
2 G. A. Olah, *Angew. Chem., Int. Ed.*, 2013, **52**, 104–107.
3 S. Kattel, P. Liu and J. G. Chen, *J. Am. Chem. Soc.*, 2017, **139**, 9739–9754.
4 K. Li and J. G. Chen, *ACS Catal.*, 2019, **9**, 7840–7861.
5 S. Roy, A. Cherevotan and S. C. Peter, *ACS Energy Lett.*, 2018, **3**, 1938–1966.
6 B. M. Tackett, E. Gomez and J. G. Chen, *Nat. Catal.*, 2019, **2**, 381–386.

7 R. P. Ye, J. Ding, W. Gong, M. D. Argyle, Q. Zhong, Y. Wang, C. K. Russell, Z. Xu, A. G. Russell, Q. Li, M. Fan and Y. G. Yao, *Nat. Commun.*, 2019, **10**, 5698.
8 J. Artz, T. E. Müller, K. Thenert, J. Kleinekorte, R. Meys, A. Sternberg, A. Bardow and W. Leitner, *Chem. Rev.*, 2018, **118**, 434–504.
9 M. Behrens, F. Studt, I. Kasatkin, S. Kühl, M. Hävecker, F. Abild-Pedersen, S. Zander, F. Girgsdies, P. Kurr, B.-L. Kniep, M. Tovar, R. W. Fischer, J. K. Nørskov and R. Schlögl, *Science*, 2012, **336**, 893–897.
10 S. Kuld, M. Thorhauge, H. Falsig, C. F. Elkjær, S. Helveg, I. Chorkendorff and J. Sehested, *Science*, 2016, **352**, 969–974.
11 S. Zander, E. L. Kunkes, M. E. Schuster, J. Schumann, G. Weinberg, D. Teschner, N. Jacobsen, R. Schlögl and M. Behrens, *Angew. Chem., Int. Ed.*, 2013, **52**, 6536–6540.
12 P. L. Hansen, J. B. Wagner, S. Helveg, J. R. Rostrup-Nielsen, B. S. Clausen and H. Topsøe, *Science*, 2002, **295**, 2053–2055.
13 J. D. Grunwaldt, A. M. Molenbroek, N. Y. Topsøe, H. Topsøe and B. S. Clausen, *J. Catal.*, 2000, **194**, 452–460.
14 H. Zhao, R. Yu, S. Ma, K. Xu, Y. Chen, K. Jiang, Y. Fang, C. Zhu, X. Liu, Y. Tang, L. Wu, Y. Wu, Q. Jiang, P. He, Z. Liu and L. Tan, *Nat. Catal.*, 2022, **5**, 818–831.
15 O. Martin, A. J. Martín, C. Mondelli, S. Mitchell, T. F. Segawa, R. Hauert, C. Drouilly, D. Curulla-Ferré and J. Pérez-Ramírez, *Angew. Chem., Int. Ed.*, 2016, **55**, 6261–6265.
16 A. Bavykina, I. Yarulina, A. J. Al Abdulghani, L. Gevers, M. N. Hedhili, X. Miao, A. R. Galilea, A. Pustovarenko, A. Dikhtiarenko, A. Cadiau, A. Aguilar-Tapia, J. L. Hazemann, S. M. Kozlov, S. Oud-Chikh, L. Cavallo and J. Gascon, *ACS Catal.*, 2019, **9**, 6910–6918.
17 S. Kattel, W. Yu, X. Yang, B. Yan, Y. Huang, W. Wan, P. Liu and J. G. Chen, *Angew. Chem., Int. Ed.*, 2016, **55**, 7968–7973.
18 M. R. Gogate and R. J. Davis, *Catal. Commun.*, 2010, **11**, 901–906.
19 X. Jiang, X. Nie, X. Guo, C. Song and J. G. Chen, *Chem. Rev.*, 2020, **120**, 7984–8034.
20 T. Lunkenbein, J. Schumann, M. Behrens, R. Schlögl and M. G. Willinger, *Angew. Chem., Int. Ed.*, 2015, **54**, 4544–4548.
21 Y. Wang, S. Kattel, W. Gao, K. Li, P. Liu, J. G. Chen and H. Wang, *Nat. Commun.*, 2019, **10**, 1166.
22 M. Zabilskiy, V. L. Sushkevich, D. Palagin, M. A. Newton, F. Krumeich and J. A. van Bokhoven, *Nat. Commun.*, 2020, **11**, 2409.
23 S. Kattel, P. J. Ramírez, J. G. Chen, J. A. Rodriguez and P. Liu, *Science*, 2017, **355**, 1296–1299.
24 N. Scotti, F. Bossola, F. Zaccheria and N. Ravasio, *Catalysts*, 2020, **10**, 168.
25 K. Larmier, W.-C. C. Liao, S. Tada, E. Lam, R. Verel, A. Bansode, A. Urakawa, A. Comas-Vives and C. Copéret, *Angew. Chem., Int. Ed.*, 2017, **56**, 2318–2323.
26 Q.-L. Tang, Q.-J. Hong and Z.-P. Liu, *J. Catal.*, 2009, **263**, 114–122.
27 L. C. Grabow and M. Mavrikakis, *ACS Catal.*, 2011, **1**, 365–384.
28 S. Kattel, B. Yan, Y. Yang, J. G. Chen and P. Liu, *J. Am. Chem. Soc.*, 2016, **138**, 12440–12450.
29 T. Witoon, J. Chalorngtham, P. Dumrongbunditkul, M. Chareonpanich and J. Limtrakul, *Chem. Eng. J.*, 2016, **293**, 327–336.
30 Y. Nitta, O. Suwata, Y. Ikeda, Y. Okamoto and T. Imanaka, *Catal. Lett.*, 1994, **26**, 345–354.
31 D. Gasser and A. Baiker, *Appl. Catal.*, 1989, **48**, 279–294.
32 J. Weigel, R. A. Koeppel, A. Baiker and A. Wokaun, *Langmuir*, 1996, **12**, 5319–5329.
33 I. Abbas, H. Kim, C. H. Shin, S. Yoon and K. D. Jung, *Appl. Catal., B*, 2019, **258**, 117971.
34 A. Arandia, J. Yim, H. Warraich, E. Leppäkangas, R. Bes, A. Lempelto, L. Gell, H. Jiang, K. Meinander, T. Viinikainen, S. Huotari, K. Honkala and R. L. Puurunen, *Appl. Catal., B*, 2023, **321**, 122046.
35 J. Sehested, *J. Catal.*, 2019, **371**, 368–375.
36 J. Nakamura, I. Nakamura, T. Uchijima, T. Watanabe and T. Fujitani, *Stud. Surf. Sci. Catal.*, 1996, **101 B**, 1389–1399.
37 S. Kattel, P. J. Ramírez, J. G. Chen, J. A. Rodriguez and P. Liu, *Science*, 2017, **357**, eaan8210.
38 J. Nakamura, Y. Choi and T. Fujitani, *Top. Catal.*, 2003, **22**, 277–285.
39 J. Nakamura, T. Fujitani, S. Kuld, S. Helveg, I. Chorkendorff and J. Sehested, *Science*, 2017, **357**, eaan8074.
40 N. Y. Topsøe and H. Topsøe, *Top. Catal.*, 1999, **8**, 267–270.
41 P. Amann, B. Klötzer, D. Degerman, N. Köpfle, T. Götsch, P. Lömker, C. Rameshan, K. Ploner, D. Bikaljevic, H.-Y. Wang, M. Soldemo, M. Shipilin, C. M. Goodwin, J. Gladh, J. H. Stenlid, M. Börner, C. Schlueter and A. Nilsson, *Science*, 2022, **376**, 603–608.
42 E. Frei, A. Gaur, H. Lichtenberg, L. Zwiener, M. Scherzer, F. Girgsdies, T. Lunkenbein and R. Schlögl, *ChemCatChem*, 2020, **12**, 4029–4033.
43 D. Kopač, B. Likozar and M. Huš, *Appl. Surf. Sci.*, 2019, **497**, 143783.
44 S. Polierer, J. Jelic, S. Pitter and F. Studt, *J. Phys. Chem. C*, 2019, **123**, 26904–26911.
45 A. Cao, Z. Wang, H. Li, A. O. Elnabawy and J. K. Nørskov, *J. Catal.*, 2021, **400**, 325–331.
46 M. Kauppinen, A. Posada-Borbón and H. Grönbeck, *J. Phys. Chem. C*, 2022, **126**, 15235–15246.
47 L. Gell, A. Lempelto, T. Kiljunen and K. Honkala, *J. Chem. Phys.*, 2021, **154**, 214707.
48 M. M. Kauppinen, M. M. Melander, A. S. Bazhenov and K. Honkala, *ACS Catal.*, 2018, **8**, 11633–11647.
49 B. C. Dharmalingam, A. V. Koushik, M. Mureddu, L. Atzori, S. Lai, A. Pettinau, N. S. Kaisare, P. Aghalayam and J. J. Varghese, *Appl. Catal., B*, 2023, **332**, 122743.
50 X. Liu, J. Luo, H. Wang, L. Huang, S. Wang, S. Li, Z. Sun, F. Sun, Z. Jiang, S. Wei, W. Li and J. Lu, *Angew. Chem.*, 2022, **61**, e202202330.
51 E. L. Fornero, A. L. Bonivardi and M. A. Baltanás, *J. Catal.*, 2015, **330**, 302–310.
52 J. M. Campbell and C. T. Campbell, *Surf. Sci.*, 1991, **259**, 1–17.
53 S. Sakong and A. Groß, *Surf. Sci.*, 2003, **525**, 107–118.
54 K. D. Jung and A. T. Bell, *J. Catal.*, 2000, **193**, 207–223.

55 M. D. Rhodes, K. A. Pokrovski and A. T. Bell, *J. Catal.*, 2005, **233**, 210–220.
56 R. Prins, *Chem. Rev.*, 2012, **112**, 2714–2738.
57 H. Y. T. Chen, S. Tosoni and G. Pacchioni, *ACS Catal.*, 2015, **5**, 5486–5495.
58 M. M. Bettahar, *Catal. Rev.: Sci. Eng.*, 2022, **64**, 87–125.
59 J. Wellendorff, K. T. Lundgaard, A. Møgelhøj, V. Petzold, D. D. Landis, J. K. Nørskov, T. Bligaard and K. W. Jacobsen, *Phys. Rev. B: Condens. Matter Mater. Phys.*, 2012, **85**, 235149.
60 P. E. Blöchl, *Phys. Rev. B: Condens. Matter Mater. Phys.*, 1994, **50**, 17953–17979.
61 J. Enkovaara, C. Rostgaard, J. J. Mortensen, J. Chen, M. Dułak, L. Ferrighi, J. Gavnholt, C. Glinsvad, V. Haikola, H. A. Hansen, H. H. Kristoffersen, M. Kuisma, A. H. Larsen, L. Lehtovaara, M. Ljungberg, O. Lopez-Acevedo, P. G. Moses, J. Ojanen, T. Olsen, V. Petzold, N. A. Romero, J. Stausholm-Møller, M. Strange, G. A. Tritsaris, M. Vanin, M. Walter, B. Hammer, H. Häkkinen, G. K. H. Madsen, R. M. Nieminen, J. K. Nørskov, M. Puska, T. T. Rantala, J. Schiøtz, K. S. Thygesen and K. W. Jacobsen, *J. Phys.: Condens. Matter*, 2010, **22**, 253202.
62 S. L. Dudarev, G. A. Botton, S. Y. Savrasov, C. J. Humphreys and A. P. Sutton, *Phys. Rev. B: Condens. Matter Mater. Phys.*, 1998, **57**, 1505–1509.
63 V. Korpelin, M. M. Melander and K. Honkala, *J. Phys. Chem. C*, 2022, **126**, 933–945.
64 A. R. Puigdollers, F. Illas and G. Pacchioni, *J. Phys. Chem. C*, 2016, **120**, 17604–17612.
65 J.-H. Lan, L. Wang, S. Li, L.-Y. Yuan, Y.-X. Feng, W. Sun, Y.-L. Zhao, Z.-F. Chai and W.-Q. Shi, *J. Appl. Phys.*, 2013, **113**, 183514.
66 H. Koga, A. Hayashi, Y. Ato, K. Tada, S. Hosokawa, T. Tanaka and M. Okumura, *Appl. Surf. Sci.*, 2020, **508**, 145252.
67 O. A. Syzgantseva, M. Calatayud and C. Minot, *J. Phys. Chem. C*, 2012, **116**, 6636–6644.
68 A. H. Larsen, J. J. Mortensen, J. Blomqvist, I. E. Castelli, R. Christensen, M. Dułak, J. Friis, M. N. Groves, B. Hammer, C. Hargus, E. D. Hermes, P. C. Jennings, P. B. Jensen, J. Kermode, J. R. Kitchin, E. L. Kolsbjerg, J. Kubal, K. Kaasbjerg, S. Lysgaard, J. B. Maronsson, T. Maxson, T. Olsen, L. Pastewka, A. Peterson, C. Rostgaard, J. Schiøtz, O. Schütt, M. Strange, K. S. Thygesen, T. Vegge, L. Vilhelmsen, M. Walter, Z. Zeng and K. W. Jacobsen, *J. Phys.: Condens. Matter*, 2017, **29**, 273002.
69 E. Bitzek, P. Koskinen, F. Gähler, M. Moseler and P. Gumbsch, *Phys. Rev. Lett.*, 2006, **97**, 170201.
70 G. Henkelman, B. P. Uberuaga and H. Jónsson, *J. Chem. Phys.*, 2000, **113**, 9901–9904.
71 G. Henkelman and H. Jónsson, *J. Chem. Phys.*, 2000, **113**, 9978–9985.
72 T. Frederiksen, M. Paulsson, M. Brandbyge and A.-P. Jauho, *Phys. Rev. B: Condens. Matter Mater. Phys.*, 2007, **75**, 205413.
73 R. F. W. Bader, *Atoms in Molecules: A Quantum Theory*, Oxford University Press, Oxford, 1990.
74 W. Tang, E. Sanville and G. Henkelman, *J. Phys.: Condens. Matter*, 2009, **21**, 084204.
75 M. Rühle, *Adv. Mater.*, 1997, **9**, 195–217.
76 K. T. Jung and A. T. Bell, *Catal. Lett.*, 2002, **80**, 63–68.
77 J. S. Faulkner, Y. Wang and G. M. Stocks, *Phys. Rev. Lett.*, 1998, **81**, 1905–1908.
78 S. Kozuch and S. Shaik, *Acc. Chem. Res.*, 2011, **44**, 101–110.
79 S. Kozuch, *ACS Catal.*, 2015, **5**, 5242–5255.
80 F. Studt, M. Behrens, E. L. Kunkes, N. Thomas, S. Zander, A. Tarasov, J. Schumann, E. Frei, J. B. Varley, F. Abild-Pedersen, J. K. Nørskov and R. Schlögl, *ChemCatChem*, 2015, **7**, 1105–1111.
81 D. Garay-Ruiz and C. Bo, *ACS Catal.*, 2020, **10**, 12627–12635.
82 H.-J. Chun, V. Apaja, A. Clayborne, K. Honkala and J. Greeley, *ACS Catal.*, 2017, **7**, 3869–3882.
83 D. Garay-Ruiz, *gTOFfee*, **https://gitlab.com/dgarayr/gtoffee**, (Feb. 2022).
84 A. Posada-Borbón, B. Hagman, A. Schaefer, C. Zhang, M. Shipilin, A. Hellman, J. Gustafson and H. Grönbeck, *Surf. Sci.*, 2018, **675**, 64–69.
85 B. Hagman, A. Posada-Borbón, A. Schaefer, M. Shipilin, C. Zhang, L. R. Merte, A. Hellman, E. Lundgren, H. Grönbeck and J. Gustafson, *J. Am. Chem. Soc.*, 2018, **140**, 12974–12979.
86 B. Eren, R. S. Weatherup, N. Liakakos, G. A. Somorjai and M. Salmeron, *J. Am. Chem. Soc.*, 2016, **138**, 8207–8211.

IV

COMPUTATIONAL EXPLORATION OF SUBNANO ZN AND CU SPECIES ON CU/ZRO_2: IMPLICATIONS FOR METHANOL SYNTHESIS

by

Lempelto. A.; Kauppinen, M.; Honkala, K.

J. Phys. Chem. C 2024, 128, 9492

https://doi.org/10.1021/acs.jpcc.4c01300

THE JOURNAL OF PHYSICAL CHEMISTRY C
A JOURNAL OF THE AMERICAN CHEMICAL SOCIETY

pubs.acs.org/JPCC Article

Computational Exploration of Subnano Zn and Cu Species on Cu/ZrO_2: Implications for Methanol Synthesis

Published as part of The Journal of Physical Chemistry C virtual special issue "Jens K. Nørskov Festschrift".

Aku Lempelto, Minttu Kauppinen, and Karoliina Honkala*

Cite This: https://doi.org/10.1021/acs.jpcc.4c01300 Read Online

ACCESS | Metrics & More | Article Recommendations | Supporting Information

ABSTRACT: Ternary Cu/Zn/ZrO_2 catalysts prepared recently using atomic layer deposition (ALD) have shown increased performance toward methanol synthesis. In the present computational study, we have investigated the structure, composition, and stability of various zinc- and copper-containing subnano size species on a zirconia support. Density functional theory calculations with minima hopping were used to sample the positioning and geometry of supported $Zn_xCu_yO_z$ structures up to 8 metal atoms in total. ZnO monomeric species were found to be energetically more favorable than small clusters, which could suggest a resistance to initial stage agglomeration. Ab-initio thermodynamics revealed that under typical methanol synthesis conditions, the complete reduction of ZnO and mixed ZnO/Cu clusters is unfavorable. The investigated ZnO monomers and clusters are able to provide CO_2 activation sites, with the Cu/ZnO/ZrO_2 triple interface offering the best stabilization for the adsorbed CO_2. All in all, the findings suggest that small ZnO species generated by ALD could be stabilized by the zirconia component, while contact with copper species at the interface benefits CO_2 activation.

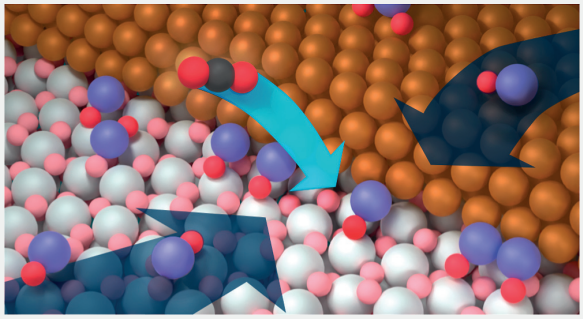

INTRODUCTION

Methanol synthesis from carbon dioxide and hydrogen is a promising approach to convert anthropogenic greenhouse gases into valuable fuels and platform chemicals. Direct carbon dioxide conversion to methanol (CTM) is an exothermic reaction

$$CO_2(g) + 3H_2(g) \rightarrow CH_3OH(g) + H_2O(g) \quad (R1)$$

that requires active and selective catalysts in order to achieve high enough conversion at relatively mild reaction conditions. Conventionally, methanol is produced from syngas using a ternary Cu/ZnO/Al_2O_3 (CZA) catalyst. In general, copper-based materials, such as the commercial CZA catalyst, are the most well-studied catalysts for methanol synthesis directly from CO_2, as well as syngas. However, relatively low conversion and methanol selectivity remain an issue for such catalysts.[1−5] Further development of active, selective, and stable CTM catalysts is required to improve the commercial process.

Ternary Cu/Zn/ZrO_2 (CZZ) systems have shown great promise as active and selective CTM catalysts. Using zirconia as an alternative support leads to increased performance, especially methanol selectivity, as compared to the commercial CZA catalyst.[2,6,7] The ternary CZZ catalysts have been shown to achieve higher production rates, total conversion, and selectivity in methanol synthesis in comparison to the binary Cu/ZnO and Cu/ZrO_2 systems alone.[7−9] One possible reason could be the formation of special active sites, such as those at the three-material interface, resulting in a synergistic effect.

However, the reaction mechanism, nature of the active site, and roles that each component plays in the binary and ternary systems are still under debate. This is mainly due to the complexity of the systems, with many different synergies between the metal and the oxide components. Several candidate active sites have been brought forward, such as Cu nanoparticles with ZnO overlayers,[10−12] Cu−ZnO and Cu−ZrO_2 interfacial sites,[2,6,9,13−17] and Cu−Zn surface alloys.[3,15,18,19] In general, copper is proposed to be responsible for the hydrogen splitting activity, while the oxide components, especially the interfacial sites, are required for activation of CO_2 and stabilization of active surface intermediates.

Received: February 28, 2024
Revised: May 9, 2024
Accepted: May 16, 2024

The structure and performance of CZZ catalysts are sensitive to both the catalyst composition and the preparation method. Many different catalyst preparation methods have been used previously, such as precipitation,[7,9,20,21] colloidal crystal templating,[9] sol−gel,[22] flame-spray pyrolysis,[23] and atomic layer deposition (ALD).[8] The preparation method can affect the total surface area of the catalyst, the dispersion and available surface area of the copper phase, and the number of basic sites. However, the structure of the catalyst is a function of the reaction conditions, and several studies have highlighted the importance of structural changes, including formation of active sites, during exposure to reactant gases.[15,23−26] For example, even if the as-prepared catalyst contains the CuZn alloy, it may no longer be present under reaction conditions due to interaction between the catalyst and the reacting gases.[15,24] Even so, the preparation method used is important for the active state of the catalyst as it is a precursor for the in situ-formed structure. Regardless of whether the most active site for the reaction is the interface of Cu and ZnO or a CuZn alloy, the preparation methods should facilitate increased contact between Cu and Zn components. Controlled tuning of the interaction between ZnO and ZrO_2 could also be desirable as the interface between the two oxides has been suggested as an active site for CO_2 adsorption and activation.[9]

ALD as a synthesis technique enables precise control over the surface structure of the catalyst.[27,28] Recently, ALD has been demonstrated as a promising preparation method for CZZ catalysts.[8] The best performing ALD synthesized CZZ consists of a ZrO_2 support, with Cu nanoparticles or clusters and a low (≈0.15 ML) coverage of ZnO monomers distributed on the surface. The best performance was achieved with the sample in which ZnO is deposited after copper rather than before. The results suggest that contact between ZnO and copper, but without Cu covering the ZnO units, is important for high activity. On the other hand, a recent study[29] found that the activity of ALD-synthesized Cu−ZnO−CeO_2 systems toward methanol production was slightly higher when Cu was deposited last. It was suggested that electron donation from Ce to Zn created Cu^+−Zn^0−Ce^{4+} sites, to which higher activity was attributed. Therefore, this effect is likely to be highly support-specific. However, the specific structure of the CZZ catalyst and the nature of the active site, especially during and after exposure to the reaction conditions, are unclear. Monomeric species are known to be highly mobile and thermodynamically driven to agglomerate into larger structures such as clusters or islands, and eventually nanoparticles.[30−32] On the other hand, dynamic evolution of highly dispersed ZnO clusters into monomeric Zn species on ZrO_2 have been recently observed with operando XAS of CZZ samples prepared with flame-spray pyrolysis.[23] The results suggest that zirconia can stabilize the monomeric Zn species through a strong interaction (facilitated by the preparation method). The atomically dispersed catalyst exhibited superior activity, which was rationalized by a mechanistic DFT study that found the H_2 dissociation to be more favorable at the atomic Zn sites as compared to Cu or Zr sites. To rationalize the structure−performance relationship of ALD-prepared CZZ catalysts, it is essential to have information about the structure, relative stability, and interaction with reactant species of the various surface motifs at different reaction conditions.

Previous computational studies have mainly employed two-component models to elucidate the role of different structural motifs found in CZZ and CZA systems.[3,4,9,13,15,16,18,19] The Zn-containing models especially differ in where and how the Zn promoter is incorporated into the catalyst. Zn-decorated extended copper surface models have been extensively used to mimic sites on alloyed nanoparticles.[3,15,18,19] In some recent models, the Zn promoter is present as an oxide, e.g., as small supported clusters[15,16,33,34] or as periodic nano stripes or ribbons.[18,33,35] Naturally, two-component models cannot capture effects that could arise at sites that form when all components are in close contact with one another. Three-component models have emerged recently in order to represent those kinds of active sites.[16,17,23] In our previous study, we employed a zirconia-supported Cu nanorod with and without Zn incorporated into the interface between the rod and support.[17] The model served as a representative of two- and three-component metal support interface sites and was used to elucidate the role of a dilute interfacial CuZn alloy. Our results showed that especially CO_2 activation was promoted by the Zn component.

Although ALD enables the controlled synthesis of monomeric ZnO promoter species on the catalyst surface, it is unclear whether those small species can resist agglomeration under the reaction conditions. Furthermore, are the monomers located on the ZrO_2 support, at the metal−support interface, or do they decorate the Cu nanoparticle? The ALD $Zn(acac)_2$ precursor has thus far been demonstrated to react with the zirconia support, but no comparable data exist for the copper component, which exists as an oxide prior to the reduction treatment. In the present study, we have compared the stability of ZnO monomers at various locations of the possible catalyst domains. Another debated aspect of the nature of Zn promoter is whether it is oxidized[12,15,24,25,36] or alloyed to Cu.[3,37−39] Even though the ALD-prepared catalyst should contain ZnO units, it is possible that under the reducing methanol synthesis conditions, ZnO would be reduced and form dilute surface alloys with Cu as has been suggested previously.[40−43]

In our present work, we have investigated the stability and structure of subnanoscale Zn and Cu species on zirconia and copper-based supports by means of density functional theory (DFT), minima hopping (MH) global optimization, and ab initio thermodynamics. We model as-prepared monomeric ALD CZZ structures as well as possible structures that result from initial stages agglomeration of the Zn monomers on the surface, surface migration, nanoalloying of Cu and Zn, vacancies on the zirconia surface, and oxidation/reduction under typical pretreatment/reaction conditions. Due to the large number of possible atomic configurations, candidate structures were sampled by MH, with the most stable structures selected for further discussion. CO_2 adsorption at various sites was investigated to probe the capability of the monomers/clusters to activate CO_2.

Our study sheds light on the ALD-fabricated tertiary CZZ catalyst structure and proposes that contact between ZnO, Cu, and ZrO_2 can promote methanol synthesis by the formation of CO_2 activation sites. We suggest that ALD is a suitable way to ensure that monomeric ZnO species are initially present and that they are in contact with the Cu/ZrO_2 interface.

■ COMPUTATIONAL DETAILS

DFT calculations were performed using GPAW[44] employing the BEEF-vdW exchange−correlation functional.[45] The wave functions were treated in the projector-augmented wave (PAW)[46] formalism. The frozen-core approximation was applied to the core electrons of all elements. The global

https://doi.org/10.1021/acs.jpcc.4c01300
J. Phys. Chem. C XXXX, XXX, XXX−XXX

optimization of clusters was obtained via the MH method.[47] To enhance the computational efficiency and evaluate a large number of structures, a double-ζ LCAO basis set was utilized in the MH calculations. Structures identified as minimum-energy candidates through MH were further optimized using a real-space grid basis, with a maximum spacing of 0.2 Å and with spin-polarization. All calculations were periodic in the horizontal directions along the surface. The Brilloiuin zone was sampled at the Γ point for the zirconia surface and Cu−ZrO_2 interface models, while a 4 × 4 × 1 and 2 × 2 × 1 Monkhorst−Pack *k*-point sampling mesh was applied to Cu(111) and CuO(111), respectively. Additionally, a Hubbard U correction[48] of 2.0 eV was applied to the d-orbitals of the zirconium atoms.[17,49] The geometry optimizations were performed using the Fast Inertial Relaxation Engine algorithm as implemented in the Atomic Simulation Environment.[50,51] Atoms in the bottom layers of surface slabs were fixed to their bulk positions (specific number of layers given below), while all other atoms were relaxed until the maximum residual force was reduced to less than 0.005 eV/Å. Partial charges on atoms were analyzed using the Bader partitioning method[52] using code developed by Tang et al.[53]

In this work, we employed a variety of zirconia-supported single atom and cluster models. The composition of the $Zn_xCu_yO_z$ clusters was varied to include pure Cu and Zn as well as mixed metal clusters and reduced and oxidized clusters. The maximum total number of metal atoms in a cluster was 6. The zirconia surface was modeled with a *m*-$ZrO_2(\bar{1}11)$ surface slab that is two stoichiometric layers thick and built as a 2 × 2 supercell (32 Zr atoms, see Figure S1). During optimizations, the bottom layers of the ZrO_2 slab were frozen in its bulk geometry. The $(\bar{1}11)$ surface of monoclinic zirconia is highly asymmetric, with four identifiable Zr cation sites and a diverse selection of oxygen sites. A primitive repeating unit of the *m*-$ZrO_2(\bar{1}11)$ surface has 16 oxygens of which 5 are on the surface. Among these, four are 3-coordinated and located between Zr atoms and the remaining one is 2-coordinated, bridging two cations.

Additional calculations were performed for selected clusters adsorbed on a Cu(111) surface, an oxidized CuO(111) surface, and a Cu−ZrO_2 interface. The Cu(111) surface was modeled as a periodic three-layer-thick slab, 10.5 × 13.6 Å in size (see Figure S1). The bottom layer was fixed to bulk geometry during optimization. Cupric oxide (CuO) was identified as the major Cu phase in the as-prepared ALD catalyst.[8] The CuO(111) is the most stable surface of CuO in all but the most reductive conditions.[54] A three-layer-thick slab of CuO(111) was therefore used to model the oxidized Cu surface. The periodic computational cell is 12.0 × 12.8 Å in size. Again, the bottom layer was kept in its bulk geometry. The initial CuO bulk structure was taken from the Crystallography Open Database[55−58] and reoptimized computationally. The periodic model for a Cu/ZrO_2 interface was adopted from our previous studies.[17,59] It comprises a 64-atom Cu nanorod placed on a zirconia surface slab (see Figure S1c). The zirconia surface was modeled as described above but as a 2 × 3 supercell to minimize the lattice mismatch between Cu and ZrO_2.

The stabilities of clusters were compared based on their formation energies. The formation energy ΔE_f of each cluster containing *x* Cu atoms, *y* Zn atoms, and *z* O atoms is calculated according to eq 1 relative to the adsorbate-free *m*-$ZrO_2(\bar{1}11)$ surface, gaseous oxygen, and bulk metal. The formation energies of clusters on Cu(111) are calculated similarly with the appropriate substitutions.

$$\Delta E_f(Cu_xZn_yO_z/ZrO_2) = E(Cu_xZn_yO_z/ZrO_2) - \left[E(ZrO_2) + xe_{Cu}^{bulk} + ye_{Zn}^{bulk} + z\frac{1}{2}E(O_2)\right] \quad (1)$$

To circumvent the known inaccuracy of the DFT energy of a gas-phase oxygen molecule,[60−62] E_{O_2} was determined through the formation of water

$$E(O_2) = 2E(H_2O) - 2E(H_2) - 2\Delta H_f^\circ(H_2O, T) \quad (2)$$

Using $\Delta H_f^\circ(H_2O, 0\ K) = 2.476$ eV from the NIST-JANAF tables,[63] eq 2 gives −32.997 eV for total energy of O_2 and the gas-phase error is $\varepsilon_{O_2} = -0.83$ eV. This matches well with previously reported values of −0.83 and −0.81 eV for the BEEF-vdW functional.[60,61] Alternatively, when the amounts of Zn and O are equal, the formation energy can be defined relative to bulk ZnO instead of bulk Zn and gas-phase O

$$\Delta E_f(Cu_xZn_yO_z/ZrO_2) = E(Cu_xZn_yO_z/ZrO_2) - \left[E(ZrO_2) + xe_{Cu}^{bulk} + ye_{Zn}^{bulk} + z\frac{1}{2}E(O_2)\right] \quad (3)$$

However, we use eq 1 unless otherwise specified. The cohesive energy, ΔE_{coh}, of a cluster is defined relative to that of isolated Cu, Zn, and O atoms adsorbed on ZrO_2.

$$\Delta E_{coh} = [E(Cu_xZn_yO_z/ZrO_2) + (N-1)E(ZrO_2)] - [xE(Cu/ZrO_2) + yE(Zn/ZrO_2) + zE(O/ZrO_2)] \quad (4)$$

N is the total number of atoms in a cluster. Equivalently, the cohesive energy can be calculated from the formation energies

$$\Delta E_{coh} = \Delta E_f(Cu_xZn_yO_z/ZrO_2) - [x\Delta E_f(Cu/ZrO_2) + y\Delta E_f(Zn/ZrO_2) + z\Delta E_f(O/ZrO_2)] \quad (5)$$

If a cluster has an equal number of Zn and O ($y = z$) atoms, then cohesive energy can also be defined relative to adsorbed ZnO monomers on ZrO_2.

$$\Delta E_{coh,ZnO} = \Delta E_f(Cu_xZn_yO_z/ZrO_2) - [x\Delta E_f(Cu/ZrO_2) + y\Delta E_f(ZnO/ZrO_2)] \quad (6)$$

When assessing cluster agglomeration, it is also useful to calculate the energy relative to two existing clusters. For this, we can define a type of agglomeration energy using the formation energies of the clusters

$$\Delta E_{agg} = \Delta E_f(AB) - [\Delta E_f(A) + \Delta E_f(B)] \quad (7)$$

https://doi.org/10.1021/acs.jpcc.4c01300
J. Phys. Chem. C XXXX, XXX, XXX−XXX

where A and B refer to the constituent clusters of the agglomerate AB. The adhesion energy, ΔE_{adh}, of a cluster is calculated relative to the cluster in the gas phase.

$$\Delta E_{adh} = E(Cu_xZn_yO_z/ZrO_2) - [E(ZrO_2) + E^*(Cu_xZn_yO_z)] \quad (8)$$

where $E^*(Cu_xZn_yO_z)$ is the energy of the cluster without the support but fixed in its adsorption geometry. The quantities above are defined equivalently on the Cu(111) surface and at the Cu/ZrO_2 interface.

Atomistic Thermodynamics. DFT data were used as the starting point for the ab initio thermodynamic treatment of the oxidation and reduction of small Cu/Zn clusters. The most thermodynamically stable oxygen content of each cluster is found by calculating the Gibbs energy of the oxidation reaction $\Delta G_r(T, p)$ for each z oxygen-containing cluster relative to that of the fully reduced cluster

$$Cu_xZn_y + z\frac{1}{2}O_2 \rightarrow Cu_xZn_yO_z \quad (R2)$$

$$\Delta G_r(T, p) = E(Cu_xZn_yO_z/ZrO_2) - [E(Cu_xZn_y/ZrO_2) + z\mu_O(T, p)] \quad (9)$$

This examination is equivalent to the one in ref 34 as well as energies of O adsorption used in ref 64 but calculated per cluster as opposed to surface area. Vibrational energy contributions of surface-bound clusters to the free energies were assumed to be minimal. Therefore, DFT energies were used for the clusters instead of the Gibbs free energies. Temperature and pressure effects were included in the chemical potential, $\mu_O(T, p)$, of oxygen. The contribution of temperature to the standard chemical potential of O_2 $\Delta\mu^\circ(T)$ was calculated using experimental values for $H - H^\circ(T_r)$ and S° taken from the NIST JANAF thermochemical tables.[63]

$$\Delta\mu^\circ(T) = \Delta H^\circ + T\Delta S^\circ = [H^\circ(T) - H^\circ(T_r)] - [H^\circ(0\ K) - H^\circ(T_r)] - T \times [S^\circ(T) - S^\circ(0\ K)] \quad (10)$$

We define the change in chemical potential relative to 0 K

$$\Delta(T, p) = \Delta\mu^\circ(T) + k_BT \log\frac{p}{p^\circ} \quad (11)$$

Thus the chemical potential of a gaseous oxygen is

$$\mu_O(T, p) = \frac{1}{2}E(O_2) + \Delta\mu_O(T, p) \quad (12)$$

where O_2 energy includes the correction according to eq 2. To estimate the chemical potential of oxygen under the highly reductive conditions typically used for CO_2 conversion, we applied the balance of molecular hydrogen and water gas: $\Delta\mu_O^\circ = \Delta\mu_{H_2O}^\circ - \Delta\mu_{H_2}^\circ$

RESULTS AND DISCUSSION

We focus on small subnanometer clusters, each comprising up to 8 Zn and Cu atoms supported on m−ZrO_2 (0−4 Zn, 0−4 Cu, including mixtures of the two). Selected clusters underwent further examination on Cu(111) and CuO(111) surfaces as well as on a Cu−ZrO_2 interface. Beyond metal-only clusters, we generated and optimized clusters with varying amounts of oxygen. Consequently, the smallest systems consisted of single Cu or Zn atoms, while the largest cluster was $Cu_4Zn_4O_4$.

ZrO_2-Supported $Cu_xZn_yO_z$ Clusters. In the ALD-prepared CZZ systems, the Cu and ZnO components are added to the zirconia support by incipient wetness impregnation (IWI) and ALD, respectively.[8] In the case of the best performing sample, the ALD step is performed last, which should ensure that some of the ZnO units are initially present on the ZrO_2 support and not covered by Cu. All minimum-energy structures optimized on monoclinic zirconia are presented in Supporting Information Figure S2 for Cu_xO_z and Zn_yO_z clusters and Figure S3 for mixed $Cu_xZn_yO_z$ clusters.

Zn_yO_z Clusters. Recent studies[8,18] that have used ALD for catalyst preparation have suggested that Zn exists approximately as atomically dispersed species on the surface of the as-prepared catalyst. Depending on their mobility and relative stability on the surface, the monomers could migrate and eventually react together to form subnanometer clusters. Given the varying reaction conditions the catalyst experiences during synthesis, pretreatment, and operation, ranging from highly oxidizing to very reductive, we considered both metallic Zn_y clusters as well as oxidized Zn_yO_z clusters. We consider the ZnO monomer as the reference system rather than separate Zn and O units as it is the assumed form of the as-prepared ALD Zn units.

In the most stable configuration, the ZnO monomer binds to a two-coordinated oxygen site on the ZrO_2 surface through the formation of a Zn−O bond. The oxygen atom of the monomer binds to a Zr top site. Adsorption at the low-coordinated O site is 1.5 eV stronger than the best geometry found for binding to a 3-coordinated oxygen, and the ZnO monomers relax to the 2-coordinated site almost independent of the starting geometry. This points to the maximum coverage of 2.24 ZnO monomers per nm^2, which is comparable to 1.9 Zn/nm^2 determined experimentally for ALD-prepared Zn/ZrO_2.[8] The formation energy of the most stable ZnO monomer is endothermic (+0.74 eV) relative to that of the ZnO bulk. The adhesion energy is −4.40 eV, and the cohesion energy relative to Zn and O adatoms is −1.51 eV. The same coordination site and similar binding strength has been previously found for sintering-resistant RuO monomers on monoclinic ZrO_2.[65] In general, subnanometer Zn_yO_z clusters tend to attach to the ZrO_2 support by bonding to the surface oxygens through the Zn atoms, particularly those with lower coordination. Additional oxygen atoms introduced as part of the clusters create extra contact points by bridging surface Zr cations and Zn atoms within the cluster. In cases where possible, $Zn^{\delta+}$ centers form planar, trigonal ZnO_3 moieties with surface and cluster oxygens. The geometric arrangement is also observed in the Zn_2O cluster, where one Zn atom is part of the trigonal shape rather than an oxygen. This type of trigonal motifs have also previously been identified in Cu(111)-supported Zn_yO_z clusters.[34] However, many nearly linear O−Zn−O moieties are also identifiable, as exemplified by Zn_2O_2. It is noteworthy that oxygen atoms act as bridges between Zn centers, although $Zn^{\delta+}$ can also directly form bonds with one another, as seen in Zn_2O and Zn_3O_2. Stoichiometric 1:1 Zn/O clusters are the most stable, and all show $E_f = -1.35$ per atom, whereas removing or adding oxygen makes the clusters progressively less stable. In some overoxidized clusters, two oxygens can form O−O bonds, resembling an adsorbed O_2

https://doi.org/10.1021/acs.jpcc.4c01300
J. Phys. Chem. C XXXX, XXX, XXX−XXX

molecule. For an example, see Zn_3O_4 in Figure S2. When the cluster size increases, the cohesive energies of stoichiometric $(ZnO)_n$ clusters are close to 0 eV with respect to ZnO monomers on zirconia (see Table S1). Therefore, no clear thermodynamic driving force is present for the formation of oxidized ZnO subnano clusters (see Figure 1). There exists, however, still the tendency toward bulk ZnO formation, as can be seen by the positive formation energies in Table S1.

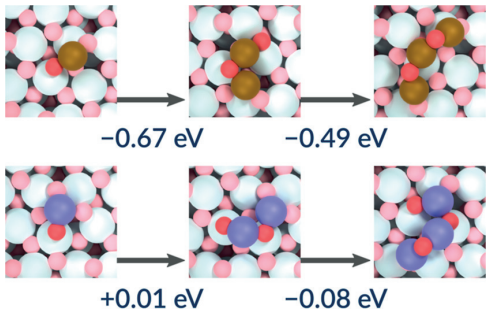

Figure 1. Stepwise energy differences of building a cluster from adsorbed atoms at infinite separation during the initial stages of Cu_xO_z and Zn_yO_z agglomeration. Brown: Cu, purple: Zn, red: O.

The possibility of Zn monomer species to exist as reduced metal adatoms, e.g., due to highly reducing conditions, was also considered. The single Zn adatom is most stable on a Zr cation top site where it settles above the surface at a Zr−Zn distance of ≈3.5 Å. The variation in energy between all Zr sites available is less than 0.1 eV. Metallic 2−4 atom Zn clusters have structures where Zn atoms are similarly located on Zr top sites. These Zn_y clusters display longer Zn−Zn distances than bulk Zn, decreasing the distance with an increase in cluster size. Figure 2 shows that Zn_3 and Zn_4 take trigonal shapes, with the

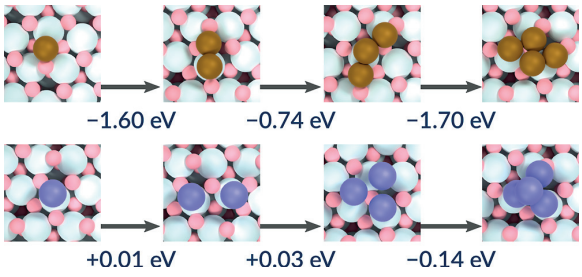

Figure 2. Stepwise energy differences of building a cluster from adsorbed atoms at infinite separation during the initial stages of Cu_x and Zn_y agglomeration. Brown: Cu, purple: Zn.

latter being in a pyramidal form, although a planar rhombic Zn_4 is only 0.1 eV less stable. These geometries are similar as those previously reported for small Rh clusters on m-ZrO_2,[30] with the exception that Rh_2 shows no significant Rh−Rh bond elongation compared to bulk Rh. Notably, the formation energies of the most stable Zn adatom and metallic clusters are endothermic by 0.6 eV per cluster atom (see Table S1), which is very close to that of the ZnO units described above but significantly less endothermic than the +2.1 eV value that we calculated for a Cu atom. The formation energies of metal adatoms are typically strongly endothermic.[30,32] Here, we find that while there is ultimately a thermodynamic driving force for large Zn particle growth, the initial stages of agglomeration are nearly thermoneutral (Figure 2).

Despite zirconia's tendency to resist reduction, several studies have shown evidence for the formation of oxygen vacancies on its surface either near metal−zirconia interfaces or single metal sites.[49,66−68] The oxygen vacancies formed have been found to enhance adsorbate binding[69,70] to ZrO_2 and suggested as the cause for increased activity toward CO_2 conversion.[66] They are also known to act as anchor sites that can stabilize single atoms on catalyst surfaces.[30,71] We therefore addressed how the ZnO promoter binds to ZrO_2 surface vacancies. Previous computational studies have found that the vacancy formation energy is the least endothermic for the 2-coordinated oxygen on the m-$ZrO_2(\bar{1}11)$ surface.[65,70,72] Therefore, we chose it as the model vacancy site for $Cu_xZn_yO_z$ binding. As can be seen from the relative energies in Table S4, oxygen vacancies on the ZrO_2 surface bind all clusters more strongly than the pristine zirconia surface, often by several eV, and can thus act as anchors. Furthermore, oxygen-containing clusters are stabilized more than reduced clusters. Notably, nonoxidized Zn and Zn_2 show the smallest differences, only being stabilized by ≈0.5 eV. A ZnO monomer that is captured by an oxygen vacancy can spontaneously donate its oxygen to fill in the vacancy, breaking the Zn−O bond in the process (see Figure S5). Other oxygen-containing clusters, as well as the CuO monomer, donate oxygen to fill the vacancy but are not dissociated in the process. In these cases, then, the binding geometries are effectively the same as the binding of a cluster with one less oxygen on pristine ZrO_2.

Mixed Clusters. Although copper tends to form larger nanoparticles on a monoclinic zirconia surface,[73,74] the formation of mixed clusters with Zn cannot be ruled out, as the thermodynamic feasibility of mixing Cu and Zn is evident based on the computed formation energy of BCC-packed CuZn (α-brass) being −0.16 eV per CuZn unit. Experiments also demonstrate the possibility of Cu−Zn (nano)alloys formation when the conditions become reductive.[24,40−43] Although multiple studies point to ZnO being the more stable state under the high-pressure reaction conditions,[24,26,75] other works have attributed a high activity for CO_2 conversion to alloyed/metallic Zn sites on the catalyst surface.[3,43,76,77] Our investigation delves into the interaction between ZnO subnano structures, present in the as-prepared catalyst, and Cu particles. The aim is to understand whether stable Cu−Zn mixtures could form under reaction conditions. This scheme describes the thermodynamic feasibility of a process where small copper species detach from large copper nanoparticles to react with ZnO species that are not initially in contact with the copper component of the catalyst. Ultimately, such a process would also depend on kinetics of Cu particle disintegration (e.g., via the Ostwald ripening process[32]) and migration of Cu species, which is beyond the scope of the present study. The stability of reduced and oxidized Cu_xO_z clusters was also determined as they could exist as transient species during the agglomeration process and besides serve as reference systems for the stability of the mixed clusters.

A single Cu adatom binds to the 2-coordinated oxygen site of the zirconia surface. Small Cu_x clusters are similarly attached to the surface via Cu−O bonds and take flat or linear shapes, which maximize oxygen contact. As expected, the growth of Cu agglomerates is thermodynamically favorable (see Figure 2), which is consistent with the formation of larger Cu nanoparticles unless kinetically limited. Generally, mixed

https://doi.org/10.1021/acs.jpcc.4c01300
J. Phys. Chem. C XXXX, XXX, XXX−XXX

Cu_xZn_y clusters take similar shapes and placements as Cu_x clusters of the same size do and are geometrically flat, maximizing contact with the support. Similarly, oxidized mixed clusters bear a large resemblance to Cu_xO_z and Zn_xO_z structures. All clusters exhibit a tendency to bind to low-coordinated oxygen sites in both their reduced and their oxidized forms. The structures are generally more stable when a maximal number of oxygens are in contact with the zirconia surface. However, when multiple oxygens are present in the cluster, this effect is restricted by internal forces within the cluster, and thus some oxygen stays out of contact with the support. Internally, Zn−Zn bonds are uncommon in mixed clusters, and the zincs are typically separated by Cu and O atoms in the lowest-energy configurations. The structures of mixed clusters on ZrO_2 can be seen in Figure S3. Figure 3

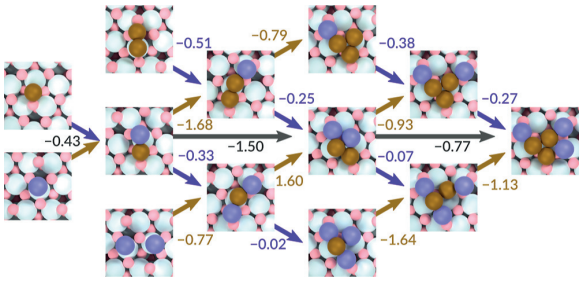

Figure 3. Stepwise agglomeration of mixed, nonoxidized Cu_xZn_y clusters from Cu, Zn, and CuZn units adsorbed on ZrO_2. The numbers are agglomeration energies (eq 7) in eV associated with introducing a Cu (up), Zn (down), or CuZn unit (horizontal) from infinite separation into the cluster. Brown: Cu, purple: Zn.

shows the initial stages of the agglomeration of nonoxidized mixed clusters. At each step, the agglomeration is energetically favorable. However, after the initial combination of Cu and Zn, the agglomeration energies of additional Zn atoms become clearly less negative, mirroring the case of Zn_y clusters. In situations where an individual Zn adatom can combine with a Zn_y or Cu_x cluster, the formation of a mixed cluster is thermodynamically favored over the formation of a pure Zn cluster (see Figure S6). Furthermore, while ZnO monomers do not show a clear tendency to create Zn_yO_y agglomerates, the formation energies of mixed metal clusters (Table S1) show that mixing with copper could provide an alternative route for initial stage agglomeration. However, verifying this would require further computational and experimental investigations into the mechanism and kinetics of Cu particle disintegration/agglomeration.

Clusters on Cu Surfaces. During catalyst preparation and CO_2 hydrogenation, small Zn or ZnO deposits may also form on larger Cu nanoparticles—either due to the chosen preparation method, such as ALD.[8,18] Although a reaction between $Zn(acac)_2$ and copper has not been explicitly demonstrated, in principle, some of the ZnO units could be deposited on the copper particles as well as the ZrO_2 support, when the ALD step is performed after IWI. Alternatively, strong metal−support interaction between Cu and ZnO has been suggested to result in the migration of the ZnO component to form an overlayer on top of the Cu component.[26,78,79] However, a previous study has asserted that Zn may need to be in its reduced form for substantial migration of Zn on top of Cu particles to occur.[78] Interfaces between ZnO islands and Cu particles are proposed as active sites for CO_2 adsorption and activation in a CZA system.[2,15,18,36,80] Consequently, the Cu−ZnO interaction can also contribute to the activity in ternary CZZ systems. To explore this further, several Cu_xO_z and Zn_yO_z clusters (see Table S2 and Figure S4) were optimized on a Cu(111) surface, representing a scenario where they are positioned on top of larger metallic Cu particles.

The geometries of the optimized Zn_yO_z clusters on Cu(111) are presented in Figure S4. Metallic Zn clusters are more Zn_y particles and are generally more stable on Cu(111) by ≈0.6 eV per Zn than they are on zirconia. However, both their formation and cohesive energies approach effectively zero, showcasing a behavior opposite that on the zirconia surface, where the formation of ZrO_2-bound Zn atoms is endothermic. The average Zn−Zn distance in unoxidized clusters is 2.7 Å and comparable to that of bulk Zn as well as the Cu−Cu distance of the underlying surface, agreeing well with the previously reported value.[34] Moreover, the study reported only marginal energy differences between reduced Zn_y clusters of various shapes. These results suggest that the energy benefit of forming a Zn_y cluster structure is relatively small. The ZnO monomer and Zn_yO_z clusters show structural motifs similar to those seen on a zirconia surface. These motifs are the same as were identified in a recent study,[34] and the structures found here are very similar. Binding to the Cu surface happens through both Cu−O and Cu−Zn bonds. Calculating the difference in the formation energies, ΔE_f given in Table S2, for each cluster on ZrO_2 and Cu(111) allows us to determine whether adsorption is more favorable on a metal or oxide surface. The formation energies of Zn_yO_z species on a Cu(111) surface are 0.5 to 0.9 eV less negative compared to equivalent clusters on zirconia. Therefore, there is a thermodynamic tendency for oxidized Zn to migrate onto the zirconia support if it is formed on the Cu surface during catalyst preparation. Conversely, the migration of ZnO units from the zirconia surface to the Cu and, consequently, the formation of ZnO overlayers is thermodynamically unlikely. Additionally, it is uncertain if encapsulation of a Cu component, similar to that reported for CZA systems, would be feasible when the ZnO units are widely dispersed on the surface and their loading is low.

Cupric oxide has been identified as the primary oxidized Cu phase in as-prepared catalysts produced using ALD prior to reductive pretreatment.[8] Hence, it is pertinent to examine the binding of ZnO on CuO(111). Two zinc−oxygen clusters, ZnO and Zn_2O_2, were considered as representatives of the highly dispersed small ZnO species that have been suggested to exist in the as-prepared catalyst after ALD.[8,18] The ZnO monomer favors a horizontal geometry with Zn binding to a surface oxygen and a Cu top site. The ZnO formation energy is ≈+1.6 eV on CuO(111), being only slightly higher than on Cu(111) but significantly more endothermic than on ZrO_2. This indicates that ZnO monomers are thermodynamically more stable on the ZrO_2 support than Cu particles, regardless of the Cu-oxidation state. The ΔE_{agg} of two ZnO monomers combining on CuO(111) is exothermic by −1.08 eV, showing that agglomeration is similarly favorable as it is on Cu(111).

Clusters at Interfaces. The interfaces forming between Cu particles and the supporting ZrO_2 play a crucial role in multicomponent systems, potentially displaying unique activity. Numerous computational studies have underscored the importance of the Cu−ZrO_2 interface as an active site for

https://doi.org/10.1021/acs.jpcc.4c01300
J. Phys. Chem. C XXXX, XXX, XXX−XXX

CO_2 activation and hydrogenation.[13,17,59,81] Consequently, it is reasonable to investigate the behavior of ZnO promoters in this context. We calculated the stability of the ZnO and Zn_2O_2 units at the Cu−ZrO_2 interface using a supported nanorod model from our previous studies.[17,59] Figure 4 displays the

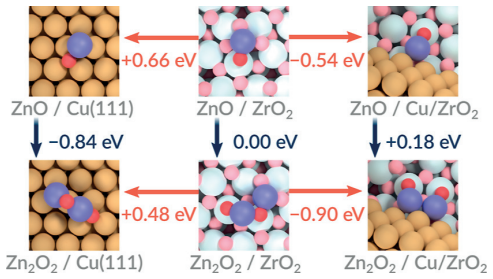

Figure 4. Blue arrows represent the energy differences of building a Zn_2O_2 cluster from two infinitely separated ZnO units on each support. Orange arrows depict diffusion of the cluster to different sites on the surface of a CZZ catalyst. The orange energy values are relative to the cluster on zirconia. Brown: Cu, purple: Zn, red: O. Lighter colored atoms are part of the support.

most favorable ZnO and Zn_2O_2 binding structures at the Cu−ZrO_2 interface, showing that Zn interacts with the Cu rod and that O binds to the Zr cation. The relative energies in Figure 4 demonstrate that the ZnO unit is 0.54 eV more stable at the interface than on the ZrO_2 surface and 1.20 eV more stable than that on the Cu(111). While ZnO agglomeration is thermoneutral on ZrO_2, it is unfavorable at the interface, as indicated by the endothermic agglomeration energy of +0.18 eV for the Zn_2O_2 formation from two ZnO units.

In summary, the binding of ZnO monomers is stabilized by the Cu−ZrO_2 interface, leading to a thermodynamic tendency for them to migrate from Cu and ZrO_2 surfaces and into interfacial areas. While the Cu(111) surface is the least stable support for Zn_yO_z species to bind to, it is the most favorable location for their agglomeration. Conversely, the initial ZnO agglomeration is thermoneutral on zirconia and slightly endothermic at the Cu−ZrO_2 interface. It should be noted that this thermodynamic examination cannot take into account the possible kinetic barriers of cluster diffusion on Cu and ZrO_2 surfaces or across a metal−oxide interface. Methods such as mean-field or Monte Carlo microkinetic modeling[82] and ab initio molecular dynamics simulations[83] could be used to gain further understanding of the rate of agglomeration/sintering.

Cluster Composition under Reaction Conditions. The extent of reductive or oxidative conditions varies widely between the catalyst preparation steps and the operation conditions for the conversion of CO_2 to methanol. During synthesis, the catalyst undergoes an oxidative pretreatment, such as heating under synthetic air (80% oxygen).[8] On the other hand, the CTM reaction is carried out under high pressures ranging from 10 to 50 bar in a mixture of typically 1:3 CO_2 and H_2.[2] Despite extensive research efforts, the precise oxidation state of Zn under reaction conditions remains a source of debate.[2,3,12,15,24,26,37,41,76,77,84−87] As has been noted before,[24,26,41] the disparate results can largely be explained by the diverse conditions and the pressure gap between catalyst preparation, ex situ characterization studies, and the reaction conditions. To address this ambiguity, we employ atomistic thermodynamics to assess the stability of both reduced and oxidized clusters at conditions relevant to catalyst pretreatment and CO_2 conversion to methanol.

As the phase diagrams presented in Figure illustrate, small Zn clusters adsorbed on zirconia exhibit greater stability in their oxidized forms—even under the highly reductive reaction conditions of hydrogenation of CO_2 to methanol. As the initial agglomeration of ZnO on ZrO_2 is practically thermoneutral, the promoter may be present in a wide variety of sizes, ranging from ZnO monomers to larger clusters. However, the stoichiometric 1:1 composition (Zn_yO_y) proves to be the thermodynamically most stable form among all of the Zn_yO_z clusters considered, both in the reductive atmosphere used in CTM as well as conditions corresponding to the oxidative pretreatment that is a part of catalyst preparation. We note that the Gibbs energies of oxidation are often very close to one another (e.g., Figure 5a). Therefore, while the most stable compositions at each oxygen chemical potential are highlighted, in reality, many states may exist as an ensemble. The activation barriers of oxygen gas adsorption or the

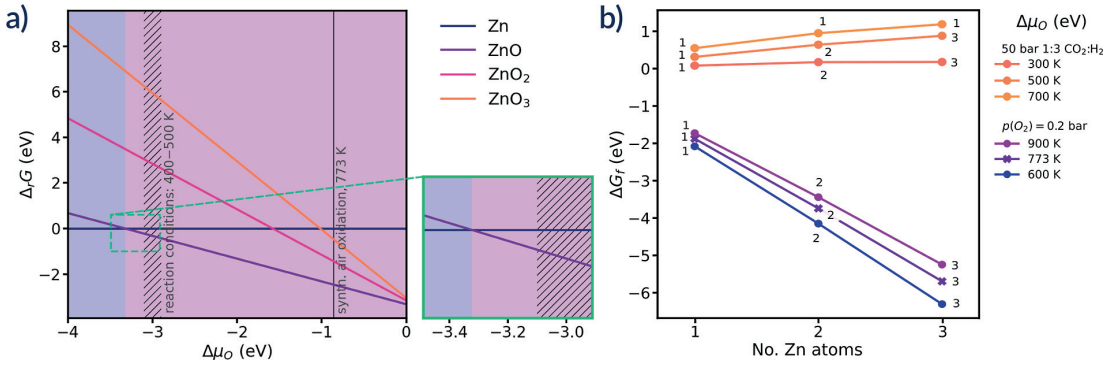

Figure 5. (a) Phase diagrams showing the relative stabilities of zirconia-supported Zn_1O_z species with different oxygen contents (from eq 9) as a function of oxygen chemical potential. Colored lines corresponding to each cluster show their energies relative to the fully reduced cluster and gas-phase O_2. The background is colored according to the lowest-energy state for ease of identification. Oxygen chemical potentials relevant to pretreatment and CTM reaction conditions are indicated with vertical lines and regions with diagonal hatching, respectively. (b) Formation energies at several oxygen chemical potentials in the regions of the reaction and oxidative pretreatment conditions. The values of ΔG_f are calculated according to eq 1 by substituting μ_O for $\frac{1}{2}E(O_2)$. The numbers inside the graphs indicate the number of oxygen atoms in the most stable structures.

https://doi.org/10.1021/acs.jpcc.4c01300
J. Phys. Chem. C XXXX, XXX, XXX−XXX

$Zn + H_2O \leftrightarrow ZnO + H_2$ process were not studied here but may bring further nuance to the situation, as the reduction or oxidation of certain clusters could be kinetically limited. As Figure 5b shows, the Gibbs free energy of formation becomes increasingly more negative for larger cluster sizes at oxidizing conditions. The differences in ΔG_f become smaller as the temperature increases. A similar trend with respect to temperature has been previously observed for Zn_yO_z clusters on Cu(111).[34] However, we find that at the methanol synthesis reaction conditions, the difference between monomers and larger clusters is nonexistent or even reversed. This indicates that monomers may be more able to resist agglomeration during the reaction as opposed to during the oxidizing pretreatment. For all conditions, the formation free energy change is monotonic.

The oxidation characteristics of small Cu clusters are more diverse. Under oxidative conditions, Cu clusters again display the highest stability in a stoichiometric composition (see Figure S8). However, in a reductive atmosphere, a single Cu atom adsorbed on zirconia is more likely to exist as an adatom with no additional oxygen. For Cu_2 and Cu_3 clusters, the thermodynamics favor partial oxidation. However, the oxidation energies of different cluster compositions can be very similar. In particular, Cu_3O_z clusters are all no more than 0.3 eV apart in the range of typical reaction conditions. The partial oxidation of small Cu_x units is preferred, in contrast to the stoichiometric oxidation of Zn_yO_y. This is consistent with bulk oxide formation energies: CuO formation energy is −1.48 eV and for ZnO, it is −3.47 eV relative to bulk metal and gas-phase oxygen. This, together with the considerable agglomeration and cohesive energies of Cu_z clusters, is consistent with experimental results that have generally identified large Cu deposits with a significant amount of reduced Cu.[8,88−90] The redox properties of mixed $Cu_xZn_yO_z$ clusters primarily resemble those of small Zn clusters in that completely metallic clusters are thermodynamically unfavored (see Figure S9). However, the oxygen content per metal atom varies. The ab initio thermodynamics indicate that metallic alloy clusters are not stable under reaction conditions, although there is a possibility of forming mixed oxidized clusters.

CO_2 Adsorption and Activation. Methanol synthesis requires activation of the inert CO_2 molecule on the catalyst surface. Activation may take place through adsorption and bending of the molecule, followed by dissociation or hydrogenation. The bent adsorption configuration could be, e.g., a $CO_2^{\delta-}$ on a metal surface, or a carbonate-like CO_3^{2-} on a metal oxide, which both require charge transfer from the catalyst to the molecule. The computed formate pathways on metal surfaces often imply that CO_2 activation occurs through direct reaction between linear CO_2 and a dissociated hydrogen species on the surface.[3,4,15,90] In previous studies,[13,17,59,81] it has been found that the Cu/ZrO_2 interface is capable of adsorbing and activating CO_2, enabling the surface reaction between adsorbed bent CO_2 species and hydrogen to produce a carboxyl (COOH) instead of formate. In line with the previous studies,[3,4,17,81,91] we find that a (111) facet of Cu weakly physisorbs CO_2 in a linear, nonactivated configuration, with an adsorption energy of −0.21 eV. On ZrO_2, CO_2 adsorbs in a trigonal, carbonate-like geometry, wherein the carbon atom coordinates to a ZrO_2 lattice oxygen and the oxygens of the adsorbate rest on $Zr^{\delta+}$ sites. The most favorable adsorption site is the 2-coordinated lattice oxygen, where E_{ads} = −0.62 eV. However, one-fifth of surface oxygens are 2-coordinated and the adsorption energies to other sites are only mildly exothermic varying from −0.09 to −0.16 eV. When adsorbed, the CO_2 takes a small negative charge of −0.20*e*, which is in the same order as has been determined before.[13] Previous computational studies using diverse models for Cu−ZrO_2 interfaces[13,17,59,81] indicate that CO_2 adsorbs at a Cu−ZrO_2 interface in a bent geometry. In our previous study, we found that CO_2 attaches to the Cu component through the carbon atom with both oxygens binding to the nearest Zr cations.[17] The adsorption energy is −0.63 eV, which is comparable to that at the most stable adsorption site on ZrO_2. Our earlier work demonstrated that incorporating Zn into the Cu matrix at the interface can strengthen CO_2 adsorption by up to 0.66 eV compared to the Cu-only interface.[17] Here, we investigate the adsorption of CO_2 on ZnO monomers on ZrO_2, Cu(111), and the Cu−ZrO_2 interface to further quantify the promoting effect of ZnO.

Figure 6 illustrates CO_2 adsorption geometries and energies at potential active sites on a Cu/ZnO/ZrO_2 catalyst,

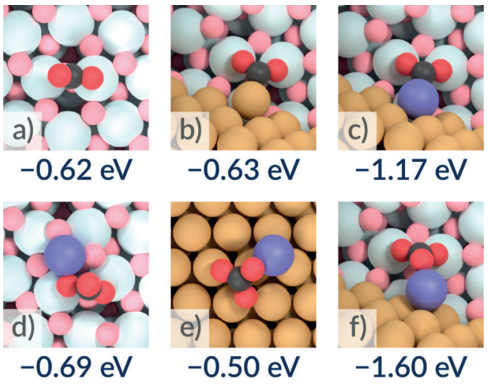

Figure 6. CO_2 adsorption energies on different supports and Zn-promoter sites: (a) ZrO_2, (b) Cu−ZrO_2 interface, (c) CuZn−ZrO_2 interface (Zn-poor), (d) ZnO/ZrO_2, (e) ZnO/Cu(111), (f) ZnO/Cu−ZrO_2.

particularly when ZnO is deposited with ALD. In the preferred binding configuration on the zirconia supported ZnO, CO_2 forms bonds between its carbon atom and the oxygen of the ZnO monomer and between its oxygen atoms and Zr surface cations. The adsorption energy of −0.69 eV is only slightly more negative than that of the most stable adsorption geometry on promoter-free ZrO_2. In contrast to a bare Cu(111) surface, CO_2 bound to the oxygen atom of a ZnO unit on Cu(111) is clearly activated and stable featuring an adsorption energy of −0.42 eV. The activation is evident from the carbonate-like structure, which is similar to that observed on zirconia. CO_2 bound to ZnO has a slight negative charge of −0.20*e*—the same as the charge of a CO_2 molecule adsorbed on ZrO_2 in a carbonate geometry (see Table S5 for atomic charges). The dispersion of Zn_yO_z units on Cu particles can increase the number of sites where activated CO_2 interacts with the Cu catalyst. This could facilitate the reaction between adsorbed CO_2 and dissociated hydrogen that is produced on Cu particles. Previous computational studies have similarly explored the adsorption of CO_2 to ZnO clusters on copper surfaces. For example, one study modeled the ZnO/Cu interface using a hydrogen-terminated $Zn_6O_7H_7$ cluster model.[15] In this case, CO_2 adsorption and activation was

https://doi.org/10.1021/acs.jpcc.4c01300
J. Phys. Chem. C XXXX, XXX, XXX−XXX

achieved at the edge of the cluster with the molecule binding to the Cu surface through its carbon and to the cluster through its oxygen. However, the binding energy was found to be endothermic by +0.47 eV, making it unfavorable. The disparity in CO_2 adsorption energy between this model and ours is likely explained by their inclusion of the H termination, which reduces the reactivity of the cluster toward CO_2 activation. Another study using a graphitic-like ZnO layer model supported on a Cu(111) surface suggested that the adsorption of CO_2 to ZnO edges was facilitated by the presence of oxygen vacancies in the zinc oxide.[18] At the vacancy site, CO_2 binds to the ZnO layer through both carbon and oxygen atoms with an adsorption energy of −0.56 eV. However, we find that stoichiometric ZnO monomers also act as efficient adsorption sites.

While the Cu−ZrO_2 interface is already capable of activating CO_2, ZnO units that have migrated to the interface can also serve as sites for CO_2 adsorption and activation. In the most stable structure, the molecule again binds to the oxygen of the ZnO unit, forming the familiar carbonate-like structure and taking a negative charge of −0.29*e*. The oxygens originally belonging to the molecule reside on the zirconia surface, mirroring their positioning during adsorption to the interface without ZnO. The corresponding adsorption energy of −1.60 eV indicates significantly stronger adsorption compared to adsorption at the simple Cu−ZrO_2 interface (−0.63 eV) and somewhat stronger than adsorption at mixed CuZn−ZrO_2 interfaces (−1.1 to −1.3 eV).[17] It is also markedly stronger than that of the adsorption of CO_2 to zirconia alone. The atomic charges in the ZnO-bound CO_2 are similar on Cu and ZrO_2 surfaces and the interface, and thus, charge transfer cannot explain enhanced binding. In our recent DFT study, we found that CO_2 adsorption on the Cu−ZrO_2 interface depends both on electronic as well as structural features.[59] Enhanced binding may be due to the conformational flexibility of the ZnO monomer at the interface, which allows a bidentate binding geometry and a lower geometric strain for the formed CO_3 moiety. Nevertheless, this demonstrates that dispersed Zn can have a substantial impact on CO_2 binding at Cu/ZrO_2 interfaces regardless of its oxidation state. In a recent computational study,[16] the ZnO/Cu and inverse ZrO_2−Cu interfaces were modeled using a $Zn_1Zr_2O_3$ cluster model deposited on Cu(111). This model effectively activated and bound CO_2, with the molecule coordinated to the Zr center of the cluster through an oxygen. The adsorption energy of −1.07 eV falls within the same range as the aforementioned CuZn−ZrO_2 interfaces. However, the authors report significantly weaker binding (E_{ads} = −0.17 eV) on the ZnO/Cu side of the cluster.

After the successful adsorption of CO_2, the reaction can continue through a formate (HCOO) intermediate or via the reverse water−gas shift pathway (COOH intermediate) and eventually into methanol. A recent computational study[92] examining the binding of CO and CO_2 at a Cu/MgO interface determined the binding free energy of CO_2 to be −0.36 eV. It was suggested that at this stage, the adsorption may be strong enough to lead to catalyst poisoning and thus reduced conversion activity. While the free energies of the adsorbed molecules were not determined here, the strongly exothermic CO_2 binding to ZnO monomers as well as the known stability of HCOO on zirconia[13,17,81] may pose similar challenges if the barriers for further hydrogenation steps are high. In the past, the intermediate networks along both pathways have been studied on zirconia, Cu/CuZn surfaces, and metal−oxide interfaces.[3,4,13,15,17,81] From these results, one can conclude that certain sites are more optimal for the binding of different reaction intermediates, as some (such as COOH) adsorb more strongly to the Cu−ZrO_2 interface, while others (such as HCOO) bind on the ZrO_2 alone. A correlation has been identified between CO_2 adsorption strength and the binding of other intermediates, including COOH, HCO, and H_2CO.[17] It should be noted that, although promising, the strongly exothermic CO_2 adsorption does not directly imply that later hydrogenation steps are selective toward methanol or other desired products. While the binding of further intermediates and their elementary reactions were excluded from the present study, the Zn_yO_z species may also act as favorable active sites for later hydrogenation steps. Optimizing the amount of ZnO on the catalyst surface may selectively stabilize some CTM intermediates.

The dissociative adsorption of H_2 is crucial for CTM. It is generally agreed to take place on Cu nanoparticles.[3,9,93−96] Typical calculated dissociative adsorption energies on Cu(111) range from −0.1 to −0.3 eV[4,81,91] and −0.2 to −0.3 eV on the Cu(211) step site.[3,81] To investigate if ZnO monomers on zirconia influence H_2 dissociation, we considered H_2 adsorption and dissociation over the ZnO monomer. The heterolytic cleavage of H_2 leads to a structure where the proton is on the monomer oxygen and the hydride sits on the Zn cation (see Figure S10a). The dissociative adsorption energy is −1.28 eV. Alternatively, H_2 may adsorb on the monomer O atom only, in which case the formation of a H_2O species is possible. The formation of water leads to the breaking of the Zn−O bond (Figure S10b). The separated water molecule is strongly bound to the zirconia surface with an adsorption energy of −1.38 eV. The separated Zn center behaves as described earlier. However, this process is 0.76 eV less favorable relative to the aforementioned heterolytic cleavage and adsorption.

CONCLUSIONS

Our results show that monomeric ZnO units are resistant to initial stages of agglomeration on the zirconia surface, as there is no significant thermodynamic driving force to form small clusters. Instead, alloying ZnO with copper single atoms is a thermodynamically feasible pathway for particle growth, which could result in mixed metal particles of varying degrees of oxidation. Ab initio thermodynamic analysis shows that even under the reducing methanol synthesis conditions, the ZnO and mixed ZnO/Cu clusters on zirconia are not completely reduced. Formation free energies imply that ZnO monomers could be more resistant to agglomeration at the reaction conditions as opposed to oxidizing pretreatment conditions. Furthermore, ZnO migration to the copper−zirconia interface is thermodynamically favorable, whereas migration to the extended Cu nanoparticle (111) facets is not preferred. However, ZnO clustering is more feasible on the copper surface. If the ZnO species present on Cu are large enough (beyond the sizes explored in the present work), they may be able to resist migration to the interface and the support. Our results do not rule out the presence of larger structures, such as ZnO islands, on the copper particles, especially for larger ZnO loadings.

Small ZnO clusters are able to adsorb and activate CO_2 on ZrO_2, Cu(111), and the Cu−ZrO_2 interface. CO_2 binding is strongest at the Cu−ZrO_2 interface where dispersed ZnO

https://doi.org/10.1021/acs.jpcc.4c01300
J. Phys. Chem. C XXXX, XXX, XXX−XXX

promoter units are also thermodynamically most stable and resistant to forming larger ZnO structures. The Cu−ZnO−ZrO_2 interface offers stronger adsorption than the promoter-free Cu−ZrO_2 or nanoalloyed CuZn−ZrO_2 interfaces. ZnO dispersed on the surface of a Cu particle may also offer sites where CO_2 can be activated upon adsorption, as opposed to the physisorption typical of Cu surfaces. Our results offer an atomic-level look at the behavior of the hypothesized highly dispersed ZnO on a zirconia support and the origin of their promoting effect.

■ ASSOCIATED CONTENT

Data Availability Statement

The computed structures presented in this study are openly available to download from the Finnish Fairdata service at https://doi.org/10.23729/81cea552-50db-47b9-ac58-477977cbc71d.

Supporting Information

The Supporting Information is available free of charge at https://pubs.acs.org/doi/10.1021/acs.jpcc.4c01300.

Illustrations of global minimum energy structures, a full list of formation-, adhesion-, and cohesive energies, additional figures for the atomistic thermodynamics of $Cu_xZn_yO_z$ species, and atomic charges in CO_2 adsorption geometries (PDF)

■ AUTHOR INFORMATION

Corresponding Author

Karoliina Honkala − *Department of Chemistry, Nanoscience Center, University of Jyväskylä, Jyväskylä FI-40014, Finland;* orcid.org/0000-0002-3166-1077; Email: karoliina.honkala@jyu.fi

Authors

Aku Lempelto − *Department of Chemistry, Nanoscience Center, University of Jyväskylä, Jyväskylä FI-40014, Finland;* orcid.org/0000-0002-7731-0395

Minttu Kauppinen − *Department of Chemistry, Nanoscience Center, University of Jyväskylä, Jyväskylä FI-40014, Finland;* orcid.org/0000-0001-8721-3719

Complete contact information is available at: https://pubs.acs.org/10.1021/acs.jpcc.4c01300

Notes

The authors declare no competing financial interest.

■ ACKNOWLEDGMENTS

We thank Prof. Riikka Puurunen and her research group for fruitful discussions on ALD in catalysis and in CTM chemistry. The work was funded by Academy of Finland (project 329977). A.L. also acknowledges a kind grant by the Vilho, Yrjö, and Kalle Väisälä Foundation of the Finnish Academy of Science and Letters. Electronic structure calculations were carried out using computational resources provided by the CSC—IT Center for Science, Espoo, Finland (https://www.csc.fi/en/) and computer capacity from the Finnish Grid and Cloud Infrastructure (urn:nbn:fi:research-infras-2016072533).

■ REFERENCES

(1) Tackett, B. M.; Gomez, E.; Chen, J. G. Net reduction of CO_2 via its thermocatalytic and electrocatalytic transformation reactions in standard and hybrid processes. *Nat. Catal.* **2019**, *2*, 381−386.

(2) Kattel, S.; Liu, P.; Chen, J. G. Tuning Selectivity of CO_2 Hydrogenation Reactions at the Metal/Oxide Interface. *J. Am. Chem. Soc.* **2017**, *139*, 9739−9754.

(3) Behrens, M.; Studt, F.; Kasatkin, I.; Kühl, S.; Hävecker, M.; Abild-Pedersen, F.; Zander, S.; Girgsdies, F.; Kurr, P.; Kniep, B.-L.; et al. The Active Site of Methanol Synthesis over Cu/ZnO/Al_2O_3 Industrial Catalysts. *Science* **2012**, *336*, 893−897.

(4) Grabow, L. C.; Mavrikakis, M. Mechanism of methanol synthesis on Cu through CO_2 and CO hydrogenation. *ACS Catal.* **2011**, *1*, 365−384.

(5) Etim, U. J.; Song, Y.; Zhong, Z. Improving the Cu/ZnO-Based Catalysts for Carbon Dioxide Hydrogenation to Methanol, and the Use of Methanol As a Renewable Energy Storage Media. *Front. Energy Res.* **2020**, *8*, 545431.

(6) Scotti, N.; Bossola, F.; Zaccheria, F.; Ravasio, N. Copper−Zirconia Catalysts: Powerful Multifunctional Catalytic Tools to Approach Sustainable Processes. *Catalysts* **2020**, *10*, 168.

(7) Arena, F.; Barbera, K.; Italiano, G.; Bonura, G.; Spadaro, L.; Frusteri, F. Synthesis, characterization and activity pattern of Cu−ZnO/ZrO_2 catalysts in the hydrogenation of carbon dioxide to methanol. *J. Catal.* **2007**, *249*, 185−194.

(8) Arandia, A.; Yim, J.; Warraich, H.; Leppäkangas, E.; Bes, R.; Lempelto, A.; Gell, L.; Jiang, H.; Meinander, K.; Viinikainen, T.; et al. Effect of atomic layer deposited zinc promoter on the activity of copper-on-zirconia catalysts in the hydrogenation of carbon dioxide to methanol. *Appl. Catal. B: Environ.* **2023**, *321*, 122046.

(9) Wang, Y.; Kattel, S.; Gao, W.; Li, K.; Liu, P.; Chen, J. G.; Wang, H. Exploring the ternary interactions in Cu−ZnO−ZrO_2 catalysts for efficient CO_2 hydrogenation to methanol. *Nat. Commun.* **2019**, *10*, 1166.

(10) Le Valant, A.; Comminges, C.; Tisseraud, C.; Canaff, C.; Pinard, L.; Pouilloux, Y. The Cu−ZnO synergy in methanol synthesis from CO_2, Part 1: Origin of active site explained by experimental studies and a sphere contact quantification model on Cu + ZnO mechanical mixtures. *J. Catal.* **2015**, *324*, 41−49.

(11) Vesborg, P. C.; Chorkendorff, I.; Knudsen, I.; Balmes, O.; Nerlov, J.; Molenbroek, A. M.; Clausen, B. S.; Helveg, S. Transient behavior of Cu/ZnO-based methanol synthesis catalysts. *J. Catal.* **2009**, *262*, 65−72.

(12) Lunkenbein, T.; Schumann, J.; Behrens, M.; Schlögl, R.; Willinger, M. G. Formation of a ZnO Overlayer in Industrial Cu/ZnO/Al_2O_3 Catalysts Induced by Strong Metal-Support Interactions. *Angew. Chem., Int. Ed.* **2015**, *54*, 4544−4548.

(13) Larmier, K.; Liao, W.-C. C.; Tada, S.; Lam, E.; Verel, R.; Bansode, A.; Urakawa, A.; Comas-Vives, A.; Copéret, C. CO_2-to-Methanol Hydrogenation on Zirconia-Supported Copper Nanoparticles: Reaction Intermediates and the Role of the Metal−Support Interface. *Angew. Chem., Int. Ed.* **2017**, *56*, 2318−2323.

(14) Tang, Q.-L.; Hong, Q.-J.; Liu, Z.-P. CO_2 fixation into methanol at Cu/ZrO_2 interface from first principles kinetic Monte Carlo. *J. Catal.* **2009**, *263*, 114−122.

(15) Kattel, S.; Ramírez, P. J.; Chen, J. G.; Rodriguez, J. A.; Liu, P. Active sites for CO_2 hydrogenation to methanol on Cu/ZnO catalysts. *Science* **2017**, *355*, 1296−1299.

(16) Dharmalingam, B. C.; Koushik V, A.; Mureddu, M.; Atzori, L.; Lai, S.; Pettinau, A.; Kaisare, N. S.; Aghalayam, P.; Varghese, J. J. Unravelling the role of metal-metal oxide interfaces of Cu/ZnO/$ZrO_2Al_2O_3$ catalyst for methanol synthesis from CO_2: Insights from experiments and DFT-based microkinetic modeling. *Appl. Catal. B: Environ.* **2023**, *332*, 122743.

(17) Lempelto, A.; Gell, L.; Kiljunen, T.; Honkala, K. Exploring CO_2 hydrogenation to methanol at a CuZn-ZrO_2 interface via DFT calculations. *Catal. Sci. Technol.* **2023**, *13*, 4387−4399.

(18) Liu, X.; Luo, J.; Wang, H.; Huang, L.; Wang, S.; Li, S.; Sun, Z.; Sun, F.; Jiang, Z.; Wei, S.; et al. In Situ Spectroscopic Characterization and Theoretical Calculations Identify Partially Reduced ZnO_{1-x}/Cu Interfaces for Methanol Synthesis from CO_2. *Angew. Chem., Int. Ed.* **2022**, *61*, No. e202202330.

(19) Kauppinen, M.; Posada-Borbón, A.; Grönbeck, H. Methanol Synthesis Over PdIn, In_2O_3, and CuZn From First-Principles Microkinetics: Similarities and Differences. *J. Phys. Chem. C* **2022**, *126*, 15235−15246.
(20) Dong, X.; Li, F.; Zhao, N.; Xiao, F.; Wang, J.; Tan, Y. CO_2 hydrogenation to methanol over $Cu/ZnO/ZrO_2$ catalysts prepared by precipitation-reduction method. *Appl. Catal. B: Environ.* **2016**, *191*, 8−17.
(21) Zhan, H.; Shi, X.; Tang, B.; Wang, G.; Ma, B.; Liu, W. The performance of Cu/Zn/Zr catalysts of different Zr/(Cu+Zn) ratio for CO_2 hydrogenation to methanol. *Catal. Commun.* **2021**, *149*, 106264.
(22) Huang, C.; Chen, S.; Fei, X.; Liu, D.; Zhang, Y. Catalytic Hydrogenation of CO_2 to Methanol: Study of Synergistic Effect on Adsorption Properties of CO_2 and H_2 in $CuO/ZnO/ZrO_2$ System. *Catalysts* **2015**, *5*, 1846−1861.
(23) Yang, M.; Yu, J.; Zimina, A.; Sarma, B. B.; Pandit, L.; Grunwaldt, J.; Zhang, L.; Xu, H.; Sun, J. Probing the Nature of Zinc in Copper-Zinc-Zirconium Catalysts by Operando Spectroscopies for CO_2 Hydrogenation to Methanol. *Angew. Chem., Int. Ed.* **2023**, *62*, No. e202216803.
(24) Zabilskiy, M.; Sushkevich, V. L.; Palagin, D.; Newton, M. A.; Krumeich, F.; van Bokhoven, J. A. The unique interplay between copper and zinc during catalytic carbon dioxide hydrogenation to methanol. *Nat. Commun.* **2020**, *11*, 2409.
(25) Laudenschleger, D.; Ruland, H.; Muhler, M. Identifying the nature of the active sites in methanol synthesis over $Cu/ZnO/Al_2O_3$ catalysts. *Nat. Commun.* **2020**, *11*, 3898.
(26) Beck, A.; Zabilskiy, M.; Newton, M. A.; Safonova, O.; Willinger, M. G.; van Bokhoven, J. A. Following the structure of copper-zinc-alumina across the pressure gap in carbon dioxide hydrogenation. *Nat. Catal.* **2021**, *4*, 488−497.
(27) van Ommen, J. R.; Goulas, A.; Puurunen, R. L. Atomic Layer Deposition. In *Kirk-Othmer Encyclopedia of Chemical Technology*; Wiley, 2021; pp 1−42..
(28) Zhang, B.; Qin, Y. Interface Tailoring of Heterogeneous Catalysts by Atomic Layer Deposition. *ACS Catal.* **2018**, *8*, 10064−10081.
(29) Jiang, K.; Zhao, H.; Chen, Y.; Li, B.; Zhang, Z.; Cao, F.; Wu, L.; Tang, Y.; Li, T.; Tan, L. Tuning interfaces between Cu and oxide via atomic layer deposition method for CO_2 hydrogenation to methanol. *Catal. Sci. Technol.* **2024**, *14*, 261−266.
(30) Kauppinen, M. M.; Melander, M. M.; Honkala, K. First-principles insight into CO hindered agglomeration of Rh and Pt single atoms on: M-ZrO_2. *Catal. Sci. Technol.* **2020**, *10*, 5847−5855.
(31) Di Liberto, G.; Pacchioni, G. Modeling Single-Atom Catalysis. *Adv. Mater.* **2023**, *35*, 2307150.
(32) Ouyang, R.; Liu, J.-X.; Li, W.-X. Atomistic Theory of Ostwald Ripening and Disintegration of Supported Metal Particles under Reaction Conditions. *J. Am. Chem. Soc.* **2013**, *135*, 1760−1771.
(33) Reichenbach, T.; Mondal, K.; Jäger, M.; Vent-Schmidt, T.; Himmel, D.; Dybbert, V.; Bruix, A.; Krossing, I.; Walter, M.; Moseler, M. Ab initio study of CO_2 hydrogenation mechanisms on inverse ZnO/Cu catalysts. *J. Catal.* **2018**, *360*, 168−174.
(34) Reichenbach, T.; Walter, M.; Moseler, M.; Hammer, B.; Bruix, A. Effects of Gas-Phase Conditions and Particle Size on the Properties of Cu(111)-Supported Zn_yO_x Particles Revealed by Global Optimization and Ab Initio Thermodynamics. *J. Phys. Chem. C* **2019**, *123*, 30903−30916.
(35) Mondal, K.; Megha; Banerjee, A.; Fortunelli, A.; Walter, M.; Moseler, M. Ab Initio Modeling of the ZnO-Cu(111) Interface. *J. Phys. Chem. C* **2022**, *126*, 764−771.
(36) Palomino, R. M.; Ramírez, P. J.; Liu, Z.; Hamlyn, R.; Waluyo, I.; Mahapatra, M.; Orozco, I.; Hunt, A.; Simonovis, J. P.; Senanayake, S. D.; et al. Hydrogenation of CO_2 on ZnO/Cu(100) and ZnO/Cu(111) Catalysts: Role of Copper Structure and Metal−Oxide Interface in Methanol Synthesis. *J. Phys. Chem. B* **2018**, *122*, 794−800.
(37) Kuld, S.; Thorhauge, M.; Falsig, H.; Elkjaer, C. F.; Helveg, S.; Chorkendorff, I.; Sehested, J.; Elkjær, C. F.; Helveg, S.; Chorkendorff, I.; et al. Quantifying the promotion of Cu catalysts by ZnO for methanol synthesis. *Science* **2016**, *352*, 969−974.
(38) Fujitani, T.; Nakamura, J. The effect of ZnO in methanol synthesis catalysts on Cu dispersion and the specific activity. *Catal. Lett.* **1998**, *56*, 119−124.
(39) Choi, Y.; Futagami, K.; Fujitani, T.; Nakamura, J. The role of ZnO in Cu/ZnO methanol synthesis catalysts — morphology effect or active site model? *Appl. Catal., A* **2001**, *208*, 163−167.
(40) Topsøe, N.; Topsøe, H. On the nature of surface structural changes in Cu/ZnO methanol synthesis catalysts. *Top. Catal.* **1999**, *8*, 267−270.
(41) Grunwaldt, J. D.; Molenbroek, A. M.; Topsøe, N. Y.; Topsøe, H.; Clausen, B. S. In situ investigations of structural changes in Cu/ZnO catalysts. *J. Catal.* **2000**, *194*, 452−460.
(42) Kuld, S.; Conradsen, C.; Moses, P. G.; Chorkendorff, I.; Sehested, J. Quantification of Zinc Atoms in a Surface Alloy on Copper in an Industrial-Type Methanol Synthesis Catalyst. *Angew. Chem., Int. Ed.* **2014**, *53*, 5941−5945.
(43) Amann, P.; Klötzer, B.; Degerman, D.; Köpfle, N.; Götsch, T.; Lömker, P.; Rameshan, C.; Ploner, K.; Bikaljevic, D.; Wang, H.-Y.; et al. The state of zinc in methanol synthesis over a Zn/ZnO/Cu(211) model catalyst. *Science* **2022**, *376*, 603−608.
(44) Enkovaara, J.; Rostgaard, C.; Mortensen, J. J.; Chen, J.; Dułak, M.; Ferrighi, L.; Gavnholt, J.; Glinsvad, C.; Haikola, V.; Hansen, H. A.; et al. Electronic structure calculations with GPAW: a real-space implementation of the projector augmented-wave method. *J. Phys. Cond. Mater.* **2010**, *22*, 253202.
(45) Wellendorff, J.; Lundgaard, K. T.; Møgelhøj, A.; Petzold, V.; Landis, D. D.; Nørskov, J. K.; Bligaard, T.; Jacobsen, K. W. Density functionals for surface science: Exchange-correlation model development with Bayesian error estimation. *Phys. Rev. B* **2012**, *85*, 235149.
(46) Blöchl, P. E. Projector augmented-wave method. *Phys. Rev. B* **1994**, *50*, 17953−17979.
(47) Goedecker, S. Minima hopping: An efficient search method for the global minimum of the potential energy surface of complex molecular systems. *J. Chem. Phys.* **2004**, *120*, 9911−9917.
(48) Dudarev, S. L.; Botton, G. A.; Savrasov, S. Y.; Humphreys, C. J.; Sutton, A. P. Electron-energy-loss spectra and the structural stability of nickel oxide: An LSDA+U study. *Phys. Rev. B* **1998**, *57*, 1505−1509.
(49) Korpelin, V.; Melander, M. M.; Honkala, K. Reducing the Irreducible: Dispersed Metal Atoms Facilitate Reduction of Irreducible Oxides. *J. Phys. Chem. C* **2022**, *126*, 933−945.
(50) Hjorth Larsen, A.; Jørgen Mortensen, J.; Blomqvist, J.; Castelli, I. E.; Christensen, R.; Dułak, M.; Friis, J.; Groves, M. N.; Hammer, B.; Hargus, C.; et al. The atomic simulation environment—a Python library for working with atoms. *J. Phys. Condens. Mater.* **2017**, *29*, 273002.
(51) Bitzek, E.; Koskinen, P.; Gähler, F.; Moseler, M.; Gumbsch, P. Structural Relaxation Made Simple. *Phys. Rev. Lett.* **2006**, *97*, 170201.
(52) Bader, R. F. W. *Atoms in Molecules: A Quantum Theory International series of monographs on chemistry*; Oxford University Press: Oxford, 1990; .
(53) Tang, W.; Sanville, E.; Henkelman, G. A grid-based Bader analysis algorithm without lattice bias. *J. Phys.: Condens. Matter* **2009**, *21*, 084204.
(54) Gattinoni, C.; Michaelides, A. Atomistic details of oxide surfaces and surface oxidation: the example of copper and its oxides. *Surf. Sci. Rep.* **2015**, *70*, 424−447.
(55) Crystallography Open Database, 2023. http://www.crystallography.net/cod/(accessed 2023-05-11).
(56) Downs, R. T.; Hall-Wallace, M. The American Mineralogist Crystal Structure Database. *Am. Mineral.* **2003**, *88*, 247−250.
(57) Gražulis, S.; Chateigner, D.; Downs, R. T.; Yokochi, A. F. T.; Quirós, M.; Lutterotti, L.; Manakova, E.; Butkus, J.; Moeck, P.; Le Bail, A. Crystallography Open Database − an open-access collection of crystal structures. *J. Appl. Crystallogr.* **2009**, *42*, 726−729.

https://doi.org/10.1021/acs.jpcc.4c01300
J. Phys. Chem. C XXXX, XXX, XXX−XXX

(58) Vaitkus, A.; Merkys, A.; Gražulis, S. Validation of the Crystallography Open Database using the Crystallographic Information Framework. *J. Appl. Crystallogr.* **2021**, *54*, 661−672.
(59) Gell, L.; Lempelto, A.; Kiljunen, T.; Honkala, K. Influence of a Cu−zirconia interface structure on CO_2 adsorption and activation. *J. Chem. Phys.* **2021**, *154*, 214707.
(60) Sargeant, E.; Illas, F.; Rodríguez, P.; Calle-Vallejo, F. Importance of the gas-phase error correction for O_2 when using DFT to model the oxygen reduction and evolution reactions. *J. Electroanal. Chem.* **2021**, *896*, 115178.
(61) Almeida, M. O.; Kolb, M. J.; Lanza, M. R. V.; Illas, F.; Calle-Vallejo, F. Gas-Phase Errors Affect DFT-Based Electrocatalysis Models of Oxygen Reduction to Hydrogen Peroxide. *ChemElectroChem* **2022**, *9*, No. e202200210.
(62) Montemore, M. M.; van Spronsen, M. A.; Madix, R. J.; Friend, C. M. O_2 Activation by Metal Surfaces: Implications for Bonding and Reactivity on Heterogeneous Catalysts. *Chem. Rev.* **2018**, *118*, 2816−2862.
(63) Chase, M.; Davies, C.; Downey, J.; Frurip, D.; McDonald, R.; Syverud, A. *NIST JANAF thermochemical tables*; National Institute of Standards and Technology: Gaithersburg, 1986; ..
(64) Reuter, K.; Scheffler, M. Oxide formation at the surface of late 4d transition metals: insights from first-principles atomistic thermodynamics. *Appl. Phys. A: Mater. Sci. Process.* **2004**, *78*, 793−798.
(65) Thang, H. V.; Tosoni, S.; Fang, L.; Bruijnincx, P.; Pacchioni, G. Nature of Sintering-Resistant, Single-Atom Ru Species Dispersed on Zirconia-Based Catalysts: A DFT and FTIR Study of CO Adsorption. *ChemCatChem* **2018**, *10*, 2634−2645.
(66) Pacchioni, G. From CO_2 to Methanol on $Cu/ZnO/Al_2O_3$ Industrial Catalyst. What Do We Know about the Active Phase and the Reaction Mechanism? *ACS Catal.* **2024**, *14*, 2730−2745.
(67) Ruiz Puigdollers, A.; Schlexer, P.; Tosoni, S.; Pacchioni, G. Increasing oxide reducibility: The role of metal/oxide interfaces in the formation of oxygen vacancies. *ACS Catal.* **2017**, *7*, 6493−6513.
(68) Bazhenov, A. S.; Kauppinen, M. M.; Honkala, K. DFT Prediction of Enhanced Reducibility of Monoclinic Zirconia upon Rhodium Deposition. *J. Phys. Chem. C* **2018**, *122*, 6774−6778.
(69) Hinuma, Y.; Toyao, T.; Kamachi, T.; Maeno, Z.; Takakusagi, S.; Furukawa, S.; Takigawa, I.; Shimizu, K.-i. Density Functional Theory Calculations of Oxygen Vacancy Formation and Subsequent Molecular Adsorption on Oxide Surfaces. *J. Phys. Chem. C* **2018**, *122*, 29435−29444.
(70) Ozkan, D. M.; Uzun, A.; Caglayan, B. S.; Aksoylu, A. E. A DFT study on the role of oxygen vacancy on m-ZrO_2 $(\overline{1}11)$ in adsorption and dissociation of CO_2. *Surf. Sci.* **2023**, *736*, 122336.
(71) Liu, J. Catalysis by Supported Single Metal Atoms. *ACS Catal.* **2017**, *7*, 34−59.
(72) Syzgantseva, O. A.; Calatayud, M.; Minot, C. Revealing the Surface Reactivity of Zirconia by Periodic DFT Calculations. *J. Phys. Chem. C* **2012**, *116*, 6636−6644.
(73) Zhao, H.; Yu, R.; Ma, S.; Xu, K.; Chen, Y.; Jiang, K.; Fang, Y.; Zhu, C.; Liu, X.; Tang, Y.; et al. The role of $Cu_1−O_3$ species in single-atom Cu/ZrO_2 catalyst for CO_2 hydrogenation. *Nat. Catal.* **2022**, *5*, 818−831.
(74) Witoon, T.; Chalorngtham, J.; Dumrongbunditkul, P.; Chareonpanich, M.; Limtrakul, J. CO_2 hydrogenation to methanol over Cu/ZrO_2 catalysts: Effects of zirconia phases. *Chem. Eng. J.* **2016**, *293*, 327−336.
(75) Zabilskiy, M.; Sushkevich, V. L.; Newton, M. A.; Van Bokhoven, J. A. Copper-Zinc Alloy-Free Synthesis of Methanol from Carbon Dioxide over Cu/ZnO/Faujasite. *ACS Catal.* **2020**, *10*, 14240−14244.
(76) Nakamura, J.; Choi, Y.; Fujitani, T. On the issue of the active site and the role of ZnO in Cu/ZnO methanol synthesis catalysts. *Top. Catal.* **2003**, *22*, 277−285.
(77) Nakamura, J.; Fujitani, T.; Kuld, S.; Helveg, S.; Chorkendorff, I.; Sehested, J. Comment on "Active sites for CO_2 hydrogenation to methanol on Cu/ZnO catalysts. *Science* **2017**, *357*, No. eaan8074.
(78) Beck, A.; Huang, X.; Artiglia, L.; Zabilskiy, M.; Wang, X.; Rzepka, P.; Palagin, D.; Willinger, M. G.; van Bokhoven, J. A. The dynamics of overlayer formation on catalyst nanoparticles and strong metal-support interaction. *Nat. Commun.* **2020**, *11*, 3220.
(79) Wang, R.; Wang, H.; Weng, X.; Dai, J.; Gong, Z.; Zhao, C.; Lu, J.; Cui, Y.; Bao, X. Exploring the phase transformation in ZnO/Cu(111) model catalysts in CO_2 hydrogenation. *J. Energy Chem.* **2021**, *60*, 150−155.
(80) Senanayake, S. D.; Ramírez, P. J.; Waluyo, I.; Kundu, S.; Mudiyanselage, K.; Liu, Z.; Liu, Z.; Axnanda, S.; Stacchiola, D. J.; Evans, J.; et al. Hydrogenation of CO_2 to Methanol on CeOx/Cu(111) and ZnO/Cu(111) Catalysts: Role of the Metal−Oxide Interface and Importance of Ce3+ Sites. *J. Phys. Chem. C* **2016**, *120*, 1778−1784.
(81) Polierer, S.; Jelic, J.; Pitter, S.; Studt, F. On the Reactivity of the Cu/ZrO_2 System for the Hydrogenation of CO_2 to Methanol: A Density Functional Theory Study. *J. Phys. Chem. C* **2019**, *123*, 26904−26911.
(82) Dietze, E. M.; Abild-Pedersen, F.; Plessow, P. N. Comparison of Sintering by Particle Migration and Ripening through First-Principles-Based Simulations. *J. Phys. Chem. C* **2018**, *122*, 26563−26569.
(83) Hu, S.; Li, W.-X. Sabatier principle of metal-support interaction for design of ultrastable metal nanocatalysts. *Science* **2021**, *374*, 1360−1365.
(84) Sehested, J. Industrial and scientific directions of methanol catalyst development. *J. Catal.* **2019**, *371*, 368−375.
(85) Nakamura, J.; Nakamura, I.; Uchijima, T.; Watanabe, T.; Fujitani, T. Model studies of methanol synthesis on copper catalysts. *Stud. Surf. Sci. Catal.* **1996**, *101 B*, 1389−1399.
(86) Zander, S.; Kunkes, E. L.; Schuster, M. E.; Schumann, J.; Weinberg, G.; Teschner, D.; Jacobsen, N.; Schlögl, R.; Behrens, M. The role of the oxide component in the development of copper composite catalysts for methanol synthesis. *Angew. Chem., Int. Ed.* **2013**, *52*, 6536−6540.
(87) Kattel, S.; Ramírez, P. J.; Chen, J. G.; Rodriguez, J. A.; Liu, P. Response to Comment on "Active sites for CO_2 hydrogenation to methanol on Cu/ZnO catalysts. *Science* **2017**, *357*, No. eaan8210.
(88) Koitaya, T.; Yamamoto, K.; Uruga, T.; Yokoyama, T. Operando Characterization of Copper−Zinc−Alumina Catalyst for Methanol Synthesis from Carbon Dioxide and Hydrogen by Ambient-Pressure Hard X-ray Photoelectron Spectroscopy. *J. Phys. Chem. C* **2023**, *127*, 13044−13054.
(89) Agrell, J.; Birgersson, H.; Boutonnet, M.; Melián-Cabrera, I.; Navarro, R.; Fierro, J. Production of hydrogen from methanol over Cu/ZnO catalysts promoted by ZrO_2 and Al_2O_3. *J. Catal.* **2003**, *219*, 389−403.
(90) Studt, F.; Behrens, M.; Kunkes, E. L.; Thomas, N.; Zander, S.; Tarasov, A.; Schumann, J.; Frei, E.; Varley, J. B.; Abild-Pedersen, F.; et al. The Mechanism of CO and CO_2 Hydrogenation to Methanol over Cu-Based Catalysts. *ChemCatChem* **2015**, *7*, 1105−1111.
(91) Kopač, D.; Likozar, B.; Huš, M. Catalysis of material surface defects: Multiscale modeling of methanol synthesis by CO_2 reduction on copper. *Appl. Surf. Sci.* **2019**, *497*, 143783.
(92) Cao, A.; Wang, Z.; Li, H.; Elnabawy, A. O.; Nørskov, J. K. New insights on CO and CO_2 hydrogenation for methanol synthesis: The key role of adsorbate-adsorbate interactions on Cu and the highly active MgO-Cu interface. *J. Catal.* **2021**, *400*, 325−331.
(93) Li, K.; Chen, J. G. CO_2 Hydrogenation to Methanol over ZrO_2-Containing Catalysts: Insights into ZrO_2 Induced Synergy. *ACS Catal.* **2019**, *9*, 7840−7861.
(94) Fornero, E. L.; Bonivardi, A. L.; Baltanás, M. A. Isotopic study of the rates of hydrogen provision vs. methanol synthesis from CO_2 over Cu−Ga−Zr catalysts. *J. Catal.* **2015**, *330*, 302−310.
(95) Campbell, J. M.; Campbell, C. T. The dissociative adsorption of H_2 and D_2 on Cu(110): activation barriers and dynamics. *Surf. Sci.* **1991**, *259*, 1−17.
(96) Sakong, S.; Groß, A. Dissociative adsorption of hydrogen on strained Cu surfaces. *Surf. Sci.* **2003**, *525*, 107−118.

https://doi.org/10.1021/acs.jpcc.4c01300
J. Phys. Chem. C XXXX, XXX, XXX−XXX

DEPARTMENT OF CHEMISTRY, UNIVERSITY OF JYVÄSKYLÄ
RESEARCH REPORT SERIES

1. Vuolle, Mikko: Electron paramagnetic resonance and molecular orbital study of radical ions generated from (2.2)metacyclophane, pyrene and its hydrogenated compounds by alkali metal reduction and by thallium(III)trifluoroacetate oxidation. (99 pp.) 1976
2. Pasanen, Kaija: Electron paramagnetic resonance study of cation radical generated from various chlorinated biphenyls. (66 pp.) 1977
3. Carbon-13 Workshop, September 6-8, 1977. (91 pp.) 1977
4. Laihia, Katri: On the structure determination of norbornane polyols by NMR spectroscopy. (111 pp.) 1979
5. Nyrönen, Timo: On the EPR, ENDOR and visible absorption spectra of some nitrogen containing heterocyclic compounds in liquid ammonia. (76 pp.) 1978
6. Talvitie, Antti: Structure determination of some sesquiterpenoids by shift reagent NMR. (54 pp.) 1979
7. Häkli, Harri: Structure analysis and molecular dynamics of cyclic compounds by shift reagent NMR. (48 pp.) 1979
8. Pitkänen, Ilkka: Thermodynamics of complexation of 1,2,4-triazole with divalent manganese, cobalt, nickel, copper, zinc, cadmium and lead ions in aqueous sodium perchlorate solutions. (89 pp.) 1980
9. Asunta, Tuula: Preparation and characterization of new organometallic compounds synthesized by using metal vapours. (91 pp.) 1980
10. Sattar, Mohammad Abdus: Analyses of MCPA and its metabolites in soil. (57 pp.) 1980
11. Bibliography 1980. (31 pp.) 1981
12. Knuuttila, Pekka: X-Ray structural studies on some divalent 3d metal compounds of picolinic and isonicotinic acid N-oxides. (77 pp.) 1981
13. Bibliography 1981. (33 pp.) 1982
14. 6^{th} National NMR Symposium, September 9-10, 1982, Abstracts. (49 pp.) 1982
15. Bibliography 1982. (38 pp.) 1983
16. Knuuttila, Hilkka: X-Ray structural studies on some Cu(II), Co(II) and Ni(II) complexes with nicotinic and isonicotinic acid N-oxides. (54 pp.) 1983
17. Symposium on inorganic and analytical chemistry May 18, 1984, Program and Abstracts. (100 pp.) 1984
18. Knuutinen, Juha: On the synthesis, structure verification and gas chromatographic determination of chlorinated catechols and guaiacols occuring in spent bleach liquors of kraft pulp mill. (30 pp.) 1984
19. Bibliography 1983. (47 pp.) 1984
20. Pitkänen, Maija: Addition of BrCl, B_2 and Cl_2 to methyl esters of propenoic and 2-butenoic acid derivatives and ^{13}C NMR studies on methyl esters of saturated aliphatic mono- and dichlorocarboxylic acids. (56 pp.) 1985
21. Bibliography 1984. (39 pp.) 1985
22. Salo, Esa: EPR, ENDOR and TRIPLE spectroscopy of some nitrogen heteroaromatics in liquid ammonia. (111 pp.) 1985

23. Humppi, Tarmo: Synthesis, identification and analysis of dimeric impurities of chlorophenols. (39 pp.) 1985
24. Aho, Martti: The ion exchange and adsorption properties of sphagnum peat under acid conditions. (90 pp.) 1985
25. Bibliography 1985 (61 pp.) 1986
26. Bibliography 1986. (23 pp.) 1987
27. Bibliography 1987. (26 pp.) 1988
28. Paasivirta, Jaakko (Ed.): Structures of organic environmental chemicals. (67 pp.) 1988
29. Paasivirta, Jaakko (Ed.): Chemistry and ecology of organo-element compounds. (93 pp.) 1989
30. Sinkkonen, Seija: Determination of crude oil alkylated dibenzothiophenes in environment. (35 pp.) 1989
31. Kolehmainen, Erkki (Ed.): XII National NMR Symposium Program and Abstracts. (75 pp.) 1989
32. Kuokkanen, Tauno: Chlorocymenes and Chlorocymenenes: Persistent chlorocompounds in spent bleach liquors of kraft pulp mills. (40 pp.) 1989
33. Mäkelä, Reijo: ESR, ENDOR and TRIPLE resonance study on substituted 9,10-anthraquinone radicals in solution. (35 pp.) 1990
34. Veijanen, Anja: An integrated sensory and analytical method for identification of off-flavour compounds. (70 pp.) 1990
35. Kasa, Seppo: EPR, ENDOR and TRIPLE resonance and molecular orbital studies on a substitution reaction of anthracene induced by thallium(III) in two fluorinated carboxylic acids. (114 pp.) 1990
36. Herve, Sirpa: Mussel incubation method for monitoring organochlorine compounds in freshwater recipients of pulp and paper industry. (145 pp.) 1991
37. Pohjola, Pekka: The electron paramagnetic resonance method for characterization of Finnish peat types and iron (III) complexes in the process of peat decomposition. (77 pp.) 1991
38. Paasivirta, Jaakko (Ed.): Organochlorines from pulp mills and other sources. Research methodology studies 1988-91. (120 pp.) 1992
39. Veijanen, Anja (Ed.): VI National Symposium on Mass Spectrometry, May 13-15, 1992, Abstracts. (55 pp.) 1992
40. Rissanen, Kari (Ed.): The 7. National Symposium on Inorganic and Analytical Chemistry, May 22, 1992, Abstracts and Program. (153 pp.) 1992
41. Paasivirta, Jaakko (Ed.): CEOEC'92, Second Finnish-Russian Seminar: Chemistry and Ecology of Organo-Element Compounds. (93 pp.) 1992
42. Koistinen, Jaana: Persistent polychloroaromatic compounds in the environment: structure-specific analyses. (50 pp.) 1993
43. Virkki, Liisa: Structural characterization of chlorolignins by spectroscopic and liquid chromatographic methods and a comparison with humic substances. (62 pp.) 1993
44. Helenius, Vesa: Electronic and vibrational excitations in some

biologically relevant molecules. (30 pp.) 1993

45. Leppä-aho, Jaakko: Thermal behaviour, infrared spectra and x-ray structures of some new rare earth chromates(VI). (64 pp.) 1994
46. Kotila, Sirpa: Synthesis, structure and thermal behavior of solid copper(II) complexes of 2-amino-2- hydroxymethyl-1,3-propanediol. (111 pp.) 1994
47. Mikkonen, Anneli: Retention of molybdenum(VI), vanadium(V) and tungsten(VI) by kaolin and three Finnish mineral soils. (90 pp.) 1995
48. Suontamo, Reijo: Molecular orbital studies of small molecules containing sulfur and selenium. (42 pp.) 1995
49. Hämäläinen, Jouni: Effect of fuel composition on the conversion of fuel-N to nitrogen oxides in the combustion of small single particles. (50 pp.) 1995
50. Nevalainen, Tapio: Polychlorinated diphenyl ethers: synthesis, NMR spectroscopy, structural properties, and estimated toxicity. (76 pp.) 1995
51. Aittola, Jussi-Pekka: Organochloro compounds in the stack emission. (35 pp.) 1995
52. Harju, Timo: Ultrafast polar molecular photophysics of (dibenzylmethine)borondifluoride and 4-aminophthalimide in solution. (61 pp.) 1995
53. Maatela, Paula: Determination of organically bound chlorine in industrial and environmental samples. (83 pp.) 1995
54. Paasivirta, Jaakko (Ed.): CEOEC'95, Third Finnish-Russian Seminar: Chemistry and Ecology of Organo-Element Compounds. (109 pp.) 1995
55. Huuskonen, Juhani: Synthesis and structural studies of some supramolecular compounds. (54 pp.) 1995
56. Palm, Helena: Fate of chlorophenols and their derivatives in sawmill soil and pulp mill recipient environments. (52 pp.) 1995
57. Rantio, Tiina: Chlorohydrocarbons in pulp mill effluents and their fate in the environment. (89 pp.) 1997
58. Ratilainen, Jari: Covalent and non-covalent interactions in molecular recognition. (37 pp.) 1997
59. Kolehmainen, Erkki (Ed.): XIX National NMR Symposium, June 4-6, 1997, Abstracts. (89 pp.) 1997
60. Matilainen, Rose: Development of methods for fertilizer analysis by inductively coupled plasma atomic emission spectrometry. (41 pp.) 1997
61. Koistinen, Jari (Ed.): Spring Meeting on the Division of Synthetic Chemistry, May 15-16, 1997, Program and Abstracts. (36 pp.) 1997
62. Lappalainen, Kari: Monomeric and cyclic bile acid derivatives: syntheses, NMR spectroscopy and molecular recognition properties. (50 pp.) 1997
63. Laitinen, Eira: Molecular dynamics of cyanine dyes and phthalimides in solution: picosecond laser studies. (62 pp.) 1997
64. Eloranta, Jussi: Experimental and theoretical studies on some

quinone and quinol radicals. (40 pp.) 1997

65. Oksanen, Jari: Spectroscopic characterization of some monomeric and aggregated chlorophylls. (43 pp.) 1998
66. Häkkänen, Heikki: Development of a method based on laser-induced plasma spectrometry for rapid spatial analysis of material distributions in paper coatings. (60 pp.) 1998
67. Virtapohja, Janne: Fate of chelating agents used in the pulp and paper industries. (58 pp.) 1998
68. Airola, Karri: X-ray structural studies of supramolecular and organic compounds. (39 pp.) 1998
69. Hyötyläinen, Juha: Transport of lignin–type compounds in the receiving waters of pulp mills. (40 pp.) 1999
70. Ristolainen, Matti: Analysis of the organic material dissolved during totally chlorine-free bleaching. (40 pp.) 1999
71. Eklin, Tero: Development of analytical procedures with industrial samples for atomic emission and atomic absorption spectrometry. (43 pp.) 1999
72. Välisaari, Jouni: Hygiene properties of resol-type phenolic resin laminates. (129 pp.) 1999
73. Hu, Jiwei: Persistent polyhalogenated diphenyl ethers: model compounds syntheses, characterization and molecular orbital studies. (59 pp.) 1999
74. Malkavaara, Petteri: Chemometric adaptations in wood processing chemistry. (56 pp.) 2000
75. Kujala Elena, Laihia Katri, Nieminen Kari (Eds.): NBC 2000, Symposium on Nuclear, Biological and Chemical Threats in the 21st Century. (299 pp.) 2000
76. Rantalainen, Anna-Lea: Semipermeable membrane devices in monitoring persistent organic pollutants in the environment. (58 pp.) 2000
77. Lahtinen, Manu: *In situ* X-ray powder diffraction studies of Pt/C, CuCl/C and Cu_2O/C catalysts at elevated temperatures in various reaction conditions. (92 pp.) 2000
78. Tamminen, Jari: Syntheses, empirical and theoretical characterization, and metal cation complexation of bile acid-based monomers and open/closed dimers. (54 pp.) 2000
79. Vatanen, Virpi: Experimental studies by EPR and theoretical studies by DFT calculations of α-amino-9,10-anthraquinone radical anions and cations in solution. (37 pp.) 2000
80. Kotilainen, Risto: Chemical changes in wood during heating at 150-260 °C. (57 pp.) 2000
81. Nissinen, Maija: X-ray structural studies on weak, non-covalent interactions in supramolecular compounds. (69 pp.) 2001
82. Wegelius, Elina: X-ray structural studies on self-assembled hydrogen-bonded networks and metallosupramolecular complexes. (84 pp.) 2001
83. Paasivirta, Jaakko (Ed.): CEOEC'2001, Fifth Finnish-Russian Seminar: Chemistry and Ecology of Organo-Element Compounds. (163 pp.) 2001
84. Kiljunen, Toni: Theoretical studies on spectroscopy and

atomic dynamics in rare gas solids. (56 pp.) 2001

85. Du, Jin: Derivatives of dextran: synthesis and applications in oncology. (48 pp.) 2001
86. Koivisto, Jari: Structural analysis of selected polychlorinated persistent organic pollutants (POPs) and related compounds. (88 pp.) 2001
87. Feng, Zhinan: Alkaline pulping of non-wood feedstocks and characterization of black liquors. (54 pp.) 2001
88. Halonen, Markku: Lahon havupuun käyttö sulfaattiprosessin raaka-aineena sekä havupuun lahontorjunta. (90 pp.) 2002
89. Falábu, Dezsö: Synthesis, conformational analysis and complexation studies of resorcarene derivatives. (212 pp.) 2001
90. Lehtovuori, Pekka: EMR spectroscopic studies on radicals of ubiquinones Q-*n*, vitamin K_3 and vitamine E in liquid solution. (40 pp.) 2002
91. Perkkalainen, Paula: Polymorphism of sugar alcohols and effect of grinding on thermal behavior on binary sugar alcohol mixtures. (53 pp.) 2002
92. Ihalainen, Janne: Spectroscopic studies on light-harvesting complexes of green plants and purple bacteria. (42 pp.) 2002
93. Kunttu, Henrik, Kiljunen, Toni (Eds.): 4th International Conference on Low Temperature Chemistry. (159 pp.) 2002
94. Väisänen, Ari: Development of methods for toxic element analysis in samples with environmental concern by ICP-AES and ETAAS. (54 pp.) 2002
95. Luostarinen, Minna: Synthesis and characterisation of novel resorcarene derivatives. (200 pp.) 2002
96. Louhelainen, Jarmo: Changes in the chemical composition and physical properties of wood and nonwood black liquors during heating. (68 pp.) 2003
97. Lahtinen, Tanja: Concave hydrocarbon cyclophane π-prismands. (65 pp.) 2003
98. Laihia, Katri (Ed.): NBC 2003, Symposium on Nuclear, Biological and Chemical Threats – A Crisis Management Challenge. (245 pp.) 2003
99. Oasmaa, Anja: Fuel oil quality properties of wood-based pyrolysis liquids. (32 pp.) 2003
100. Virtanen, Elina: Syntheses, structural characterisation, and cation/anion recognition properties of nano-sized bile acid-based host molecules and their precursors. (123 pp.) 2003
101. Nättinen, Kalle: Synthesis and X-ray structural studies of organic and metallo-organic supramolecular systems. (79 pp.) 2003
102. Lampiselkä, Jarkko: Demonstraatio lukion kemian opetuksessa. (285 pp.) 2003
103. Kallioinen, Jani: Photoinduced dynamics of $Ru(dcbpy)_2(NCS)_2$ – in solution and on nanocrystalline titanium dioxide thin films. (47 pp.) 2004
104. Valkonen, Arto (Ed.): VII Synthetic Chemistry Meeting and XXVI Finnish NMR Symposium. (103 pp.) 2004

105. Vaskonen, Kari: Spectroscopic studies on atoms and small molecules isolated in low temperature rare gas matrices. (65 pp.) 2004
106. Lehtovuori, Viivi: Ultrafast light induced dissociation of $Ru(dcbpy)(CO)_2I_2$ in solution. (49 pp.) 2004
107. Saarenketo, Pauli: Structural studies of metal complexing Schiff bases, Schiff base derived *N*-glycosides and cyclophane π-prismands. (95 pp.) 2004
108. Paasivirta, Jaakko (Ed.): CEOEC'2004, Sixth Finnish-Russian Seminar: Chemistry and Ecology of Organo-Element Compounds. (147 pp.) 2004
109. Suontamo, Tuula: Development of a test method for evaluating the cleaning efficiency of hard-surface cleaning agents. (96 pp.) 2004
110. Güneş, Minna: Studies of thiocyanates of silver for nonlinear optics. (48 pp.) 2004
111. Ropponen, Jarmo: Aliphatic polyester dendrimers and dendrons. (81 pp.) 2004
112. Vu, Mân Thi Hong: Alkaline pulping and the subsequent elemental chlorine-free bleaching of bamboo (*Bambusa procera*). (69 pp.) 2004
113. Mansikkamäki, Heidi: Self-assembly of resorcinarenes. (77 pp.) 2006
114. Tuononen, Heikki M.: EPR spectroscopic and quantum chemical studies of some inorganic main group radicals. (79 pp.) 2005
115. Kaski, Saara: Development of methods and applications of laser-induced plasma spectroscopy in vacuum ultraviolet. (44 pp.) 2005
116. Mäkinen, Riika-Mari: Synthesis, crystal structure and thermal decomposition of certain metal thiocyanates and organic thiocyanates. (119 pp.) 2006
117. Ahokas, Jussi: Spectroscopic studies of atoms and small molecules isolated in rare gas solids: photodissociation and thermal reactions. (53 pp.) 2006
118. Busi, Sara: Synthesis, characterization and thermal properties of new quaternary ammonium compounds: new materials for electrolytes, ionic liquids and complexation studies. (102 pp.) 2006
119. Mäntykoski, Keijo: PCBs in processes, products and environment of paper mills using wastepaper as their raw material. (73 pp.) 2006
120. Laamanen, Pirkko-Leena: Simultaneous determination of industrially and environmentally relevant aminopolycarboxylic and hydroxycarboxylic acids by capillary zone electrophoresis. (54 pp.) 2007
121. Salmela, Maria: Description of oxygen-alkali delignification of kraft pulp using analysis of dissolved material. (71 pp.) 2007
122. Lehtovaara, Lauri: Theoretical studies of atomic scale impurities in superfluid ^{4}He. (87 pp.) 2007
123. Rautiainen, J. Mikko: Quantum chemical calculations of structures, bonding, and spectroscopic properties of some sulphur and selenium iodine cations. (71 pp.) 2007
124. Nummelin, Sami: Synthesis, characterization, structural and

retrostructural analysis of self-assembling pore forming dendrimers. (286 pp.) 2008

125. Sopo, Harri: Uranyl(VI) ion complexes of some organic aminobisphenolate ligands: syntheses, structures and extraction studies. (57 pp.) 2008
126. Valkonen, Arto: Structural characteristics and properties of substituted cholanoates and *N*-substituted cholanamides. (80 pp.) 2008
127. Lähde, Anna: Production and surface modification of pharmaceutical nano- and microparticles with the aerosol flow reactor. (43 pp.) 2008
128. Beyeh, Ngong Kodiah: Resorcinarenes and their derivatives: synthesis, characterization and complexation in gas phase and in solution. (75 pp.) 2008
129. Välisaari, Jouni, Lundell, Jan (Eds.): Kemian opetuksen päivät 2008: uusia oppimisympäristöjä ja ongelmalähtöistä opetusta. (118 pp.) 2008
130. Myllyperkiö, Pasi: Ultrafast electron transfer from potential organic and metal containing solar cell sensitizers. (69 pp.) 2009
131. Käkölä, Jaana: Fast chromatographic methods for determining aliphatic carboxylic acids in black liquors. (82 pp.) 2009
132. Koivukorpi, Juha: Bile acid-arene conjugates: from photoswitchability to cancer cell detection. (67 pp.) 2009
133. Tuuttila, Tero: Functional dendritic polyester compounds: synthesis and characterization of small bifunctional dendrimers and dyes. (74 pp.) 2009
134. Salorinne, Kirsi: Tetramethoxy resorcinarene based cation and anion receptors: synthesis, characterization and binding properties. (79 pp.) 2009
135. Rautiainen, Riikka: The use of first-thinning Scots pine (*Pinus sylvestris*) as fiber raw material for the kraft pulp and paper industry. (73 pp.) 2010
136. Ilander, Laura: Uranyl salophens: synthesis and use as ditopic receptors. (199 pp.) 2010
137. Kiviniemi, Tiina: Vibrational dynamics of iodine molecule and its complexes in solid krypton - Towards coherent control of bimolecular reactions? (73 pp.) 2010
138. Ikonen, Satu: Synthesis, characterization and structural properties of various covalent and non-covalent bile acid derivatives of N/O-heterocycles and their precursors. (105 pp.) 2010
139. Siitonen, Anni: Spectroscopic studies of semiconducting single-walled carbon nanotubes. (56 pp.) 2010
140. Raatikainen, Kari: Synthesis and structural studies of piperazine cyclophanes – Supramolecular systems through Halogen and Hydrogen bonding and metal ion coordination. (69 pp.) 2010
141. Leivo, Kimmo: Gelation and gel properties of two- and three-component Pyrene based low molecular weight organogelators. (116 pp.) 2011
142. Martiskainen, Jari: Electronic energy transfer in light-harvesting complexes isolated from *Spinacia oleracea* and from three

photosynthetic green bacteria *Chloroflexus aurantiacus*, *Chlorobium tepidum*, and *Prosthecochloris aestuarii*. (55 pp.) 2011

143. Wichmann, Oula: Syntheses, characterization and structural properties of [O,N,O,X´] aminobisphenolate metal complexes. (101 pp.) 2011
144. Ilander, Aki: Development of ultrasound-assisted digestion methods for the determination of toxic element concentrations in ash samples by ICP-OES. (58 pp.) 2011
145. The Combined XII Spring Meeting of the Division of Synthetic Chemistry and XXXIII Finnish NMR Symposium. Book of Abstracts. (90 pp.) 2011
146. Valto, Piia: Development of fast analysis methods for extractives in papermaking process waters. (73 pp.) 2011
147. Andersin, Jenni: Catalytic activity of palladium-based nanostructures in the conversion of simple olefinic hydro- and chlorohydrocarbons from first principles. (78 pp.) 2011
148. Aumanen, Jukka: Photophysical properties of dansylated poly(propylene amine) dendrimers. (55 pp.) 2011
149. Kärnä, Minna: Ether-functionalized quaternary ammonium ionic liquids – synthesis, characterization and physicochemical properties. (76 pp.) 2011
150. Jurček, Ondřej: Steroid conjugates for applications in pharmacology and biology. (57 pp.) 2011
151. Nauha, Elisa: Crystalline forms of selected Agrochemical actives: design and synthesis of cocrystals. (77 pp.) 2012
152. Ahkola, Heidi: Passive sampling in monitoring of nonylphenol ethoxylates and nonylphenol in aquatic environments. (92 pp.) 2012
153. Helttunen, Kaisa: Exploring the self-assembly of resorcinarenes: from molecular level interactions to mesoscopic structures. (78 pp.) 2012
154. Linnanto, Juha: Light excitation transfer in photosynthesis revealed by quantum chemical calculations and exiton theory. (179 pp.) 2012
155. Roiko-Jokela, Veikko: Digital imaging and infrared measurements of soil adhesion and cleanability of semihard and hard surfaces. (122 pp.) 2012
156. Noponen, Virpi: Amides of bile acids and biologically important small molecules: properties and applications. (85 pp.) 2012
157. Hulkko, Eero: Spectroscopic signatures as a probe of structure and dynamics in condensed-phase systems – studies of iodine and gold ranging from isolated molecules to nanoclusters. (69 pp.) 2012
158. Lappi, Hanna: Production of Hydrocarbon-rich biofuels from extractives-derived materials. (95 pp.) 2012
159. Nykänen, Lauri: Computational studies of Carbon chemistry on transition metal surfaces. (76 pp.) 2012
160. Ahonen, Kari: Solid state studies of pharmaceutically important molecules and their derivatives. (65 pp.) 2012

161. Pakkanen, Hannu: Characterization of organic material dissolved during alkaline pulping of wood and non-wood feedstocks. (76 pp.) 2012
162. Moilanen, Jani: Theoretical and experimental studies of some main group compounds: from closed shell interactions to singlet diradicals and stable radicals. (80 pp.) 2012
163. Himanen, Jatta: Stereoselective synthesis of Oligosaccharides by *De Novo* Saccharide welding. (133 pp.) 2012
164. Bunzen, Hana: Steroidal derivatives of nitrogen containing compounds as potential gelators. (76 pp.) 2013
165. Seppälä, Petri: Structural diversity of copper(II) amino alcohol complexes. Syntheses, structural and magnetic properties of bidentate amino alcohol copper(II) complexes. (67 pp.) 2013
166. Lindgren, Johan: Computational investigations on rotational and vibrational spectroscopies of some diatomics in solid environment. (77 pp.) 2013
167. Giri, Chandan: Sub-component self-assembly of linear and non-linear diamines and diacylhydrazines, formulpyridine and transition metal cations. (145 pp.) 2013
168. Riisiö, Antti: Synthesis, Characterization and Properties of Cu(II)-, Mo(VI)- and U(VI) Complexes With Diaminotetraphenolate Ligands. (51 pp.) 2013
169. Kiljunen, Toni (Ed.): Chemistry and Physics at Low Temperatures. Book of Abstracts. (103 pp.) 2013
170. Hänninen, Mikko: Experimental and Computational Studies of Transition Metal Complexes with Polydentate Amino- and Aminophenolate Ligands: Synthesis, Structure, Reactivity and Magnetic Properties. (66 pp.) 2013
171. Antila, Liisa: Spectroscopic studies of electron transfer reactions at the photoactive electrode of dye-sensitized solar cells. (53 pp.) 2013
172. Kemppainen, Eeva: Mukaiyama-Michael reactions with α-substituted acroleins – a useful tool for the synthesis of the pectenotoxins and other natural product targets. (190 pp.) 2013
173. Virtanen, Suvi: Structural Studies of Dielectric Polymer Nanocomposites. (49 pp.) 2013
174. Yliniemelä-Sipari, Sanna: Understanding The Structural Requirements for Optimal Hydrogen Bond Catalyzed Enolization – A Biomimetic Approach.(160 pp.) 2013
175. Leskinen, Mikko V: Remote β-functionalization of β'-keto esters. (105 pp.) 2014
176. 12th European Conference on Research in Chemistry Education (ECRICE2014). Book of Abstracts. (166 pp.) 2014
177. Peuronen, Anssi: N-Monoalkylated DABCO-Based N-Donors as Versatile Building Blocks in Crystal Engineering and Supramolecular Chemistry. (54 pp.) 2014
178. Perämäki, Siiri: Method development for determination and recovery of rare earth elements from industrial fly ash. (88 pp.) 2014

179. Chernyshev, Alexander, N.: Nitrogen-containing ligands and their platinum(IV) and gold(III) complexes: investigation and basicity and nucleophilicity, luminescence, and aurophilic interactions. (64 pp.) 2014
180. Lehto, Joni: Advanced Biorefinery Concepts Integrated to Chemical Pulping. (142 pp.) 2015
181. Tero, Tiia-Riikka: Tetramethoxy resorcinarenes as platforms for fluorescent and halogen bonding systems. (61 pp.) 2015
182. Löfman, Miika: Bile acid amides as components of microcrystalline organogels. (62 pp.) 2015
183. Selin, Jukka: Adsorption of softwood-derived organic material onto various fillers during papermaking. (169 pp.) 2015
184. Piisola, Antti: Challenges in the stereoselective synthesis of allylic alcohols. (210 pp.) 2015
185. Bonakdarzadeh, Pia: Supramolecular coordination polyhedra based on achiral and chiral pyridyl ligands: design, preparation, and characterization. (65 pp.) 2015
186. Vasko, Petra: Synthesis, characterization, and reactivity of heavier group 13 and 14 metallylenes and metalloid clusters: small molecule activation and more. (66 pp.) 2015
187. Topić, Filip: Structural Studies of Nano-sized Supramolecular Assemblies. (79 pp.) 2015
188. Mustalahti, Satu: Photodynamics Studies of Ligand-Protected Gold Nanoclusters by using Ultrafast Transient Infrared Spectroscopy. (58 pp.) 2015
189. Koivisto, Jaakko: Electronic and vibrational spectroscopic studies of gold-nanoclusters. (63 pp.) 2015
190. Suhonen, Aku: Solid state conformational behavior and interactions of series of aromatis oligoamide foldamers. (68 pp.) 2016
191. Soikkeli, Ville: Hydrometallurgical recovery and leaching studies for selected valuable metals from fly ash samples by ultrasound-assisted extraction followed by ICP-OES determination. (107 pp.) 2016
192. XXXVIII Finnish NMR Symposium. Book of Abstracts. (51 pp.) 2016
193. Mäkelä, Toni: Ion Pair Recognition by Ditopic Crown Ether Based bis-Urea and Uranyl Salophen Receptors. (75 pp.) 2016
194. Lindholm-Lehto, Petra: Occurrence of pharmaceuticals in municipal wastewater treatment plants and receiving surface waters in Central and Southern Finland. (98 pp.) 2016
195. Härkönen, Ville: Computational and Theoretical studies on Lattice Thermal conductivity and Thermal properties of Silicon Clathrates. (89 pp.) 2016
196. Tuokko, Sakari: Understanding selective reduction reactions with heterogeneous Pd and Pt: climbing out of the black box. (85 pp.) 2016
197. Nuora, Piia: Monitapaustutkimus LUMA-Toimintaan liittyvissä oppimisympäristöissä tapahtuvista kemian oppimiskokemuksista. (171 pp.) 2016

198. Kumar, Hemanathan: Novel Concepts on The Recovery of By-Products from Alkaline Pulping. (61 pp.) 2016
199. Arnedo-Sánchez, Leticia: Lanthanide and Transition Metal Complexes as Building Blocks for Supramolecular Functional Materials. (227 pp.) 2016
200. Gell, Lars: Theoretical Investigations of Ligand Protected Silver Nanoclusters. (134 pp.) 2016
201. Vaskuri, Juhani: Oppiennätyksistä opetussuunnitelman perusteisiin - lukion kemian kansallisen opetussuunnitelman kehittyminen Suomessa vuosina 1918-2016. (314 pp.) 2017
202. Lundell Jan, Kiljunen Toni (Eds.): 22nd Horizons in Hydrogen Bond Research. Book of Abstracts. 2017
203. Turunen, Lotta: Design and construction of halogen-bonded capsules and cages. (61 pp.) 2017
204. Hurmalainen, Juha: Experimental and computational studies of unconventional main group compounds: stable radicals and reactive intermediates. (88 pp.) 2017
205. Koivistoinen Juha: Non-linear interactions of femtosecond laser pulses with graphene: photo-oxidation, imaging and photodynamics. (68 pp.) 2017
206. Chen, Chengcong: Combustion behavior of black liquors: droplet swelling and influence of liquor composition. (39 pp.) 2017
207. Mansikkamäki, Akseli: Theoretical and Computational Studies of Magnetic Anisotropy and Exchange Coupling in Molecular Systems. (190 p. + included articles) 2018.
208. Tatikonda, Rajendhraprasad: Multivalent N-donor ligands for the construction of coordination polymers and coordination polymer gels. (62 pp.) 2018
209. Budhathoki, Roshan: Beneficiation, desilication and selective precipitation techniques for phosphorus refining from biomass derived fly ash. (64 pp.) 2018
210. Siitonen, Juha: Synthetic Studies on 1-azabicyclo[5.3.0]decane Alkaloids. (140 pp.) 2018
211. Ullah, Saleem: Advanced Biorefinery Concepts Related to Non-wood Feedstocks. (57 pp.) 2018
212. Ghalibaf, Maryam: Analytical Pyrolysis of Wood and Non-Wood Materials from Integrated Biorefinery Concepts. (106 pp.) 2018

DEPARTMENT OF CHEMISTRY, UNIVERSITY OF JYVÄSKYLÄ
DISSERTATIONS PUBLISHED IN THE JYU DISSERTATIONS RESEARCH SERIES

1. Bulatov, Evgeny: Synthetic and structural studies of covalent and non-covalent interactions of ligands and metal center in platinum(II) complexes containing 2,2′-dipyridylamine or oxime ligands. (58 pp.) 2019. JYU Dissertations 70.
2. Annala, Riia: Conformational Properties and Anion Complexes of Aromatic Oligoamide Foldamers. (80 pp.) 2019. JYU Dissertations 84.
3. Isoaho, Jukka Pekka: Dithionite Bleaching of Thermomechanical Pulp - Chemistry and Optimal Conditions. (73 pp.) 2019. JYU Dissertations 85.
4. Nygrén, Enni: Recovery of rubidium from power plant fly ash. (98 pp.) 2019. JYU Dissertations 136.
5. Kiesilä, Anniina: Supramolecular chemistry of anion-binding receptors based on concave macromolecules. (68 pp.) 2019. JYU Dissertations 137.
6. Sokolowska, Karolina: Study of water-soluble p-MBA-protected gold nanoclusters and their superstructures. (60 pp.) 2019. JYU Dissertations 167.
7. Lahtinen, Elmeri: Chemically Functional 3D Printing: Selective Laser Sintering of Customizable Metal Scavengers. (71 pp.) 2019. JYU Dissertations 175.
8. Larijani, Amir: Oxidative reactions of cellulose under alkaline conditions. (102 pp.) 2020. JYU Dissertations 217.
9. Kolari, Kalle: Metal-metal contacts in late transition metal polymers. (60 pp.) 2020. JYU Dissertations 220.
10. Kauppinen, Minttu: Multiscale computational investigation of catalytic properties of zirconia supported noble metals. (87 pp.) 2020. JYU Dissertations 231.
11. Ding, Xin: Halogen Bond in Crystal Engineering: Structural Studies on Crystals with Ruthenium Centered Complexes and 1-(4-Pyridyl)-4-thiopyridine Zwitterion as Halogen Bond Acceptors. (59 pp.) 2020. JYU Dissertations 323.
12. Neuvonen, Antti: Toward an Understanding of Hydrogen-Bonding Bifunctional Organocatalyst Conformations and Their Activity in Asymmetric Mannich Reactions. (77 pp.) 2020. JYU Dissertations 336.
13. Kortet, Sami: 2,5-Diarylpyrrolidines and Pyroglutamic-Acid-Derived 2-Diarylmethyl-5-Aryl-Pyrrolidines: Their Synthesis and Use in Asymmetric Synthesis. (221 pp.) 2020. JYU Dissertations 337.
14. Saarnio, Ville: Fluorescent probes, noble metal nanoparticles and their nanocomposites: detection of nucleic acids and other biological targets. (80 pp.) 2021. JYU Dissertations 361.
15. Chernysheva, Maria: σ-hole interactions: the effect of the donors and acceptors nature in selenoureas, thioureas, halogenated species, substituted benzenes, and their adducts. (72 pp.) 2021. JYU Dissertations 370.
16. Bulatova, Margarita: Noncovalent interactions as a tool for supramolecular self-assembly of metallopolymers. (62 pp.) 2021. JYU Dissertations 377.

17. Romppanen, Sari: Laser-spectroscopic studies of rare earth element- and lithium-bearing minerals and rocks. (66 pp.) 2021. JYU Dissertations 393.
18. Kukkonen, Esa: Nonlinear optical materials through weak interactions and their application in 3D printing. (58 pp.) 2021. JYU Dissertations 441.
19. Kuosmanen, Riikka: The Effect of Structure on the Gel Formation Ability and the Properties of Bile Acid Based Supramolecular Organogels. (68 pp.) 2021. JYU Dissertations 465.
20. Reuna, Sini: Development of a Method for Phosphorus Recovery from Wastewaters. (67 pp.) 2022. JYU Dissertations 486.
21. Taipale, Essi: Synthetic and Structural Studies on the Effect of Non-Covalent Interactions on N(*sp2*)-Heterocyclic Molecules. (67 pp.) 2022. JYU Dissertations 496.
22. Järvinen, Teemu: Molecular Dynamics View on Matrix Isolation. (143 pp.) 2022. JYU Dissertations 544.
23. Kumar, Parveen: Synthesis and Structural Studies on Halogen(I) Complexes. (160 pp.) 2022. JYU Dissertations 549.
24. Forsblom, Samu: Design and Construction of Metal-Organic Polyhedra. (212 pp.) 2022. JYU Dissertations 569.
25. Korpelin, Ville: Computational Studies of Catalytic Active Site Properties and Reactions at the Metal–Oxide Interface. (78 pp.) 2022. JYU Dissertations 578.
26. Vuori, Hannu: Extending Benson Group Increment Theory to Compounds of Phosphorus, Silicon, and Boron with Computational Chemistry. (59 pp.) 2022. JYU Dissertations 581.
27. Pallerla, Rajanish: Studies Towards Synthesis of Favipiravir & Humilisin E. (139 pp.) 2023. JYU Dissertations 611.
28. Taponen, Anni: Radical-Ion Salts based on Thiazyls and Tetracyanoquinodimethane: Hysteretic Magnetic Bistability in a Multicomponent System. (66 pp.) 2023. JYU Dissertations 613.
29. Aho, Noora: Molecular Dynamics Simulations of Acids and Bases in Biomolecular Environments. (78 pp.) 2023. JYU Dissertations 614.
30. Sabooni Asre Hazer, Maryam: Electronic and Optical Properties of Gold Clusters with Carbene Ligands using Density Functional Theory Calculations. (68 pp.) 2023. JYU Dissertations 650.
31. Kinnunen, Virva-Tuuli: Improving the Accuracy of Single Particle ICP-MS Analyses of Au and Ag Nanoparticles. (67 pp.) 2023. JYU Dissertations 689.
32. Kulomäki, Suvi: Preconcentration, Speciation, and Determination of Mercury in Natural Waters by Inductively Coupled Plasma Mass Spectrometry. (61 pp.) 2023. JYU Dissertations 725.
33. Schirmer, Johanna: Effects of Two-Photon Oxidation for the Development of Graphene-Bio Interfaces. (69 pp.) 2023. JYU Dissertations 726.
34. Halmemies, Eelis: Chemical Changes in the Industrial Extractive-Containing Sidestreams of Norway Spruce (*Picea abies*) during Storage. (84 pp.) 2024. JYU Dissertations 737.

35. Alaranta, Johanna: Synthesis of Monomethine Cyanine Dyes and Gold Nanoclusters and their Applications as Fluorescent Probes. (67 pp.) 2024. JYU Dissertations 766.
36. Chevigny, Romain: Out-of-equilibrium and in-equilibrium amino acid-based supramolecular gels: Transient self-assembly and hybrid materials. (79 pp.) 2024. JYU Dissertations 768.
37. Mahajan, Shreya: Exploring the Applicability of Amine-Containing Metal–Organic Frameworks on Direct Air Capture of Carbon Dioxide. (69 pp.) 2024. JYU Dissertations 819.
38. Lehmann, Annika: Experimental and Computational Studies of Reactive Main Group Species: Low-Coordinate Complexes, Multiple Bonding, and Hydrometallation. (65 pp.) 2024. JYU Dissertations 829.